KU LEUVEN

ARENBERG DOCTORAL SCHOOL
Faculty of Science

Development, synthesis and characterization of multifunctional nanomaterials

Brullot Ward

Dissertation presented in partial
fulfillment of the requirements for the
degree of Doctor in Science

May 2014

Development, synthesis and characterization of multifunctional nanomaterials

Brullot WARD

Examination committee:
Prof. dr. K. Binnemans, chair
Prof. dr. T. Verbiest, supervisor
dr. V.K. Valev, co-supervisor
Prof. dr. M. Van der Auweraer
Prof. dr. S. De Feyter
Prof. dr. G. Koeckelberghs
Prof. dr. V. Liégeois
(Université de Namur)

Dissertation presented in partial fulfillment of the requirements for the degree of Doctor in Science

May 2014

Uitgegeven in eigen beheer, Brullot Ward, Celestijnenlaan 200D box 2425, B-3001 Heverlee (Belgium)

ISBN XXX-XX-XXXX-XXX-X
D/XXXX/XXXX/XX

Abstract

To achieve the societal and technological ambitions set for nanotechnology in general, multifunctional magnetic-plasmonic nanostructures can be a great asset. Such multifunctional materials, in which magnetic and plasmonic functionalities are combined at the nanoscale, can be used to unravel fundamental interactions between light and magnetism at that same scale. Further, they can also be applied in e.g. biomedicine for cancer therapy, catalysis for improved reaction rates at lower temperatures, sensors for magnetic field strength and miniaturized optical components such as optical isolators.

In the first part of this work we present the calculated optical properties of core-shell magnetic-plasmonic nanospheres and nanorods as a function of nanostructure composition, size, and shape with a focus on biomedical applications. With this knowledge it is possible to rationally design and synthesize structures that possess a plasmon band in the advantageous biomedical near-infrared spectral window region and other optical properties such as scattering and absorption cross sections as desired for potential application in life sciences.

To deal with the disadvantages of previously used synthesis protocols for nanoparticle-based thin film magnetic-plasmonic materials, a novel synthetic protocol was devised. The protocol itself, the resulting materials and their linear, nonlinear and magneto-optical properties are described in the second part of this work.

Using short bifunctional molecular linkers, we produced magnetic-plasmonic nanoparticle multilayers by a novel Layer-by-Layer (LbL) synthesis on glass substrates. No polymers or polyelectolytes were required during synthesis. Resulting nanocomposites, incorporating gold, silver and magnetite nanoparticles were homogeneous over a large area, had large nanoparticle filling fractions and showed tunability of the plasmon wavelength over a very broad spectral range by changing composite thickness through the number of added nanoparticle layers. Theoretical calculations were performed to verify and explain the observed optical properties of these magnetic-plasmonic assemblies. The calculations and the comparison with experimental observations lead us to a more nuanced view of the LbL self-assembly process as a function of layers. Nonlinear optical microscope images confirmed homogeneity of the sample and the generated nonlinear optical signals. Spectral nonlinear optical measurements showed that gold-magnetite nanoparticle multilayers combine and simultaneously enhances second and third order nonlinear optical processes. Large magneto-optical responses were measured for gold-magnetite composites and the influence of the plasmonic gold nanoparticles was established.

These results show that the developed Layer-by-Layer synthesis protocol can be used to produce homogeneous thin films of good quality. Advantageous and tuneable optical properties, large magneto-optical responses and the observed nonlinear optical resonance enhancements of such thin films make them attractive candidates for further fundamental research into e.g. magnetoplasmonics and for application in sensors or optical components.

Beknopte samenvatting

Om aan de vooropgestelde maatschappelijke en technologische ambities voor nanotechnologie te voldoen kunnen multifunctionele magnetisch-plasmonische nanostructuren een grote troef zijn. Dergelijke multifunctionele materialen, waarin magnetische en plasmonische functies op de nanoschaal worden gecombineerd kunnen worden gebruikt om de fundamentele interacties tussen licht en magnetisme op diezelfde schaal te ontrafelen. Verder kunnen ze ook worden toegepast in vb. de geneeskunde voor kankertherapie, in katalyse voor verbeterde reactiesnelheden bij lagere werkingstemperaturen, in sensoren voor magnetische veldsterkte en in geminiaturiseerde optische componenten zoals optische isolatoren.

In het eerste deel van dit werk stellen we de berekende optische eigenschappen voor van kern-schaal magnetisch-plasmonische nanosferen en -staven in functie van samenstelling, grootte en vorm met de focus op biomedische applicaties. Met deze kennis is het mogelijk om rationeel ontworpen nanostructuren te synthetiseren die een plasmonband bezitten in het voor biomedische toepassingen voordelige nabij-infrarood spectraal venster en met andere optische eigenschappen zoals verstrooiing en absorptie doorsnedes die gewenst zijn voor potentiële toepassingen in de biowetenschappen.

Omwille van de nadelen van eerder gebruikte syntheseprotocollen voor nanopartikel-gebaseerde magnetisch-plasmonische dunne filmen werd een nieuw syntheseprotocol ontwikkeld. Het protocol zelf, de resulterende materialen en hun lineaire, niet-lineaire en magneto-optische eigenschappen worden beschreven in het tweede deel van dit werk.

Door een nieuw ontwikkelde laag-na-laag synthese met korte bifunctionele moleculaire linkers produceerden we magnetisch-plasmonische nanopartikel multilagen op glazen substraten. Tijdens de synthese werden geen polymeren of polyelectrolyten gebruikt. De resulterende nanocomposieten waarin goud, zilver en magnetiet nanopartikels werden samengebracht waren homogeen over grote oppervlaktes en hadden grote nanopartikel vulfracties. Hun plasmongolflengte kon worden aangepast over een groot spectraal bereik door het veranderen van dikte van de composiet, wat mogelijk was door het aantal afgezette lagen te variëren. Theoretische berekeningen werden uitgevoerd om de geobserveerde optische eigenschappen van deze magnetisch-plasmonische structuren te verifiëren en te verklaren. De resultaten van de berekeningen en de vergelijking hiervan met de experimentele observaties leidden ons naar een meer genuanceerd beeld van het laag-na-laag zelf-assemblage proces als functie van het aantal afgezette lagen. Niet-lineair optische microscopiebeelden bevestigden de homogeniteit van het staal en de gegenereerde niet-lineaire optische signalen. Spectrale niet-lineair optische metingen toonden aan dat goud-magnetiet nanopartikel multilagen tweede- en derde-orde niet-lineaire optische processen combineren en simultaan versterken. Sterke magneto-optische signalen werden gemeten voor goud-magnetiet nanocomposieten en de invloed van de plasmonische goud nanopartikels vastgesteld.

Deze resultaten tonen aan dat het ontwikkelde laag-na-laag syntheseprotocol gebruikt kan worden voor het produceren van homogene dunne filmen van goede kwaliteit. Voordelige en aanpasbare optische eigenschappen, sterke magneto-optische signalen en de geobserveerde resonantieversterking van niet-lineair optische processen van zulke dunne filmen maakt dat deze aantrekkelijke kandidaten zijn voor verder fundamenteel onderzoek in vb. magnetoplasmonica en voor toepassingen zoals sensoren of optische componenten.

List of Abbreviations

AFM	Atomic force microscopy
APTMS	Aminopropyltrimethoxy silane
DDA	Discrete dipole approximation
DLS	Dynamic light scattering
FE	Faraday Ellipticity
FR	Faraday Rotation
FT-IR	Fourier transform infrared spectroscopy
HHG	Higher harmonic generation
IVCT	Intervalence charge transfer
LSPR	Localized surface plasmon resonance
Mag	Magnetite
MAIL	Multiphoton-absorption-induced-luminescence
MNP	Magnetite nanoparticle
MRI	Magnetic resonance imaging
NDL	Nanoparticle double layer
NIR	Near-infrared
NP	Nanoparticle
PEG	Polyethylene glycol
SEM	Scanning electron microscopy
SERS	Surface-enhanced Raman scattering
SFM	Scanning force microscopy
SHG	Second harmonic generation
TEM	Transmission electron microscopy
THG	Third harmonic generation
TPL	Two-photon luminescence
UV-vis	UV-visible
UV-vis-NIR	UV-visible-near-infrared
VSM	Vibrating sample magnetometry
XRD	X-ray diffraction

List of Symbols

α	Polarization
α-Fe_2O_3	Hematite
β	Full width at half maximum
γ-Fe_2O_3	Maghemite
ϵ	Dielectric function
$\epsilon_{extinction}$	Molar coefficient of extinction
ϵ_m	Medium dielectric constant
ϵ_{molar}	Spectroscopic molar coefficient
$\epsilon_{scattering}$	Molar coefficient of scattering
ζ	Orientation parameter
η_F	Faraday ellipticity angle
θ_F	Faraday rotation angle
θ	Scattering angle
λ	Wavelength
λ_{max}	Plasmon wavelength
μ_m	Magnetic moment
μ_e	Electric dipole moment
τ	Relaxation time
τ_i	Intrinsic relaxation time
τ_m	Measuring time
χ	Optical electric field susceptibility
χ_m	Magnetic susceptibility
ω	Frequency
B	Magnetic flux density
$C_{\text{absorption}}$	Absorption cross section
$C_{\text{extinction}}$	Extinction cross section
$C_{\text{scattering}}$	Scattering cross section
D	Dimension of crystallites
$\mathbf{E}$	Electric field
E_0	Applied electric field

E_{AD}	Electric field due to the adjacent dipole
E_{nf}	Electric near-field
E_{P}	Potential energy
E_{surface}	Electric field at the surface
Fe_3O_4	Magnetite
$\mathbf{H}$	Applied magnetic field
K	Magnetic anisotropy energy
k_{B}	Boltzmann constant
L	Path length
L(a)	Langevin function
LbL	Layer-by-Layer
$\mathbf{M}$	Magnetization
M_{S}	Saturation magnetization
n	Refractive index
N_{A}	Avogadro constant
n_{medium}	Refractive index of the medium
$\mathbf{P}$	Polarization
q	Scattering vector
$Q_{\mathrm{absorption}}$	Absorption efficiency
$Q_{\mathrm{extinction}}$	Extinction efficiency
$Q_{\mathrm{scattering}}$	Scattering efficiency
R	Radius
S	Shape factor
T	Temperature
T_{B}	Blocking temperature
U	Interaction energy
V	Verdet constant

Contents

Chapter 1

General introduction to magnetic-plasmonic nanomaterials

Technical and societal challenges and ambitions in the past have always been accompanied and met by the development, design and production of novel materials. From the search to lightweight ultra strong materials for space applications and novel components for improved solar panels to the production of radiation-resistant materials for construction of nuclear power plants, science and technology have been constantly pushing material's capabilities past their limits.

In addressing the grand challenges of today's and future societies such as improved and affordable welfare and healthcare for all, global climate change, sustainable economies, ensuring security and abundant production of and reliable access to energy, nutrients and water, nanotechnology is destined to be a key research and industrial priority for the 21st century.[1,2] As nanotechnology is expected to advance fundamental knowledge on a variety of topics and provide employment through commercialization of successful technologies, vast amounts of both private and public resources are invested in nanotechnology initiatives. Interest and optimism in the applicability and economic viability of nano-based technologies are further evidenced by a nearly exponential upward trend in the number of patents requested and issued.[3,4]

The term nanomaterials is coined for all materials that have a characteristic dimension in the size range from 1 to 100nm (see Figure 1.1).[1,2] Materials in

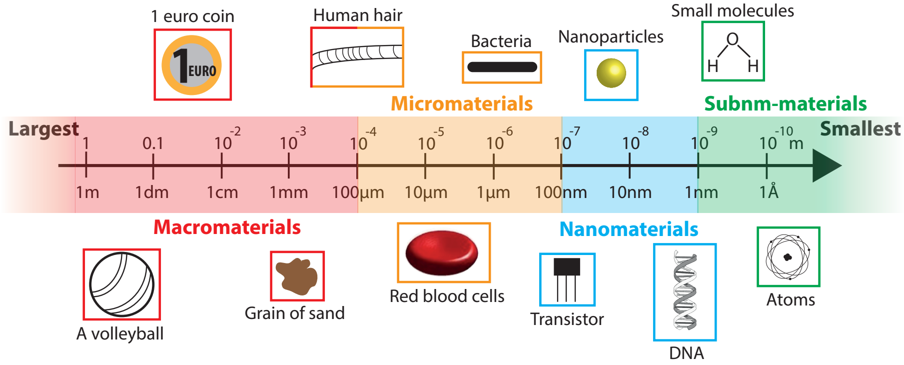

Figure 1.1: Nanomaterials have a characteristic dimension in the size range from 1 to 100nm. The presented length scale offers a frame of reference for the reader.

this size range are said to be intermediate between molecules and bulk matter in all aspects. More concretely, compared to bulk materials, nanomaterials exhibit different and useful physicochemical properties attributed fully to their small sizes. Due to confinement effects and increased surface to volume ratios in nanostructures, for example their melting point, chemical reactivity, catalytic activities, optical properties, fluorescence, magnetic susceptibility and conductivity all change with size.[5–8] Energy states that exist individually in molecules and in continuous bands in bulk crystals become discretized and the energetic separation between these discretized states and thus also the density of states becomes dependent on the size of the entity.[8]

A wealth of materials are in the nano size range including fullerenes,[9] carbon nanotubes,[10] graphene,[11] DNA superstructures,[12] rotaxanes,[13] semiconductor quantum dots,[14] zeolites,[7] metallic or insulating nanoparticles (NPs),[15–17] but also structures produced via e.g. E-beam lithography,[18] atomic layer deposition and direct laser writing.[19,20]

In the history of man-made materials, nano-sized structures have been in use since as early as the 4th century as colorant in glasses (plasmonic nanoparticles).[21] From the 20th century on, nanomaterials have been in use for the production of e.g. tyres (carbon black),[22] or tooth-paste and paint (amorphous silica).[22,23] These nanomaterials and the mentioned applications require only roughly defined specifications and in most cases the nano-component only serves a single, passive purpose.

In recent years, much research attention has focused on developing and synthesizing well-defined 'active' multifunctional nanomaterials as they greatly expand the possibilities for fundamental and applied research. For some combinations of functions, properties of multifunctional materials are more than merely the sum of the properties of the constituting materials due to interplays between the present functionalities.

Possible functional combinations are plentiful ranging from combining semiconductor quantum dots with a functional organic shell for biomedical sensing applications,[14] to gold nanoparticle/DNA rotaxane hybrid materials for fluorescence switching,[24] chiral assemblies of gold nanoparticles on DNA-origami-scaffolded helices for tuneable circular dichroism responses,[25] graphene-nanoparticle-based hybrid materials for sensing applications,[26] and multifunctional biocompatible iron oxide nanoparticles for simultaneous diagnostics and therapy.[27]

The work presented in this dissertation focuses on the development, synthesis and characterization of multifunctional magnetic-plasmonic nanomaterials. Such materials, in which magnetic and plasmonic nano-sized components are combined, provide a particularly interesting combination of functionalities both from a fundamental and from an applied point of view. With the promise of unravelling the fundamental interactions between light and magnetism at the nanoscale and potential applications in e.g. biomedicine, catalysis, sensors and active miniaturized optical components, magnetic-plasmonic nanomaterials can help achieve the ambitious societal and technical goals set for nanotechnology in general.

In this chapter we will further introduce the reader to the field by first describing briefly the possible synthesis strategies for nanomaterials in general followed by the properties and synthesis of uniquely magnetic or plasmonic nanostructures. Then we describe the synthesis, properties and applications of magnetic-plasmonic nanomaterials. As last the rationale and research goals are formulated, together with an outline of this dissertation.

1.1 Synthesis of multifunctional nanomaterials: top-down or bottom-up?

Some single compound nano-sized materials are inherently multifunctional. Gold nanoparticles are a good example as they i.e. exhibit interesting optical properties, can be used for local heating and are catalytically active (see section 1.4).

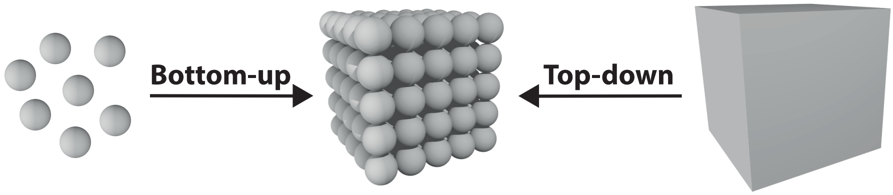

Figure 1.2: The two main strategies to produce multifunctional nanomaterials: bottom-up and top-down.

For many other interesting combinations of functionalities, such as the magnetic-plasmonic case, integrating multiple functional components is required or results in additional advantages.

In general, there exist two synthetic strategies to produce nanostructures: top-down and bottom-up.

1.1.1 Top-down methods

Top-down methods are used to fabricate nano-objects starting from larger entities (see Figure 1.2).

Examples of top-down methods are electron beam lithography,[18] nanoimprint lithography,[28] photolithography,[29] x-ray lithography,[30] focused ion beam techniques,[31,32] proton beam writing,[33] direct laser writing,[19,20] and dip-pen lithography.[34] Also many variants of these techniques have been developed.

In many, if not all, of the above mentioned techniques and their variants the achievable resolution mainly relies on the resolution of the manipulating tool. For example, in direct laser writing the resolution for writing nanostructures is dependent on the wavelength and spot waist of the used laser beam. Dip-pen lithography can theoretically achieve a resolution as good as the size of the used AFM tip. Furthermore, most of these techniques such as x-ray lithography, focused ion beam and proton beam writing require expensive equipment and highly specialized operators.

1.1.2 Bottom-up techniques

In contrast to top-down methods, bottom-up techniques start from smaller building blocks and assemble them to achieve a nanostructured material (see

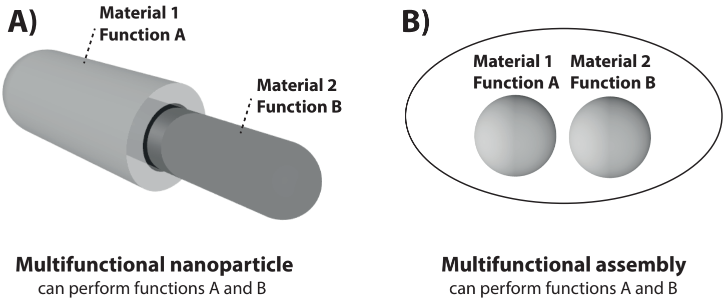

Figure 1.3: Producing multifunctional nanostructures can be done by integrating all required materials and functions in a single entity (A) or by assembling monofunctional building blocks to render the whole assembly multifunctional (B).

Figure 1.2). This implies that the achievable resolution in many bottom-up methods is limited by the size of the building blocks and not by the resolution of a manipulation tool. Bottom-up techniques in general allow to fabricate much smaller structures than top-down methods.[8]

Currently, major advantages of bottom-up approaches for the synthesis of nanomaterials are the flexibility, cost and availability. Flexibility is reflected in the fact that many more types of materials can be integrated through bottom-up than through top-down approaches and interchanging compounds is most often straightfoward. Further, most bottom-up techniques allow modification of large substrate areas. Compared to many top-down methods, usually no expensive or hard-to-operate equipment is required which in turn lowers the costs and increases the availability. The main disadvantage in general is a lesser degree of spatial control that hinders the synthesis of well-defined 3D structures.

1.2 Multifunctional single entities or assemblies

Generally speaking, rendering a nanosized material multifunctional can be achieved in two ways. The first is to endow a single particle or entity with the desired functionalities. A second is to integrate multiple functional entities or particles in an assembly, rendering the assembly as a whole multifunctional.

1.2.1 Multifunctional nanoparticles

Integrating all desired functionalities in a single entity or particle is a first way to create multifunctional nanomaterials. In the case of magnetic-plasmonic nanomaterials, magnetic and plasmonic components would need to be integrated in a single nano-sized structure (see Figure 1.3A).

Options for integrating multiple materials or functions in a single nano-entity are e.g. dumbbell configurations in which materials are physically connected,[35,36] or core/shell geometries where a single or multiple core nanoparticles are coated or surrounded by a shell material.[36]

Core/shell geometries are an elegant and flexible way to produce integrated functional nanostructures. For synthesizing e.g. magnetic-plasmonic nanoparticles one could synthesize a magnetic core and coat it with a plasmonic material.

Core/shell morphologies reported in literature include organic/organic,[37,38] metal/metal,[39] metal-oxide/metal-oxide,[40] semi-conductor/semi-conductor,[36] metal/metal-oxide,[41] metal-oxide/organic,[42–44] semi-conductor/organic,[45] organic/metal and metal/organic.[46] Although the list above is long and by no means exhaustive, not all compounds are mutually compatible to use in core-shell nanomaterials.[47]

Besides the above mentioned binary combinations also more complex systems have been synthesized that integrate multiple materials in multiple shells.[36,39,41]

1.2.2 Assembling multiple functional components

When the desired functions or components are present in several nano-sized entities, these entities need to be assembled to achieve a multifunctional system (see Figure 1.3B). As an example, separate magnetic and plasmonic nanoparticles can be connected to form a magnetic-plasmonic assembly.

A well-developed general framework to assemble nano-sized functional entities in larger structures is the Layer-by-Layer method based on self-assembly. In this method, building blocks of a single material are deposited on top of each other one layer at a time. A unique feature is that the assembly process is based on 'passive' physicochemical recognition and does not require active, *in-situ* manipulation of building blocks.[8] Major advantages of this framework are that the total thickness of the deposited structure can be controlled to a certain degree just by the number of deposited layers and that the technique is very useful for producing large areas covered with deposited structures. Furthermore, no expensive equipment or highly trained personnel is required.

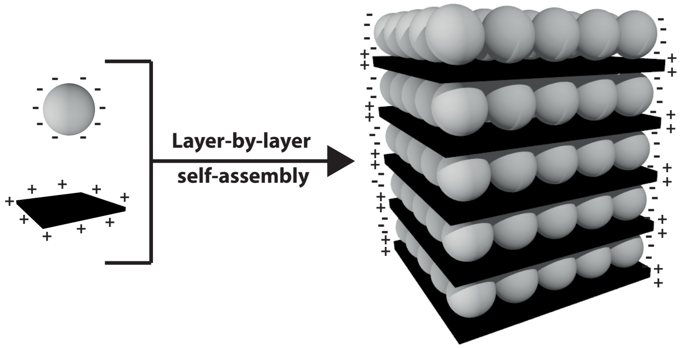

Figure 1.4: Layer-by-Layer self-assembly based on dominant electrostatic interactions using polyelectrolytes is a popular technique to assemble nanoparticles in a thin film superstructure. The depicted assembly is an idealized visualization.

For such self-assembly processes to work it is important that the different building blocks of consecutively added layers possess complementary physicochemical properties. Attractive forces between different building blocks are like the glue or cement between the layers. These attractive forces can be van der Waals, hydrogen bonding, covalent or electrostatic in nature. While all of the aforementioned forces are actively or passively in use for the construction of Layer-by-Layer thin films, the majority of current research relies on electrostatic interactions as the dominant force (see Figure 1.4).[8, 48, 49]

Examples of Layer-by-Layer self-assembly based construction of multifunctional thin films based on nano-sized inorganic structures are Au NP/polyelectrolyte,[50–52] polyelectrolyte polymer nanoparticles,[53] dendrimer/TiO_2 polyelectrolyte multilayers,[54] TiO_2 polyelectrolyte multilayers,[55, 56] Ag NP/polyelectrolyte,[57] Pt NP/polyelectrolyte,[58] SiO_2 NP/polyelectrolyte,[59] and iron oxide NP/polyelectrolye.[60–62]

Please note that the term Layer-by-Layer nanoparticles is also in use for core-shell nanoparticles with multiple layers deposited on top of the core using the same mechanism as for the discussed morphology above.[63–66] In the context of this dissertation, the term Layer-by-Layer will be used only for the process to fabricate structures starting from multiple nano-sized building blocks.

1.3 Magnetic nanoparticles

In this section we briefly introduce the synthesis and properties of magnetic nanoparticles, one of the functional components of bottom-up fabricated magnetic-plasmonic nanomaterials.

A wealth of nano-sized magnetic compounds is available. In general, to obtain a material with large magnetic susceptibilities, atoms with large magnetic moments need to be incorporated. Elements that have been used for the synthesis of magnetic nanoparticles include iron (Fe), nickel (Ni), cobalt (Co) and also barium (Ba).[67] All kinds of elementary compositions, phases and geometries of magnetic nanoparticles have been synthesized, such as metal oxides (e.g. Fe_3O_4 or $MnFe_2O_4$), pure metals (e.g. Fe), rare earth doped nanoparticles,[68] or metal alloys (e.g. FePt).[67,69–72]

The rest of this section will be focused on iron oxide nanoparticles, as they are the used magnetic component in the work performed for this dissertation. The choice for iron oxide was based on several advantageous properties of these structures. First, large magnetic moments are present in some iron oxide structures. Second, relatively straightforward, rapid and economical synthetic procedures are available to prepare iron oxide nanoparticles in relatively large quantities. Third, iron oxide nanoparticles show low toxicity, which facilitates experimental procedures and is important for biologically related applications. And last, since iron oxide nanoparticles are under very intensive study for all sorts of applications in biomedicine, sensor technology, purification strategies and other there exists a large body of literature on their structural, chemical and physical properties.[44,67,69–80]

1.3.1 Iron oxides

While many phases of iron oxides exist the most relevant in the context of magnetic nanoparticles are magnetite (Fe_3O_4), maghemite (γ-Fe_2O_3) and hematite (α-Fe_2O_3).[44,67,81]

Magnetite

Magnetite (Fe_3O_4 or $FeO \cdot Fe_2O_3$) is also known as black iron oxide and exhibits the strongest net magnetic moment of all iron oxides. As can be inferred from the structural formula, magnetite is composed of both ferrous (II) and ferric (III) iron atoms.

Magnetite is a member of the cubic ferrites, which are also called ferrospinels because their crystal structure is closely related to that of the mineral spinel, $MgO \cdot Al_2O_3$. The structure consists of eight formula units, or a total of 56 atoms per unit cell.[79] The oxygen ions are packed in a face-centered cubic arrangement and the metal ions occupy the spaces between them. There are two kinds of vacancies available, tetrahedral A sites and octahedral B sites. Only one-eight of the A sites and one-half of the B sites are occupied by metal ions. Magnetite exhibits an *inverse spinel* structure in which the divalent ions occupy B sites and the trivalent ions are equally divided between the A and B sites. The divalent ions occupy the B sites in a random fashion, i.e., they are disordered. When the divalent metal ions occupy the A sites and the trivalent ions the B sites, the structure is called *normal spinel*, since it then has exactly the same structure as the original spinel mineral.[79,82,83]

Maghemite

Maghemite (γ-Fe_2O_3) has a dark brown color and a similar crystal structure as magnetite. The difference is that there are vacancies in the cation sublattice and the result can be called a *defect spinel*. In general, maghemite can be described as a more oxidized form of magnetite. The mineral mostly occurs as a weathering product of magnetite in soils and forms continuous solutions with this structure. Furthermore, the crystal structure is metastable with respect to hematite, classifying it as an intermediate structure between magnetite and hematite.[81,82,84]

Hematite

Hematite, also known as ferric oxide, has a black or grey color in bulk material and blood-red when finely divided. It is the oldest known of the iron oxides and present around the world in rocks and soils. Thermodynamically, hematite is extremely stable at standard temperature and pressure and is often the end product of transformation series of other iron oxides.[81] Hematite crystallizes in the rhombohedral system with an hexagonal close-packed arrangement of oxygens and Fe^{3+} ions occupying octahedral sites.

1.3.2 Synthesis - Forced hydrolysis method

Many efficient protocols for the synthesis of magnetic iron oxide nanoparticles have been published. Popular synthesis mechanisms are co-precipitation, thermal decomposition, hydrotermal synthesis, the use of micelles, chemical vapor deposition, laser pyrolysis, spray pyrolis, sol-gel methods, high-energy ball milling, synthesis by biological organism or within the confined space of nanoreactors.[44, 67, 69–72, 81, 85–90]

All of these methods have their merits and disadvantages. Major differences lie in the used starting products, the cost of the required equipment and of course the size, size dispersion, shape and surface coating of the resulting nanoparticles.

Iron oxide nanoparticles used in the context of this dissertation were synthesized using a modified forced hydrolysis polyol method. Motivation for using this technique is based upon three arguments. First is that the method is suited for making relatively large amounts of high quality particles in 24h.[91] Second, it is a very cost effective technique since the starting materials are cheap and no expensive equipment is required. Third, due to the weak binding of the coating molecules to the particles' surfaces, subsequent functionalization by exchange reactions is straightforward.

The used forced hydrolysis technique is based on the dissolution of metal salts in a polyol with subsequent heating or reflux. The liquid polyol, e.g. ethylene glycol, act as solvent for the metallic precursor, reducing agent and in some cases as a complexing agent for the metallic cations. Selected polyols also allow to perform hydrolysis reactions in a large temperature range under atmospheric pressure.[92] In a forced hydrolysis protocol, the polyol-metal precursor solution with possible additives such as coating molecules and water is heated to reflux under constant stirring.[69]

Most polyvalent cations, like iron ions, easily hydrolyze and deprotonate coordinated water molecules. These processes are greatly accelerated when temperature is increased. Since hydrolysis products are intermediates to precipitation of metal (hydrous) oxides, these complexes can be generated at the proper rate to eventually yield uniform particles by adjustment of pH and temperature. In addition, coordinated anions can affect precipitation and particle morphology.[91] By choosing the proper coating or capping molecules and controlling the kinetics of the precipitation, non-agglomerated nanoparticles with a well-defined shape and size can be obtained.

Forced hydrolysis methods have been used to synthesize e.g. magnetite,[93] hematite,[94] cobalt ferrite,[92] and other nanostructured materials.[95]

1.3.3 Magnetic properties

Iron oxides exhibit magnetic behavior due to the presence of iron atoms with unpaired electron spins. Fe^{2+} and Fe^{3+} ions have four and five unpaired electrons respectively and thus posses a magnetic moment of 4 or 5 Bohr magnetons.[83] The magnetic properties of the material in which these magnetic atoms are incorporated depends strongly on the crystal structure.

Classification of materials based on their magnetic properties can be done using the magnetic susceptibility (χ_m) as criterium. This material parameter relates the degree of magnetization ($\mathbf{M}$) of the material to the magnetic field applied ($\mathbf{H}$) as shown in Equation 1.1.[79]

$$\mathbf{M} = \chi_m \mathbf{H} \tag{1.1}$$

1. Diamagnetic (i.e. Cu, He): χ_m is small and negative.
2. Paramagnetic (Na, Al) or antiferromagnetic (MnO, FeO): χ_m is small and positive.
3. Ferromagnetic (Fe, Co, Ni) or ferrimagnetic (Fe_3O_4): χ_m is large, positive and nonlinear.

Representations of the magnetic structures exhibiting the magnetic behaviors mentioned above are shown in Figure 1.5.

Bulk magnetism of iron oxides

In magnetite, Fe^{3+} ions are distributed in two different lattice sites with opposing magnetic spin directions, canceling out the magnetic moments. The permanent magnetic interactions in the structure arise from the magnetic moments of the Fe^{2+} ions as shown in Figure 1.6A. This distribution of magnetic moments in the crystal structure render magnetite a ferrimagnetic material.[79]

For maghemite, which is also a ferrimagnetic material, the saturation magnetization that can be achieved is lower than for magnetite. This despite that maghemite is only composed of ferric (III) iron ions with a higher magnetic moment than ferrous iron (II) ions. The lower saturation magnetization can be attributed to the defective spinel structure which prevents perfect alignment of the magnetic moments in the material.

Ferrimagnetic materials have a substantial spontaneous magnetization at room temperature which makes them industrially important. Like ferromagnetic substances, they consist of magnetically saturated domains and exhibit the phenomena of magnetic saturation and hysteresis. They also lose their magnetization and become paramagnetic above their Cure temperature, T_c.

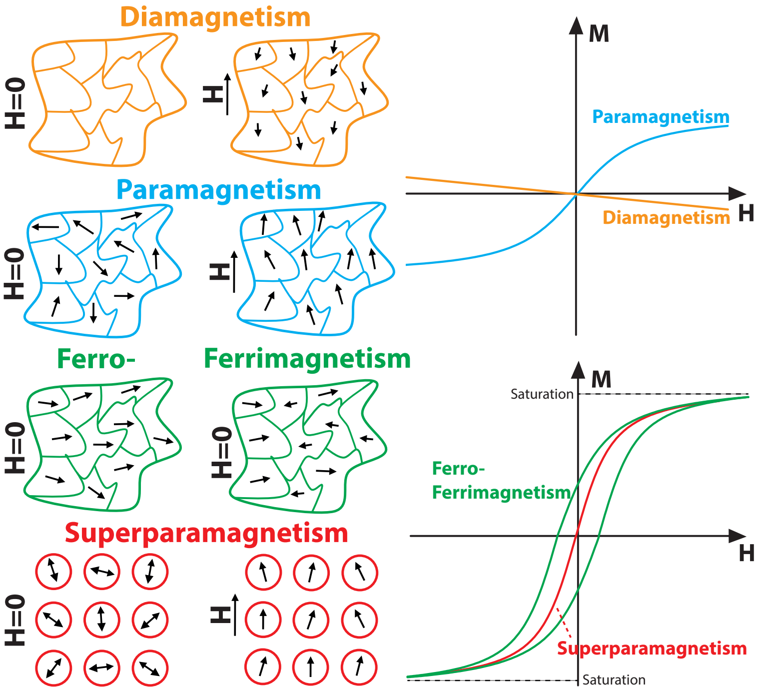

Figure 1.5: Visualization of magnetic orderings and their magnetization responses (M) as a function of applied magnetic field strength (H). Note that for ferro- and ferri-magnetism, materials are assumed to be magnetized first.

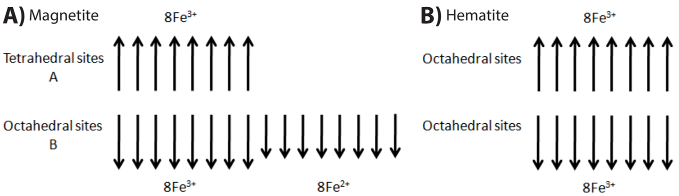

Figure 1.6: Arrangements of magnetic moments in the crystal structures of A) magnetite (ferrimagnetic) and B) hematite (antiferromagnetic).

This can be explained by the fact that above the Curie temperature, the influence of thermal agitation on the atomic magnetic moments is larger than the tendency to align to the applied field, causing randomization of the magnetic moments.[79,83,96]

Hematite, as opposed to magnetite and maghemite has an antiferromagnetic structure. The spin alignments are as shown in Figure 1.6B, rendering hematite an almost non-magnetic material.[79,83]

Superparamagnetism

Magnetic properties of materials undergo dramatic changes upon decreasing size. When the size of a particle composed of magnetic atoms is small enough, the energy necessary to divide itself into magnetic domains is higher than the energy needed to remain as a single magnetic domain in which the present magnetic moments rotate coherently behaving as one large moment.[97]

Several attempts to calculate the mono-domain limit for iron oxide particles have been published. Calculations for spherical magnetite nanoparticles by Kittel resulted in a diameter of 35.4nm,[98] while Brown Jr. comes to a result of 29.7nm.[80] For cubic particles, a higher shape anisotropy has to be taken into account and the critical size could be up to 50nm.[80] In general, depending on the geometry and the associated anisotropy energy, the mono-domain limit will be in the range from 25-100nm.

The energy barrier ΔE that must be overcome before a mono-domain particle can reverse its magnetization can be estimated by considering a uniaxial, single-domain particle with a certain magnetic anisotropy energy K (see Figure 1.7). This anisotropy energy keeps a particle magnetized in a particular direction and is generally proportional to the particle volume. If V is the volume of the particle, then the energy barrier is equal to KV.

Besides anisotropy energy, fluctuations of thermal energy at microscopic scale have to be taken into account. If the dimension of a particle becomes very small, then also KV will become very small. Thermal fluctuations at a certain temperature can then suffice to overcome the anisotropic forces and reverse the magnetization of a particle, even in absence of an applied field. Because this behavior is practically identical to that observed for a normal paramagnet, Bean and Livingstone proposed the name *superparamagnetism*.[79,97,99]

The relaxation of the magnetization of these particles can be described by an Arrhenius-type law:

$$M(t) = M_0 e^{-t/\tau} \tag{1.2}$$

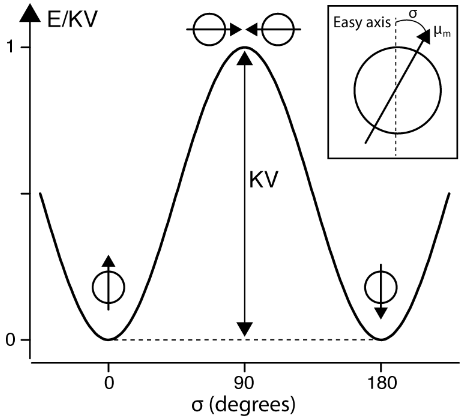

Figure 1.7: The energy barrier that needs to be overcome to flip the magnetic moment in absence of an externally applied magnetic field in a uniaxial single-domain particle is equal to KV.

where M_0 is the initial magnetization and τ the characteristic relaxation time which is a function of the energy barrier ΔE and temperature.

The observed magnetic behavior depends on the relative values of the measuring time τ_m and the intrinsic relaxation time of the particles τ_i. If τ_m is larger than τ_i, then the relaxation is faster than the magnetization orientation observed in the measurement time window allowing the system to reach thermodynamical equilibrium. In these conditions, the particles are said to be in the superparamagnetic regime. If τ_m is smaller then τ_i, thermodynamical equilibrium will not be achieved and quasi-static magnetic properties will be observed. The particles are then said to be in the blocked regime. The temperature dividing both regimes is called the blocking temperature (T_B) which is related to ΔE.

For $\tau_m = 100s$, a typical magnetometric measuring time, the relation between the volume of the particle, blocking temperature and anisotropy factor can be written as:

$$T_B \approx \frac{KV}{25k_B} \tag{1.3}$$

This means that the larger the particles, the higher the blocking temperature will be.[79, 97, 100] Using the measured blocking temperature and knowledge on the system under study the particle size can be estimated.

Important to note is that interactions between superparamagnetic systems can have a strong influence on the observed blocking temperature. As an example, if superparamagnetic particles interact strongly, their magnetic moments become coupled and it will be more difficult to align the resulting moment at a given temperature. This is observed as an increase of the blocking temperature and could lead to an overestimation of the core magnetic diameter.[97, 101]

Superparamagnetic nanoparticle ensembles & the Langevin equation

If magnetic anisotropy is neglected and with the knowledge that magnetic moments in typical superparamagnetic ensembles are much larger, a superparamagnetic system can be described by using the theory of paramagnetism.[79, 97]

Assume a system that has achieved thermal equilibrium at a temperature T subjected to a magnetic field $\mathbf{H}$. At this particular temperature all particles are in the superparamagnetic region, or otherwise stated $KV << k_B T$. The potential energy of each magnetic moment in the applied magnetic field, E_p, can then be represented by

$$E_p = -\mu_{\mathbf{m}} \cdot \mathbf{H} = -\mu_m H cos\phi \tag{1.4}$$

with $\mu_{\mathbf{m}}$ the magnetic moment and ϕ the angle between the direction of the magnetic moment and the applied magnetic field.

To obtain the number of moments between ϕ and $\phi + d\phi$ as function of the applied field $\mathbf{H}$, consider each moment surrounded by a sphere of unitary volume. In absence of a field the number of magnetic vectors going through a unit area of surface of the sphere (dn) is the same at any point on that surface. This means that dn is proportional to the area: $dA = 2\pi sin\phi d\phi$.

In a state of thermal equilibrium, the probability of an atom possessing an energy E_p is given by a Boltzmann distribution. The number of moments between ϕ and $\phi + d\phi$ will then be proportional to dA multiplied by the Boltzmann factor as shown in Equation 1.5.

$$\begin{aligned} dn &= Z dA e^{\frac{-E_p}{k_B T}} \\ &= 2\pi Z e^{\frac{(\mu_m H cos\phi)}{k_B T}} sin\phi d\phi \end{aligned} \tag{1.5}$$

with Z a proportionality factor determined by

$$\int_0^n dn = n \tag{1.6}$$

Stating $a = \mu_m H/k_B T$ in equation 1.5, one can can arrive at

$$2\pi Z \int_0^{\pi} e^{acos\phi} sin\phi d\phi = n \tag{1.7}$$

The total magnetization M of a system can be calculated by multiplying the number of magnetic moments dn and the contribution $\mu_m cos\phi$ of each moment and integrating over the total number of magnetic moments:

$$M = \int_0^{n} \mu_m cos\phi dn \tag{1.8}$$

Considering previous equations one can arrive at

$$\begin{aligned} M &= 2\pi Z \mu_m \int_0^{\pi} e^{acos\phi} sin\phi cos\phi d\phi \\ &= \frac{n\mu_m \int_0^{\pi} e^{acos\phi} sin\phi cos\phi d\phi}{\int_0^{\pi} e^{acos\phi} sin\phi d\phi} \end{aligned} \tag{1.9}$$

In order to evaluate these integrals, it is stated that $x = cos\phi$ and $dx = -sin\phi d\phi$, which results in

$$\begin{aligned} M &= \frac{n\mu_m \int_1^{-1} xe^{ax} dx}{\int_{-1}^{1} e^{ax} dx} \\ &= n\mu_m \left(\frac{e^a + e^{-a}}{e^a - e^{-a}} - \frac{1}{a} \right) \\ &= n\mu_m \left(cotha - \frac{1}{a} \right) \end{aligned} \tag{1.10}$$

where $n\mu_m$ is the maximum possible magnetic moment that can be achieved by the material, corresponding to a perfect alignment of all magnetic moments to the external field. This is also called a complete saturated state, symbolized by M_S, which makes that Equation 1.10 can be rewritten as:

$$\frac{M}{M_S} = cotha - \frac{1}{a} = L(a) \tag{1.11}$$

where $L(a)$ is called the Langevin function.

From the Langevin formulation it follows that

1. When $a = \mu_m H/k_B T$ is sufficiently large, saturation of the magnetization will occur. This phenomenon can be physically explained by considering that either a large applied field H or low temperature T or both are necessary to overcome the disaligning effect of thermal agitation.

2. If a is small, then the magnetization varies linearly with the applied field, since the Langevin function can then be expressed as a series as

$$L(a) = \frac{a}{3} - \frac{a^3}{45} + \frac{2a^5}{945} - \dots \tag{1.12}$$

which indicates that at small a the magnetization varies as $L(a) = a/3$ with H.

Note that the equations will not completely be obeyed if not all particles in the assembly are of the same size, since then the moment per particle is not constant, or when superparamagnetic particles' magnetic moments couple.

1.3.4 Linear and nonlinear optical properties

In this subsection we will first report on the linear optical properties of magnetite iron oxide nanoparticles and then briefly introduce nonlinear optical phenomena in general. And last the nonlinear optical properties of iron oxide nanoparticles will be summarized.

Linear optical properties

In the UV-visible (UV-vis) spectral region (±300-900nm) magnetite (Fe_3O_4) nanoparticles show a single broad and strong resonance around 370-390nm.[73–75, 102] Intervalence charge transfer (IVCT) processes have been attributed to be the cause of this resonance.[73]

In general, IVCT transitions occur between two neighbouring cations in a mixed-valence system.[73, 103–105] Through optical excitation, an electron is passed from the cation with the smallest to the one with the largest formal charge. For Fe_3O_4, these cations are Fe^{2+} and Fe^{3+}, which weakly bind across the shared edges of Fe-O polyhedra. Electronic transitions between the Fe-Fe bonding and anti-bonding orbitals are the direct cause of the IVCT transitions.[73]

Nonlinear optical properties

When applying very intense light to materials (e.g. laser light), the resulting polarization **P**, i.e. the response of the material to the incident electric field **E**, is no longer linearly correlated to the electric field strength of the incident light.[106] To describe this 'nonlinear' optical regime, we can expand the induced polarization in a Taylor series in terms of the incident electric field.[106–108]

$$\begin{aligned}\mathbf{P}_{ind} &= \mathbf{P}^{(1)} + \mathbf{P}^{(2)} + \mathbf{P}^{(3)} + \cdots \\ &= \chi^{(1)}\mathbf{E}(\omega) + \chi^{(2)}\mathbf{E}(\omega)\mathbf{E}(\omega) + \chi^{(3)}\mathbf{E}(\omega)\mathbf{E}(\omega)\mathbf{E}(\omega) + \cdots \end{aligned} \tag{1.13}$$

The first-order susceptibility $\chi^{(1)}$ describes the linear optical properties of matter, such as absorbance and reflectance. Nonlinear optical effects are described by the higher order terms starting from $\chi^{(2)}$. Second-order effects characterized by $\chi^{(2)}$, such as second harmonic generation (SHG) in which light is generated at frequency 2ω or half of the fundamental wavelength, are quadratic in the electric field. Third harmonic generation (THG), in which light is generated at frequency 3ω or one-third of the fundamental wavelength, and two-photon luminescence (TPL), the simultaneous absorption of two photons to generate luminescence, are described by the third order susceptibility $\chi^{(3)}$. Note that all susceptibilities are frequency dependent and can be strongly enhanced when optical resonances are present in the material.[106]

Nonlinear optical effects such as SHG, hyper-Rayleigh scattering, THG, two-photon absorption and others are very popular to characterize materials but are also widely commercially applied in e.g. the fabrication of lasers, semi-conductor quality control, all-optical switching and optical limiting goggles.[106–121]

Iron oxide nanoparticles have been reported to show large nonlinear optical responses. For example, they have been used as tracking labels in nonlinear microscopy studies.[122] Third-order nonlinear optical measurements on iron oxides have been performed by e.g. Garcia *et al.*, who found values on the order of 10^{-10}esu for the third order optical susceptibility ($\chi^{(3)}$) of α-Fe_2O_3 at 800nm as measured by Z-scan techniques.[76] Hashimoto *et al.* measured the third harmonic generation of iron oxides in thin films with a fundamental wavelength of 1900nm and observed for magnetite large values up to 4×10^{-10}esu for the electronic contribution to $\chi^{(3)}$.[77]

1.3.5 Magneto-optical properties

Faraday rotation and ellipticity

Magneto-optical measurements probe the interaction of light and magnetic fields in a medium or material. Faraday rotation (FR) and Faraday ellipticity (FE) are two prominent examples of magneto-optical effects.

Faraday rotation, discovered by Michael Faraday in 1845,[123] is a magneto-optical effect that causes a rotation of the polarization plane of a light beam through

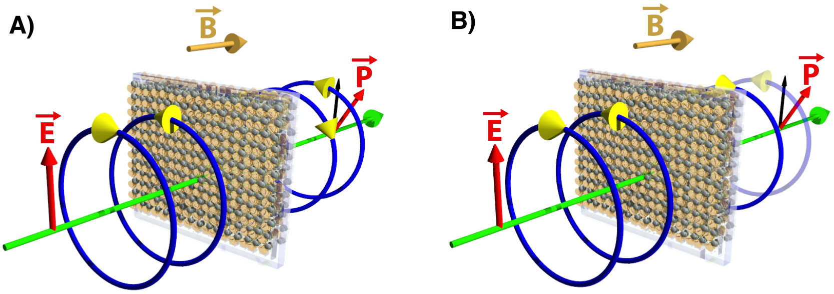

Figure 1.8: Faraday rotation (A) and ellipticity (B) are the magnetic-field induced differences in refraction and absorption for circularly polarized light and cause a rotation of the polarization plane of a polarized incident light beam.

the application of a magnetic field in the propagation direction of the beam. The rotation of the polarization plane originates in the magnetic field-induced circular birefringence, i.e. a *difference in refraction* for left- and right-handed circularly polarized light, influencing a monochromatic and polarized light beam as it travels through the magnetized medium or material (see Figure 1.8A).

Faraday ellipticity, also known as magnetic circular dichroism, is the *difference in absorption* for left- and right-handed circularly polarized light under influence of a magnetic field in the propagation direction of the light beam (see Figure 1.8B).

Important to note is that both FR and FE are non-reciprocal effects, a beam of light that is sent multiple times through the same (magnetized) medium will acquire a rotation angle of the plane of polarization that is linearly related to the number of passages through the sample.[124] This property is used for the fabrication of optical isolators applied e.g. to remove unwanted reflections in laser setups.

For Faraday rotation, the angle of rotation acquired after passing through the (magnetized) medium or material by the polarized light beam is

$$\theta_F = VBL \tag{1.14}$$

where B stands for the magnetic flux density in the propagation direction, L the path length of the light in the sample and V the Verdet constant. The Verdet constant is a material property and quantifies the Faraday rotation. Generally, the magnitude of V depends on the wavelength of the incident light, temperature and refractive index of the material under study.

The relationship between the Faraday ellipticity angle η_F and the magnetic flux density B in the propagation direction is the same as for Faraday rotation.

FR and FE have been studied for inorganic materials such as glasses or materials including paramagnetic ions,[125,126] metallic nanoparticles,[127,128] semi-conductors,[129] and organic materials such as small molecules,[130,131] rare earths,[132] conjugated polymers,[133–135] graphene,[136] liquid crystals,[137] and are used for e.g. magnetic field sensors,[138–141] quantum memory,[142] optical isolators, switches and modulators.[130,143–147]

Magneto-optical properties of iron oxides

Iron oxide nanoparticles are well-studied materials in terms of their magneto-optical properties. In general their Verdet constants are large, although of course dependent on the morphology, phase, interparticle distance and possibly concentration in the carrier compound and others.[74,124]

Magneto-optical measurements were performed on e.g. magnetite-polymer composites,[74,75,148] silica gels containing maghemite[149] and ferrofluids based on magnetite, maghemite and cobalt ferrite nanoparticles.[141,150] Experimental results were modeled by Maxwell-Garnett[75] and modified discrete dipole approximation[74] theory and explained in terms of electronic transitions.[73]

1.4 Plasmonic nanostructures

Next to magnetic, plasmonic components are required to synthesize magnetic-plasmonic nanostructures. This section is a brief introduction to plasmons, localized surface plasmon resonances and plasmonic near-field coupling. Furthermore, the nonlinear and magneto-optical properties of plasmonic nanostructures are summarized.

1.4.1 What are plasmons?

The interaction of metals with electromagnetic radiation, i.e. light, is largely dictated by the free conduction electrons present in the material. These free electrons are highly polarizable and thus interact strongly with the electric component of the incoming light.

As a first simplification in discussing the origin of plasmon resonances, we regard the conduction electrons in noble metals as a free electron (plasma) gas, as first described by Paul Drude in 1900 to explain conductivity in metals.[151] Plasmons can be described in the classical picture as an oscillation of this free electron density against the fixed positive ions in a metal. When placed in a time-varing electric field, the free electrons in a metal structure will oscillate at the frequency of the applied field. At the plasmon resonance frequency or wavelength, these oscillations become very large, electrons are displaced over a large distance relative to the positively charged metal lattice and a separation of charges results. Quasi-particle plasmons are a quantization of this kind of oscillation.

Plasmons play a large role in the optical properties of metals. Light of frequency below the plasma frequency is reflected, because the electrons in the metal screen the electric field of the light. Light of frequency above the plasma frequency is transmitted, because the electrons cannot respond fast enough to screen it. In most metals, the plasma frequency is in the ultraviolet, making them shiny (reflective) in the visible range.

Some metals, such as copper and gold, have electronic interband transitions in the visible range, whereby specific light energies (colors) are absorbed, yielding their distinct color.

1.4.2 Localized Surface Plasmon Resonance (LSPR) in noble metal nanoparticles

Nanoparticles of noble metals such as gold and silver show interesting optical effects in the visible and near-infrared regions of the electromagnetic spectrum. They usually exhibit distinctive bright colors, which differ from their bulk metal counterparts.

Colloidal gold, small particles suspended in a liquid, is already in use since medieval times and earlier as staining pigment for glasses,[152] component of medicines as in e.g. “Aurum Potabile” proposed by alchemists Michael Scot and Roger Bacon in the 13th and Paracelcus in the 16th century,[153] and for photographic processes (chrysotype) as developed by John Herschel in the 19th century.[152] One of the first to state that the bright colors originate in the optical response of colloidal noble metal nanoparticles much smaller than the wavelength of light was Michael Faraday in 1857.[154] The first synthesis of a diluted gold colloid was published by Richard Zsigmondy in 1898.[155] In 1925, he received the Nobel Prize in Chemistry for “his demonstration of the heterogeneous nature of colloid solutions and for the methods he used”. The optical properties of spherical gold nanoparticles were explained by Gustav Mie

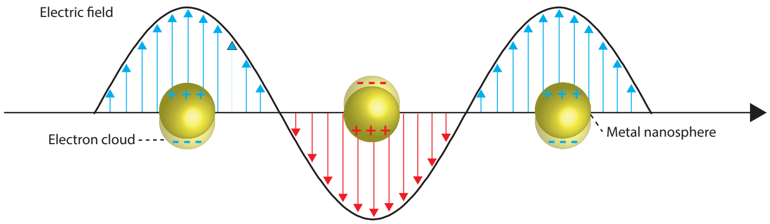

Figure 1.9: Under influence of a time-varying electric field, the free electrons in metal nanoparticles oscillate. At the plasmon resonance frequency these oscillations are greatly enhanced resulting in time-varying charge separations, which in turn act as a source of radiation

in a publication in 1908, where he calculates the scattering of electromagnetic radiation by a sphere through solving the Maxwell equations.[156]

The overall displacement of the electrons at the plasmon resonance with respect to the positively charged lattice leads to a restoring force. In contrast to the plasmon polaritons in large metal structures, the plasmon resonance is said to be localized, hence localized surface plasmon resonance (see Figure 1.9). At the plasmon resonance frequency the induced electron oscillations are greatly enhanced resulting in time-varying charge separations. Such accelerating charges act as a secondary source of radiation.

In general, LSPRs impart nanoparticles with unusual optical properties, such as strongly enhanced size-, shape- and medium-dependent light absorption and Mie scattering. Furthermore, in the near-field spatial region, LSPR excitation results in strong confinement and enhancement of the amplitudes of electric field components surrounding the nanostructures.

For spherical particles that are much smaller than the wavelength of light, the quasi-static approximation is valid. This means we assume that the electric field of incoming light is homogeneous over the particle. For small particles within the quasi-static approximation, the dominant oscillations will be dipolar. So in modeling the optical properties of such small particles, only dipolar interactions will be taken into account in first approximations. The electric field scattered by the small spherical particle into the far field will then be identical to the electrostatic field of a dipole μ_e located at the center of the sphere.

The dipole is induced by the external field E_0 and has the value $\mu_e = \epsilon\alpha(\omega)E_0$, with α denoting the polarizability. Using the Clausius-Mossotti relation one can calculate the polarizability of a particle:

$$\alpha = 2S\epsilon_0 V \left(\frac{\epsilon - \epsilon_m}{\epsilon + 2\epsilon_m} \right) \tag{1.15}$$

In Equation 1.15 ϵ_0 is the vacuum permittivity, V the volume of the particle and ϵ_m the medium dielectric constant. S is a shape factor for which the value is 2 for a spherical particle. The complex and wavelength-dependent dielectric function of the metal ϵ can be written as $\epsilon(\omega) = \epsilon_r(\omega) + i\epsilon_i(\omega)$, with ϵ_r the real and ϵ_i the imaginary part.

Assuming a small or weakly frequency-dependent imaginary part of the dielectric function, we can derive from Equation 1.15, that a resonance, i.e. a very strong response, in α can be expected in spherical nanoparticles when

$$\epsilon_r = -2\epsilon_m \tag{1.16}$$

This large resonance is the origin of LSPR. Dielectric functions with negative real components can be found in some metals such as gold and silver at optical frequencies. They thus exhibit LSPR in the visible range. From Equations 1.15 and 1.16 we can extract the parameters that influence the LSPR. These are the size or volume and the shape of the particle, the dielectric constant of the medium and the dielectric function of the material. The real part of the material's dielectric function determines the frequency or wavelength of the LSPR (Equation 1.16), while the imaginary part determines broadening and damping of the resonance.[157–160]

For gold and silver nanoparticles with a diameter of 10nm, the LSPR is in the visible range. Gold nanoparticles have a LSPR centered around 510nm and silver around 350nm when in vacuum ($\epsilon_m = 1$; see Figure 1.10) as calculated via Mie theory. As stated in the previous paragraph, both the position and the broadness of this plasmon resonance can be tuned by changing one of the aforementioned parameters. For example, changing the refractive index of the medium, which implies changing the dielectric constant of the medium through $n = \sqrt{\epsilon_r \mu_{e,r}}$, will influence the plasmon wavelength as can be inferred from Equation 1.16. As calculated by Mie theory, increasing the ϵ_m or equivalently n_{medium} quite drastically red-shifts the LSPR wavelength and strongly enhances the plasmon intensity (see Figures 1.11 and 1.12) for both Au and Ag nanoparticles.

Important to note is that, as stated earlier, for larger metallic structures including films, gratings or other patterns the surface plasmons are not localized but propagating (surface plasmon polaritons). In a simplified picture, the free electron gas that sustains the plasma oscillations is not spatially confined to a small volume such as for small nanoparticles. A direct consequence of

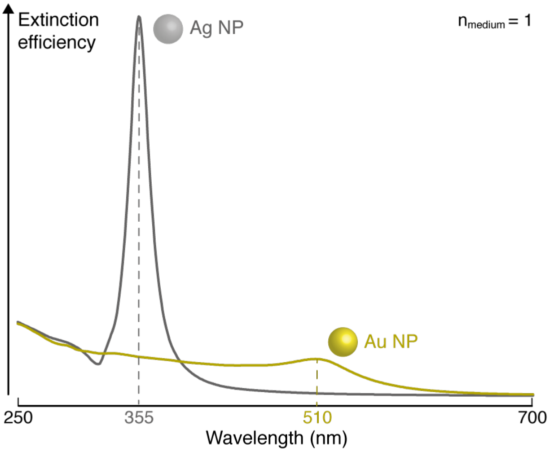

Figure 1.10: The localized single plasmon resonance of silver (350nm) and gold (510nm) nanoparticles when in vacuum ($\epsilon_m = 1$) are in the UV-vis range.

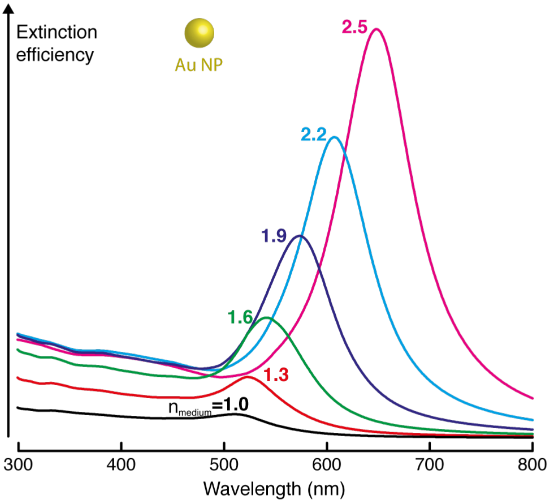

Figure 1.11: Increasing the refractive index of the medium for Au NPs red-shifts the LSPR wavelength and strongly enhances the intensity of the resonance as can be inferred from Equation 1.16 and calculated using Mie scattering theory.

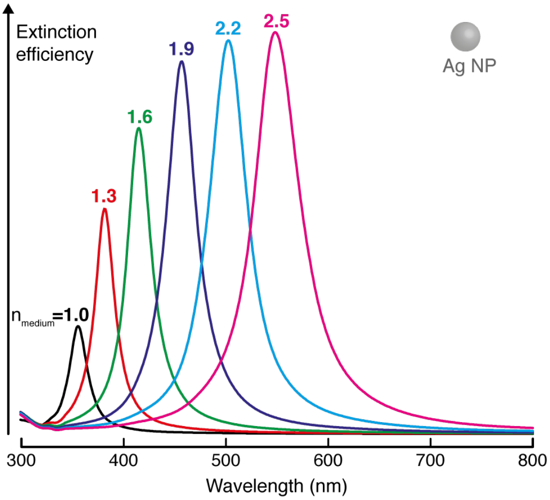

Figure 1.12: Also for Ag NPs, increasing the refractive index of the medium red-shifts the plasmon resonance wavelength and strongly enhances the intensity.

this difference is that excitation conditions for both types of surface plasmon resonances, localized and propagating, are different. While for LSPRs the only condition is the correct photon energy or wavelength, excitation of propagating plasmons also requires a correct angle for the incident plasmon excitating light beam (the wave vectors of the photon and the surface plasmon wave need to match).[161]

1.4.3 Plasmonic near-fields, plasmon coupling and the exciton coupling model

Besides far-field effects, plasmon resonances also have a large impact on the electric field magnitudes directly surrounding plasmonic nanoparticles. At the plasmon frequencies, such particles act as tiny lenses that concentrate the incoming light in a very small volume around their surface. In the quasi-static dipole approximations, one can calculate the electrical field at the surface of a particle to be:[162]

$$E_{surface} = \frac{(1+S)\epsilon_m}{(\epsilon + S\epsilon_m)} E_0 \tag{1.17}$$

which means that at the LSPR frequency, a large enhancement of the electric field surrounding the surface is anticipated. Such enhancements can be up to 200 and 3500 times for silver spheres and nanorods respectively. This strong near-field enhancement is used in a great deal of experiments and techniques such as surface-enhanced Raman scattering (SERS),[163] second harmonic generation,[164–167] magneto-optical phenomena,[168, 169] and others.

If we consider the nanoparticle to be an emitting dipole, the near-field due to the nanoparticle decays with distance as $1/r^3$. This means that if two plasmonic particles are put very close to each other, their near-fields can interact and couple. Formally, one can say that the total electric field on each particle is the sum of the incident field E_0 and the induced near-field of the nearest neighbours E_{nf}.

$$E_{total} = E_0 + E_{nf} \tag{1.18}$$

Such near-field interactions or plasmon couplings result in changes of the LSPR frequency or wavelength and line width. In the simplest example, when two gold nanoparticles are put in close vicinity, the plasmon wavelength deviates from that of 2 single gold nanoparticles. Parameters that influence the modulation of the coupled plasmon wavelength and intensity are the partricle's plasmonic material, the distance between the particles and the number of particles present in the assembly as the total influence of E_{nf} becomes larger.

This simple near-field coupling model fails to explain the dependence of the coupled plasmon wavelength and intensity on the orientation angle of the assembly as compared to the incoming electric field vector and on the polarization of the incoming field. It was observed for optically coupled silver nanodisks that when the light was polarized parallel to the interparticle axis, the red-shift of the coupled plasmon resonance was much more significant than for light polarized perpendicular to this axis. In the same way, Jain et al. showed that when gold nanorods couple tail-to-tail, a red-shift was measured, while when the rods linked side-by-side, the coupled plasmon showed a significant blue-shift.[170, 171]

To explain these observations we will resort to the exciton-coupling model, which was developed to clarify the optical behavior of interacting dipolar organic molecules.[172–174] Two dipolar organic molecules that dimerize in a head-to-tail conformation (J-dimers) show a red-shifted absorption band as compared to that of a single molecules. For the same molecules when dimerizing parallel (H-dimer), a blue-shifted absorption band is observed. The exciton-coupling model describes these shifts as a function of the angle between transition dipole moments.

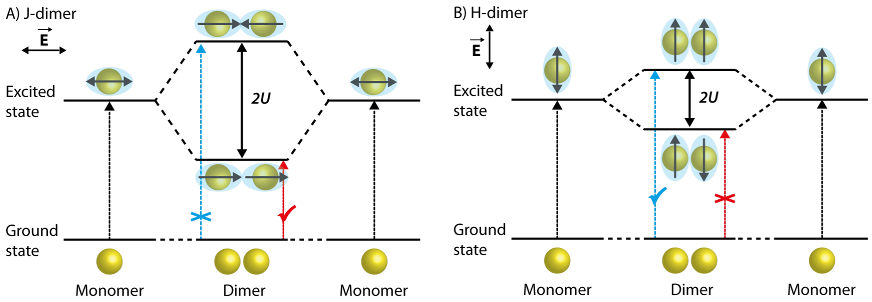

Figure 1.13: Schematic of the energy level splitting resulting from the dipolar interaction of chromophores in a dimer, showing symmetric and antisymmetric coupling of excitons for (a) H aggregate geometry and (b) J aggregate geometry.[160]

In the assumption that plasmonic nanoparticles can be described as dipolar, the exciton coupling model can be used to explain the optical properties of near-field coupled plasmonic particles (see Figure 1.13). According to the exciton theory, when two dipolar entities dimerize, their excited-state levels split into a lower- and a higher-lying energy state as compared to the single dipole excitated state. The excited-state levels of the dimer can be attributed to different arrangements of the transition dipoles, symmetric or anti-symmetric. Primarily Coulombic interactions between the transition dipole moments of the single dipolar entities account for the energy splitting between the excited states of the dimer.

For each interacting dipolar entity, the total electric field experienced can be written as the sum of the incident field E_0 and the field due to the adjacent dipole E_{AD}:

$$\begin{aligned} E &= E_0 + E_{AD} \\ &= E_0 + \frac{\zeta \mu_e}{4\pi\epsilon_0 r^3} \end{aligned} \tag{1.19}$$

Equation 1.19 shows that the field experienced depends cubicly on the inter-dipole distance. Through the parameter ζ the mutual orientation of the interacting dipoles is incorporated in the model as

$$\zeta = 3cos\phi_1 cos\phi_2 - cos\phi_{12} \tag{1.20}$$

where ϕ_{12} is the angle between the directions of the two dipoles, ϕ_1 is the angle between the direction of dipole 1 and the inter-dipole axis, and ϕ_2 is the angle between the direction of dipole 2 and the inter-dipole axis.

The interaction energy U between the two dipolar entities can be calculated from Equation 1.19 to be:

$$U = -\frac{\zeta |\mu_e|^2}{4\pi\epsilon_0 r^3} \tag{1.21}$$

It should be pointed out that for isotropically polarizable nanospheres the direction of the induced dipoles is not inherent to the nanospheres themselves but to the polarization of the incident light.

When the incident light is polarized along the interparticle axis, the (induced) dipoles will also be directed along this axis. From Equation 1.20 we calculate that $\zeta = 2$ for such a conformation. Equation 1.21 then shows that the interaction energy U is negative, implying an attractive interaction for dipoles aligned symmetrically (see Figure 1.13A). A red-shift of the plasmon resonance wavelength is observed for such a J-type dimer. As the dipoles cancel out for the anti-symmetric configuration of dipoles in a homodimeric assembly, this transition is optically forbidden and thus dark.

When the polarization of the incident light, and thus also the direction of the induced dipoles is perpendicular to the inter-particle axis (H-type), $\zeta = -1$. The interaction energy is then positive which implies a repulsive interaction for a symmetrically arranged dipoles (see Figure 1.13B). A blue-shift can be observed but smaller in magnitude due to a smaller interaction energy as compared to the J-type dimer. As the dipoles cancel out for the energetically lower-lying asymmetric configuration of dipoles, this transition is optically forbidden for a homodimer.

In the case of anisotropic materials, e.g. nanorods, this anisotropy needs to be taken into account when applying the exciton-coupling model. A nanorod for example has both a longitudinal and a transversal plasmon mode that can be excited. When using the exciton-coupling theory it is important to recognize these different modes and to assign the correct energy states of the plasmonically coupled dimer.

For heterodimers in terms of materials, shape or size it is possible that optically forbidden transitions in the homodimeric case become allowed.

As the observed red-shift of the resonance in the J-type dimeric case depends on the interaction energy between the two dipoles it is expected that when the strength of the optically allowed dipole coupling between two plasmonic entities increases, that also the relative red-shift should increase. As such, the red-shift expressed as $\Delta\lambda/\lambda_0$ is an indicator for the plasmonic coupling strength.

1.4.4 Beyond the dipole approximation and the exciton coupling model

Although the dipole approximation and the exciton coupling model help to qualitatively explain many observations in optically coupled plasmonic entities, it is not a complete description of the system. As for the dipole and the quasi-static approximations for entities much smaller than the wavelength of the incident light, the exciton coupling theory is not correct for larger entities. Higher order multipole interactions then need to be taken into account.

Also the increase in coupling strength between two dipoles as a function of inter-dipole spacing is not accurate. The exciton coupling model predicts that the coupling strength between two dipoles increases as a function of $1/r^3$ (see Equation 1.21) but in practice the coupling strength increases much faster for very small inter-particle distances. For those close distances, also higher order multipole modes have to be included in the description.

When going beyond the dipole approximation for a finite-sized particle in an incident field E_0, one can describe the resulting near-field as a Taylor expansion for all multipolar modes such as dipole, quadrupole, octopole and others. Higher multipole orders decay more rapid with increasing distance from the radiation source with $1/r^4$ for quadrupoles and $1/r^5$ for octupoles. This means that the smaller the distance from the radiation source, the larger the number of multipole orders that need to be taken into account. The existence of multipolar excitations for plasmonic entities in close proximity has been shown both experimentally and theoretically, for example in silver and gold nanoparticles and nanodisks with varying interparticle gaps.[171,175–178]

1.4.5 Synthesis and applications of plasmonic nanoparticles

Due to strong global research efforts, many synthesis methods were developed for plasmonic nanoparticles of various shapes, sizes and materials. Examples for gold and silver nanoparticles are thermal decomposition,[179] spontaneous formation in block copolymer solutions,[180] reduction of metal salts using phosphorus,[181] peroxides,[182] glycerol,[183] polyols,[184] sodium borohydride,[185,186] ascorbic acid,[187] citrate,[188–190] polymers,[191] or UV-light,[192] via electrochemical methods,[193] and synthesis in biological organisms.[194]

Applications of plasmonic nanoparticles are plentiful and range from biomedicine to sensors and catalysis.

Biomedically, plasmonic particles show efficient heating at their plasmon wavelength (λ_{max}) due to the strongly enhanced absorption,[195] which is exploited in medical cancer therapies such as photothermal therapy[17,196–198] or heat-induced release of antitumor drugs.[199,200] Plasmonic heating is also used in diagnostic techniques such as photoacoustic,[201] or photothermal imaging.[195] The superior scattering efficiencies of plasmonic nanostructures have been used in biomedical contexts for e.g. contrast agents in optical coherence tomography.[202] Some types of metallic nanoparticles also possess antibacterial properties.[182,187,203]

Gold and silver nanoparticles are also much-used in catalysis for oxidation, reduction, cyclization and coupling reactions.[6,204–209]

Due to the sensitivity of the optical and conductive properties of plasmonic nanoparticles to environmental parameters, they are excellent components for sensor applications. Examples are sensors for hydrogen peroxide,[210] biological markers,[211] and a range of other molecules that can be used e.g. to monitor food or environmental quality and for medical diagnostics.[212]

Other applications are e.g. gold nanoparticle ink for printing conductive circuits,[213] plasmonic nanoparticles for light harvesting,[214,215] or as solar cell sensitizers.[216–219]

1.4.6 Calculating linear optical properties of nanostructures

For many envisioned experiments and applications, and also to retrieve structural information, the optical properties of magnetic-plasmonic nanoparticles are important. Theoretical modeling allows to predict the optical properties of nanostructures and to explain observed optical spectra as a function of structural and environmental parameters.

In the context of this dissertation two modeling approaches were used: Mie theory calculations for spherical nanoparticles and the discrete dipole approximation (DDA) for nanostructures of arbitrary geometry.

Mie theory for spherical nanoparticles

As stated earlier, Gustav Mie solved Maxwell's equations to calculate extinction spectra (absorption and scattering) for small spherical particles of arbitrary size in the beginning of the 20th century. While only applicable for spherical particles it still remains an important theoretical tool since it is an analytically exact solution to Maxwell's equations and implemented in many computer codes.[160, 220, 221]

More recently, algorithms to calculate the optical properties of multi-layered spherical core-shell nanoparticles have been published and implemented in user-friendly computer programs such as MieLab, which was used to calculate optical spectra of core-shell nanoparticles in this work.[221]

Required input parameters are the total size of the core-shell nanoparticles, the thicknesses of all layers, the refractive index of the medium and the complex dielectric function or refractive index as a function wavelength for all materials present in the nanoparticle. The calculated properties are the extinction, scattering, and absorption efficiencies ($Q_{\mathrm{extinction}}$, $Q_{\mathrm{scattering}}$ and $Q_{\mathrm{absorption}}$) as a function of wavelength.

From the calculated $Q_{\mathrm{extinction}}$, $Q_{\mathrm{scattering}}$ and $Q_{\mathrm{absorption}}$ spectra, the plasmon resonance wavelength λ_{max} can be obtained. Further, the corresponding extinction, scattering, and absorption cross sections ($C_{\mathrm{extinction}}$, $C_{\mathrm{scattering}}$ and $C_{\mathrm{absorption}}$) can be obtained by multiplying the calculated efficiencies with the geometrical cross-sectional area of the structures in the incoming light. These cross sections represent a geometrical area of a particle that contributes to the extinction, absorption, or scattering and can be directly related to molar coefficients used in spectroscopy.

Discrete dipole approximation for nanostructures of arbitrary geometry

As exact solutions of Maxwell's equations are only known for spherical geometries, approximations are required to calculate the optical properties of structures of other arbitrary geometry.

Calculating optical spectra for nanostructures with an arbitrary geometry can be done with several numerical techniques, such as the multiple multipole,[222] the finite difference time domain method[223] or the discrete dipole approximation (DDA) method. The DDA method was chosen to calculate the optical spectra of nanostructures for the work in this dissertation because it has proven to be a powerful technique for calculating optical characteristics of structures with an arbitrary geometry in a dielectric environment.[160, 220, 224–227]

Although originally devised to study the optical properties of molecular aggregates much smaller than the wavelength of light,[228] the DDA method including retardation effects to model larger interstellar dust grains was published by Purcell and Pennypacker in 1973.[229]

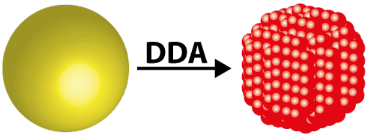

Figure 1.14: In the DDA method nanostructures of arbitrary geometry are approximated as an array of polarizable point dipoles. Here a sphere is represented by 485 dipoles as an example. In the performed calculations this number is much higher to reduce the inter-dipole spacing and improve accuracy.

In the discrete dipole approximation a continuum target is approximated by a finite array of polarizable points. As calculation of the optical scattering properties of a finite array of dipoles can be solved exactly, the only approximation is the replacement of the continuum target by an array of point dipoles (see Figure 1.14). These point dipoles acquire dipole moments in response to the local electric fields as described by their polarizabilities. As each point dipole can act as a local radiation source of electric fields and thus interact with the neighboring dipoles, these interactions are taken into account in the DDA method, which is sometimes also referred to as the coupled dipole approximation.

The DDA method allows calculation of the optical properties of structures of any geometry, as long as the structure can be approximated by an array of dipoles of which the inter-dipole spacing is much smaller than the geometrical size. Geometries are also not limited to a single entity, assemblies of particles can also be modeled. As the required calculating power, and thus CPU time, increases rapidly as a function of assigned point dipoles, calculations of large structures or with high accuracy (many dipoles and small inter-dipole separations) can be time-consuming.

Draine and Flatau implemented the DDA method in a computer code called DDSCAT, which is much used in current literature.[160, 220, 224–227] Required input parameters are the geometry of the structure, the total size as represented by an effective radius, the refractive index of the medium, the number of dipoles used, the polarizabilities of these dipoles and the complex dielectric functions or refractive indices of all used materials.

As for the Mie theory calculations described previously, the calculated properties are the extinction, scattering, and absorption efficiencies as a function of wavelength from which other properties can be derived.

Conversion to molar coefficients

The calculated cross sections (in cm^2) can be converted to molar coefficients (in $L.mol^{-1}.cm^{-1}$) used in spectroscopy. The formula used is,[230]

$$\epsilon_{molar} = \frac{C_i N_A}{1000.ln(10)} = \frac{C_i}{3.82 \times 10^{-21}} \tag{1.22}$$

in which ϵ represents the molar coefficient, C_i the relevant cross section and N_A the Avogadro constant.

1.4.7 Nonlinear and magneto-optical properties of plasmonic nanostructures

At the surface plasmon resonance wavelength, large enhancements of electric fields are induced. As many nonlinear optical phenomena are strongly dependent on the local electric field strength, plasmonic nanostructures are very interesting to enhance nonlinear optical response (see Equation 1.13). Examples are surface plasmon enhanced Raman scattering (SERS),[163] second harmonic generation (SHG),[164–167, 231] hyper-Rayleigh scattering,[232] third harmonic generation,[233–236] or multiphoton-absorption-induced luminescence (MAIL).[237–239]

Although magneto-optical responses in purely plasmonic nanostructures are generally small, Sepulveda *et al.* showed that the magneto-optical activity of nanosized gold disks is substantial.[240] The response is attributed to the increase of the magnetic Lorentz force induced by the large collective movement of the conduction electrons when the LSPR is excited using circularly polarized light. As this behavior is due to the free electrons in gold, it is stated by the authors that any ‘Drude metal’ should exhibit substantial magneto-optical activity. Wysin *et al.* further investigated the effect of interband transitions in metallic nanoparticles on their Faraday rotation response.[128] The authors concluded that these transitions need to be included in a full description of the magneto-optical activity of metallic nanoparticles.

1.5 Magnetic-plasmonic nanomaterials

Magnetic-plasmonic nanostructures are integrated magnetic and plasmonic materials. Because of their attractive properties and the long list of potential applications in a range of sectors, research into such integrated materials has surged. In this section first a brief overview of synthesis methods is given, followed by the properties and applications of magnetic-plasmonic structures. Last, elements of the emerging field of magnetoplasmonics, where the interplays of magnetic fields and plasmon resonances are studied and exploited, will be summarized.

1.5.1 Synthesis of magnetic-plasmonic nanostructures

Many magnetic-plasmonic structures reported in literature were fabricated using top-down methods.[241–248] For the work presented in this dissertation only bottom-up techniques were used to fabricate magnetic-plasmonic nanostructures. This because of the advantages mentioned in section 1.1.2.

As already stated in section 1.1.2, making multifunctional, i.e. magnetic-plasmonic, nanostructures can be done either by integrating the required functional components in a single entity or assembling several monofunctional entities in a larger assembly.

Core-shell nanomaterials

An elegant approach to integrate multiple functional materials in a single entity is to synthesize core-shell nanoparticles. In such a particle the core of one material is surrounded by a shell of a different material rendering the total core-shell structure multifunctional.

Many synthetic protocols for magnetic-plasmonic core-shell nanoparticles of all kinds of materials, shapes and sizes have been reported. Examples include metal-oxides/metal,[168,169,249–254] metal/metal-oxides,[41,255] and metal/metal.[39,256]

The magnetic and plasmonic components are in very close contact in such core-shell structures, which is a clear advantage when a maximal interaction between the two components is desired. Further, for applications that involve movement the integrated nanostructure, like in magnetically guided magnetic-plasmonic nanoparticles useful in biomedicine, single-entity magnetic-plasmonic nanostructures are a prerequisite.

Assemblies of magnetic and plasmonic nanoparticles

In contrast to the rather extensive literature on core-shell magnetic-plasmonic nanoparticles, only a few reports on magnetic-plasmonic nanomaterials based on assemblies of magnetic and plasmonic nanoparticles have been published.

Caminale *et al.* prepared magnetic-plasmonic samples by depositing plasmonic nanoparticles in the grooves of a LiF surface and then coating these plasmonic particles with iron oxide nano crystals.[257]

Magnetic-plasmonic microcapsules were synthesized by assembling gold and maghemite nanoparticles at the oil-water interface of microdroplets generated in a microfluidic device by Hassan *et al.*.[258]

Further, Wang *et al.* integrated core-shell magnetic-plasmonic nanoparticles in an assembly.[259] They synthesized magnetite nanospheres and coated them with a gold shell capped by thiolates. Subsequent cross-linking of the coating molecules resulted in a magnetic-plasmonic thin film assembly.

1.5.2 Properties and applications of magnetic-plasmonic nanostructures

Integrating two or more materials of which the functionalities do not interact results in a novel material of which the properties are the sum of the integrated materials.

Core-shell nanoparticles

Magnetic-plasmonic core-shell nanoparticles already attract considerable interest for use in biomedical applications.[78, 260] Figure 1.15 shows the relevant processes in such hybrid nanostructures. Incident photons can be absorbed or scattered, generating plasmon bands, heat, or scattering contrast. External magnetic fields can be used to generate heat through conversion of AC magnetic field energy losses, to facilitate guidance of particles, and to generate extra contrast in MRI.[261–264]

Non-biomedical applications of magnetic-plasmonic core-shell nanoparticles include magnetically recoverable catalysts,[255, 265–267] nanoparticles for magnetic separation of molecules conjugated to the metallic shell,[251, 268] or waste-water treatment.[269]

Multifunctional assemblies

Magnetic-plasmonic thin films based on nanoparticles could be used for concomitant magnetic field and plasmonic heating of membranes to improve flux or magnetic field heating of a film containing plasmonic catalysts.[270–272]

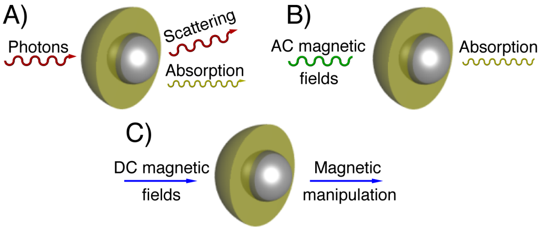

Figure 1.15: Overview of relevant processes in core-shell magnetic-plasmonic nanoparticles composed of a magnetic core and a plasmonic shell for biomedical applications; A) scattering or absorption of photons; B) absorption of AC magnetic field energy; C) use of DC magnetic fields to magnetically manipulate the nanostructures.

For (linear, nonlinear and magneto-) optical experiments and applications, thin film structures have the advantages of increased stability, fixed morphology and ease of handling (see the next section on magnetoplasmonics).[110,257] Further, making combination of magnetic and plasmonic components and their linear and non-linear optical properties might result in materials that show resonant enhancement of non-linear effects at multiple wavelengths.

1.5.3 Magnetoplasmonics

Magnetoplasmonics, the field that studies the interactions between magnetism and plasmon resonances originated in the 1970's when the influences of external magnetic fields on surface plasmons in metals and semiconductors were first studied.[273–275] Research into magneto-optical recording and the desired enhancement of magneto-optical responses in active materials, usually metallic bilayers, was responsible for the majority of the publications on the subjects in the following decades.[276–283]

More recently, the more general availability of nanofabrication tools, the extension of many optical models to include magneto-optical effects and the rapidly expanding research field of plasmonics have been driving the interest in magnetoplasmonics.[161] Magnetoplasmonics at the nanoscale can be used to control the properties of propagating light on metallic structures and to enhance magneto-optical effects.[161,284–286]

To realize miniaturized photonic/plasmonic circuit components such as switches, isolators or modulators, a reliable and ultrafast mechanism to change the optical properties of the plasmonic material is required. While mechanisms based on temperature,[287] nanoscale crystal phase changes,[288] or photons,[289,290] have been published, external magnetic field-induced changes in plasmonic properties are excellent candidate effects as they are ultrafast,[291] and depend on magnitude of the applied field as well as its direction (see section 1.3.5 on magneto-optics).[245]

In search for materials with improved magneto-optical responses or with improved control over nanoscale light propagation using external magnetic fields for application in e.g. sensors,[292] or telecommunications,[286,293] magnetoplasmonic nanomaterials are attractive research subjects.

Plasmon-enhanced magneto-optics in nanomaterials

In the context of this dissertation, a short overview of plasmon-enhanced magneto-optics in magnetic-plasmonic nanomaterials is given.

Using a Maxwell-Garnett approach Hui and Stroud predicted in 1987 an enhanced magneto-optical Faraday effect at the plasmon frequency for a low concentration of granular inclusions in a Faraday-inactive matrix.[294] Later, Xia, Hui and Stroud extended the calculations to include a wider range of inclusion concentrations using an effective-medium approximation.[295] These predictions were then confirmed in e.g. Co-Ag granular films.[276–278]

More recently, plasmon-assisted magneto-optical enhancements were for example observed for magnetite nanocrystals on gold surfaces,[296] gold-coated iron oxide nanoparticles,[168] dumbbell-like $\mathrm{Ag-CoFe_2O_3}$ nanoparticle pairs,[297] garnets embedded with gold nanoparticles,[298–300] semiconductor crystals with gold nanoparticles,[301] magnetic-plasmonic sandwich structures,[241,242] core-shell Co-Ag nanoparticles,[256] gold gratings on a planar ferromagnetic dielectric,[244,245] molecularly thin ferromagnetic material on gold surfaces,[243] nanosized Ni disks,[302] nickel G-shaped nanostructures,[246] and plasmonic nanodisks on a magnetic substrate.[247,248]

The origin of the enhancement of the magneto-optical effects is the very large local enhancement of the electromagnetic fields through plasmon resonances. When a magneto-optically and a plasmonically active entity are optically coupled, i.e. in close vicinity of each other, the magneto-optical response is enhanced to a degree that correlates with the electromagnetic field strength in the magneto-optically active entity.[161,168,248,257,294,295]

If the plasmon resonance in the magnetoplasmonic system is spectrally far from the magneto-optical resonance then the magneto-optical enhancement occurs with the same spectral features as the plasmon resonance itself. In the case where the plasmon and magneto-optical resonance spectrally overlap, the enhanced local electromagnetic field produced by the plasmonic component can strongly enhance the magneto-optical response in the active magnetic material.[168, 248, 257]

As stated already in section 1.4.2, the difference in excitation conditions between systems sustaining propagating or localized surface plasmons is that for propagating plasmons the wavevectors must match. Concretely, this means that in order to have efficient excitation of propagating plasmons, the angle of the incident beam needs to be correct.[161] This might not be a problem for most experiments although angle-independent excitation of plasmon resonances (as for LSPRs) and thus also of plasmon-enhanced effects can be a great asset for both fundamental and applied experiments.

1.6 Objectives & outline

For magnetic-plasmonic nanomaterials to be used for fundamental experiments and future applications, synthesis protocols and the properties of these materials need to be studied and optimized.

1.6.1 Objectives

In many applications of core-shell magnetic-plasmonic nanoparticles in biomedicine, such as photothermal therapy, scattering microscopy or photoacoustic imaging, the spectral position and strength of the plasmon response of the integrated nanostructures is of great importance. The optical properties of homogeneous and core-shell nanospheres and nanorods in general have already been assessed theoretically and experimentally.[17, 159, 160, 220, 223, 303] More specifically, magnetite-gold core-shell spherical NPs have been experimentally produced.[168, 250–254] Although hybrid structures have been synthesized, no theoretical framework for the rational design of magnetic-plasmonic nanostructures for life science applications, based on optical characteristics, has been reported yet.

Spurred by a strong interest in efficient nonlinear optical materials, magnetoplasmonics, plasmon-enhanced magneto-optical effects and active plasmonics, the demand for hybrid magnetic-plasmonic nanoparticle-based thin film materials of optical quality is high. Previously, nanocomposites were synthesized on non-transparent or grooved substrates[257] using polymers as a dispersion medium for spin-coated or drop-casted samples,[130, 304, 305] or polyelectrolyte interlayers in Layer-by-Layer synthesis.[62] Polymers and polyelectrolytes have the disadvantages that nanoparticle filling fractions are inherently limited and that they possibly introduce undesired background signal, chemical incompatibility and interfere with signal acquisition.

The ability to reliably synthesize high optical quality magnetic-plasmonic nanocomposites with high nanoparticle filling fractions and without introducing unnecessary background signals facilitates experiments and is a prerequisite to interpret results correctly. Furthermore, for many experiments or applications, such as optical Faraday isolators, (partial) transparency is a must.[161,244]

The **aims of the performed work** were three-fold. As first, to provide a rational design framework for core-shell magnetic-plasmonic nanoparticles based on their optical properties and focused on biomedical applications. Secondly, to develop a novel synthetic protocol for homogeneous thin film nanoparticle-based magnetic-plasmonic nanomaterial with a variable sample thickness and tuneable optical properties and without using possibly interfering polymers and polyelectrolytes. Third, to characterize the linear, nonlinear and magneto-optical properties of such magnetic-plasmonic nanomaterials.

1.6.2 Outline

The outline of this dissertation is as follows.

In **Chapter 2**, we present the calculated optical properties of core-shell magnetic-plasmonic nanospheres and nanorods as a function of nanostructure composition, size, and shape. Furthermore, the optical characteristics of magnetic-plasmonic nanostructures were quantitatively compared with those of organic dyes applied in biomedical environments. With this knowledge it is possible to rationally design and synthesize structures that possess a plasmon band in the advantageous biomedical near-infrared spectral window region and other optical properties as desired for potential application in life sciences.

Subsequent chapters detail the synthesis and characterization of magnetic-plasmonic nanoparticle multilayers.

The ability to synthesize properly functionalized (superpara)magnetic nanoparticles is one of the prerequisites to make nanoparticle-based multifunctional magnetic-plasmonic nanomaterials. Iron oxide was chosen as the ideal material for nanoparticle synthesis. To use these particles as building blocks for multifunctional nanomaterials, iron oxide phase, physical size, hydrodynamic diameter and the optical, magnetic and magneto-optical properties of the synthesized particles need to be known. To characterize these properties for non-interacting iron oxide nanoparticles we prepared ferrofluids, which are thermodynamically stable dispersions of superparamagnetic nanoparticles in suitable solvents, using polyethylene glycol (PEG) coated nanoparticles. In **Chapter 3**, we first introduce the used synthesis method for iron oxide nanoparticles and the protocol for modifying the surface of the synthesized particles with the desired functional end-group and then present the results of the characterization experiments.

In **Chapter 4** we present a versatile Layer-by-Layer synthesis method on glass substrates using short bifunctional, i.e. with two functional groups, molecular linkers that results in homogeneous samples with very high nanoparticle filling fractions. Tunable plasmon properties, of both silver- and gold-magnetite nanocomposites, over a broad spectral range combined with angle-independent optical properties and a variable composite thickness make these high quality composites an ideal platform for magnetoplasmonic research.

To explain the observed optical properties of the magnetic-plasmonic nanoparticle multilayers we resorted to modelling. The results of these calculations are presented in **Chapter 5**. First the influences of distances, dielectric constants, incident light polarization, number of adjacent nanoparticles and angle relative to the incoming light on the optical properties of coupled plasmonic nanoparticle assemblies were determined. While the trends for the influences of such parameters on the optical properties of plasmonic systems are known in general, we calculate them specifically for particles in the size range we used and assemblies relevant for the experimentally synthesized nanoparticle multilayers. Then we extended the calculations to include magnetic-plasmonic nanoparticle assemblies and attempt to model the experimental multilayers. From the comparison between the calculated and the experimentally obtained spectra for magnetic-plasmonic nanoparticle multilayers we gained more insight in the Layer-by-Layer synthesis mechanism of these multilayers.

Results of measurements of the nonlinear optical properties of gold-magnetite nanoparticle multilayers are presented in **Chapter 6**. Inorganic nanoparticles, such as gold or iron oxide nanoparticles, exhibit large nonlinear susceptibilities and fast response times but at different wavelengths due to their (coupled) surface plasmon and intervalence charge transfer resonances respectively. Combining such nanoparticles should result in interesting materials that possess multiple nonlinear optical resonances.

Finally, in **Chapter 7** the results of magneto-optical Faraday rotation and ellipticity measurements on Au-magnetite nanoparticle multilayers are shown. Magnetoplasmonic enhancements were observed and the influence of the sample thickness explored.

Chapter 2

Core-shell magnetic-plasmonic iron oxide-gold nanoparticles

Calculated optical properties of hybrid structures

This chapter is a reproduction of the following publication that has been adapted to form only:

W. Brullot, V.K. Valev, T. Verbiest.
Magnetic-plasmonic nanoparticles for the life sciences: Calculated optical properties of hybrid structures.
Nanomedicine: NBM **8** (5), 559-568 (2012).

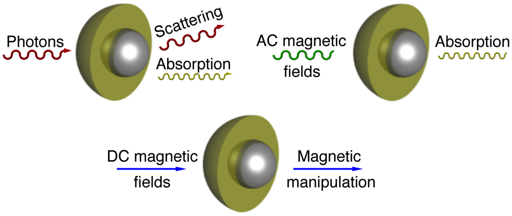

Abstract

Magnetic-plasmonic nanoparticles, combining magnetic and plasmonic components, are promising structures for use in life sciences. Optical properties of core-shell magnetite-gold nanostructures, such as the wavelength of the plasmon resonance, the extinction cross section, and the ratio of scattering to absorption at the plasmon wavelength are critical parameters in the search for the most suitable particles for envisioned applications.

Using Mie theory and the discrete dipole approximation (DDA), optical spectra as a function of composition, size, and shape of core-shell nanospheres and nanorods were calculated. Calculations were done using simulated aqueous media, used throughout the life sciences.

Our results indicate that in the advantageous near-infrared region (NIR), although magnetic-plasmonic nanospheres produced by available chemical methods lack the desirable tunability of optical characteristics, magnetic-plasmonic nanorods can achieve the desired optical properties at chemically attainable dimensions. The presented results can aid in the selection of suitable magnetic-plasmonic structures for applications in life sciences.

2.1 Introduction

Both plasmonic and magnetic nanomaterials are currently under intensive investigation for use in biomedical applications, and many findings have already been commercially exploited.[78, 196, 306, 307] The field of magnetic-plasmonic nanostructures, in which plasmonic and magnetic materials are combined, however, is only just emerging. Such multifunctional structures are commonly called “theranostic” structures in biomedical contexts due to their therapeutic and diagnostic potentials.[78, 260]

Magnetic nanostructures used in biomedical applications are usually composed of iron oxides, such as magnetite or maghemite because these materials combine high magnetic susceptibilities with very low toxicity.[78, 79] Spherical iron or iron oxide based nanoparticles (NPs) can be prepared by a variety of well-known synthesis methods. Most methods currently available provide iron oxide nanospheres with an average diameter well below the superparamagnetic limit,[44] which is about 30nm for magnetite.[80] Above the superparamagnetic limit, iron oxide NPs become ferri- or ferromagnetic. Besides spherical or cube-shaped particles, iron oxide nanorods have also been chemically synthesized.[308, 309] For example, Kumar et al,[309] have synthesized 12×48nm magnetite nanorods. If superparamagnetic NPs are surrounded by a suitable coating layer, they can be dispersed in a carrier liquid (e.g., water) and form a stable magnetic fluid or ferrofluid.[306] Ferri- or ferromagnetic NPs, i.e., above the superparamagnetic limit, require an extensive stabilizing hydrophilic coating layer in aqueous environments to prevent precipitation due to magnetostatic interactions.[310]

Biocompatible magnetic particles or fluids can be used as magnetic drug-targeting agents,[311] magnetic resonance imaging (MRI) contrast agents,[78] and as an agent for localized AC magnetic field hyperthermia.[306] Another interesting application is magnetic separation of species in solution using magnetic NPs conjugated with a specific binding agent.[256]

Plasmonic NPs, i.e., NPs exhibiting localized surface plasmon resonances, can show strong optical resonances for visible and near-infrared wavelengths.[160, 196, 220] This is due to the collective oscillations of free conduction electrons when illuminated with light at the plasmon wavelength (λ_{max}). For metallic NPs, e.g. gold and silver,[160, 220] this resonance mode is called a localized surface plasmon resonance (LSPR). Plasmon resonances endow nanostructures with unique optical properties, such as strongly enhanced absorption and scattering at the plasmon resonance wavelength. The intensity and position of the plasmon resonance heavily depend on the size and shape of the plasmonic structure and the surrounding medium.

Plasmonic particles show efficient heating at λ_{max} due to the strongly enhanced absorption,[195] which is exploited in medical cancer therapies such as photothermal therapy[17, 196, 197] or heat- induced release of antitumor drugs.[199] Plasmonic heating is also used in diagnostic techniques such as photoacoustic[201] or photothermal imaging.[195] The superior scattering efficiencies of plasmonic nanostructures have been used in biomedical contexts for optical biosensors[211] and contrast agents for imaging in, for example, optical coherence tomography.[202]

The position of the plasmon band is of great importance for biomedical applications. Hemoglobin and water, the dominant contributors to the absorption spectrum of living tissue, show a minimum in their absorption spectra in the NIR of the spectrum (650-900nm).[312, 313] As such, the NIR is the preferred region to position λ_{max} for optical biomedical applications. Structures consisting of a dielectric core surrounded by a plasmonic shell, like silica-gold core-shell nanospheres, show redshifted plasmon bands and have recently been used as NIR photothermal probes.[160, 196]

Gold is predominantly used as plasmonic metal for biomedical applications because of its biocompatibility, well-defined synthesis routes, resistance to oxidation, and flexible conjugation possibilities with organic molecules.[195, 202, 307]

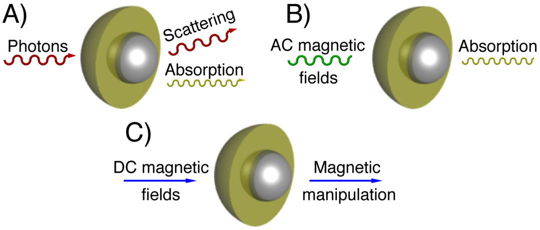

Figure 2.1: Overview of relevant processes in hybrid magnetic-plasmonic nanoparticles composed of a magnetic core and a plasmonic shell; A) scattering or absorption of photons; B) absorption of AC magnetic field energy; C) use of DC magnetic fields to magnetically manipulate the nanostructures.

Magnetic-plasmonic nanostructures are integrated magnetic and plasmonic materials. Although the individual materials already allow many applications, integrated nanostructures greatly extend the possibilities. Figure 2.1 shows the relevant processes in such hybrid nanostructures. Incident photons can be scattered or absorbed, generating plasmon bands, heat, or scattering contrast. External magnetic fields can be used to generate heat through conversion of AC magnetic field energy losses, facilitate guidance of particles, and generate extra contrast in MRI. Such multimodal structures have a very broad applicability. Some examples are the use of magnetic-plasmonic nanostructures for MRI and photothermal therapy[261] or for simultaneous MRI and drug release.[262] Other possibilities include following DC magnetic field guided magnetic-plasmonic particles by scattering imaging, combining magnetic separation in solution with plasmonic detection methods, or concomitant magnetic hyperthermia and photothermal therapy for cancer treatment.

In many, if not all, envisioned applications, the position and strength of the LSPR response of the integrated nanostructures is of great importance. The optical properties of homogeneous and core-shell nanospheres and nanorods have already been assessed theoretically and experimentally.[17, 159, 160, 220, 223, 303] Experimentally, magnetite-gold core-shell spherical NPs have been produced,[168, 250–254] but to our best knowledge, none with a magnetite core larger than the superparamagnetic limit. Although hybrid structures have been synthesized, no theoretical framework for the rational design of magnetic-plasmonic nanostructures for life science applications, based on optical characteristics, has been reported yet.

Important to note is that besides the separate magnetic and plasmonic properties of hybrid structures taken into account in current work, interplay, called magnetoplasmonics, exists between both components. A prominent example of this interplay is enhancement of magneto-optical effects through plasmon excitation.[168, 314, 315] For nanostructures such as those studied in this work, such magnetoplasmonic effects generally influence only the polarization state of the optical beam while passing through the sample.[316] The polarization state of light is only important for the rodlike shapes, because they are anisotropic, and as NPs in tissue generally rotate, the polarization state of the used light is of minor importance for biomedical applications. Therefore, magnetoplasmonic effects are not taken into account in current work.

In this work, optical properties such as $\lambda_{\max}$, the extinction cross section ($C_{\text{extinction}}$), and the ratio of scattering to absorption cross sections ($C_{\text{scattering}}/C_{\text{absorption}}$) at $\lambda_{\max}$ of magnetic-plasmonic magnetite-gold nanostructures were calculated. The influence of nanostructure composition, size, and shape on these optical properties was investigated. Furthermore, the optical characteristics of magnetic-plasmonic nanostructures were quantitatively compared with those of organic dyes applied in biomedical environments.

For core-shell spheres, calculations were performed using the analytically correct Mie theory for multilayered spherical structures.[160, 220, 221] Calculating optical spectra for nanostructures with an arbitrary geometry can be done with several numerical techniques, such as the multiple multipole,[222] the finite difference time domain method[223] or the DDA method. The DDA method was chosen to calculate the optical spectra of nanorod structures because it has proven to be a powerful technique for calculating optical characteristics of structures with an arbitrary geometry in a dielectric environment.[160, 220]

Magnetite and gold were respectively chosen as magnetic and plasmonic material for the performed calculations because both materials have been intensively studied. Magnetite is a very well-known material possessing the highest saturation magnetization of all iron oxides,[79] and gold is the predominantly used plasmonic material in biosciences.

The findings and insights can aid in the rational design of magnetic-plasmonic nanostructures with applications in the life sciences.

2.2 Calculation method

Extinction, scattering, and absorption efficiencies ($Q_{\text{extinction}}$, $Q_{\text{scattering}}$ and $Q_{\text{absorption}}$) as a function of wavelength for core-shell nanospheres were calculated using Mie theory. Calculations were performed using MieLab.[221] Input parameters were the thickness of each layer in the spherical nanostructure,

R_i , the complex dielectric functions, ?$_i$, and the complex refractive index of the medium. This last parameter was chosen to be that of water, $1.33 + 0i$, because many environments encountered in biomedical applications, such as blood or perfused tissues, can be approximated as aqueous environments.

To improve comparability with previous seminal work,[17,160] bulk dielectric functions of materials were used.[317,318] Corrections for size are generally calculated via the damping constant, which has an effect only as a possible line broadening mechanism.[319] Furthermore, because most of the calculated structures are above the size limit for corrections, the influence of not correcting for size on the predicted trends and values are minimal.

The dimensions of core-shell nanospherical structures cannot be represented by a single radius but are defined by the total radius for the structure (R_{total}) as the sum of the radii of the magnetic core (R_{core}) and the surrounding dielectric shell (R_{shell}). Optical properties of core-shell nanospheres were calculated for two sets of structures. One has a fixed R_{total} and varying R_{core}, and a second has a fixed R_{core}/R_{total} ratio while varying R_{total}. As such, the influences of the two defining structural parameters, size and core-shell ratio, on the optical properties were investigated.

Optical characteristics of magnetic-plasmonic nanorods were calculated using the DDA method.[226,320] Nanorods were modeled as cylinders with hemispherical end caps,[159] and the aspect ratio was defined as the ratio of the total length of the rod, including the hemispherical end caps, to the maximal diameter.

To represent the size of nanorod structure, an effective radius (R_{eff})) was defined. This $R_{eff)}$ is equal to the radius of a sphere that possesses the same volume as that of the nanorod. To describe the core-shell nature of the calculated nanorod structures, the R_{core}/R_{total} ratio is used. As such, nanorods can be structurally described by their aspect ratio, the effective radius and the R_{core}/R_{total} ratio.

Calculations were performed for a fixed orientation of the nanorods whereby the propagation of the incident light wave is perpendicular to the long axis of the structure. This was done to ensure excitation of the longitudinal dipolar localized surface plasmon resonance. Two orthogonal polarizations of the incoming light were used, one with the electric field perpendicular and the other parallel to the long axis of the nanorod.

From the calculated spectra of the $Q_{extinction}$, $Q_{scattering}$ and $Q_{absorption}$ efficiencies and λ_{max} can be obtained. The corresponding extinction, scattering, and absorption cross sections ($C_{extinction}$, $C_{scattering}$ and $C_{absorption}$) can be obtained by multiplying the calculated efficiencies with the geometrical cross-sectional area of the structures in the incoming light. These cross sections represent a geometrical area of a particle that contributes to the extinction, absorption, or scattering and can be directly related to molar coefficients used in spectroscopy.

Knowing the absolute values of the calculated cross sections, it is possible to calculate $C_{\mathrm{scattering}}/C_{\mathrm{absorption}}$ at λ_{max}, which is an important parameter when selecting particles for applications. This parameter indicates the relative degree with which a structure scatters or absorbs light and is a key factor in choosing the suitable structure for the foreseen application. For some applications, scattering of light is the main process, as in, for example, resonance scattering imaging, whereas others require a high absorption coefficient, such as photothermal therapy. The first application requires a high and the second a low $C_{\mathrm{scattering}}/C_{\mathrm{absorption}}$ ratio.

As stated earlier, the calculated cross sections (in cm^2) can be converted to molar coefficients (in $\mathrm{L.mol^{-1}.cm^{-1}}$) used in spectroscopy. The formula used is,[230]

$$\epsilon_{molar} = \frac{C_i N_A}{1000.ln(10)} = \frac{C_i}{3.82 \times 10^{-21}} \tag{2.1}$$

in which ϵ represents the molar coefficient, C_i the relevant cross section and N_A the Avogadro constant. As molar coefficients are known for many organic dyes used in biomedical applications, a useful comparison between these dyes and magnetic-plasmonic nanostructures becomes possible.

2.3 Results

As stated in the Calculation method section (2.2), three important optical parameters were obtained from the calculated $Q_{\mathrm{extinction}}$, $Q_{\mathrm{scattering}}$ and $Q_{\mathrm{absorption}}$ spectra. These were λ_{max}, the corresponding cross sections ($C_{\mathrm{extinction}}$, $C_{\mathrm{scattering}}$ and $C_{\mathrm{absorption}}$), and $C_{\mathrm{scattering}}/C_{\mathrm{absorption}}$ at λ_{max}.

It is important to note that these parameters are not independent. Because the dielectric functions of the materials change throughout the spectrum, the cross sections and their ratio at λ_{max} also change when shifting λ_{max}.

The general influence of the structural parameters of core-shell nanospheres and nanorods, i.e., size, core-shell ratio, and shape, on the optical characteristics can be rationalized. Keeping all other parameters constant, increasing size is expected to cause a redshift of λ_{max} due to the electromagnetic retardation effect[168] and an increase in $C_{\mathrm{extinction}}$ at λ_{max} due to the extra amount of contributing material present in a single particle. The influence of size on the $C_{\mathrm{scattering}}/C_{\mathrm{absorption}}$ ratio at λ_{max} depends on the dielectric functions of the constituting materials at the shifted λ_{max} and also on the size- and wavelength-dependent Rayleigh scattering.

Increasing the core-shell ratio, i.e., coating the particles with a thinner metallic shell generally results in a redshift of λ_{max}. This response can be explained by considering the inside and outside of the gold shell as separate species, generating plasmon modes that couple across the shell to result in the observable optical spectra. As such, thinner shells facilitate coupling of the plasmon modes, resulting in a redshift of λ_{max}.[303] A large core-shell ratio also causes a decrease in $C_{\text{extinction}}$ at λ_{max} due to a lower amount of plasmonic metal per particle. As for the size parameter, the influence of the core-shell ratio on the $C_{\text{scattering}}/C_{\text{absorption}}$ ratio at λ_{max} depends on the dielectric functions of the materials at the shifted λ_{max}.

The aspect ratio is a third variable parameter for magnetic-plasmonic nanorods. Increasing the aspect ratio is expected to cause a redshifted λ_{max} for the longitudinal plasmon band due to the increased path length for electron oscillation along the long axis.[321] Furthermore, increasing the aspect ratio is likely to result in a larger $C_{\text{extinction}}$ at λ_{max}. This larger $C_{\text{extinction}}$ can be attributed to enhanced coupling between the inner and outer plasmon modes of the plasmonic shell of core-shell structures with a higher aspect ratio.[321]

In the following paragraphs, results of calculations on core- shell magnetite-gold nanospheres and nanorods will be discussed. The general considerations described in the earlier paragraphs will be of great help when rationalizing the obtained results.

2.3.1 Magnetic-plasmonic nanospheres

As stated earlier, available chemical synthesis routes mostly provide magnetite cores with an average radius of 5nm, whereas the superparamagnetic limit for such structures is approximately 15nm. Calculated optical properties for core-shell nanospheres with an R_{core} of 5nm or 15nm and increasingly thinner gold shells are shown in Figure 2.2. These spectra indicate the shift of λ_{max} by simultaneously changing the composition and size of the core-shell nanospheres.

As expected, calculations showed that a thinner shell exhibits a greater redshift in comparison with a thicker shell and shows a lower $Q_{\text{extinction}}$ due to a decrease in the amount of gold per particle. The calculated results are consistent with experimentally obtained results for similar systems.[168, 252–254] From Figure 2.2A it is evident that coating magnetite particles with an R_{core} of 5nm with a gold shell does not provide efficient tuning of the plasmon band, nor high $Q_{\text{extinction}}$ throughout the NIR.

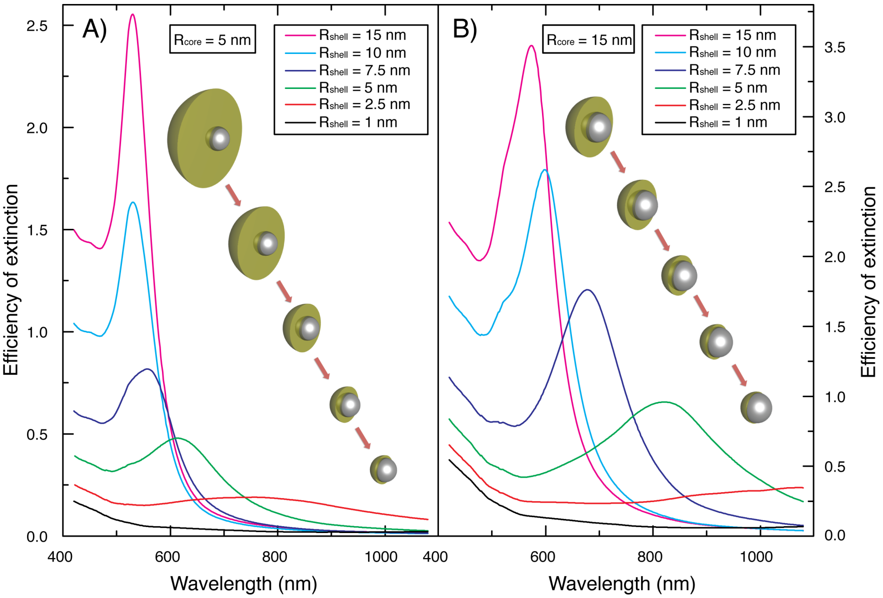

Figure 2.2: $Q_{extinction}$ as a function of wavelength for core-shell nanospheres with A) an R_{core} of 5nm or B) an R_{core} of 15nm and an increasing gold shell thickness (R_{shell}). The spectra show redshifts of λ_{max} and decreasing $Q_{extinction}$ at λ_{max} with decreasing shell thickness.

As can be seen from 2.2B, coating particles with a size around the superparamagnetic limit with a gold shell reveals two compositions, with a 5nm and a 7.5nm gold shell, to show plasmon bands in the advantageous NIR. These results indicate a trend in which magnetic-plasmonic nanospheres consisting of larger cores show higher tunabilities in the NIR. Furthermore, small spherical NPs as calculated here, exhibit very small $C_{scattering}/C_{absorption}$ ratio at λ_{max} due to the size and wavelength dependence of Rayleigh scattering. This diminishes their applicability in scattering applications.

Despite that core-shell magnetite-gold nanospheres larger than the superparamagnetic limit have, to our best knowledge, not been experimentally synthesized yet, optical characteristics as a function of structural parameters for such nanostructures were calculated. This provides deeper insight into the trends of optical properties indicated by the results described in the previous paragraph.

Calculated optical spectra for core-shell nanospheres with a fixed R_{total} of 70nm and a varying R_{core} of 70, 60, 50, 40, and 0nm are shown in Figure 2.3 A. The calculated plasmon peaks are located in the advantageous NIR of the spectrum. As for the smaller core-shell nanospheres calculated earlier, structures with an increasingly thinner gold shell show an increasingly more redshifted λ_{max}. Although a slight decrease of the maximum $Q_{extinction}$ can be observed for a decreasing volume of gold, high efficiencies are calculated for all studied core-shell nanospheres. Besides the dipolar plasmon band, another resonant peak can be observed at a shorter wavelength. The existence of this band can be attributed to quadrupolar interactions in the dielectric shell.[160]

Figures 2.3B-F show the calculated spectra of $Q_{extinction}$, $Q_{scattering}$ and $Q_{absorption}$ of core-shell nanospherical structures with fixed R_{total} of 70nm and stepwise increasing R_{core}. From the graphs it is apparent that not only λ_{max} shifts but also that the relative contributions of scattering and absorption drastically change with altering core-shell composition.

In Figure 2.4, the dependencies of λ_{max}, $C_{extinction}$ and $C_{scattering}/C_{absorption}$ at λ_{max} on the R_{core}/R_{total} ratio with fixed R_{total} and on R_{total} with fixed R_{core}/R_{total} are plotted. In the first case R_{total} is fixed to 70nm and in the second case R_{core}/R_{total} is fixed to 0.857.

From Figures 2.4A and 2.4B, it is evident that λ_{max} can be readily tuned throughout the NIR by varying the R_{core}/R_{total} ratio or R_{total}. Extinction cross sections at λ_{max} of the calculated structures are shown in Figures 2.4C and 2.4D. By increasing the core volume relative to the shell volume, a decrease of the $C_{extinction}$ is observed. The explanation is that gold is the dominant contributor to the $C_{extinction}$ at λ_{max} and that a smaller fraction of the total volume is gold in structures with a large R_{core}/R_{total}l ratio.

If the R_{core}/R_{total} is kept constant, an increase in the total size results in a larger $C_{extinction}$ at λ_{max}. The explanation is that the increase in total size augments the amount of material present in a single nanostructure, enhancing $C_{extinction}$., The $C_{scattering}/C_{absorption}$ at λ_{max} for the studied structures are shown in Figures 2.4E and 2.4F.

It can be seen that increasing the R_{core}/R_{total} ratio causes a decrease in $C_{scattering}/C_{absorption}$ at λ_{max} whereas an increase in R_{total} induces an increase for the same ratio. As stated in the general considerations earlier, the observed trends can be explained by contributions from Rayleigh scattering and the dielectric functions of the constituting materials.

The findings presented here are consistent with the general considerations about plasmonic shells described earlier and show great similarities with the results for silica-gold core-shell NPs calculated by Jain *et. al.*[160]

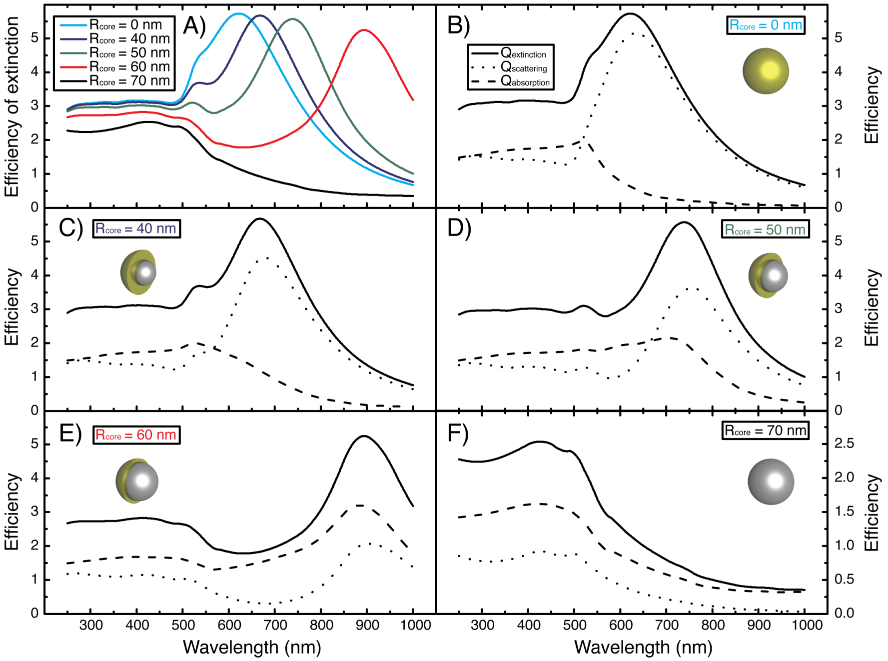

Figure 2.3: Calculated optical properties of core-shell nanospheres for a fixed R_{total} of 70nm; A) $Q_{extinction}$ for all calculated R_{core}; B-F) $Q_{extinction}$ (solid line), $Q_{scattering}$ (dotted line) and $Q_{absorption}$ (dashed line) for R_{core} equal to 70nm, 60nm, 50nm, 40nm and 0nm. The spectra indicate the shifts of λ_{max} and changes in $Q_{extinction}$ and contributions of $Q_{scattering}$ and $Q_{absorption}$ with altering magnetic-plasmonic nanosphere composition.

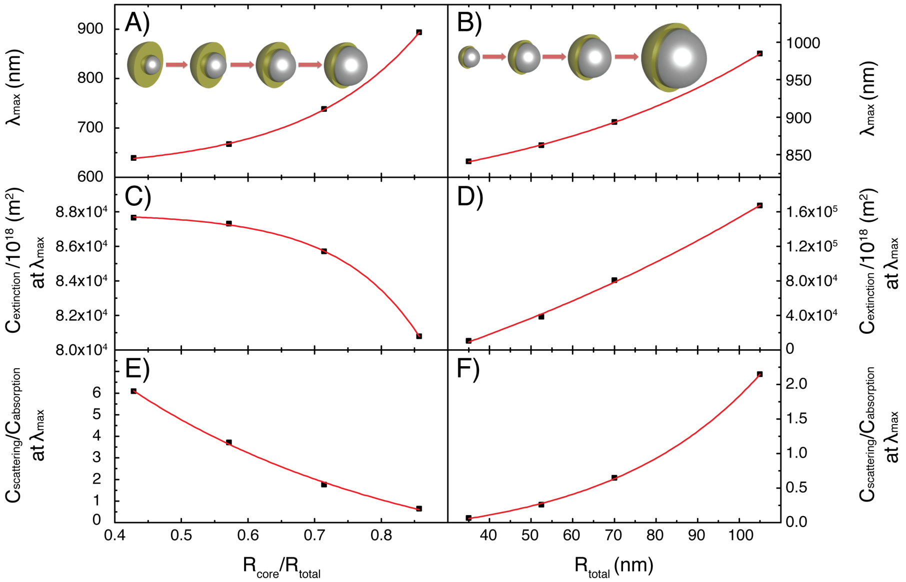

Figure 2.4: Dependencies of λ_{max}, $C_{\text{extinction}}$ and the $C_{\text{scattering}}/C_{\text{absorption}}$ ratio at λ_{max} on the $R_{\text{core}}/R_{\text{total}}$ ratio and R_{total}.

As stated earlier, to our knowledge no magnetic-plasmonic magnetite-gold core-shell nanospheres with a magnetite core as large as those used in our calculations have been synthesized. Nevertheless, the presented results show clear trends for all calculated properties and provide insight in the optical mechanisms at hand.

2.3.2 Magnetic-plasmonic nanorods

As stated earlier, core-shell nanorods can be described by three structural parameters: effective radius, aspect ratio, and $V_{\text{core}}/V_{\text{total}}$ ratio. During DDA calculations, each parameter was subsequently varied, and the two others remained constant. As such, calculations were performed for three different sets of core-shell magnetite-gold nanorods.

The first set consisted of nanorods with a fixed R_{eff}=10nm, a fixed aspect ratio of 3 (dimensions: 12x36nm) and a $V_{\text{core}}/V_{\text{total}}$ ratio varying from 0 to 1. A second set of calculations involved structures with a fixed volume of R_{eff}=10nm, a fixed $_{\text{core}}/V_{\text{total}}$ ratio of 0.2, and a varying aspect ratio from 1 (sphere) to 5. The calculation for the spherical structure in this series used Mie theory. For the last set of calculations a fixed $_{\text{core}}/\text{V}_{\text{total}}$ ratio of 0.2, a fixed aspect ratio of 3 and a varying R_{eff} of 5, 10, 15, or 20nm were used. Combined results of these three sets of calculations allowed investigation of the influence of each of the three parameters ($_{\text{core}}/\text{V}_{\text{total}}$, aspect ratio and R_{eff}) on the optical properties of the core-shell nanorods.

The resulting $\text{Q}_{\text{extinction}}$ of the aforementioned calculations are shown in Figures 2.5A-C. As is evident from Figure 2.5 A, an increase in the $\text{V}_{\text{core}}/\text{V}_{\text{total}}$ ratio causes a redshift. This can be explained in the same way as it is for the core-shell nanospheres: By increasing the $\text{V}_{\text{core}}/\text{V}_{\text{total}}$ ratio, the gold shell surrounding the core becomes thinner, which facilitates the coupling of plasmonic modes across the shell, resulting in a redshift. It can also be seen from the same figure that a decrease in absolute $\text{Q}_{\text{extinction}}$ is observed for an increasing $\text{V}_{\text{core}}/\text{V}_{\text{total}}$ ratio. This can be explained by the fact that with increasing $\text{V}_{\text{core}}/\text{V}_{\text{total}}$ ratio, the contribution of gold decreases.

Figure 2.5B shows the results of calculations on nanorods with different aspect ratios. Redshifts of the longitudinal dipolar plasmon resonance can be observed with increasing nanorod aspect ratio, accompanied by an increase in absolute $\text{Q}_{\text{extinction}}$. This is consistent with the explanation earlier; increasing aspect ratio increases the path length for electron oscillation along the long axis, causing redshifts.

It can be learned from Figure 2.5C that increasing the volume of a nanorod with all other parameters unchanged leads to modest redshifts and an increase of $\text{Q}_{\text{extinction}}$. As for core-shell nanospheres, the explanation for this phenomenon is that the increase in total size augments the amount of material present in a single nanostructure, enhancing $\text{C}_{\text{extinction}}$. Obtained results are graphically summarized per variable parameter in Figure 2.6.

As shown in Figures 2.6A-C, λ_{max} can be tuned throughout the NIR by changing the composition, shape, or size of the nanorods. Figure 2.6C shows that changing the R_{eff} has only a modest effect on λ_{max} because the redshift with augmenting size is small in comparison with a change in aspect ratio or $\text{V}_{\text{core}}/\text{V}_{\text{total}}$ ratio. The extinction cross section can be varied over a very broad range by changing one of the defining parameters, as can be observed in Figures 2.6D-F. Although changing the $\text{V}_{\text{core}}/\text{V}_{\text{total}}$l ratio allows only modest tuning, varying the size of the structure provides the most efficient means for tuning $\text{C}_{\text{extinction}}$ at λ_{max}. As is evident from Figures 2.6G-I, the range over which the $\text{C}_{\text{scattering}}/\text{C}_{\text{absorption}}$ ratio can be altered by changing the composition, shape, or size of the nanorods is quite narrow.

As can be observed in Figure 2.6I, the most effective way for tuning the $\text{C}_{\text{scattering}}/\text{C}_{\text{absorption}}$ ratio is altering the size, which can be explained by the

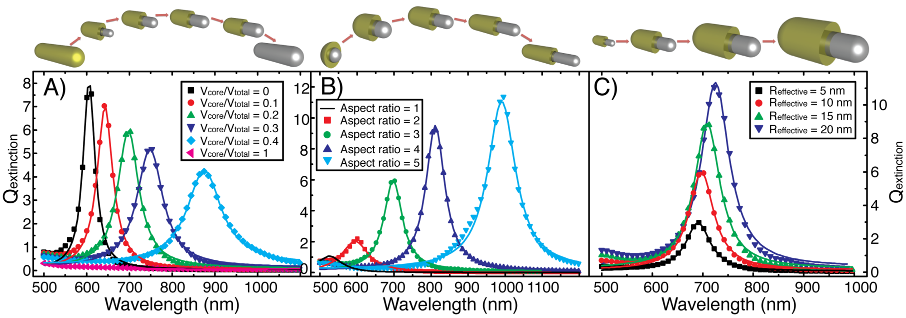

Figure 2.5: Calculated optical spectra of the $Q_{extinction}$ for three different sets of nanorods. A) Fixed aspect ratio = 3, fixed R_{eff}=10nm, varying V_{core}/V_{total} from 0 to 1; B) Fixed V_{core}/V_{total} = 0.2, fixed R_{eff}=10nm, varying aspect ratio from 1 to 5; C) Fixed V_{core}/V_{total} = 0.2, fixed aspect ratio = 3, varying R_{eff} = 5, 10, 15 and 20nm. Note that the solid lines are fits to the data using Lorentzian curves. Spectra were calculated as the average response of two input polarizations, one in the plane of and one perpendicular to the long axis of the nanorods. Results show the redshift of λ_{max} and the changes in $Q_{extinction}$when changing size, shape or composition of the core-shell nanorods.

size dependence of Rayleigh scattering. The obtained results are consistent with the general considerations for core-shell nanorods.

Magnetite nanorods with dimensions of 12×48nm, similar to the structure used in the calculations with an aspect ratio of 4 and R_{eff} of 10nm, have been chemically synthesized by Kumar et al.[309] This demonstrates that the dimensions of the nanorod structures used in our calculations are realistic. Althought pure iron oxide nanorods have been successfully synthesized,[308, 309] to our knowledge no magnetite-gold core-shell analog has been produced.

As with the core-shell nanospheres, the findings on magnetic-plasmonic nanorods can be used to select suitable particles for an envisioned application. For example, if a scattering imaging application is envisioned for which particles with a λ_{max} around 900nm and a large $C_{extinction}$ are required, Figure 2.6 shows that particles with a large V_{core}/V_{total}l ratio, a high aspect ratio and a large R_{eff} are best suited.

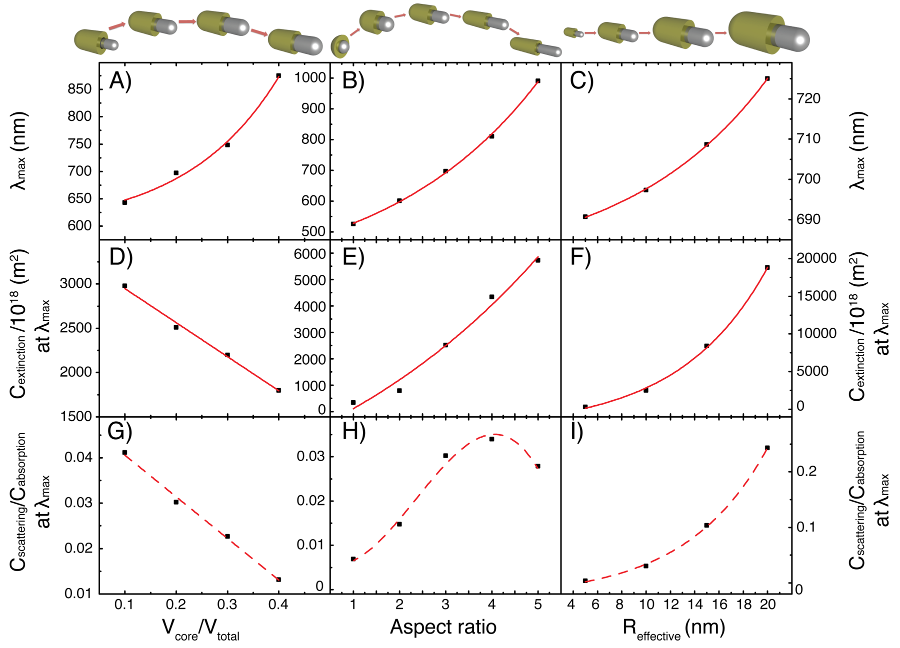

Figure 2.6: Dependencies of λ_{max}, $C_{extinction}$ and the $C_{scattering}/C_{absorption}$ ratio at λ_{max} on the V_{core}/V_{total} ratio, the aspect ratio and R_{eft}.

2.3.3 Quantitative comparison of magnetic-plasmonic nanospheres and nanorods

It is important to note that the trends observed for core-shell nanospheres and nanorods for similar parameters show great resemblance, as was expected from general considerations. Increasing the R_{core}/R_{total} ratio for core-shell nanospheres or the V_{core}/V_{total} ratio for nanorods results in a redshifted λ_{max}, a decrease in the $C_{extinction}$ at λ_{max}, and a decrease in the $C_{scattering}/C_{absorption}$ ratio at λ_{max}.

The same similarity was present for the size parameter. An increase in R_{total} for core-shell nanospheres or R_{eff} for nanorods causes an increase in λ_{max}, the $C_{extinction}$ and the $C_{scattering}/C_{absorption}$ ratio at λ_{max} for both types of structures. These analogies arise because the same mechanisms operate in both structures.

Besides the similarity in the observed relative trends for the calculated structures, large absolute differences exist between the core-shell nanospheres and nanorod structures when properties per unit of volume are calculated. The results of these calculations are summarized in Table 2.1.

For the calculations, we compare core-shell nanospheres with an R_{total} of 70nm and a core-shell nanorod with an R_{eff} of 10nm and an aspect ratio of 3. Both studied structures have a $V_{\mathrm{core}}/V_{\mathrm{total}}$ ratio of 0.2.

The first calculated parameter is the shift of λ_{max} on a per volume basis. This shift is three orders of magnitude larger per unit of volume for the magnetic-plasmonic nanorods with aspect ratio 3 than for the nanospheres. A second assessed parameter is the $C_{\mathrm{extinction}}$ per unit of volume at λ_{max}. An order of magnitude larger $C_{\mathrm{extinction}}/\mathrm{nm}^3$ at λ_{max} is calculated for the magnetic-plasmonic nanorod with aspect ratio 3 than for the core-shell spherical structure.

From these results we can learn that although, theoretically, both core-shell nanospheres and nanorods can be tuned to have the same optical properties, these will be achieved at much smaller and more realistic volumes for core-shell nanorods.

2.3.4 Quantitative comparison of magnetic-plasmonic nanostructures and organic dyes

Organic dyes are frequently used in optical applications in the life sciences. To assess the applicability of the calculated magnetic-plasmonic nanostructures, we compared them with popular organic dyes. This comparison is only possible based on molar coefficients calculated from the cross sections using Equation 2.1.

For example, for a core-shell nanorod with an R_{eff} of 10nm, a $V_{\mathrm{core}}/V_{\mathrm{total}}$ ratio of 0.2, and an aspect ratio of 3, the molar coefficient of extinction, $\epsilon_{\mathrm{extinction}}$, is 1.1×10^{10}L.mol^{-} ^{1}.cm^{-1} at the plasmon wavelength. Organic photosensitizers used for photodynamic therapy such as commercially available Photofrin ($\epsilon_{\mathrm{extinction}} = 2.2\times10^4$L.mol^{-} ^{1}.cm^{-1}) or MACE ($\epsilon_{\mathrm{extinction}} = 4.0\times10^4$L.mol^{-} ^{1}.cm^{-1}) or experimental phtalocyanines and napthalocyanines ($\epsilon_{\mathrm{extinction}} = 1.0\times10^5$L.mol^{-} ^{1}.cm^{-1} l.mol- 1.cm-1) or organic dyes such as heptamethine indocyanines ($\epsilon_{\mathrm{extinction}} = 2\times10^5$L.mol^{-} ^{1}.cm^{-1}) show 5 to 6 orders of magnitude lower molar coefficients than plasmonic inorganic NPs do.[313, 322]

Organic fluorescent molecules used for cellular imaging, such as Fluorescein[323] ($\epsilon_{molar} = 9.2\times10^4$L.mol^{-} ^{1}.cm^{-1} at 482.5nm) or BODIPY dyes[324] (ϵ_{molar}

$= 5.0\times10^4$L.mol^{-1}.cm^{-1} at 512nm), exhibit molar coefficients at emission wavelengths that are 3 to 4 orders of magnitude smaller than for the core-shell nanorod referred to above ($\epsilon_{\mathrm{scattering}} = 1.9\times10^8$L.mol^{-1}.cm^{-1} at 697nm).

In comparison with popular organic dyes, magnetite-gold nanostructures can possess higher molar coefficients, showing the applicability of such structures.

2.4 Conclusions

Using Mie theory and DDA, optical properties of magnetic-plasmonic magnetite-gold nanospheres and nanorods were calculated. The influences of structural parameters as composition, size, and shape were investigated. From the results, we found that optical properties, such as λ_{max}, the $\mathrm{C}_{\mathrm{extinction}}$, and the $\mathrm{C}_{\mathrm{scattering}}/\mathrm{C}_{\mathrm{absorption}}$ ratio at λ_{max} of both core-shell nanospheres and nanorods, can be tuned by varying the structural parameters.

It was calculated that magnetic-plasmonic nanospheres, which can be produced by available chemical synthetic methods, cannot provide efficient tuning of λ_{max} throughout the NIR, nor the desired extinction efficiencies, and they are not suited for scattering applications due to a negligible $\mathrm{C}_{\mathrm{scattering}}/\mathrm{C}_{\mathrm{absorption}}$ ratio at λ_{max}.

On the other hand, core-shell nanorods show much larger values for the $\mathrm{C}_{\mathrm{extinction}}$ and the λ_{max} shift on a per volume basis than core-shell nanospheres. Furthermore, magnetic-plasmonic nanorods show orders of magnitude larger molar extinction and scattering coefficients than organic materials used in current cancer treatment.

With this knowledge it is possible to design and synthesize structures that possess a plasmon band in the advantageous NIR and other optical properties as desired for potential application in life sciences.

Core-shell nanosphere			Core-shell nanorod		
Parameter	Value	Unit	Parameter	Value	Unit
R_{total}	70	nm	$R_{effective}$	10	nm
V_{total}	1.4×10^{6}	nm^3	V_{total}	4189	nm^3
V_{core}/V_{total}	0.2		V_{core}/V_{total}	0.2	
Aspect ratio	1		Aspect ratio	3	
$\Delta\lambda_{max}$	48	nm	$\Delta\lambda_{max}$	86	nm
$\Delta\lambda_{max}/nm^3$	3.34×10^{-5}	nm/nm^3	$\Delta\lambda_{max}/nm^3$	0.02	nm/nm^3
$C_{extinction}/nm^3$	0.061	$\times10^{-18}m^2/nm^3$	$C_{extinction}/nm^3$	0.6	$\times10^{-18}m^2/nm^3$

Table 2.1: Values for parameters calculated on a per-volume basis for a core-shell nanosphere and a core-shell nanorod (aspect ratio 3) with the same V_{core}/V_{total} ratio

Chapter 3

Synthesis and properties of superparamagnetic iron oxide nanoparticles

The results presented in this chapter are partly based on the following publication:

W. Brullot, N. K. Reddy, J. Wouters, V. K. Valev, B. Goderis,
J. Vermant, T. Verbiest.
Versatile ferrofluids based on polyethylene glycol coated iron oxide nanoparticles.
Journal of Magnetism and Magnetic Materials **324**, 1919-1925 (2012).

Prof. dr. B. Goderis performed the X-ray diffraction experiments and dr. N. Reddy and Prof. dr. J. Vermant were responsible for the rheological results presented in the publication. J. Wouters provided general assistance for performed experiments and analysis.

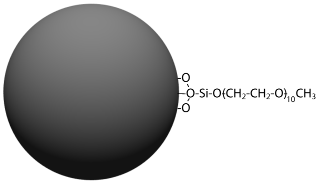

Abstract

The ability to synthesize properly functionalized (superpara)magnetic nanoparticles is one of the prerequisites to make nanoparticle-based multifunctional magnetic-plasmonic nanomaterials. Furthermore, iron oxide phase, physical size, hydrodynamic diameter and the optical, magnetic and magneto-optical properties of the synthesized particles need to be known if they are to be used as building block for multifunctional nanomaterials.

To characterize these properties for non-interacting iron oxide nanoparticles we prepared ferrofluids, which are thermodynamically stable dispersions of superparamagnetic nanoparticles in suitable solvents, using polyethylene glycol (PEG) coated nanoparticles. In this chapter, we first introduce the used synthesis method for iron oxide nanoparticles and the protocol for modifying the surface of the synthesized particles with the desired functional end-group and then present the results of the characterization experiments.

Saturation magnetization, the absorbance in the UV-vis-NIR and the magneto-optical properties of the synthesized iron oxide nanoparticles are beneficial. Measured Verdet constants for the ferrofluids are very significant.

The beneficial properties and the straightforward and reproducible synthesis of these magnetite nanoparticles make them the ideal (superpara)magnetic component for magnetic-plasmonic assemblies.

3.1 Introduction

Superparamagnetic nanoparticles are a required component of the envisioned magnetic-plasmonic nanoparticle-based nanomaterials. As stated in the general introduction, many protocols for the synthesis and functionalization of iron oxide nanoparticles have been published.[42, 102, 325–327] Criteria used to select the iron oxide nanoparticle synthesis and functionalization methods were complexity, cost, flexibility in choice of the organic coating and stability of the link between the nanoparticle and the coating.

The selected methods, forced hydrolysis synthesis and silane chemistry for the functionalization procedure, fullfil al these criteria. The forced hydrolysis method allows fast and cost-effective synthesis of magnetite nanoparticles coated with n-octylamine. This n-octylamine can be replaced by another coating molecule using siloxane molecules in a facile method. Chemical bonds between the surface of iron oxide nanoparticles and siloxanes are covalent and many siloxanes are commercially available, offering the desired strength and flexibility.

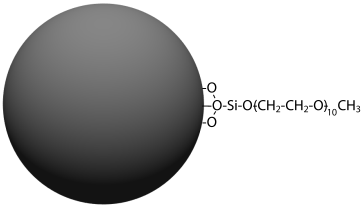

Figure 3.1: An iron oxide nanoparticle of which the surface was modified with PEG silane.

To use these siloxane-functionalized iron oxide nanoparticles in magnetic-plasmonic nanomaterials, physical size and magnetic, optical and magneto-optical properties need to be known. Measuring these properties requires non-interacting nanoparticles. To obtain an ensemble of non-interacting particles, we prepared ferrofluids, which are thermodynamically stable dispersions of (superpara)magnetic nanoparticles in a carrier solvent.[100, 328]

We prepared ferrofluids by coating the as-synthesized nanoparticles with a polyethylene glycol (PEG) siloxane molecule. PEG is very soluble in polar solvent, quite inert to chemical treatments and provides strong sterical stabilization of nanoparticles in dispersions.[327, 329] An impression of an iron oxide nanoparticle coated with a PEG silane is shown in Figure 3.1.

Using the prepared ferrofluids we measured the magnetic, optical and magneto-optical properties of an ensemble of non-interacting superparamagnetic iron oxide nanoparticles and acquired the necessary knowledge to use these particles as building blocks in magnetic-plasmonic nanoparticle-based nanomaterials.

3.2 Materials and methods

3.2.1 Synthesis of iron oxide nanoparticles

Iron oxide nanoparticles were synthesized using an in-house modified force hydrolysis method.[330] Briefly stated, analytical grade ferric chloride ($FeCl_3$) was used as salt precursor, ethylene glycol as solvent and reductans and n-octylamine as capping agent and preliminary coating layer. Typically, 37.5ml ethylene glycol and 25ml n-octylamine were poured into a flask and heated to 150°C. In a beaker, 2.4g $FeCl_3$ was dissolved in 10ml ethylene glycol and 3.5ml of purified water. After dissolving the salt, the ferric iron solution was added dropwise to the flask and further heated to reflux at 150°C for 24h. When the synthesis had ended, particles were precipitated from the reaction mixture using a magnet and washed with acetone. After washing the particles three times, they were dried in vacuo to obtain a powder of iron oxide nanoparticles with a typical yield of 1g.

3.2.2 Functionalization and ferrofluid synthesis

The functionalization protocol using siloxanes started with dispersing previously synthesized n-octylamine coated nanoparticles in solvent by sonicating for ±2h to ensure maximal dispersion of the particles. Typically the amount used was 100mg nanoparticles per 100ml solvent. The solvent of choice depends on the desired functional group, as a certain solubility of the siloxane in the solvent is required. For the siloxanes that possess the two functional groups we want to use, PEG silane (methoxy(polyethyleneoxy)propyltrimethoxy silane, ABCR Chemicals) and aminopropyltrimethoxy silane (APTMS, ABCR Chemicals), the used solvents were toluene and methanol respectively.

After dispersing the as-synthesized n-octylamine coated particles, 1ml of PEG silane or ATPMS per 100mg nanoparticles was added, together with trace amounts of acetic acid (CH_3COOH). The latter acts as a catalyst for the hydrolysis and condensation of silane groups on the particleś surface and thus for the exchange reaction as a whole. The mixture was then again sonicated for ±2h to ensure an optimal reaction medium.

For the APTMS protocol, the reaction medium was taken out of the sonicator after ±2h and put on a magnet to precipitate the superparmagnetic APTMS coated iron oxide nanoparticles. The precipitated particles were washed three times with acetone and magnetically precipitated to remove any excess reagents and dried *in vacuo* at room temperature. For the PEG silane protocol, after sonication, the majority of the toluene was evaporated using a rotavapor. The dispersion was then put on a magnet and heptane was added to promote precipitation of coated particles. Precipitated particles were washed three times with acetone and dried *in vacuo*.

To produce ferrofluids, *in vacuo* dried PEG coated particles were redispersed in a desired solvent and concentration for formation of a ferrofluid by adding a known amount of coated particles to a certain volume of solvent (e.g. PEG 400 or water) and sonicated for ±2h to gain an isotropic ferrofluid.

3.2.3 Characterization techniques

Here we list all characterization techniques used:

Transmission electron microscopy (TEM) - Were done on a JEOL JEM2100 apparatus using an acceleration voltage of either 80kV or 200kV.

X-ray diffraction (XRD) - Room temperature XRD patterns of powders were collected with a horizontal Geigerflex diffractometer in reflection mode (Bragg-Brentano geometry), mounted on a Rigaku RU-200B rotating Cu-anode ($\lambda =$ 1.54Å) at a power of 4kW. The widths of the divergence, receiving and scattering slits were 2°, 0.15mm and 0.5°, respectively. The diffracted X-ray photons were collected after Ni-filtering on a scintillation counter. Powders were presented on a grease-coated glass plate. Data were taken pointwise for 20s in steps of 0.02° between 3 and 95° 2θ (with θ being half the diffraction angle). A silicon standard was measured under similar conditions to ensure a proper diffraction angle calibration and to allow for a correction of the peak widths due to instrumental broadening. A polynomial background was subtracted.

Vibrating sample magnetometry (VSM) - Magnetization data were obtained from vibrating sample magnetometry (VSM) experiments performed on a VSM Maglab setup from Oxford Instruments at 300K.

Fourier transform infrared spectra (FT-IR) - To obtain infrared spectra, samples were measured on a Bruker Alpha FT-IR Spectrometer with a spectral range from 4000cm^{-1} until 375cm^{-1}.

Dynamic light scattering (DLS) - DLS measurements were performed on an ALV CGS-3 (Langen, Germany) compact goniometer system equipped with a multi-tau digital correlator (ALV/LSE-5003). The light source was a 10mW 632.8nm He-Ne laser. Temperature was controlled by a circulating fluid bath with an accuracy of ±0.1°C. Samples were equilibrated at the set temperature for 30min prior to any measurements. The experiments were carried out at scattering angles from 30-150° or 6.83×10^{-3}nm^{-1} < q < 2.55×10^{-2}nm^{-1}, where q is the scattering vector given by q=4nπsin(θ/2)/λ, with n the refractive index of the solution and θ the scattering angle.

Magneto-optical Faraday rotation (FR) and Faraday ellipticity (FE) - FR measurements were done on two experimental setups. The first setup consisted of an 830nm diode laser combined with an AC electromagnet (857Hz), a Wollaston prism and two photodiodes. The details of this setup were published elsewhere.[331, 332] Spectral Faraday rotation measurements were done on a second setup using a Xenon arc lamp combined with a photo-elastic modulator, a 1T DC magnet and a photomultiplier tube. This last setup was simultaneously used to record spectral FE data.

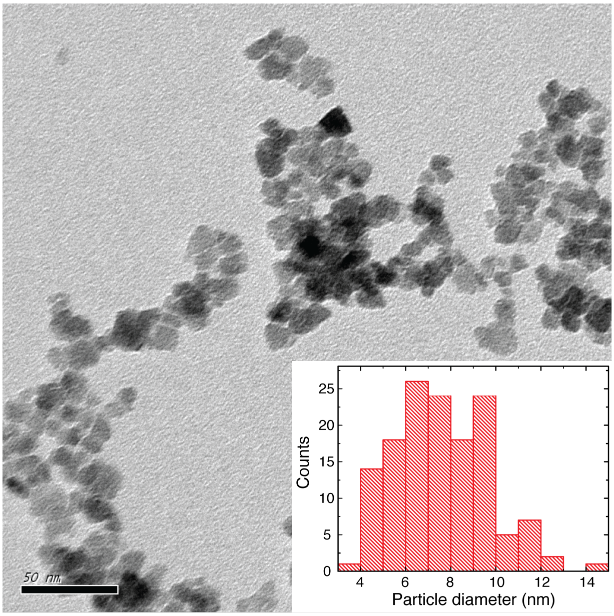

Figure 3.2: Transmission electron microscopy image of PEG coated nanoparticles. Inset: histogram of the counted particle diameters

UV-visible-near-infrared (UV-vis-NIR) - Measurements were done on a Perkin-Elmer Lambda 90

UV-Vis-NIR, Faraday rotation and Faraday ellipticity measurements were done using 9μm thick liquid films of the ferrofluid under study. Liquid thin films were produced by letting the fluid diffuse into a standard liquid crystal glass.

3.3 Results & discussion

3.3.1 Characterization of the iron oxide core

PEG coated coated iron oxide nanoparticles were characterized by TEM measurements (Figure 3.2). The obtained size histogram was fitted to a lognormal model. TEM results showed that the particles were highly crystalline and had an average core diameter of 7.63 ± 2.09nm.

The most relevant part of the background corrected XRD pattern is shown in Figure A.1 of Appendix A. The observed spectrum is mainly due to magnetite, Fe_3O_4.[333] The dimension of the crystallites, D_{hkl}, was estimated to be equal to 7.0 ± 0.5nm based on the full width at half maximum, β, of the [400] reflection and using Scherrers equation:

$$D_{hkl} = \frac{\lambda}{\beta cos\theta} \tag{3.1}$$

Both the TEM and XRD size estimates are well below the size limit for superparamagnetic behavior, which is about 20–25nm for magnetite.[98, 334]

Magnetization versus applied field loops at 300K of dry PEG coated particles were measured using VSM. Neglible coercivity and magnetic remanence were observed (see Figure A.2), indicating superparamagnetic behavior.[97]

Magnetization loops of weakly interacting superparamagnetic systems can be described by a Langevin function. The length of the PEG silane used as coating molecule was calculated using an MM2 Force field energy minimization. Results show a staggered conformation with a length of approximately 4.6nm. As the polymeric PEG chains exhibit high degrees of steric hindering, particles even in dry powder will not be in contact with each other. This diminishes the interaction effects that constitute deviations from Langevin behavior.

Thus, assuming non-interacting particles and uniform size, an estimate of the magnetic diameter can be obtained by fitting the data with a simple Langevin function. Using the density of magnetite ($5.15 g/cm^3$) and the experimentally measured saturation magnetization of 58emu/g, a magnetic core diameter of 7.95nm was calculated. Notice that this last value overestimates the structural size but is in good agreement with the values obtained from TEM and XRD measurements.

3.3.2 Characterization of functionalized particles

After coating the synthesized particles with PEG silane, the dried coated particles could be dispersed in hydrophilic solvents, affirming the effectiveness of the silanization procedure. In order to further verify the success of the silanization procedure, FTIR experiments were conducted on dry powders of n-octylamine coated particles and PEG coated particles. The particles were diluted in a 1/100 ratio in solid potassium bromide (KBr) and measured in transmission. The results of the measurements (see Figures A.3 and A.4) showed

Table 3.1: Overview of samples used. The three columns are the names of the samples used in this work, the mass percentage (m%) and the volume percentage (V%) of particles in PEG 400.

Name	**m%**	**V%**
0%	0	0
1%	1.01	0.78
2.5%	2.51	1.94
5%	5.03	3.89
7.5%	7.54	5.83
10%	10.07	7.79
15%	15.07	11.66

the disappearance of amine peaks and the onset of PEG silane specific bands, confirming the exchange of n-octylamine at the surface for PEG silane and indicating a successful functionalization.

To be sure that no or only a minimal amount of clustering or aggregation of coated nanoparticles occurred when PEG coated particles were dispersed in solvents, which is needed to have non-interacting particles, DLS experiments were performed on PEG coated particles dispersed in PEG 400 to assess the hydrodynamic properties of the coated nanoparticles. A hydrodynamic diameter of 48.50 ± 2.nm was calculated from the results (see Figure A.5). Note that the size distribution obtained from DLS measurements correspond to an higher average than the one obtained from XRD or TEM measurements because DLS also takes into account the nanoparticle coating and the surrounding solvent shell. The measured hydrodynamic diameter indicates that no large aggregates are present and that the properties measured can be, in first approximation, related to an ensemble of non-interacting nanoparticles.

3.3.3 Characterization of ferrofluids

Ferrofluids were prepared by dispersing a known mass of dry PEG coated particles in PEG 400 as described above. The exact concentrations used in this work are shown in Table 3.1. Volume percentages were calculated from the mass percentages of particles using the densities of magnetite and PEG silane, the core size observed in TEM measurements and the thickness of the coating layer as calculated (4.6nm), assuming a fully covered surface.

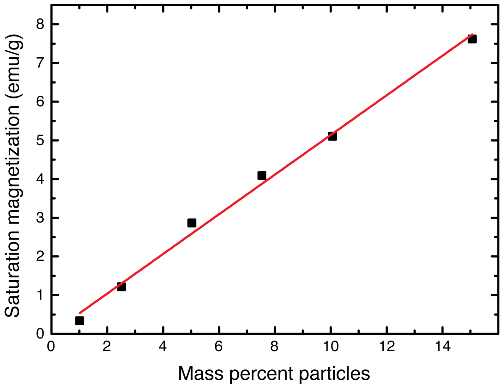

Figure 3.3: M_S a.f.o mass percent particles in the ferrofluid as measured by VSM experiments. A linear increase of M_S with increasing mass percentages of particles was observed.

Magnetic properties

Magnetization vs. applied field hysteresis loops were measured using VSM to assess the magnetic properties of the synthesized ferrofluids (see Figure A.6). As expected for ferrofluids, being an idealized ensemble of non-interacting superparamagnetic nanoparticles, no coercivity or remanent magnetization was observed. The saturation magnetizations (M_S) as a function of the mass percentage of particles in the ferrofluids are depicted in 3.3. A linear increasing trend of the M_S as a function of the mass percentage of particles was observed.

Optical properties

For optical and magneto-optical experiments and applications, it is very important that the absorbance of liquid thin ferrofluid films in relevant regions of the spectrum is sufficiently low. Transparency is essential to prevent a large loss of signal while transmitting light through the sample. The prepared thin films were of superior optical quality, being optically isotropic without any visible aggregation present.

The UV-vis-NIR spectra recorded for 9μm liquid thin films of the ferrofluids are shown in Figure 3.4. Two features can be observed in the UV-vis-NIR spectra. As first, as already mentioned in the general introduction, there is a

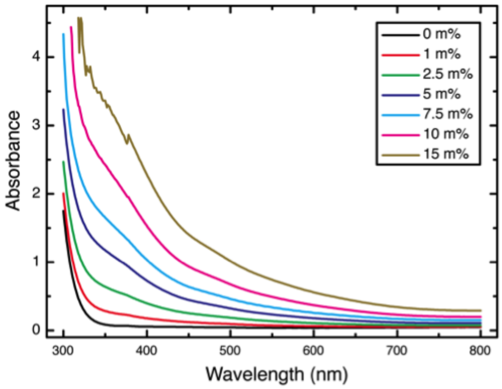

Figure 3.4: UV-vis-NIR spectra of the produced ferrofluids in $9 \mu m$ liquid thin films. Features are the IVCT resonance in magnetite nanoparticles around 370nm and the sharp rise of absorbance in the UV due to Rayleigh scattering and substrate absorbance

broad absorbance band around 370nm due to the IVCT resonance exhibited by magnetite nanoparticles.[73, 335] A second feature is the sharp rise in absorbance in the UV-region. This rise can be explained by Rayleigh scattering of the nanoparticles and by absorbance of the glass substrates. It is also evident that the general absorbance increases with the mass percentage of particles dispersed in the ferrofluids.

The absorbance at 800nm, far from resonant features, increased linearly with increasing mass percentages of particles in the ferrofluids (see Figure 3.5), showing that dispersing the dry nanoparticles was successful.

Magneto-optical properties

To assess the potential of the fluids as magneto-optical sensor elements, Faraday rotation (θ_F) and Faraday ellipticity (η_F) experiments were performed. Faraday rotation is the difference in refraction and Faraday ellipticity the difference in absorption for left- and right circularly polarized light when a material is subjected to a magnetic field in the propagation direction of the light beam. For Faraday rotation, the angle of rotation θ_F is given by the equation

$$\theta_F = VBL \tag{3.2}$$

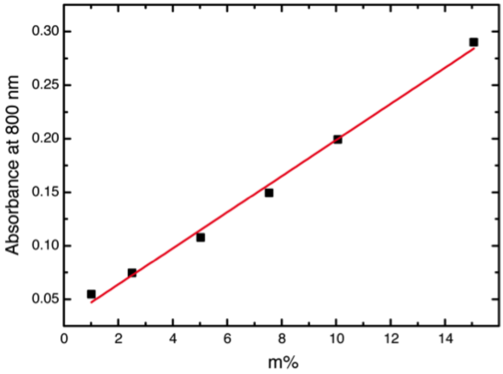

Figure 3.5: Absorbance of the ferrofluids at 800nm wavelength increases linearly as a function of mass percentage of particles in the fluid, demonstrating successful dispersion of nanoparticles in the fluid.

where B stands for the component of the magnetic field in the propagation direction, L the path length of the light in the sample and V the Verdet constant. The latter is a material property and quantifies the Faraday rotation. The magnetic flux density, B, can be decomposed in the applied magnetic field H and the magnetization as a response of materials to this applied field M. As such, we can rewrite Equation 3.2 to

$$\theta_F = V(H + M)L \tag{3.3}$$

The magnetization, M, is further caused by a diamagnetic term linear in magnetic field from the glass background, surrounding air and organic substances and a superparamagnetic term from the nanoparticles. As seen in subsection 3.3.1, the magnetization response of the used nanoparticles as a function of applied magnetic field is best described by a Langevin function. Equations 3.2 and 3.3 are also valid for Faraday ellipticity data. Fitting the obtained experimental Faraday rotation and ellipticity data was done using following equations:

$$\theta_F = A_\theta + B_\theta\left(\left(\frac{cosh(CH)}{sinh(CH)}\right) - \left(\frac{1}{CH}\right)\right) + D_\theta H \tag{3.4}$$

$$\eta_F = A_\eta + B_\eta\left(\left(\frac{cosh(CH)}{sinh(CH)}\right) - \left(\frac{1}{CH}\right)\right) + D_\eta H \tag{3.5}$$

Where A represents an offset factor, B is directly proportional to Faraday rotation or ellipticity, C is a parameter within the Langevin function which determines the shape of the curve and D represents the linear diamagnetic response. Using these equations for fitting ensures a correct treatment of the background signal from diamagnetic substances. For this work, the only important parameters are B_θ and B_η, since these are directly proportional to Faraday rotation and ellipticity. To increase the accuracy of the fitting procedure, all measured wavelengths of both Faraday rotation and ellipticity were simultaneously fitted. When using small magnetic fields, as in the AC Faraday measurements, a linear fitting procedure with Equation 3.2 is appropriate. This because the magnetization, and thus the Faraday rotation and ellipticity responses, of the nanoparticles in small fields are linear to the applied magnetic field.[97] Using two experimental setups, the AC and DC magnetic field Faraday rotation and the DC magnetic field Faraday ellipticity were measured.

Important to note is that if a ferrofluid is subjected to a magnetic field, the superparamagnetic nanoparticles tend to align due to magnetostatic interactions. These induced morphological changes have an effect on the transmission and polarization of light passing through the sample.[336] To avoid large influences of these phenomena on the measurements, data was only recorded after the system was stabilized at a certain magnetic field strength.

In Figure 3.6, the normalized Faraday rotation responses of the 2.5, 5, 10 and 15 mass percent particles in PEG 400 ferrofluids as a function of wavelength are shown. By convention, the Verdet constant of glass was taken to be positive. The features present in the spectra, i.e. a valley around 460nm, a cross-over around 550nm and a positive tail at longer wavelengths, were also observed in magnetite-polymer composites,[74, 75] silica gels containing maghemite[149] and ferrofluids based on maghemite and cobalt ferrite,[150] modeled by Maxwell-Garnett[75] and modified discrete dipole approximation[74] theory and explained in terms of electronic transitions.[73]

It can be seen that while the 2.5m% sample barely exposed such features, these were very clear for the 15m% sample. As the errors on the measurements for the used setup were on the order of 5%, caution must be taken regarding quantitative statements. Qualitatively, it can be stated that increasing the mass percentage of particles in the fluids accentuated the features present in the spectra. The valley around 460nm became deeper and Faraday rotation responses for longer wavelengths rose with increasing mass percentages of particles.

Nor a redshift of the valley peak feature around 460nm, or of the crossover wavelength with increasing mass percentage of particles, as observed by other groups,[74, 75] could be confirmed within the studied concentration range. According to Smith *et al.*,[74] who used a modified discrete dipole approximation method to calculate the Verdet spectra as a function of interparticle spacing, the shifts of spectral features occur through optical coupling of neighbouring nanoparticles. According to the authors, this effect only occurs when the interparticle spacing is smaller than 8nm. Using the sizes of our particles obtained with TEM and DLS and the densities for magnetite and PEG silane, estimates of the interparticle distances in our agglomeration-free ferrofluids were calculated. In the most concentrated sample with 15 mass percent of particles, the interparticle distance was approximately 120nm. This distance thus was too large to see an interparticle optical field coupling effect. Furthermore, coupling was highly likely to be counteracted by the strong repulsive forces exerted by the PEG chains, keeping the particles well apart.

Results for Faraday ellipticity measurements are shown in Figure 3.7. Spectral features present were a valley centered around 420nm, a very broad band with a maximum around 560nm and two cross-over points around 460nm and 730nm. From Figure 3.7 it can be seen that increasing the mass percent of superparamagnetic iron oxide nanoparticles in ferrofluids also increasingly accentuated the spectral features present in the FE spectra.

As stated earlier, Faraday rotation is the difference in refraction and Faraday ellipticity the difference in absorption for left- and right circularly polarized light when a material is subjected to a magnetic field in the propagation direction of the light beam. Faraday rotation and Faraday ellipticity are connected to the real and the imaginary part of the off-diagonal components of the dielectric material function.[73, 337] According to the Kramers-Kronig relations, this means that Faraday rotation and ellipticity are coupled.[338] This is apparent when comparing Figures 3.6 and 3.7. While the Faraday rotation has a minimum around 460nm, Faraday ellipticity for crosses from positive to negative around that wavelength. Vice versa, the broad peak feature present in the Faraday ellipticity spectra around 560nm correlates to a crossover of the Verdet constant in the Faraday rotation spectra.

To accurately assess the Verdet constants of the synthesized ferrofluids, an AC magnetic field setup using a diode laser at 830nm, a Wollaston prism and two photodiodes was used. This wavelength was chosen because DC Faraday rotation measurements show a large signal in that region, combined with a very low absorbance of the signal as observed in UV-vis-NIR spectra.

Results are shown in Figure 3.8. As was expected, the Verdet constant rises linearly with increasing mass percentage of iron oxide nanoparticles in the fluids. The achieved Verdet constants are very significant for hydrophilic magnetite ferrofluids with values up to $3.92 \times 10^{5}{}^{\circ}.\mathrm{T}^{-1}.\mathrm{m}^{-1}$ for the ferrofluid sample with 15 mass percent of particles. Important to note is that this is not the largest attainable Verdet constant, since according to the data shown in Figure 3.6, the

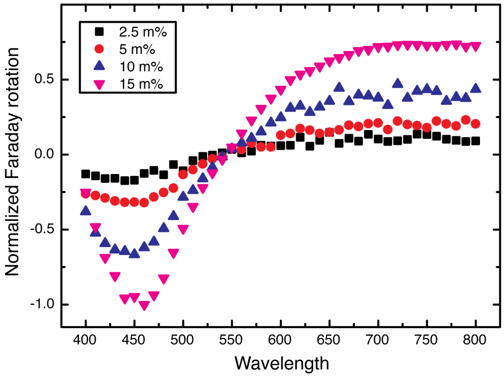

Figure 3.6: Normalized DC Magnetic field Faraday rotation of ferrofluids as a function of wavelength. Increasing the mass percentage of particles accentuates the spectral features that are present.

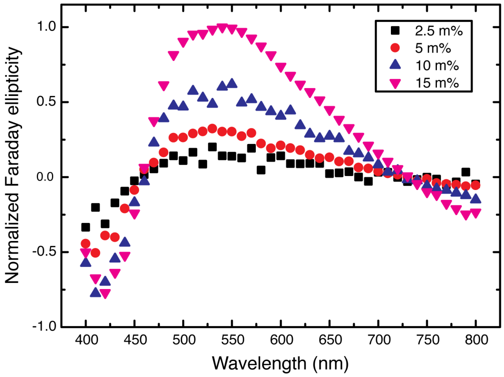

Figure 3.7: Normalized DC magnetic field Faraday ellipticity of ferrofluids as a function of wavelength. Increasing the mass percentage of particles accentuates the spectral features that are present.

Verdet constant will be the largest around 460nm. Numerical results obtained on the ferrofluids synthesized in this work are summarized in Table 3.2.

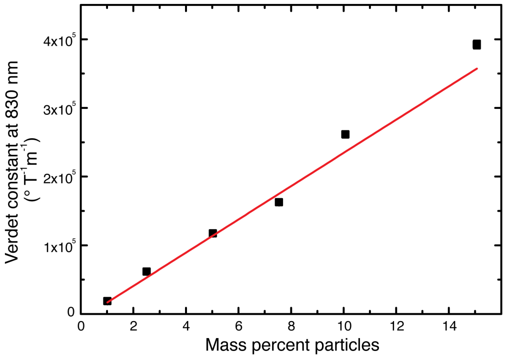

Figure 3.8: AC magnetic field Verdet constants at 830 nm as a function of mass percent particles in the fluids. Increasing the mass percentage linearly increases the Verdet constant at both wavelengths.

Table 3.2: Summary of obtained results.

Sample	**M_S** (emu.g^{-1})	**Verdet** 830nm (°.T^{-1}.m^{-1})
0%	/	/
1%	0.34	1.9×10^4
2.5%	1.21	6.2×10^4
5%	2.86	1.2×10^5
7.5%	4.09	1.6×10^5
10%	5.10	2.6×10^5
15%	7.62	3.92×10^5

3.4 Conclusion

In conclusion, we synthesized magnetite iron oxide nanoparticles, functionalized them using siloxane chemistry and thoroughly characterized them. To characterize non-interacting iron oxide nanoparticles, we prepared ferrofluids based on PEG coated nanoparticles in water or PEG 400 as solvent. We observed that the saturation magnetization, the absorbance in the UV-vis-NIR and the AC magnetic field Faraday rotation at 830nm increased linearly with increasing mass percent of particles in the fluids. DC Faraday rotation and ellipticity experiments revealed spectral features, which depend on the mass percent of particles present. Measured Verdet constants for the ferrofluids are very significant.

In this chapter we showed the synthesis, functionalization and full characterization of the produced iron oxide nanoparticles. The facile synthesis and functionalization and the observed beneficial magnetic, optical and magneto-optical properties show that these nanoparticles can be used as the superparamagnetic building block of the envisioned magnetic-plasmonic nanomaterials.

Chapter 4

Synthesis of magnetic-plasmonic nanoparticle multilayers

This Chapter is a reproduction of the following publication that has been adapted to form only:

W. Brullot, R. Strobbe, M. Bynens, M. Bloemen, P.J. Demeyer, W. Vanderlinden, S. De Feyter, V.K. Valev, T. Verbiest. Layer-by-Layer synthesis and tunable optical properties of hybrid magnetic-plasmonic nanocomposites using short bifunctional molecular linkers. *Materials Letters*, 18, 99-102 (2014)

R. Strobbe and M. Bynens performed AC magnetic field heating and adsorption experiments, M. Bloemen and P.J. Demeyer provided TEM images of nanoparticles and SEM images of multilayers respectively and dr. W. Vanderlinden and Prof. dr. S. De Feyter performed the AFM/SFM measurements and analyzed these results.

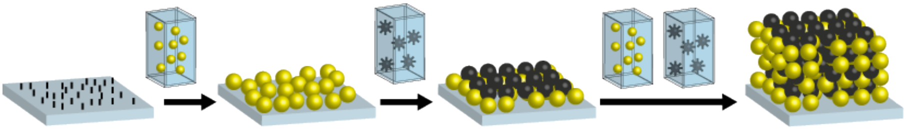

Abstract

Spurred by research in magnetoplasmonics, plasmon-enhanced magneto-optical effects and active plasmonics, the demand for hybrid magnetic-plasmonic nanoparticle-based materials of optical quality is high. Currently used synthesis methods involve possibly interfering polymer media or polyelectrolyte interlayers, grooved supports or non-transparent substrates.

To obtain homogeneous, partially transparent and polymer/polyelectrolyte-free magnetic-plasmonic nanocomposites with angle-independent optical properties, we produced hybrid gold-magnetite and silver-magnetite nanocomposites by a novel Layer-by-Layer synthesis using short bifunctional molecular linkers on glass substrates. Resulting nanocomposites had high nanoparticle filling fractions and showed tunability of the plasmon wavelength over a very broad spectral range by changing composite thickness through the number of added nanoparticle layers.

The angle-independence of optical properties and the abilities to switch the plasmonic material and to tune the plasmon resonances of the magnetic-plasmonic composites make these materials a unique platform for magnetoplasmonic research.

4.1 Introduction

Research into nanoparticle-based magnetoplasmonics, active plasmonics and plasmon-enhanced magneto-optics has strongly intensified.[161,168,169,257,339] Such research holds promise for both unraveling fundamental questions about magnetic-plasmonic interactions as well as applications in sensing, optical switching and optical components fabrications.

The ability to reliably synthesize high optical quality magnetic-plasmonic nanocomposites with high nanoparticle filling fractions and without introducing unnecessary background signal facilitates experiments and is a prerequisite to interpret results correctly. Furthermore, for many experiments or applications, such as optical Faraday isolators, (partial) transparency is a must.[161,244]

Previously, nanocomposites were synthesized on non-transparent or grooved substrates[257] using polymers as a dispersion medium for spin-coated or drop-casted samples or polyelectrolyte interlayers in Layer-by-Layer synthesis.[62,130,305] Polymers and polyelectrolytes have the disadvantages that nanoparticle filling fractions are inherently limited and that they possibly introduce undesired background signal, chemical incompatibility and interfere with signal acquisition.

Furthermore, such molecules introduce an undefined and often large distance between adjacent nanoparticles, impeding correct interpretation of results.

Here we present a versatile Layer-by-Layer synthesis method on glass substrates using short bifunctional, i.e. with two functional groups, molecular linkers that results in homogeneous samples with very high nanoparticle filling fractions and controlled distances between adjacent particles. Tunable plasmon properties, of both silver- and gold-magnetite nanocomposites, over a broad spectral range combined with angle-independent optical properties and a variable composite thickness make these high quality composites an ideal platform for magneto-plasmonic research.

4.2 Materials & methods

Materials

All obtained chemicals were used without further purification. Anhydrous iron(III)trichloride (98%), n-octylamine (99+%) and ethanediol (for analysis) were purchased from Acros Organics. (3-Aminopropyl)trimethoxysilane (APTMS; 97%) was obtained from ABCR. Gold(III)chloride trihydrate (99.9+%), sulfuric acid (95-97%) and Nochromix cleaning agent were purchased from Sigma-Aldrich. Acetic acid (100%) was bought from VWR, silver nitrate from UCB, tri-sodium citrate (99.5+%) from Chem-Lab and sodium borohydride (98+%) from Janssen Chemica.

Synthesis and functionalization of iron oxide nanoparticles

Iron oxide nanoparticles were synthesized using an in-house modified force hydrolysis method.[102]

For functionalization, 300mg of n-octylamine coated nanoparticles was dispersed in 300ml methanol using an ultrasonic bath. Then 3ml APTMS was added, together with three drops of acetic acid and the mixture was further sonicated for 2h. After washing with acetone through magnetically assisted precipitation and drying in vacuum, a powder of amine-functionalized iron oxide nanoparticles was obtained. These functionalized nanoparticles could then be redispersed in MeOH in a desired concentration using ultrasonication. Functionalized particles had a size of 7.98±2.4nm and showed superparamagnetic behavior with a saturation magnetization of 18.88emu/g.

All information regarding synthesis, functionalization and characterization of the magnetite iron oxide nanoparticles can be found in Chapter 3.

Synthesis of metal nanoparticles

For the gold colloid synthesis, a method based on an aqueous citrate reduction was employed.[190] After synthesis, a deep red colored dispersion was obtained. This dispersion was diluted 5 times with MilliQ water before use to obtain a final Au concentration of 0.2mM. Au nanoparticles had a size of 9.25±1.31nm and exhibited a clear plasmon resonance centered on 530nm (See Figures B.1 and B.2).

Silver nanoparticles were produced using a method based on an aqueous sodium borohydride reduction in the presence of citrate capping molecules.[340] The pale yellow colored dispersion was used without further dilution. Ag nanoparticles showed a plasmon resonance at 400nm and had a size of 9.59±0.27nm as measured by TEM (See Figures B.3 and B.4). Final Ag concentration was 0.15mM.

Synthesis of nanoparticle multilayers

Synthesis started by cleaning glass microscope slides ($16\times16\text{mm}^2$) with NoChromix cleaning solution (7g/100ml NoChromix in MilliQ water, add 100ml sulfuric acid 97%) for 1h (Figures 4.1A-D). These cleaned substrates were then functionalized with APTMS (1vol% in MeOH, 1h) and rinsed with MeOH and water.[190]

A first metal nanoparticle layer was added by putting the functionalized substrate in 10ml of a metal NP dispersion while shaking (350rpm) for 1.5h and rinsing with water and MeOH afterwards. By putting the sample in 10ml of a 0.3mg/ml dispersion of functionalized iron oxide nanoparticles in MeOH for 1h, a layer of these nanoparticles could be added on top of the gold nanoparticle layer. After rinsing the sample with methanol and water, adding extra nanoparticle layers was possible by repeating the previous steps.

The nature of the Layer-by-Layer synthesis allows for homogeneous coating of large-area substrates.

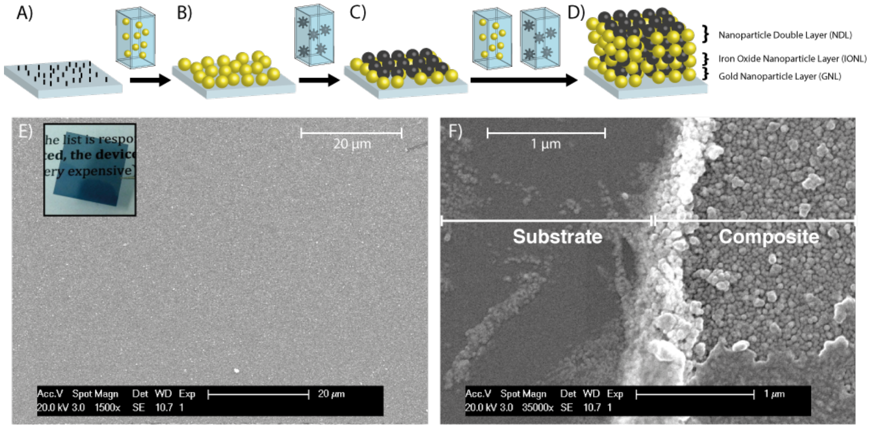

Figure 4.1: Layer-by-Layer synthesis procedure used in this work (A)-(D), a photograph of a five NDLs Au-Mag sample above a text (inset E) and large area (E) and zoomed-in (F) scanning electron microscopy images of a Au-Mag five NDLs sample.

Characterization techniques

Nanoparticle multilayers were characterized using scanning force microscopy (multimode 8 from Bruker using an AC240TS tip) and UV-visible absorbance measurements (Perkin-Elmer 900).

4.3 Results & discussion

Au-magnetite nanocomposites with different numbers of nanoparticle double layers (NDLs), which were one gold and one iron oxide nanolayer combined (Figure 4.1D), were synthesized.

A five NDLs Au-magnetite composite on a glass support is blue colored when viewed perpendicular and shows gold reflectivity if tilted. The sample is homogeneous, showing no large aggregates or defects (Figure 4.1E, inset). Scanning electron microscopy (SEM) images confirm homogeneity over at least 100μm and show a relatively smooth surface (Figure 4.1E). When zoomed in on the same sample next to a scratch, a clear height difference between substrate and sample can be observed (Figure 4.1F).

Due to the strong bonding between the silane group and the iron oxide nanoparticles on the one and the amine group of the linker molecule and the gold nanoparticles on the other hand, the samples are robust and do not release material in the storage solvent.[190,340] Stored in methanol, the composites were stable for at least 1 year as evidenced by UV-visible absorbance spectroscopy. Ultrasonic treatment of five NDLs Au-magnetite composite does not result in any change in the UV-visible absorbance spectrum, indicating the stability and robustness of the samples. Reproducibility of the method is high (See Figure B.5).

UV-visible absorbance spectra of a one NDL Au-magnetite nanocomposite show a plasmon resonance peak at approximately 520nm, corresponding to that of dispersed gold nanoparticles (Figure 4.2). By adding NDLs, a second redshifted plasmon peak due to plasmonic near-field coupling arises. When gold nanoparticles interact optically, the plasmon modes couple, resulting in redshifts of the plasmon wavelength.[170] The observed significant redshift of the plasmon wavelength in the synthesized samples from 530nm to 650nm indicates that gold nanoparticles are interacting strongly and thus are close to each other. The presence of magnetite nanoparticles is evidenced by the absorbance peak due to intervalence charge transfer (IVCT) centered around 385nm.[73]

A linear relationship between the absorbance maximum and the number of layers was found (Figure 4.3), evidencing the Layer-by-Layer synthesis of the composites. The same linear relationship was found for the absorbance at the iron oxide NP IVCT and the Au LSPR and coupled plasmon modes as a function of NDLs (See Figure B.6). Changes in the UV-visible absorbance spectra as a function of added NDLs can be visually observed as a change in color of the Au-magnetite composites rom reddish pink over blue to dark blue with increasing number of NDLs.

Use of glass substrates allows for partial transparency of the composites in the UV-visible, enabling magnetoplasmonic and magneto-optical measurements and applications.

The absorbance properties of the composites, including the plasmon properties, are largely independent of the sample angle relative to the incoming light beam (See Figure B.7), which is in stark contrast to the strong angle dependence of propagating plasmon resonance excitation of continuous bulk gold layers.[161,341] Lyon et al. observed that the strict angle requirements for exciting surface plasmon modes in continuous gold layers can be partially lifted by covering the surface with gold colloids.[342] In the synthesized composites, only spherical gold nanoparticles are responsible for the plasmon behavior, which fully alleviates the incident angle requirements. Angle independent optical properties can be a great advantage for (magneto-)optical experiments and applications.

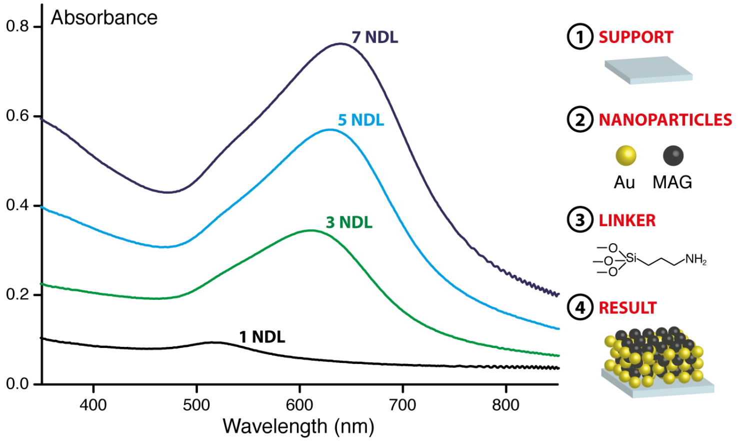

Figure 4.2: UV-visible absorbance spectra of Au-Mag composites show a redshift of the localized surface plasmon band as a function of added NDL. The presence of magnetite nanoparticles is indicated by the resonance at 385nm.

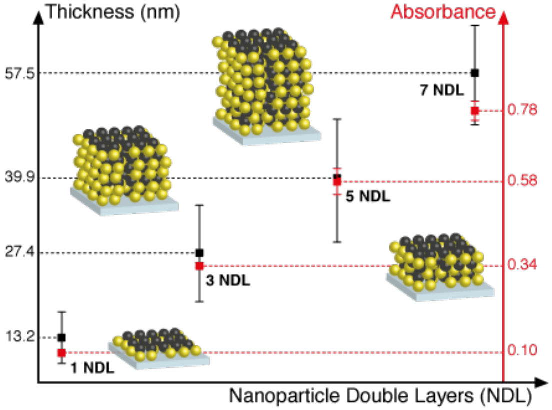

Figure 4.3: Both the thickness, as measured by scanning force microscopy, and the absorbance at maximum intensity increase linearly with increasing number of nanoparticle double layers. These results demonstrate the Layer-by-Layer construction of the Au-Mag composites

The average thickness of the Au-magnetite nanocomposites, as measured by scanning force microscopy (See Figures B.8 and B.9), increases linearly with the number of added NDLs. This confirms the Layer-by-Layer like construction (Figure 2.3). A thickness of 13.2±7.3nm was measured for a one NDL sample. When fitted with a linear equation (R^2=0.99), the average increase of thickness for one NDL after the first NDL is 7.3±0.4nm. These data are consistent with structures in which, resembling a closed-packed material, the nanoparticles of the next nanoparticle layers occupy the cavities in the previous and a high quality stacking of layers is obtained (graphics Figure 4.2). Structures with such a packed arrangement of nanoparticles allow a high nanoparticle filling fractions or occupied volume fractions up to, in the case of fully close-packed arrangements, a theoretical maximum of 74%.[343]

The number of layers that can be added is in principle unlimited, although some quality loss is likely with very high numbers of layers. Up until 10 NDLs no loss of optical quality was observed (Seef Figure B.10). Such structures with high nanoparticle filling, and the absence of polymer, polyelectrolyte or other possibly interfering interlayers and of high optical quality are well suited for studying plasmon-enhanced effects or investigating fundamentals of active plasmonics.

Using silver instead of Au nanoparticles in the Layer-by-Layer synthesis also results in stable and homogeneous nanocomposites. The UV-visible absorbance spectra of such composites show only two absorbance bands (Figure 4.4). One broad band is centered on 400nm due to the overlap of the IVCT and plasmon resonances of magnetite and single Ag nanoparticles. When more than one NDL is added, a strongly redshifted plasmon band at around 550-575nm occurs due to near-field optical coupling of Ag nanoparticles. The same as for the Au-based composites, a linear relationship between the absorbance maximum and the number of layers was found (See Figure B.11), evidencing the Layer-by-Layer synthesis of the composites.

The abilities to switch the plasmonic material and to tune the plasmon resonances of the magnetic-plasmonic composites over a very broad UV-visible spectral range as a function of added NDLs provide a unique platform for magnetoplasmonic research.

4.4 Conclusion

Magnetic-plasmonic nanocomposites of optical quality and variable thickness based on Au or Ag and magnetite nanoparticles were reproducibly synthesized on glass substrates by a polymer/polyelectrolyte-free Layer-by-Layer method

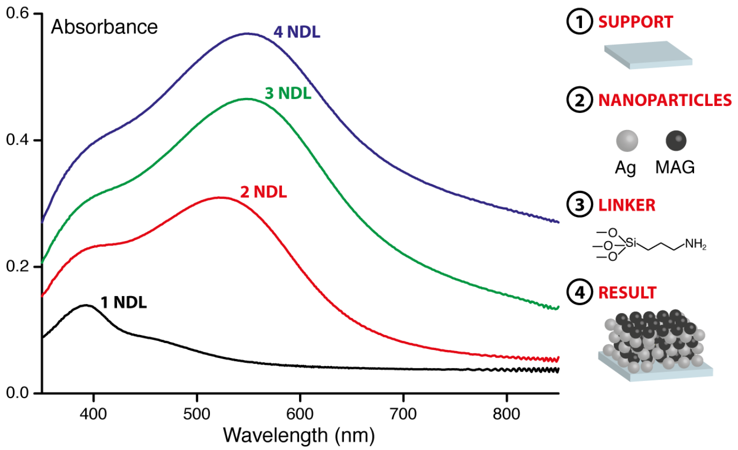

Figure 4.4: A strong redshift of the plasmon wavelength is observed in UV-visible absorbance spectra of Ag-Mag composites. The resonance of magnetite nanoparticles (385nm) overlaps with the LSPR of Ag NP.

using short bifunctional molecular linkers. High nanoparticle filling fractions in well-stacked multilayers were obtained. Plasmon resonance wavelengths could be tuned over a very broad spectral range by changing the plasmonic material or the number of added nanoparticle layers. Optical properties proved to be angle-independent. Such high quality composites without possibly interfering inter-layers provide excellent materials for research into plasmon influenced (magneto-)optical effects, active plasmonics through magnetism or possibly magnetoresistance effects.

Chapter 5

Optical properties of magnetic-plasmonic nanoparticle multilayers

Abstract

In this chapter we explain the observed optical properties of the magnetic-plasmonic nanoparticle multilayers by theoretical calculations and the comparison of the results of these calculations with experimental measurements. For this we started with calculating the influences of distances, dielectric constants, incident light polarization, number of adjacent nanoparticles and angle relative to the incoming light on the optical properties of coupled plasmonic nanoparticle assemblies.

While the trends for the influences of such parameters on the optical properties of plasmonic systems are known in general, we calculate them specifically for particles in the size range we used and assemblies relevant for the experimentally synthesized nanoparticle multilayers. Then we extended the calculations to include magnetic-plasmonic nanoparticle assemblies and attempt to model the experimental multilayers.

The calculations and the comparison with experimental observations lead us to a more nuanced view of the LbL self-assembly process as a function of layers as introduced in Chapter 4. While scanning force microscopy measurements on samples with a certain number of layers confirm a linear increase of thickness as

a function of added layers, the calculated and experimental optical properties show that instead of depositing fully filled consecutive nanoparticles layers, nanoparticles of the next added layers fill the holes in previous layers and as such improve the filling fraction of the whole structure.

The reason for this kind of behavior must still be further investigated but the optical properties do give us a good indication. For a sample that contains 1 Au nanoparticle layer or 1 NDL (1 Au and 1 magnetite layer), theory and experiment fully match when considering non-interacting (non-coupled) Au nanoparticles. This means that the nanoparticles of the first Au nanoparticle layer that is deposited on the functionalized glass substrate are randomly distributed on the substrate with an average interparticle distance larger than at least 0.5nm. Upon addition of the first amino-functionalized magnetite nanoparticle layer, the magnetite nanoparticles will attach to the already present gold nanoparticles.

The pockets, pores or cavities on the spatial level of the first Au nanoparticle layer created by attachment of magnetite particles where the distance between adjacent Au NPs is large enough have become very attractive for newly added Au nanoparticles. This because these pockets are densely packed with amino groups, attracting the positively charged gold nanoparticles. In this way, Au NPs that are added for formation of the second Au NP layer are actively filling up the holes in the previously deposited plasmonic layers. The same reasoning holds for magnetite nanoparticles that fill the pockets in previously deposited magnetic layers.

As more and more layers are added, more and more pockets in the lower-lying layers are filled, the structure shows less vacancies and the general quality, as expressed by the filling fraction of the structure, improves.

5.1 Calculation methods

As in Chapter 2 for core-shell nanorods with arbitrary aspect ratios and compositions, calculations of extinction efficiencies of nanoparticle assemblies are carried out using the discrete dipole approximation as incorporated in DDSCAT.[226, 227, 320] Used dielectric functions are the same bulk functions as used in Chapter 2. Nanoparticles were always modeled as spheres, in agreement with the experimental nanoparticles and the diameter of all nanoparticle types was kept constant at 10nm. This size was chosen based on the measured diameters of the experimental nanoparticles and taking into account the extra coating layer that is present. Nanoparticle assemblies were modelled using approximately 20.000 dipoles per nanoparticle, greatly exceeding the required dipole resolution for accurate calculations.

Throughout this chapter we will use extinction efficiencies (Q_{ext}) and not cross sections (C_{ext}) to present the calculated optical properties of nanoparticles and assemblies. Cross sections can be calculated from the efficiencies by multiplying the latter with the illuminated area of the structure under study. From the cross section one can then calculate the molar extinction coefficient as measured by UV-vis spectroscopy.

Since extinction efficiencies are not normalized to the size of the structure, comparing assembles with different sizes or morphologies is more straightforward in terms of spectral shifts of optical features. Comparing intensities of resonances of differing structures based on efficiencies on the other hand needs to be done with care.

5.2 Theoretical results

5.2.1 Plasmonic nanoparticle assemblies

To investigate the optical properties of plasmonic nanoparticle assemblies, we systematically vary the distance between nanoparticles, the number of plasmonic nanoparticles in the assembly, the refractive index of the medium, the angle between the plasmonic assembly and the incoming light and the polarization of the incoming light. Unless explicitly stated otherwise, the refractive index of the medium is 1 (vacuum) and the nanoparticles in the virtual assemblies of which the optical properties are presented in this section are always positioned on a line that is perpendicular to the propagation direction of the light. This to ensure maximal interaction of the incoming light with the present assembly.

Furthermore, except when explicitly stated otherwise, calculations are always first performed with the incoming light beam's electric field polarized along the longitudinal or long axis of the assembly, repeated for polarization along the transversal or short axis of the assembly and then averaged over both polarizations. In this way, we simulate the optical properties as observed in experiments using unpolarized light. The calculated optical spectra allow us to study the the influences of the aforementioned parameters on the optical properties and later allow us to explain the experimental UV-visible spectra of magnetic-plasmonic nanoparticle multilayers.

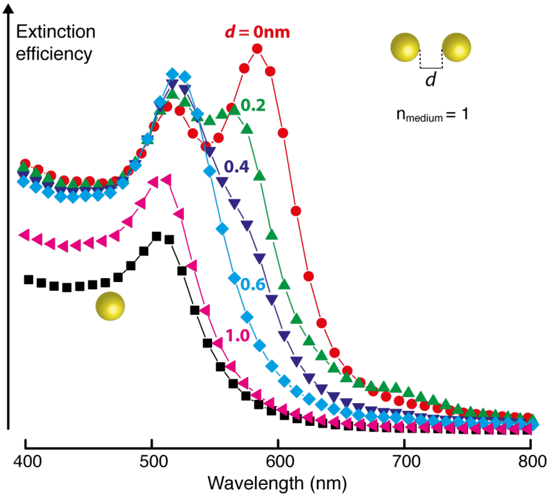

Figure 5.1: A red-shifted plasmon resonance band can be observed when 2 Au NPs are in close contact with each other and plasmonically couple. With increasing interparticle distance, the plasmonic coupling strength decreases, leading to a disappearance of the red-shifted plasmon band.

Influence of interparticle distance

The first parameter we vary is the distance between two 10nm large plasmonic nanoparticles and we look at the influence on the optical properties. For 2 Au NPs at close distance ($<$ 0.5nm), a red-shifted plasmon resonance band can be observed (see Figure 5.1). If the surfaces of the 2 NPs touch, the red-shift ($\Delta\lambda$) is maximal and reaches about 80nm as compared to the LSPR of single, isolated gold nanoparticles. For an interparticle distance larger than 0.5nm the plasmonic coupling is negligible and the coupled red-shifted plasmon resonance is no longer excited.

For Ag NPs, the general trend as observed for Au NPs holds. At close distances, the plasmonic coupling strength as evidenced by a strong red-shifted plasmon resonance (±100nm) is high (see Figure C.1). At a distance larger than 0.5nm, the plasmonic coupling strength is fully diminished and the plasmon resonance wavelength resorts to that of single, isolated silver nanoparticles.

When calculating the optical properties of a Au-Ag nanoparticle heterodimer as a function of interparticle distance, we observe that when the particles'

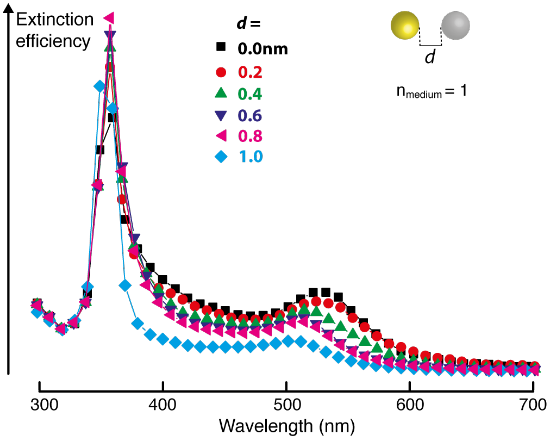

Figure 5.2: When a silver and a gold NP are put in close contact, their LSPR wavelengths show a small red-shift and the density of states in the spectral interplasmon region greatly increases leading to increased absorbance. This might be interesting for plasmon-enhancing optical effects in that spectral region.

surfaces touch, the plasmon resonances of both the Ag and Au NPs show a small red-shift (see Figure 5.2). The small shift can be explained by the large difference in LSPR wavelength, which hampers interaction. More interesting is that at close interparticle distances, the absorbance in the spectral interplasmon region (±380-490nm) strongly intensifies as compared to large interparticle distances. This implies the creation of additional densities of states in this energy space and might be interesting for plasmon-enhancing optical phenomena as the energy states in this spectral regions have a plasmon character.

Influence of the number of coupled plasmonic particles

Next to the average interparticle distance, also the number of coupled nanoparticles in a plasmonic assembly has an influence on the optical properties. To assess this influence, we calculate the optical extinction spectra for plasmonic nanoparticle chains with an increasing number of particles. The particles' surfaces touch in these chains to ensure maximal plasmon coupling strength.

Adding more gold nanoparticles in a gold plasmonic chain increases the red-shift and the intensity of the dipolar plasmon response (see Figure 5.3). This response

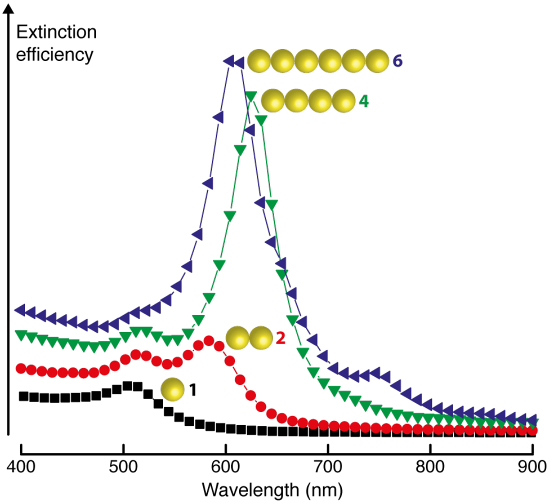

Figure 5.3: When Au NPs are put in a linear chain, the dipolar plasmon resonance strongly red-shifts with increasing numbers of nanoparticles in the chain. Multipolar resonances also become apparent when more than 4 Au NPs are coupled.

points to an increased plasmon coupling strength over the whole chain and can be understood as favorable interactions between multiple dipoles in the exciton coupling model. Another way to explain this result is by considering plasmonic nanoparticles as the box in the electron-in-a-box model. Increasing the size of the box, i.e. adding more plasmonically coupled nanoparticles, leads to a redshift of the resonance wavelength.

Another interesting observation is that when more and more particles are added, multiple resonance peaks appear in the calculated spectrum. For example, in a chain with 6 Au nanoparticles 3 peaks can be seen in the visible spectral range, which points to the existence and excitation of multipole resonances in the chain (see Figure 5.3). Assuming that the lowest-energy resonance (most red-shifted) is the dipole resonance (around 750nm) for the longitudinally polarized plasmon, we also observe a quadrupolar resonance for the same polarization (around 620nm) and the dipolar LSPR (around 530nm) for the transversally polarized plasmon.

For Ag NPs, similar trends are observed as for Au NPs (see Figure C.2). The dipolar plasmon very strongly red-shifts ($\Delta\lambda > 300$nm) when more Ag NPs are

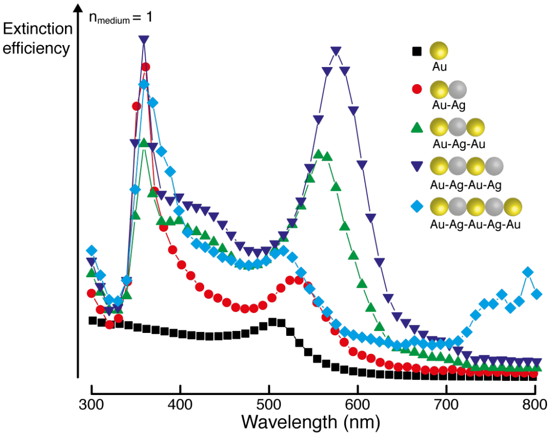

Figure 5.4: Linear chains of alternating Au and Ag NPs of increasing length show red-shifted plasmon resonances and a strong increase of absorbance and appearance of extra resonance peaks in the interplasmon region (±380-490nm). Such chains show broadband plasmon behavior, which is very interesting for plasmon-enhancing optical effects in this wavelength region.

coupled in a chain. When more than 4 nanoparticles are in the lineair assembley, multipole excitations become apparent.

For linear chains of alternating gold and silver NPs, the trend is quite particular (see Figure 5.4). While the plasmon resonance at the LSPR wavelength of Ag NPs barely red-shifts with increasing number of particles, the same resonance for gold nanoparticles does red-shift. From 4 nanoparticles in the chain onwards, again multiple resonances can be observed. For the interplasmon region (±380-490nm), a drastic increase in absorbance and the appearance of multiple resonance bands with increasing numbers of plasmonic particles points to an increasing plasmonic coupling strength. As can be seen on the spectra, plasmon resonances can be excited in a broad wavelength range from ±340-700nm and more when multiple gold and silver particles near-field couple. This broadband resonance behavior is very interesting for plasmon-enhancing optical effects in this spectral range.

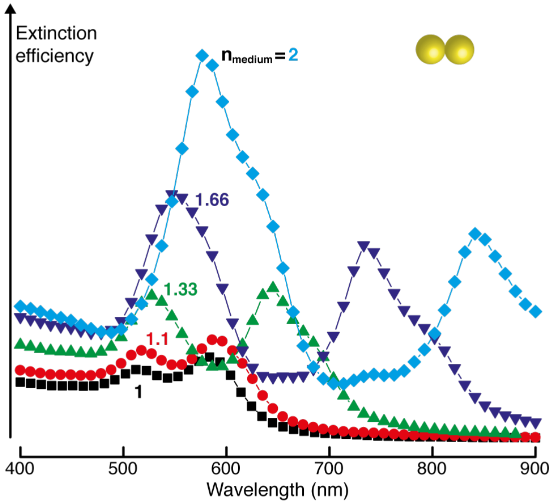

Figure 5.5: Increasing the medium refractive index for a pair of optically coupled gold nanoparticles greatly enhances the plasmon coupling strength. This is evidenced by a strong red-shift and the gain in intensity of the coupled plasmon resonance.

Influence of the medium refractive index on near-field coupling between nanoparticles

In subsection 1.4.2 the influence of the medium refractive index on the LSPR wavelength of single gold and silver nanoparticle was explained. Increasing the medium refractive index caused a red-shift and an intensification of the plasmon resonance for both metal types. In this subsection we will look at the influence of the medium refractive index on the plasmon resonances stemming from near-field coupling.

Increasing the refractive index of the medium for a pair of Au nanoparticles of which the surfaces touch increases the red-shift and the intensity of the dipolar LSPR (see Figure 5.5. For the coupled plasmon resonance the red-shift increases much more dramatically but the gain in intensity is lower. With increasing medium refractive index we can also observe the appearance of multiple resonance peaks and shoulders, which, together with the increased red-shift, points to a strong enhancement of the plasmonic coupling strength.

In a medium with a refractive index of 1, the plasmon coupling between 2 Au

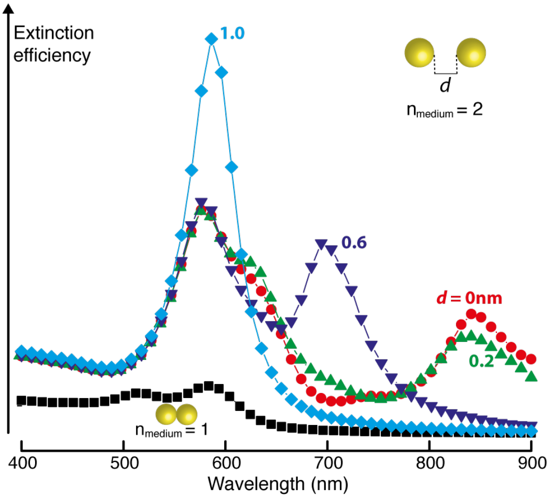

Figure 5.6: With a medium refractive index of 2, the plasmon coupling strength greatly increases in a gold nanoparticle dimer leading to strong red-shifted coupled plasmon resonances, the appearance of multipolar resonances and the extension of the interparticle gap limit for near-field plasmon coupling.

nanoparticles is completely diminished when the interparticle distance becomes larger than 0.5nm. Since we calculated that the plasmonic interaction strength greatly increases with increasing medium refractive index, the question arised whether coupling over larger interparticle gaps is possible at larger medium refractive indices. The results of our calculations show that near-field coupling between 2 Au NPs is possible up to 0.8nm if they are in a medium with refractive index 2 (see Figures 5.6, C.3 and C.3). At interparticle distances larger than 1.0nm the observed spectrum fully agrees with the calculated spectrum of single gold nanoparticles in a high refractive index medium. When at short interparticle distance in a high refractive index medium, multipole resonances appear in the spectrum of near-field coupled Au nanoparticles.

For a pair of touching silver nanospheres, increasing the medium refractive index red-shifts the dipolar LSPR as also predicted by Mie theory (subsection 1.4.2). As for the Au NP pair considered before, plasmon coupling strength greatly increases with increasing n_{medium} as evidenced by the strong red-shift of the dipolar coupled plasmon resonance and the appearance of multipole resonances (see Figure C.5).

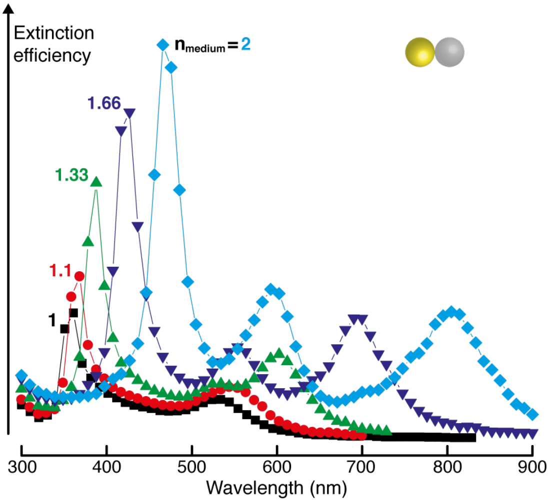

Figure 5.7: To allow near-field coupling in a Au-Ag heterodimer, n_{medium} needs to be relatively high. At larger values for n_{medium}, strongly red-shifted coupled plasmon resonances can be observed.

The maximum interparticle gap limit for near-field coupling for a pair of Ag nanoparticles in vacuum ($n_{medium} = 1$) was calculated to be approximately 0.5nm (see Figure C.1). Like for a pair of Au nanoparticles, the increased plasmon coupling strength also leads to an extension of the interparticle gap limit for near-field coupling in the case of silver nanoparticles. Calculations show that for $n_{medium} = 2$, near-field coupling is possible for interparticle gaps up to 0.8nm (see Figure C.6). Small interparticle gaps give rise to strongly red-shifted and induced multipole plasmon resonances.

As explained earlier, the calculated optical spectrum of a touching gold-silver nanosphere dimer in vacuum ($n_{medium} = 1$) shows a small red-shift for the LSPRs but a large increase in the absorbance in the interplasmon region between the Ag and the Au LSPR. This result showed that the particles interact but that the plasmonic coupling strength was rather limited. If we increase n_{medium}, the plasmonic coupling strength in the heterodimer greatly increases. Besides the anticipated red-shifts of the dipolar LSPRs, strongly red-shifted coupled plasmon resonances can also be observed at higher medium refractive indices. This result shows that a relatively high n_{medium} is necessary to allow coupling in a Au-Ag heterodimer.

From these results we learn that increasing the medium refractive index enhances the plasmonic coupling strength, induces multipolar resonances and extends the gap limit for near-field coupling for Au-Au and Ag-Ag homodimers. For Au-Ag heterodimers, a higher n_{medium} is necessary to allow plasmonic near-field coupling strong enough to produce strongly red-shifted coupled plasmon resonances.

The conclusions formulated in the previous paragraph might seem contra-intuitive at a first glance since increasing the refractive index and thus the dielectric constant renders the medium insulating and thus less permeable for electric fields. The increased insulation decreases the interaction energy between the two plasmon near-fields proportional to the increase in medium dielectric constant. For each separate particle however, the Coulombic restoring force acting on the excited electrons decreases with increasing ϵ_m. This leads to an effective increase of the electric dipole moment in each particle. As can be inferred from equation 1.21, the interaction energy between two dipoles in the exciton-coupling model is proportional to the square of the induced dipole moment. Summing up the two contributions makes that the plasmon coupling strength increases with increasing medium refractive index.[170,344]

Angle dependence of plasmonic near-field coupling

To investigate the dependence of the optical response of near-field coupled plasmonic nanoparticles on the angle between the principal axis in the assembly and the propagation direction of the incident light, we calculated these properties for Au-Au, Ag-Ag and Au-Ag touching nanosphere dimers.

For both Au-Au and Ag-Ag homodimers the observed trend is the same. If the principal axis of the nanoparticle assembly is oriented perpendicular to the propagation direction of the incident light then the red-shift and the intensity of the red-shifted coupled plasmon resonance is maximal (See Figures 5.8 and C.8). For an orientation in which both the assembly's principal and the light beam's propagation axes are parallel, the calculated spectra resort to that of a single plasmonic nanoparticle. Intermediate angles result in an intermediate red-shift and an intermediate intensity of the coupled plasmon resonance. As such, for a homodimer the ratio of the intensities at the LSPR and the red-shifted coupled plasmon resonance is a good indicator of the angle between the assembly and the incident light beam.

The explanation for the observed trend is that when the assembly's principal and the light beam's propagation axes are perpendicular, the interaction between the assembly and the incident light is maximal since the electric field component of the incoming light is oriented along the assembly's principal axis. For the

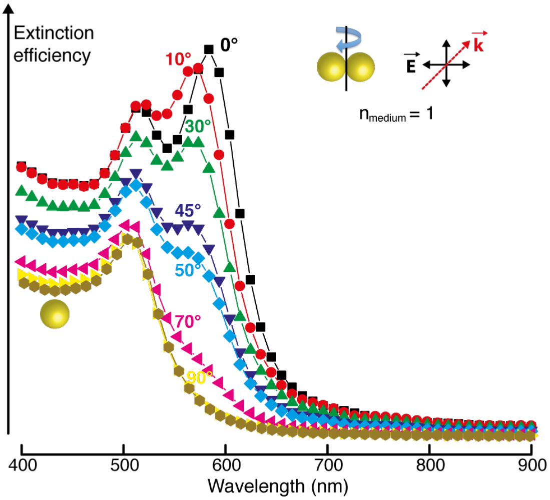

Figure 5.8: Changing the angle of the Au-Au homodimeric assembly's principal axis relative to the propagation direction of the incident light beam from perpendicular to parallel reduces the red-shift and the intensity of the red-shifted coupled plasmon resonance.

case where the principal and propagation axes are parallel, no electric field component of the light is present in the direction of the principal axis, so excitation of coupled plasmon resonances along this axis are impossible.

More formally, when considering the coupled plasmon resonance as a dipolar resonance, we can describe the angle dependence as that of a dipole in an electric field. This because according to the quasi-static approximation for particles much smaller than the wavelength of light, the electric field that the particle feels is static at any moment in time. The potential and also the interaction energy U of an electric dipole in a constant electric field is the dot product between the electric field vector **E** and the electric dipole moment μ_e:

$$U = -\mu_{\mathbf{e}} \cdot \mathbf{E} = -||\mu_e||\,||E||\,cos\theta \qquad (5.1)$$

In the case of Au-Ag nanoparticle heterodimers, the plasmon coupling strength and the interaction energy are not directly or solely reflected in the red-shift nor the intensity of the red-shifted coupled plasmon resonances as compared to the LSPR wavelength and intensity. For these heterodimers, the absorbance

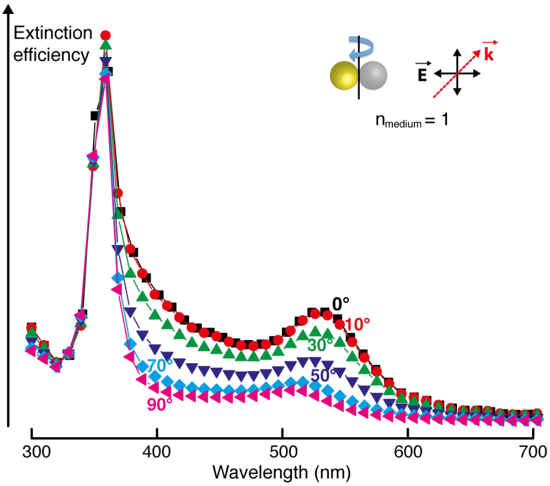

Figure 5.9: The strength of the coupled plasmon - incident light interaction is reflected in the absorbance in the interplasmon region. Maximal interaction is observed when the assembly's principal axis is perpendical to the incident light beam's propagation direction. When these axes are aligned parallel, interaction and the interplasmon absorbance are minimal.

in the interplasmon region is the major indicator for the plasmon coupling strength. When the dimer's principal axis is perpendicular to the propagation direction of the incident light, the interaction between the coupled plasmon and the incoming light's electric field vector is maximal as evidenced by a maximal absorbance in the interplasmon region. Conversely, when the axes are aligned parallel the interaction and the interplasmon extinction are minimal.

Polarization dependence of plasmonic coupling

As stated in the Calculation section (5.1), the calculated optical spectra shown so far are an average of the calculated optical properties for two polarizations of incident light, one parallel and one perpendicular to the interparticle principal axis. Here, we deconvolute this average and present the results of calculations with one incident light polarization at a time and compare them with the average.

For a pair of Au nanospheres of which the surfaces touch, the separation of the

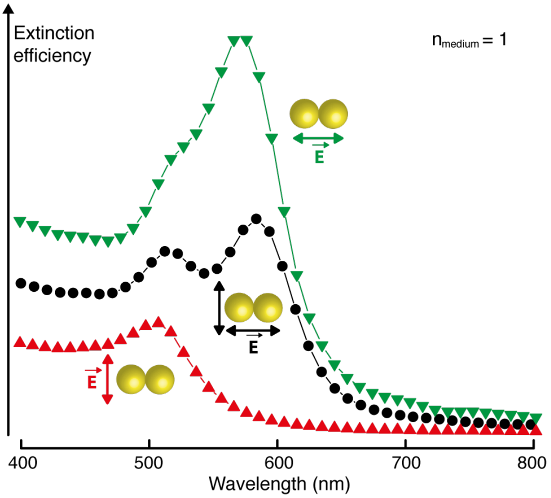

Figure 5.10: Incident light polarized perpendicular to the interparticle axis of a Au NP touching dimer results a slightly blue-shifted resonance as compared to the isolated Au LSPR. Light polarized along the interparticle axis gives rise to a strongly red-shifted coupled plasmon resonance with high intensity. Averaging over both polarizations gives an optical spectrum with two distinct plasmon resonances.

polarization contribution confirms the earlier obtained results and are consistent with the exciton coupling model. When the polarization of the incident light along the assembly's short axis, the assembly resembles an H-dimer with the two interacting dipoles residing side-by-side (see Figure 5.10). The optical response is then very similar to the LSPR response of isolated single Au NPs with the difference of a slight blue-shift, as predicted by the exciton coupling model. Incident light with polarization along the longitudinal axis renders the assembly a J-aggregate in the exciton coupling model with a dipolar head-to-tail coupling. This results in a red-shifted LSPR response and the appearance of an even more red-shifted coupled plasmon resonance, both with a strongly enhanced intensity as compared to the perpendicular polarization. Averaging over both polarizations results in the earlier presented optical spectrum showing two distinct plasmon resonances, one slightly red-shifted LSPR and one strongly red-shifted coupled plasmon resonance.

The above conclusion become even more apparent when performing the same calculations but with a refractive index of the medium of 2 instead of 1 (see

Figure C.9). If the n_{medium} is increased, the plasmon coupling strength as reflected in the red-shift of the coupled plasmon resonance also greatly increases. Incident light polarized along the interparticle axis is, as anticipated, fully responsible for this coupling strength and the accompanying red-shift. For light polarized perpendicular to the interparticle axis, a blue-shift can be observed.

Substituting gold for silver nanoparticles in the previous paragraphs results in the same trends and conclusion (see Figure C.10).

Summary of the theoretical results for plasmonic assemblies

In summary, the presented theoretical results showed that interparticle distance, the number of coupled plasmonic particles, the medium refractive index, the angle between the incident light and the assembly and the polarization of the incident light all have a profound influence on the intensity, number and wavelength of plasmon resonances in plasmonic nanosphere assemblies.

5.2.2 Magnetic-plasmonic nanoparticle assemblies

Here we report on the theoretical results exploring the influence of interparticle distance on the optical properties in magnetic-plasmonic nanoparticle assemblies. We also present the calculated optical spectra of all possible plasmonic and magnetic-plasmonic dimers and trimers.

Influence of interparticle distance in magnetic-plasmonic nanoparticle dimers

The calculated optical spectrum of a touching magnetic-plasmonic magnetite-gold nanoparticle dimer shows that compared to the spectrum of a single gold nanoparticle, the LSPR is slightly red-shifted and a new extinction band at ±380nm is introduced (see Figure 5.11). Magnetite's IVCT resonance is responsible for the band at ±380nm and the red-shift of the LSPR is induced by a (relatively small) increase in the refractive index of the medium due to the close presence of the magnetite nanoparticle. When the particles are placed at a distance from each other, the red-shift diminishes. This is because the average refractive index of the medium in close surroundings returns to the background n_{medium} with increasing interparticle distance. As expected the IVCT resonance persists.

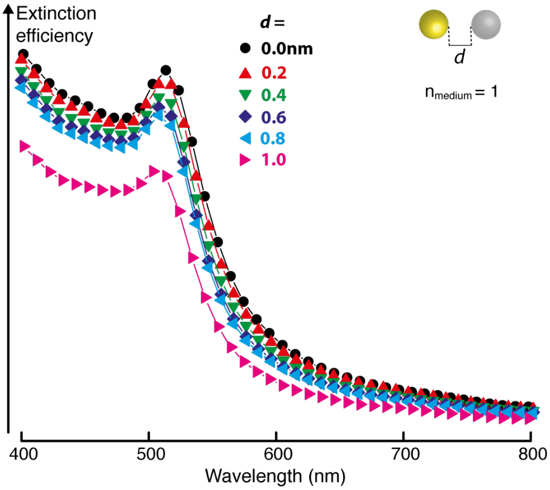

Figure 5.11: Compared to a single gold NP, the LSPR wavelength of a touching magnetite-gold dimer is slightly red-shifted due to an increase of the refractive index of the medium and a new band around ±380nm appears due to magnetite's IVCT resonance. For separated particles, the red-shift diminishes but the IVCT resonance persists.

As compared to magnetite-gold configuration, the difference for the magnetite-silver heterodimer is that in the latter case the Ag LSPR and magnetite's IVCT resonance are in close spectral vicinity. The Ag LSPR slightly red-shifts and an extra extinction feature arises in the optical spectrum for a touching heterodimer (see Figure C.11). For increasing interparticle separation distances the red-shift diminishes, the extra extinction feature disappears and both resonance peaks convolute.

Optical responses of magnetic-plasmonic nanoparticle trimers

When plotting the calculated optical spectra of all possible combinations of Au, Ag and magnetite nanoparticles in a touching linear trimer, we observe that these spectra form 3 sets of spectra (see Figure 5.12). The three sets are 1) magnetite between Au and Ag; 2) magnetite next to Au next to Ag; 3) magnetite next to Ag next to Au. In situation 1), the extinction in the interplasmon is the lowest since magnetite separates the Au and Ag nanoparticles. No large red-shifts of LSPRs are observed. In situation 2) the Au LSPR is red-shifted due

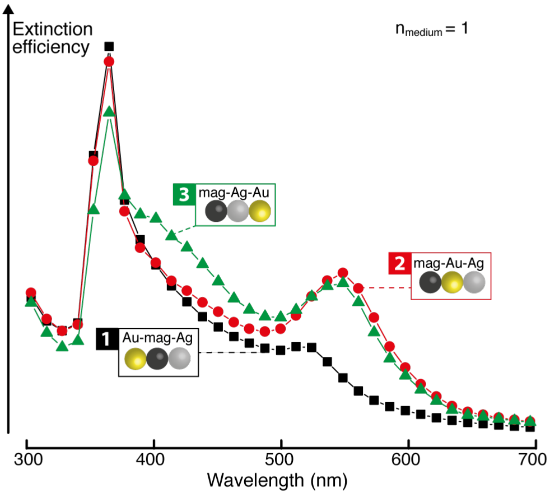

Figure 5.12: The calculated optical spectra of all possible combinations of Au, Ag and magnetite NPs for a touching linear trimer can be categorized in 3 sets of 2 combinations each based on their relative positions.

to the Au-Ag plasmon coupling effect and a refractive index increase because of the close vicinity of the magnetite. The Ag LSPR is hardly affected and in the interplasmon region, no large increase in extinction as compared to situation 1) is apparent. For situation 3), the Au LSPR is red-shifted due to the Au-Ag plasmon coupling, the Ag LSPR is red-shifted and a strong increase in the extinction in the interplasmon region is calculated due to an increased refractive index effect and the close vicinity of the magnetite NP to the Ag NP.

Since a trimer assembly of 10nm nanoparticles is still much smaller than the wavelength of light used, mirrored trimer assemblies e.g. gold-magnetite-silver and silver-magnetite-gold have the same (theoretical) optical properties.

5.2.3 Magnetic-plasmonic nanoparticle multilayers

In this section we will calculate and explain the optical spectra of a (simulated) magnetic-plasmonic multilayer system. As first, we approximate the multilayers system as a linear chain of alternating magnetic and plasmonic nanoparticles and study their optical properties. Then we will suggest a structure model based on the experimentally measured thicknesses of nanoparticle multilayers and calculate the optical spectra.

Magnetic-plasmonic nanoparticle strings

As a first approximation we model the magnetic-plasmonic nanoparticle multilayers as linear nanoparticle strings with alternating magnetic and plasmonic nanoparticles in which the surfaces of adjacent nanoparticles touch.

When building up a Au-magnetite nanoparticle string one-by-one, as in the nanoparticle multilayer system, the calculated spectra show, as expected, a steady increase of the extinction at magnetite's IVCT resonance wavelength around 380nm (see Figure 5.13). The Au NPs LSPR wavelength steadily red-shifts with increasing number of nanoparticles in the string and from 5 particles onwards a distinct second resonance peak is building up in intensity. As we know from previous calculations on purely plasmonic systems (see section 5.2.1), the observed red-shift cannot be due to near-field plasmonic coupling of gold nanoparticles. An increase in the average medium refractive index is responsible for the red-shift and appearance of a second resonance peak.

With increasing nanoparticle string length not only the number of particles increases but also the relative amount of gold nanoparticles that are surrounded by two magnetite nanoparticles. This results in the red-shift of the LSPR peak of the Au NPs. The newly appearing more red-shifted plasmon resonance is attributed to a combination of a high refractive index of the nanoparticle string as a whole and phase retardation effects. This latter size-dependent effect induces a red-shifted resonance and stems from particles or assemblies that no longer comply with the quasi-static approximation, i.e. their size has become significant compared to the wavelength of light.[345,346] As the particle string grows larger, the red-shift due to this effect also increases, as seen in the theoretical results.

The calculated dependence of the optical properties of a 10 NP long, simulating a 5 NDL sample, magnetic-plasmonic nanoparticle chain on the angle between the assembly's longitudinal axis and the incident light shows that the attribution of the most red-shifted plasmon resonance for long strings in the previous paragraph was correct (see Figure 5.14). Once this angle deviates from normal incidence the newly induced most red-shifted plasmon resonance vanishes and a single broad resonance red-shifted as compared to the LSPR persists. This is because the effective length of the nanoparticle string as 'seen" by the incident light drastically reduces with a changing angle. If the angle deviation from normal incidence is 90degrees, i.e. the assembly's longitudinal axis is parallel to the propagation vector of the incident light, then the LSPR wavelength and

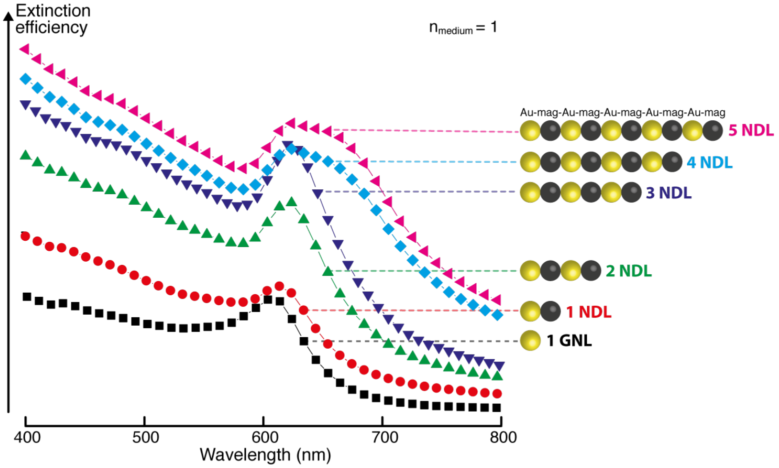

Figure 5.13: With increasing number of magnetite and gold nanoparticles and thus magnetic-plasmonic nanoparticle string length, the extinction at magnetite's IVCT resonance wavelength (±380nm) increases as expected. The LSPR wavelength of the gold nanoparticles gradually red-shifts with increasing string length and from a certain length on, a second resonance peak is induced. These observations are explained based on medium refractive index effects on plasmon resonances.

width are similar to those of a single gold nanoparticle. Since the incident light has no electric field component in the propagation direction and thus cannot excite plasmon resonances in that direction, this result is as expected.

For magnetite-Ag magnetic-plasmonic nanoparticle strings, the trends for the optical properties as a function of the number of nanoparticles are in general the same as for the magnetite-Au case (see Figures C.12 and C.13).

When considering the case of Au-magnetite-Ag-magnetite nanoparticle strings, analysis of the calculated spectra becomes somewhat more complex (see Figure 5.15). In these spectra, and certainly for the longer nanoparticle strings, index of refraction and retardation effects for both gold and silver nanoparticles have to be taken into account. For longer strings the calculated response is of a broadband nature spanning the whole 300-700nm range. Identifiable resonances are the Ag and Au LSPR and red-shifted Ag and Au NP peaks due phase retardation and index of refraction effects (see also Figure 5.12).

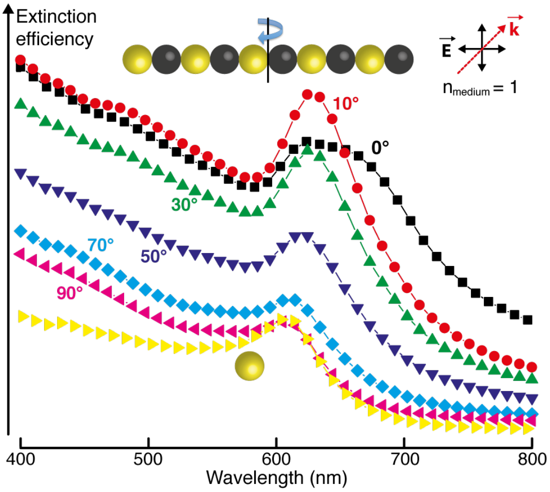

Figure 5.14: The newly induced red-shifted resonance for long nanoparticle strings vanishes when the angle of the incident light beam is deviated from normal incidence. This can be explained by a reduced effective length of the string as 'seen' by the incident light. When the light's propagation direction and the interparticle axis are parallel, the plasmon properties resemble those of a single gold nanoparticle. Since the incident light has no electric field component in the propagation directed, this result is anticipated.

Structure models for magnetic-plasmonic nanoparticle multilayers

In this section we will develop rudimentary structure models for the nanoparticle multilayers based on thickness measurements by scanning force microscopy.

In Chapter 4 Figure 4.3, the increase in thickness as a function of the number of nanoparticle double layers was shown. The thickness of the first double layer was about 13.2nm and for each added NDL the total structure became about 7.3nm thicker.

For the structure models we consider 2 types of spherical particle packings: hexagonal close-packing (hcp) and cubic lattice packing (cp) (see Figure 5.16). Structurally, the major difference lies in the size and shape of the gaps between adjacent nanoparticles. In-plane, the hcp structure has smaller, triangular shaped gaps while the cp structure has comparably somewhat larger rounded square gaps. Keeping the size of the nanoparticles in the second layer fixed for

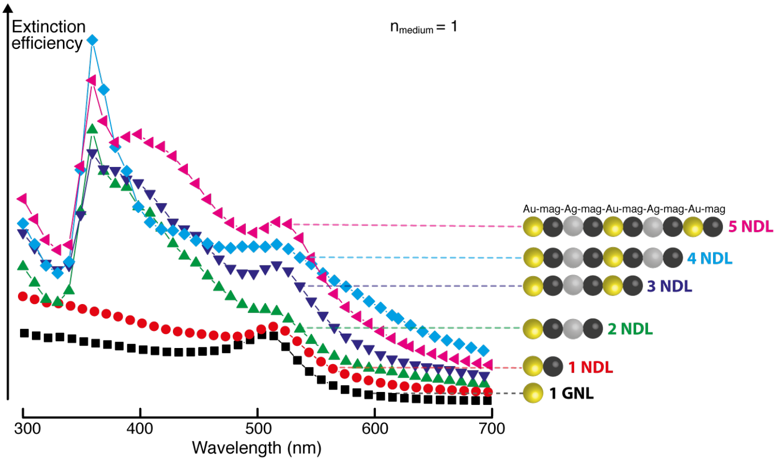

Figure 5.15: Long Au-mag-Ag-mag NP strings show a broadband resonance response from 300-700nm due to Au and Ag LSPR peaks and red-shifted resonances due to index of refraction and phase retardation effects.

both structures, this implies that adding a second layer will lead to a thicker structure in the hcp as in the cp structure. Geometric calculations show that 1 NDL of 10nm large nanoparticles results in 14.65nm and 12.42nm thick layers for hcp and cp structures respectively (see Figures C.14 and C.15). Adding an extra NDL results in an increased thickness of about 10nm in both cases.

While these models only roughly approximate the experimentally obtained values, they provide a good starting point to evaluate the optical properties of the experimental nanoparticle multilayers in terms of nanoparticle packing.

Important differences for optical properties are that in the first layers, gold nanoparticles in our case, the particles have more surface contact area in the hcp as in the cp structure. This leads of course to different optical properties. The same of course holds true for the second layer, magnetite nanoparticles in our case. In that second layer again particles have more in-plane surface contact area with neighbouring particles but also with the particles in the first layer.

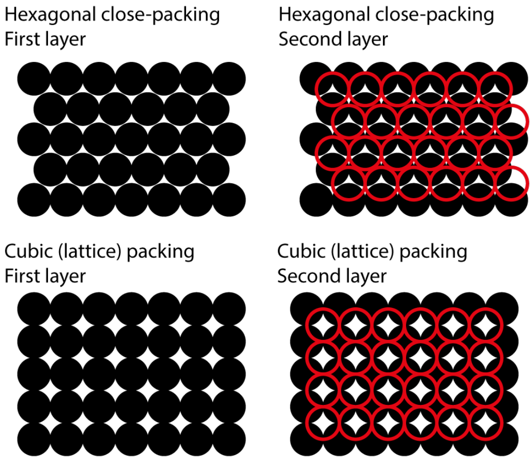

Figure 5.16: Schematic representation of the first and second particle layers in a hcp and a cp structure.

Magnetic-plasmonic nanoparticle multilayers

Here we present the results of calculations on magnetite-gold nanoparticle multilayers modelled as hcp or cp structures as explained in the previous paragraphs. As a side note: since the required computing power increases with the total volume to the third power, calculations on multilayer structures with many nanoparticles are very demanding. For that reason, the number of nanoparticles in the virtual assemblies was chosen so that the packing structure was well represented but dipole resolution remained high to provide accurate solutions.

In a single plane of hcp arranged gold nanoparticles the optical properties, just as for nanoparticle strings, depends greatly on the number of nanoparticles in the structure when not too many nanoparticles are considered (see Figure 5.17). A unit cell of the hcp structure, 3 nanoparticles arranged in a triangular shape, exhibits an optical spectrum similar to that of a nanoparticle string with 3 nanoparticles. A difference though is that the red-shift of the coupled plasmon resonance is less outspoken, as expected, because the coupling length is shorter in a hcp structure. When more nanoparticles are considered, e.g. 10 NPs arranged in a hcp plane, the plasmon resonance response becomes very broad as a result of convolution of the many possibilities of coupling in such a plane.

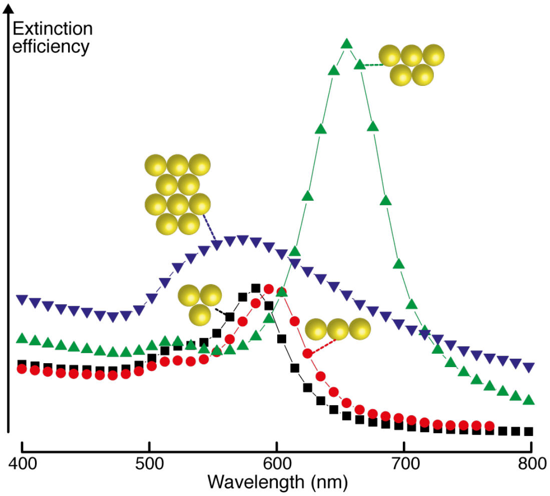

Figure 5.17: Optical properties of Au NPs arranged in a hcp plane depend greatly on the number of nanoparticles in the assembly for small numbers of considered nanoparticles. Once more nanoparticles are being considered, the plasmon response broadens due to the many possibilities of plasmon coupling in such a structure.

For a single plane of Au NPs arranged in a cp structure, the general trends are similar to those observed in the hcp case (see Figure 5.18). The major difference is that when taking into account more nanoparticles, the plasmon resonance response broadening is far less dramatic as for the hcp case. This is a direct consequence of the nanoparticle arrangements. In a hcp arrangement, the number of options for plasmon coupling trajectories is much larger as for a cp arrangement. In the latter case, nanoparticles can only couple in straight horizontal or vertical lines while diagonal coupling options exist in the hcp arrangement. This also makes that the red-shift of the coupled plasmon resonance is much smaller than for a linear chain of 4 nanoparticles. While in the latter case 4 nanoparticle couple, in the cp arrangement only 2 nanoparticles in each direction couple.

The calculated optical spectra of a magnetic-plasmonic nanoparticle multilayer system in a cp structure exhibit, as expected, 3 resonances (see Figure 5.19). Around 380nm, the IVCT resonance of magnetite is dominant followed by the slightly red-shifted but broadened LSPR around 530nm and the strongly red-shifted coupled plasmon resonance around 740nm of Au NPs. Adding a

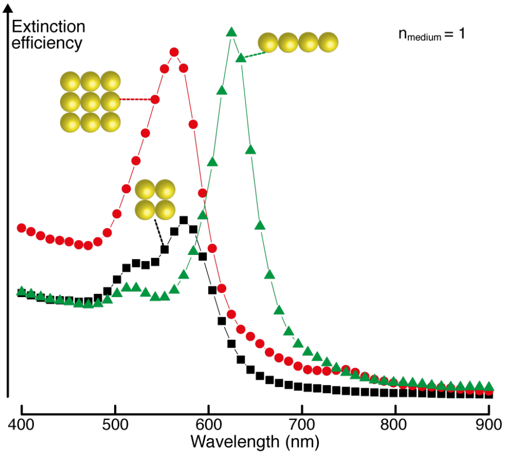

Figure 5.18: Arranging gold nanoparticles in a cp lattice gives rise to coupled plasmon resonances, as expected. For a larger lattice, the plasmon resonance broadens and shows a smaller, more red-shifted resonance.

magnetite NP layer to reduces the intensity of the resonance around 530nm and increases the intensity of the coupled plasmon resonance. This is because the greatly increased medium refractive index as sensed by the Au NPs 'promotes' plasmon coupling as observed in the calculated optical spectra of purely plasmonic assemblies earlier. Adding more gold and magnetite nanoparticle layers has a less profound impact on the optical spectra, which can be rationalized by taking into account that added layers accumulate nanoparticulate material in the propagation direction of the incident light. This resembles the case of nanoparticle strings in which the interparticle axis is parallel to the propagation direction of the incident light, resulting in only minor changes in the optical spectrum.

5.3 Comparing theory and experiment

After extensive calculations on the optical properties of plasmonic and magnetic-plasmonic dimers, strings, planes and multilayers we will now use this gained knowledge to try to explain the experimental optical spectra of magnetic-plasmonic nanoparticle multilayers. We will analyze the optical spectra of

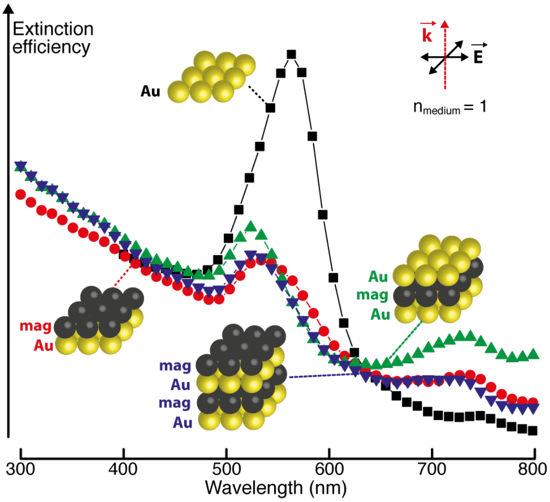

Figure 5.19: Calculated optical spectra of magnetite-gold nanoparticle multilayers modelled as a cp structure show 3 resonances attributed to magnetite's IVCT resonance, Au NP LSPR and a coupled plasmon resonance. Adding more layers results in only minor changes to the spectra since material accumulates in the propagation direction of the incident light, which has only little effect on the optical properties as calculated earlier for nanoparticle strings.

samples with a specific number of NDLs and the dependence of the optical spectra on the angle between the sample and the incident light beam.

Optical spectra as a function of the number of NDLs for gold-magnetite nanoparticle multilayers under normal light incidence show an increasingly red-shifted and more intense plasmon resonance response with increasing number of NDLs (See Figure 5.20 and Chapter 4 Figure 4.2).

A 1 NDL sample exhibits only one relatively broad plasmon resonance around the LSPR wavelength for isolated gold nanoparticles. From the theoretical calculations we can tell that on average the gold nanoparticles that self-assembled as a first nanoparticle layer are not in close contact and do not form dimers, trimers, chains or structured planes. The observed very slight red-shift as compared to the LSPR for isolated gold NPs is due to the glass substrate and the attachment of magnetite NPs to form a first NDL, which increases the medium refractive index.

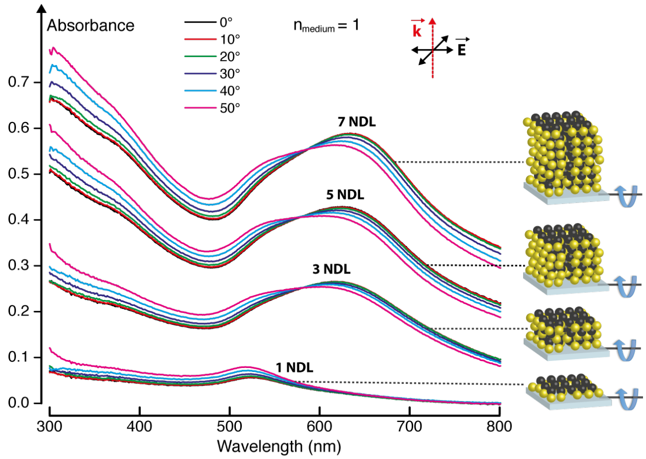

Figure 5.20: Experimental optical spectra of 1, 3, 5 and 7 NDL Au-magnetite samples as a function of angle between the incident light and the sample demonstrate in-plane plasmon coupling and increased structural quality with increasing number of NDLs.

When changing the 1 NDL sample's angle relative to the incident light beam, a small blue-shift and an increase in intensity of the plasmon resonance is observed. As can be inferred from the calculations on magnetic-plasmonic nanoparticle strings, the observed blue-shift of the plasmon resonance can be explained by the existence of magnetic-plasmonic strings in the sample plane (see section 5.2.3 and Figure 5.14 therein). This means that the space between some adjacent Au NPs in the first layer is large enough to accommodate an in-plane attachment of magnetite NPs, which makes that the latter do not only reside on top but also in the spatial plane of the first nanoparticle layer. Because SFM/AFM measurements showed that the thickness of 1 NDL is approximately 13.2nm, we know that magnetite NPs also attach on top of Au NPs. As a consequence of this pattern of self-assembly in the first NDL, many pockets, holes or cavities are created in that layer with a high density of amine functional groups from both the glass substrate's surface and the attached amino-functionalized magnetite NPs. These pockets exert a strong attractive force on the Au NPs added later to form the second NDL.

From the calculations on the angle dependence of magnetic-plasmonic nanoparticle strings, the absorbance should decrease with an increase in angle but we observe the opposite. As the angle is increased, the path length through the sample also increases and this is attributed to be the cause of the general increase of absorbance.

When more NDLs are added to the sample a second red-shifted and high-intensity resonance is induced. From the calculations we know that the observed red-shift cannot just be a medium refractive index effect on a sample represented by magnetic-plasmonic nanoparticle strings, as the red-shift is too large for that effect alone (see Figure 5.13). Near-field coupling between adjacent plasmonic nanoparticles thus must be present in the sample to obtain the experimental spectra. Furthermore, the plasmon coupling must be preferentially in planes parallel to the glass substrate plane, i.e. perpendicular to the incident light propagation direction. This is demonstrated in two ways in the spectra. Firstly, the observed red-shift through near-field plasmon coupling at normal incidence needs to stem from plasmonic assemblies with their interparticle axes preferentially perpendicular to the propagation direction of the incident light (see Figure 5.8). Secondly, changing the angle away from normal incidence blue-shifts and reduces the intensity of the coupled plasmon resonance while the LSPR response increases in absorbance. These trends agree very well with those calculated for the angle dependence of near-field coupled plasmonic assemblies and also show that the plasmon coupling needs to be in parallel planes.

For samples with more NDLs, the red-shift at normal incidence of the coupled plasmon resonance is more significant, just like the blue-shift with changing angle. This indicates that the plasmon coupling strength is larger and that the enhanced near-field coupling extends in parallel planes when more NDLs are added. Both larger in-plane plasmonic assemblies and more completely filled parallel magnetite planes resulting in a higher medium refractive index are likely to contribute to the observed effects.

From the comparison between the calculated and the experimental spectra and taking into account the linear relationship of multilayer thickness a.f.o. added NDLs as measured by AFM we can now present a more nuanced image of the self-assembled Layer-by-Layer synthesis of the magnetic-plasmonic nanoparticle multilayers. The first Au nanoparticle layer is incomplete and not structurally patterned, leaving space between adjacent nanoparticles. Amino-functionalized nanoparticles attach on top but also next to the already present Au NPs. This creates highly attractive amino-functionalized pockets for subsequently added Au NPs. These newly added Au NPs first fill the attractive pockets in the first layer but also attach on top of the present magnetite NPs making the multilayer thicker. As such, the first Au nanoparticle layer becomes more filled, which induces a red-shifted coupled plasmon resonance. The same process occurs for the then added magnetite nanoparticles, as they can also fill up vacancies left in the first magnetite nanoparticle layer. As such, with increasing number of added NDLs the multilayer structure becomes not only thicker but also more filled and thus of a better quality.

When we compare the experimental spectra for a 7 NDL Au-magnetite nanoparticle multilayer with the calculated spectra for the developed model packing structure it is very clear that they do not match. This implies that even experimental multilayers with many NDLs do not resemble a regularly packed structure. The origin of this lack of regular packing is most likely to be found in the random and spacious distribution of Au NPs in the first nanoparticle layer. If this first layer would be a regular lattice plane, the subsequently added nanoparticles would have no choice but to adhere to the underlying lattice of the first layer and form a regularly packed multilayer structure.

For silver-magnetite and gold-magnetite-silver-magnetite nanoparticle multilayers, the specific experimental spectra of course are quite different than the ones discussed for gold-magnetite (see Figures C.16 and C.17). Despite the spectral differences, all observations, trends and conclusions based on the comparison of the calculated and experimental spectra hold for the multilayers incorporating different metals. The Layer-by-Layer construction of these materials is thus the same as for the Au-magnetite case.

5.4 Conclusion

In this chapter we first calculated the optical properties of purely plasmonic and of magnetic-plasmonic nanoparticle assemblies and studied their dependence on variables such as the medium refractive index, interparticle distance and angle of incidence. Model packing structures were proposed and their optical properties calculated. From the comparison between the calculated and the experimentally obtained spectra for magnetic-plasmonic nanoparticle multilayers we gained more insight in the Layer-by-Layer synthesis mechanism of these multilayers. The first layer is filled with randomly and spaciously distributed gold nanoparticles. Vacancies left in this layer are converted to attractive pockets by attachment of amino-functionalized iron oxide nanoparticles. These pockets are then filled by newly added Au NPs. As such, with increasing number of NDLs, the multilayer structure becomes not only thicker but also gets a higher filling fraction, increasing the general optical quality of the sample.

Chapter 6

Nonlinear optical properties of magnetic-plasmonic nanoparticle multilayers

This chapter is a reproduction of the following submitted publication that has been adapted to form only:

W. Brullot, S. Van Cleuvenbergen, M. K. Vanbel, M. A. van der Veen, R. Paesen, M. Ameloot, T. Verbiest.
Nonlinear optical processes in gold-magnetite nanoparticle multilayers.
Submitted to The Journal of Physical Chemistry C (2014).

Dr. S. Van Cleuvenbergen and Dr. M. A. van der Veen assisted with the nonlinear optical measurements and the analysis. M. K. Vanbel, R. Paesen and Prof. dr. M. Ameloot performed the nonlinear optical microscopy measurements and the analysis of these results.

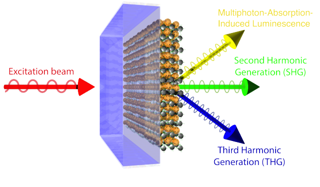

Abstract

In search for novel efficient nonlinear optical materials for applications in telecom or sensor design, many types of compounds have been studied. Inorganic nanoparticles, such as gold or iron oxide nanoparticles, exhibit large nonlinear susceptibilities and fast response times but at different wavelengths due to their (coupled) surface plasmon and intervalence charge transfer resonances respectively. Combining such nanoparticles should result in interesting materials that possess multiple nonlinear optical resonances.

Using a recently developed method, we integrated gold and magnetite nanoparticles in polymer- and polyelectrolyte-free nanoparticle multilayers with high filling fractions. In nonlinear optical microscopy and spectroscopy measurements we observed that second harmonic generation (SHG) was resonantly enhanced only by the coupled surface plasmon resonance of gold. Resonances in the magnetite nanoparticles enhanced the third harmonic generation (THG). For fundamental wavelengths 1100-1300nm, THG from magnetite and SHG from coupled plasmons of gold were simultaneously enhanced.

Our results show that materials can be developed in which both second and third order nonlinear optical processes can be simultaneously optimized.

6.1 Introduction

Composite or hybrid nanomaterials, combining several types of nanoparticles, generate major interest because they result in integrated functionalities and engineering capability for the combined properties. Layer-by-Layer (LbL) self-assembly deposition methods offer additional advantages in the control of composition and morphology. Most of these LbL methods involve the use of polymers or polyelectrolytes as spacer and stabilizing unit between consecutive layers. Disadvantages of such polymer/polyelectrolyte methods are that they inherently have limited nanoparticle filling/volume fractions and that the organic layers possibly interfere with measurements.

Recently, a novel Layer-by-Layer synthesis method yielding homogeneous and polymer/polyelectrolyte-free nanoparticle multilayers that are partially transparent in the UV-visible-near-infrared (UV-vis-NIR) wavelength region has been developed.[347] This synthesis method uses short bifunctional molecular linkers connecting the nanoparticles and allows producing nanocomposites with a defined number of nanoparticle layers of specific materials on glass substrates. Advantages of such structures for nonlinear optical measurements of nanoparticle composites are the very large filling fractions, i.e. the weight percentage or volume fraction of nanoparticles compared to the total structure is very large, and due to the dense packing, the average distance between particles in consecutive layers is small.

Gold nanoparticles (Au NPs) show a distinct localized surface plasmon resonance (LSPR) in the visible wavelength range.[348] This resonance is a collective oscillation of conduction electrons in the noble metal in response to the incident light and gives rise to local trapping and enhancement of electric fields.[160] The frequency or wavelength at which the LSPR occurs for a single gold nanoparticle is dependent on its size and shape and also on the refractive index of the surrounding matrix, but is generally around 520 nm.[157, 159] At the LSPR wavelength, strongly enhanced absorption and scattering of electromagnetic waves occurs.[17]

When plasmonic nanoparticles are brought in close proximity of each other, the electric near-fields can couple. This coupling then changes the LSPR wavelength for the coupled system relative to the single particle system. For spherical gold nanoparticles, near-field coupling leads to a strong red-shift of the LSPR wavelength due to the lower energy required to drive the plasmon oscillations.[170, 349] The near-field coupling also changes the symmetry of the electric field distribution on the nanoscale, as the coupled electric near-fields can exhibit asymmetric distributions.[163, 350] Note that the LSPR wavelength for coupled systems can be tuned by varying the average distance between nanoparticles, their size or by changing the nanoparticle material.

Surface plasmon resonances are very interesting for enhancing (non-)linear optical effects because of the large enhancements of electric fields at the plasmon wavelength. Examples are surface plasmon enhanced Raman scattering (SERS),[163] magneto-optical Faraday rotation,[168, 169] second harmonic generation (SHG),[164–167] third harmonic generation,[233–236] or multiphoton-absorption-induced luminescence (MAIL).[237–239]

Magnetite (MNPs), and iron oxide nanoparticles in general, are widely used in sensor, biomedical and magneto-optical applications due high magnetic susceptibilities and non-toxicity.[42, 102, 351] Optically, magnetite nanoparticle exhibit an intervalence charge transfer (IVCT) resonance in the visible wavelength range around 380nm.[73] Iron oxide nanoparticles have been used as tracking labels in nonlinear microscopy studies because of their high nonlinear optical responses.[122] Third-order nonlinear optical measurements on iron oxides have been performed by e.g. Garcia et al, who found values on the order of 10^{-10} esu for the third order optical susceptibility ($\chi^{(3)}$) of α-Fe2O3 at 800nm as measured by Z-scan techniques.[76] Hashimoto et al measured the third

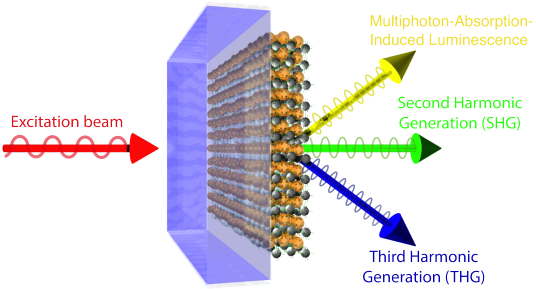

Figure 6.1: Au-magnetite nanoparticle multilayers produce resonantly enhanced Second and Third Harmonic Generation (SHG and THG) and Multiphoton-Absorption-Induced Luminescence (MAIL) upon irradiation with near-infrared (NIR) laser light. Note that the drawing is not to scale and the generated light beams are depicted under an angle for clarity.

harmonic generation (THG) of iron oxides in thin films with a fundamental wavelength of 1900nm and observed for magnetite large values up to 4×10^{-10}esu for the electronic contribution to ($\chi^{(3)}$).[77] This large value was attributed to one- and three-photon resonances. Materials exhibiting large third-order nonlinear susceptibilities are highly desirable for applications such as all optical switching,[117, 118] optical limiting,[119] or optical frequency triplers.[120]

In this work we synthesized gold-magnetite (Au-mag) nanoparticle multilayers and we exploit the different resonances present in the composite material to selectively enhance second- and third order processes (Figure 6.1). Our results, while fundamental in nature, show that it is possible to develop materials in which both the second and third order nonlinear optical processes can be simultaneously optimized.

6.2 Experimental

Synthesis of the Au-magnetite nanoparticle multilayers

Full synthesis details for the used sample are described in Chapter 4. The samples used in this work have 5 nanoparticle double layers (5 Au and 5 magnetite nanoparticle layers) on one side of the glass substrate.

Nonlinear optical microscopy imaging

Microscopy imaging was performed using a Zeiss LSM510 META (Carl Zeiss, Jena, Germany) mounted on an Axiovert 200M, and a 10x/0.3 objective (Plan-Neofluar 10x/0.3, Carl Zeiss). The excitation was provided by a femtosecond pulsed laser (MaiTai DeepSee, Spectra-Physics, CA, USA) tuned to a central wavelength of 810nm. The excitation light was linearly polarized. The SHG signal was collected in forward mode using a condenser with a numerical aperture of 0.55. Finally, the signal was detected by an analogue photomultiplier tube delivered by Zeiss.

Variable near-infrared wavelength excitation spectrally resolved nonlinear optical measurements

A Spectra-Physics Insight DeepSee ultrafast femtosecond pulsed laser, tunable from 690nm to 1300nm, was used as light source. The fundamental light intensity was adjusted using a half-wave plate and an uncoated Glan-Taylor linear polarizer. A small portion of the beam intensity was sent to a photodiode (Hamamatsu G3476-03) using a beam splitter for fundamental beam input intensity monitoring. The laser beam then passed an FEL700 cut-on long pass filter to remove all intensity with wavelengths shorter than 700nm and an uncoated N-BK7 bi-convex lens with a 50mm focal distance (LB1471), slightly focusing the beam onto the sample. The sample, of which only one side is covered with nanoparticle layers, was positioned with the covered side directed to the detector to avoid any interference effects. To choose the optimum angle for efficient THG detection, the angle of the sample was varied between 0 and 60° with the incoming laser beam. The sample was positioned at an angle of 15° because maximal THG was detected at that angle. Light emitted from the sample after illumination was collected using another uncoated N-BK7 bi-convex lens with a focal distance of 35mm. Collected light then passed 2 BG39 filters for fundamental beam wavelengths from 700-1100nm or 1 BG39 and 1 KG5 filter for fundamental beam wavelengths 1200-1300nm to remove transmitted input intensity. Having passed the optical filters, the generated light was sent through a calibrated Bruker Surespectrum 500is spectrometer and detected using an EMCCD (Hamamatsu C9100-13) cooled to -65°C. Mirrors used in the setup were Au-coated to ensure optimal reflectivity over the entire used spectrum.

For the spectral measurements, input power was kept constant at 75mW. At this input power, no optical damage was observed. Laser intensity dependent measurements were done by rotating a half-wave plate before a polarizer. Intensities were calibrated using a power meter and monitored by a photodiode.

Maximum intensity used in these measurements was also 75mW. Changing the central wavelength of the spectrometer allowed scanning the emission spectrum. Full spectra were then obtained by stitching the individually recorded spectral parts together.

Raw collected emission data were normalized for gain and exposure time and corrected for the dark background signal of the spectrometer and the response curve of the EMCCD. Transmittances of the optical filters in the setup were also taken into account. For all fundamental beam wavelengths a glass substrate was measured as reference.

Third harmonic generation measurements at 1300nm and 1500nm

The measurements were performed on a femtosecond optical parametric oscillator set-up (model OPAL, pumped by a Tsunami, Spectra-Physics). The intensity of the laser light is modulated by a chopper while the average power is kept at 75mW at both wavelengths by a combination of a half-waveplate and an uncoated Glan-Taylor linear polarizer. A small fraction of the light is lead to a photodiode to monitor the laser intensity. A long-pass filter (FEL800, Thorlabs) is used to remove any second-harmonic light from the preceding optics. The beam is then focused on the sample by a plano-convex lens (LA1027, f=50mm, Thorlabs) and collected by two more lenses (LA1131/LA1027, f=50/35mm, Thorlabs). The sample is mounted on a motorized rotation stage to adjust the incident angle for the Maker-fringe experiments. The generated third-harmonic light is selected by an interference filter at the proper wavelength and detected by a photomultiplier tube (R9880, Hamamatsu) connected to a lock-in amplifier. As a reference a Y-cut quartz crystal of known thickness (1mm) is used.

Nonlinear optical phenomena

For very intense light the induced polarization is expanded in a Taylor series in terms of the total applied field.[106] The induced polarization P can then be written as a function of field strength E as

$$P = \chi^{(1)}E + \chi^{(2)}EE + \chi^{(3)}EEE + \cdots \tag{6.1}$$

with $\chi^{(1)}$ the linear susceptibility which describes linear optical properties such as refraction and absorption, $\chi^{(2)}$ the first nonlinear susceptibility that is responsible for second-order nonlinear optical processes such as second harmonic generation (SHG), and $\chi^{(3)}$ the second nonlinear susceptibility that is responsible for third-harmonic generation and two-photon luminescence. Note that three-photon luminescence also can occur which is in principle a fifth order nonlinear optical process described by the fourth nonlinear susceptibility $\chi^{(5)}$. All susceptibilities are frequency dependent and can be strongly enhanced when the fundamental or the generated wavelength are close to an optical resonance in the material.

UV-visible absorbance measurements

A Perkin Elmer Lambda 900 spectrophotometer was used for these measurements.

6.3 Results & discussion

6.3.1 Gold-magnetite nanoparticle multilayers

The Au-mag nanoparticle multilayers used in this study consist of a glass substrate that is alternatively Layer-by-Layer (LbL) covered with gold and amino-functionalized iron oxide nanoparticles (sample depicted in Figure 6.1).[347] A 170μm thick microscope coverslip was used as substrate. This substrate was then covered on both sides with 5 Au and 5 magnetite nanoparticle layers through an LbL assembly process. To prevent undesired interference effects in the nonlinear optical measurements, one side of the substrate was cleaned, leaving only one side covered. Total thickness of the nanoparticle multilayers on one side is approximately 39.9nm as measured by scanning force microscopy measurements.

6.3.2 Nonlinear optical microscopy

Homogeneous SHG and MAIL from the nanoparticle multilayers were detected using a nonlinear optical microscope (Figure 2). Using femtosecond pulsed 810nm laser light nonlinear optical images were obtained from a 180μm×180μm region on the sample next to a scratch. SHG was detected by using a narrow 400-410nm band-pass filter (Figure 6.2 - left) and MAIL by using a filter combination that has a transparent region from 450nm to 650nm (Figure 6.2 - right). These images show that both the LbL method yields homogenous multilayers and that the nonlinear optical signals are homogeneously generated throughout the sample.

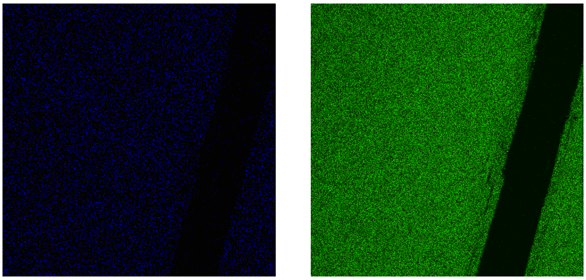

Figure 6.2: Nonlinear optical microscope images under 810nm fs pulsed laser light excitation. A scratch was made to show the clear difference in signal level between background and sample.

6.3.3 Spectrally resolved nonlinear optical measurements

Spectrally resolved nonlinear optical measurements under variable NIR wavelength excitation reveal that the Au-mag nanoparticle multilayers shows excitation wavelength dependent nonlinear optical responses (Figure 6.3). The sub-100 femtosecond pulsed fundamental laser beam was tuned between 700nm and 1300nm wavelengths at a fixed power of 75mW and the sample was positioned at a 15° angle with the incoming laser beam. The nonlinear optical responses were spectrally recorded between 350nm and 675nm.

Three distinct effects are visible in the recorded spectra. (1) SHG is produced by excitation wavelengths from 800nm to 1300nm and detected at half the fundamental wavelength from 400nm until 650nm. Detected signal levels vary with the fundamental wavelength. (2) THG is observed at 366nm, 400nm and 433nm when irradiating the sample with 1100nm, 1200nm and 1300nm respectively. The THG peaks show a sharp resonance and the detected signal levels are strongly dependent on the excitation wavelength. (3) MAIL from the sample was observed in the spectral range from 500-650nm.

At fundamental wavelengths 1100, 1200 and 1300nm, all 3 of the above effects (SHG, THG and MAIL) are simultaneously excited. The observed effects are very significant when compared to a glass substrate reference (right side Figure 6.3). At fundamental wavelength 1200nm, the raw detected nonlinear optical spectrum of the glass substrate is almost flat, while the Au-mag nanoparticle multilayers spectrum shows all three distinct features.

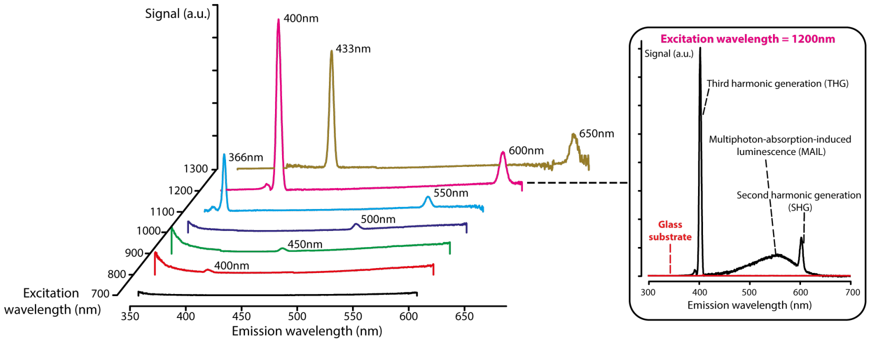

Figure 6.3: Variable NIR wavelength excitation spectrally resolved nonlinear optical measurements reveal excitation wavelength dependent nonlinear optical responses from the Au-mag nanoparticle multilayers. *Inset:* excitation at 1200nm simultaneously generates THG, SHG and MAIL from the sample. Results from measurements on glass substrates are shown as reference.

6.3.4 Second harmonic generation

While the UV-visible absorbance spectrum of the studied Au-mag nanoparticle multilayers shows three spectral resonances, it is clear from the data shown in Figure 6.4 that only the coupled plasmon modes resonantly enhance the SHG response, while the Au LSPR or the iron oxide IVCT resonance do not. The three resonances observed in the UV-visible wavelength region (black line, Figure 6.4) are magnetite's IVCT resonances around 380nm,[73] the LSPR of isolated gold nanoparticles centered on 520 nm,[157, 159] and a strong, broad resonance of coupled plasmonic near-fields between multiple Au nanoparticles around 625nm.[17, 170] Rayleigh scattering of the nanoparticles and the used substrate glass induce the strong increase in absorbance in the UV region.

From the SHG intensity data (blue squares, Figure 6.4) it is clear that both the IVCT on the MNPs and the localized surface plasmon resonances on the Au NPs do not enhance the SHG signal. On the contrary, the resonance due to coupled plasmonic near-fields greatly enhances the SHG response. Possible explanations for this observation can be based on symmetry arguments,[352, 353] electric field enhancement factors for coupled plasmons,[352–354] or additional contributions to the second harmonic generation beyond the electric dipole approximation, such as magnetic dipole or electric quadrupole,[106, 355] that need to be taken into account.

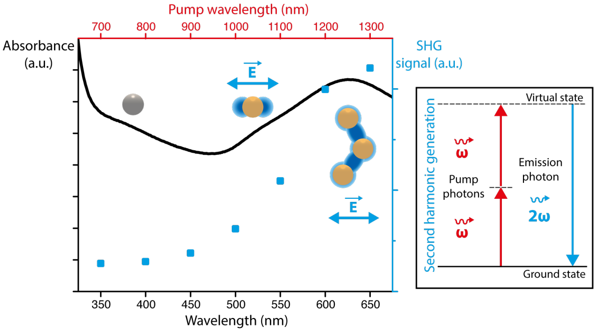

Figure 6.4: *Left:* Three peaks due to the IVCT in magnetite (385nm), the LSPR of isolated Au NPs (520nm) and the coupled plasmonic near fields (625nm) can be observed in the linear optical absorbance spectrum (black line). SHG responses (blue squares) are resonantly enhanced by the coupled Au NPs plasmon resonance but not by the LSPR of single Au NPs or the IVCT of magnetite. *Right:* SHG is generated through simultaneous excitation by two photons of the same wavelength to a virtual state and subsequent decay to the ground state, emitting a photon of half the fundamental wavelength.

Plasmonic enhancements of SHG signals have been experimentally observed earlier for gap antennas,[356] gold nanorods,[167] coupled nanoplasmonic arrays,[354] metal nanoshells, and theoretically studied for metal nanoshells,[357] and gold nanoparticle dimers.[358] Au-mag nanoparticle multilayers, integrating the IVCT, LSPR and coupled plasmon resonances, provide direct comparative confirmation of previous observations and theoretical considerations.

6.3.5 Third harmonic generation

THG from the Au-mag nanoparticle multilayers shows a strong resonantly enhanced response as a function of fundamental wavelength in the 300-450nm spectral range (Figure 6.5). Dominating the UV-visible absorbance spectrum in this wavelength range, magnetite's IVCT resonance is responsible for the observed enhancements. Data for fundamental wavelengths 1100-1300nm were obtained from the spectral measurements while the result for 1500nm was measured using a Maker Fringes setup (see Figures D.1-D.4).[166] THG only measures $\chi^{(3)}_{\mathrm{el}}$, the electronic contribution to the third order nonlinear optical susceptibility. The technique is not sensitive to other, e.g. thermal, contributions and as such gives a lower limit for the third nonlinear optical susceptibility. The electronic sensitivity in combination with the spectral overlap of the observed THG resonance and the IVCT resonance justifies the enhancement attribution to that specific resonance.

The obtained result is in agreement with the findings of Espinosa et al. who recently measured the third order nonlinear optical properties of magnetite.[359] They used the third order nonlinear optical Z-scan technique, additionally sensitive to thermal properties, with a single fundamental wavelength of 800nm and attributed the observed large $\chi^{(3)}$ values to magnetite's IVCT transition. In our experiments, THG was detected from the nanoparticle multilayers at fundamental wavelengths from 1100nm onwards, covering a broad spectral range for both the excitation as the emission wavelengths. This broad spectral response range enlarges the potential applicability in e.g. all-optical switching or higher harmonic generation microscopy.

The magnitude of the electronic contribution to the third order nonlinear optical susceptibility $\chi^{(3)}_{\mathrm{el}}$ is estimated to be 1.2×10^{-10}esu for 1200/400nm as fundamental/THG wavelengths based on relative coherent lengths and measured THG signals for the nanoparticle multilayer and a quartz reference.[77] This estimate agrees well with the values reported by other groups for iron oxides.[76, 77]

Unlike even order, such as SHG, uneven order higher harmonics generation, like THG, do not require a non-centrosymmetric electric field distribution.[106] Third harmonic responses from single spherical magnetite nanoparticles are thus symmetry-allowed. This is nicely demonstrated in the spectral results, as the THG response at 400nm is resonantly enhanced while the SHG response at the same wavelength is not.

6.3.6 Multiphoton-absorption-induced luminescence

For the analysis of the MAIL data, only Au NPs are taken into account. Magnetite, or iron oxide nanoparticles in general, show only very weak photoluminesce when illuminated with 325nm light and are known as strong quenchers of fluorescence and luminescence of attached chemical moieties.[360–364] When Au NPs are illuminated with NIR laser light, MAIL can be detected in the wavelength range from 500-650nm (Figure 6.3). The results of signal vs. laser intensity measurements show that depending on the fundamental wavelength, MAIL excitation is a two- or a three-photon process (Figure 6.6).

At the fundamental wavelengths 800nm and 1300nm, the laser intensity was varied between near zero and 75mW maximum in 10 steps using a half-wave plate and a linear polarizer. The MAIL response was measured at 600nm emission wavelength. At a fundamental wavelength of 800nm, the response as a function of

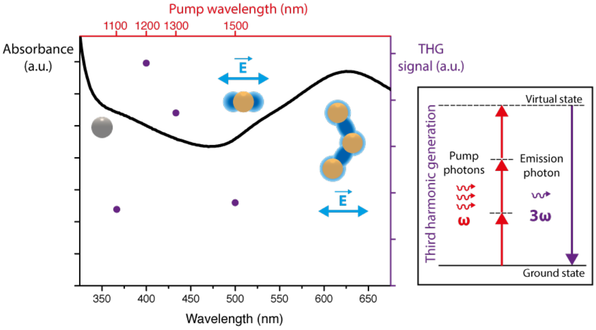

Figure 6.5: The THG response as a function of emission wavelength (purple dots) is resonantly enhanced by the IVCT transition of magnetite that dominates the corresponding spectral UV-vis absorbance region (black line).

laser intensity has a quadratic profile, indicating a two-photon excitation process (Figure 6.6 - top left). For 1300nm as fundamental wavelength the response profile is cubic, pointing to a three-photon excitation process (Figure 6.6 - top right). Single photon excitation of MAIL in Au was measured by Mooradian using fundamental wavelengths in the 300-514nm wavelength range.[365]

These results can be phenomenologically explained by the energy band structure of Au NPs.[366–368] Since the band gap between the *d* and the *sp* bands in Au NPs is too large for single NIR photon excitation, the absorption of two or three photons is necessary to bridge this energy gap (Figure 6.6 - bottom). MAIL generation is possible as long as enough energy is absorbed to excite electrons above the Fermi level. Through absorption of photons an electron-hole pair is generated in the respective bands, which generates a MAIL emission photon upon recombination. At fundamental wavelength 800nm, absorption of two photons is sufficient to excite the MAIL response, while at 1300nm three photons are required to drive the same process. A definite transition to three-photon absorption only occurs when the fundamental light beam induces SHG at a longer wavelength than the chosen MAIL detection wavelength. This is because MAIL emission implies energy loss as compared to the total input energy while higher harmonic generation (HHG) such as SHG or THG does not, causing a MAIL emission redshift compared to the corresponding HHG emission.

In this work, detecting MAIL emission at 600nm wavelength, the definite switch to three-photon absorption occurs from a fundamental wavelength of 1300nm onwards because then the SHG (at 650nm) is red-shifted as compared to the

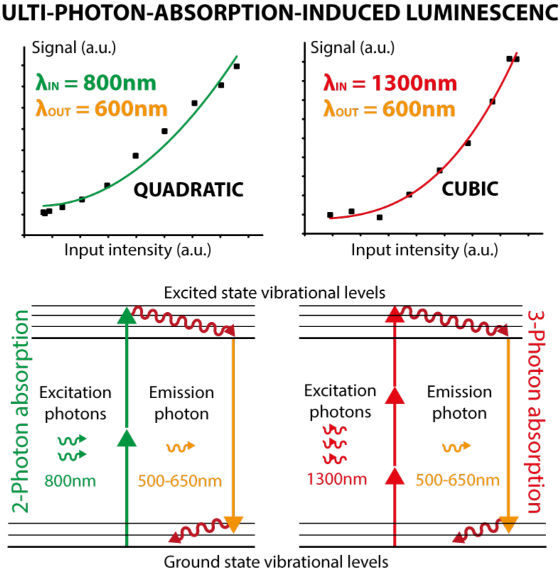

Figure 6.6: When detecting MAIL at 600nm as a function of laser intensity, the response curve is quadratic for 800nm and cubic for 1300nm fundamental beam wavelength (top graphs). As a simple model, MAIL is produced through multiphoton absorption by exciting electrons from *d* to *sp* energy bands of Au, generating electron-hole pairs that radiate photons upon recombination. The number of required absorbed photons to bridge the band gap depends on the fundamental wavelength (bottom graphs).

detection wavelength.

6.3.7 Simultaneous resonant enhancement of nonlinear optical processes

The spectral results and the extracted SHG and THG data show that at 1100, 1200 and 1300nm fundamental wavelengths simultaneous resonant enhancement of multiple nonlinear optical processes occurs in the Au-mag Nanoparticle multilayers (Figures 6.2, 6.3 and 6.4). Because of the IVCT resonance of magnetite centered at 385nm and the LSPR and coupled plasmon resonances of Au at 520nm and 625nm respectively, THG and SHG are simultaneously resonantly enhanced at the earlier stated fundamental wavelengths.

This simultaneous enhancement, combined with the observed high efficiencies for both THG and SHG, makes for added applicability of the integrated Au-mag nanoparticle multilayers. An example of application might be sensors that simultaneously detect changes in SHG and THG output. Other possible application areas are optical switches employing multiple wavelengths, simultaneous frequency doublers/triplers from the infrared to the visible spectrum or as homogeneous detection substrates for multiphoton microscopy techniques.

6.4 Conclusions

In conclusion, we determined the nonlinear optical processes in Au-mag nanoparticle multilayers in the UV-visible-NIR wavelength range. These multilayers were approximately 40nm thick and have a high nanoparticle filling fraction. Nonlinear optical microscope images confirmed homogeneity of the sample and the generated nonlinear optical signals. In macroscopic measurements, large enhancement of the SHG signal was only observed at wavelengths attributed to near-field coupled plasmon fields. The THG signals showed a strong resonance at the IVCT wavelength of magnetite. For input wavelengths in the 1100-1300nm range, simultaneous resonant enhancement of SHG and THG by different processes was observed. As such, we synthesized a material that combines and simultaneously enhances second and third order nonlinear optical processes.

In future work, we aim to engineer the nonlinear optical enhancements by changing the nanoparticle materials and use e.g. silver, which induces coupled plasmons at other wavelengths.

Chapter 7

Magneto-optical properties of magnetic-plasmonic nanoparticle multilayers

The results presented in this chapter are partly based on the following conference contribution:

W. Brullot, Stefaan Vandendriessche, Thierry Verbiest.
Magneto-optical characterization of magnetic-plasmonic gold-magnetite hybrid nanoparticle networks (AuMag-HyNANs).
Frontiers in Optics 2013, Orlando (U.S.A.), 6-10 October 2013
Abstract FTh4C.1.

S. Vandendriessche assisted with the experimental setup and data analysis.

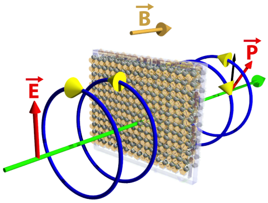

7.1 Introduction

As stated in the general introduction (section 1.5.3), a prominent example of the interplay between magnetic and plasmonic components is the enhancement of magneto-optical effects through plasmon excitation, which was first proposed by Hui and Stroud.[294, 295]

The origin of the enhancement of the magneto-optical effects is the very large local enhancement of the electromagnetic fields through plasmon resonances. When a magneto-optically and a plasmonically active entity are optically coupled, i.e. in close vicinity of each other, the magneto-optical response is enhanced to a degree that correlates with the electromagnetic field strength in the magneto-optically active entity.

Plasmon-enhanced magneto-optical effects were measured in iron oxide - gold systems such as gold-coated maghemite γ-(Fe_2O_3) nanoparticles,[168, 169] For the combination of magnetite (Fe_3O_4) and gold measurements have been performed on magnetite nanocrystals near rough gold surfaces by Shemer *et al.*[296] Moolenkamp *et al.* observed the effect of plasmon resonance enhancement in gold-magnetite nanocomposite films synthesized by chemically linking gold and magnetite nanoparticles, mixing these clusters with a transparent polymer and dropcasting a thin film.[304] Plasmon-enhanced magneto-optical effects were also observed by Caminale *et al.* for magnetite-gold samples produced by depositing metallic nanoparticles in the grooves of LiF substrates and then dipping these samples in a hexane-based dispersion of oleic acid-coated magnetite nanoparticles.[257]

In this chapter we report Faraday rotation and ellipticity measurement results of gold-magnetite nanoparticle multilayers synthesized by the protocol detailed in Chapter 4. As compared to the magnetite-gold nanoparticle systems mentioned in the previous paragraph, the prepared samples do not involve polymers or polyelectrolytes and are on a flat transparent substrate. These properties enable proper signal acquisition and are an asset for applications in which (partial) transparency is required. Further, when considering possible applications, the Layer-by-Layer protocol is suited for large-area coating, straightforward and cost-effective.

Magneto-optical measurements were performed on gold-magnetite nanoparticle multilayers of different thicknesses (number of nanoparticle double layers). The results show that both the FR and FE response increase linearly with the number of added NDLs, like for thickness and absorbance at the plasmon wavelength. Through shifts of spectral features in the magneto-optical spectra and the overall enhancement of Faraday rotation as compared to the magneto-optical response of magnetite nanoparticle ferrofluids, the influence of the presence of plasmonic gold nanoparticles was established.

The combination of attractive magneto-optical properties with the polymer-/polyelectrolyte-free Layer-by-Layer synthesis protocol that results in (partially) transparent, magnetoplasmonically active thin films makes these materials interesting for further fundamental and applied research.

7.2 Experimental methods

Gold-magnetite nanoparticle multilayers were prepared as detailed in Chapter 4. Samples with 1, 3, 5, 7 and 9 nanoparticle double layers were synthesized.

UV-visible absorbance spectra were measured on a Perkin-Elmer 900 photospectrometer.

Spectral Faraday rotation (FR) and Faraday ellipticity (FE) measurements were done using a LDLS EQ- 99 (Energetiq, USA) broadband light source combined with a spectrometer, a polarizer-analyzer pair, a photo-elastic modulator, a 1 Tesla DC magnet and a photomultiplier tube. The analysis procedure is identical to the one used for the magneto-optical measurements done on iron oxide nanopartice ferrofluids (see Chapter 3 and reference[102]).

7.3 Results & discussion

7.3.1 UV-visible absorbance spectra

UV-visible absorbance spectra of the specific Au-magnetite samples prepared for the magneto-optical experiments are similar as for samples presented in Chapters 4 and 5.

Three resonance features can be observed in the spectra (see Figure 7.1). Around 380nm, the IVCT resonance of magnetite is dominant. Two peak features at around 525nm and 650nm are due to the LSPR and coupled plasmon resonances of the gold nanoparticles in the multilayers. The observed significant red-shift of the plasmon frequency in the synthesized samples from 525nm to 650nm indicates that gold nanoparticles are interacting very strongly and thus very close to each other (see Chapter 5).

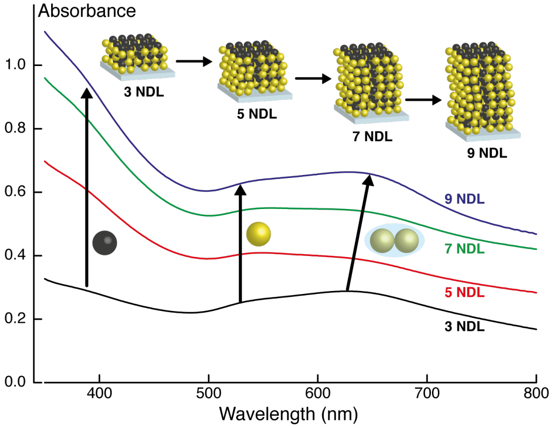

Figure 7.1: UV-visible spectra of the specific Au-mag multilayers. Three spectral regions attributed to magnetite's IVCT, single gold and coupled gold nanoparticles' plasmon resonances show an increase in absorbance when more NDLs are added.

7.3.2 Magneto-optical measurements

Magneto-optical measurements were performed and analyzed similar to those presented in Chapter 3 for magnetite ferrofluids. Faraday rotation and ellipticity data were simultaneously obtained in the spectral range from 400 to 800nm and fitted with Equations 3.4.

This procedure allows to discriminate between the diamagnetic, linear in the applied magnetic field, and superparamagnetic, Langevin, contributions to the total observed magneto-optical signal (see Figure 7.2).

Diamagnetic contributions

Diamagnetic contributions to the total magneto-optical response in the magnetic-plasmonic multilayer samples are, as expected, dominated by the magneto-optical response from the glass substrate. When comparing the diamagnetic contributions of a glass substrate and a 5 NDL multilayer sample, no significant differences can be observed (see Figure 7.2). Purely plasmonic magneto-optical responses are also linear in the applied magnetic field and thus should be observed in the diamagnetic contribution to the total magneto-optical response,

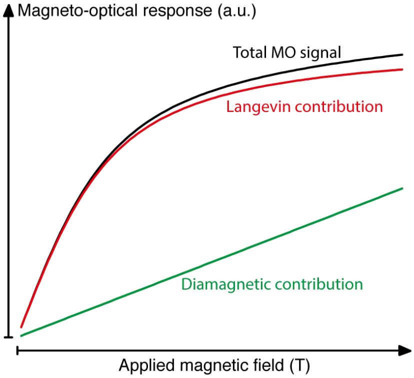

Figure 7.2: The measured magneto-optical response is composed of superparamagnetic Langevin and diamagnetic contributions. Using the correct analytical approach, these contributions can be separated.

which is not the case. This means that the purely plasmonic response must be much smaller than that of the glass substrate. Since the thickness of the glass slide is ±170μm, the volume fraction of glass is orders of magnitudes larger than that of gold nanoparticles, which explains the absence of a diamagnetic plasmonic contribution.

Faraday rotation and ellipticity

The Faraday rotation results exhibit three features of importance (see Figure 7.4). A broad valley feature around 450nm, a crossover point (sign change) around 575nm and a long wavelength tail were observed. When increasing the number of layers and thus the thickness of the samples, the signals at the valley feature around 450nm and the long wavelength tail drastically increase while no wavelength shift of the cross-over point was observed.

Using the thicknesses of the samples as determined by AFM measurements (see Chapter 4), a Verdet constant (in deg.T^{-1}.m^{-1}) could be calculated. For the 7 NDL sample, the Verdet constant was 8.7×10^5deg.T^{-1}.m^{-1} at 400nm and 6.5×10^5deg.T^{-1}.m^{-1} at 800nm, which are large values.

The spectral features present in the Faraday ellipticity results are a peak around 425nm, a broad vally around 575nm and two cross-over points around 475nm and 750nm (see Figure 7.5). Increasing the number of layers increases the

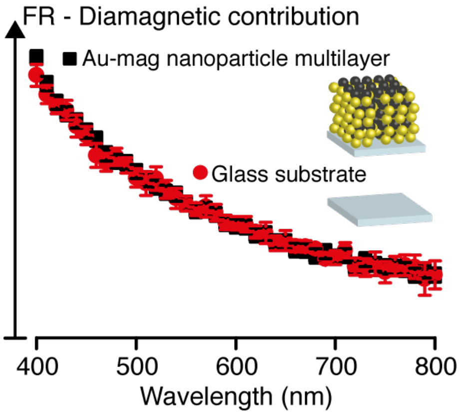

Figure 7.3: When comparing the diamagnetic contributions of a glass substrate and a 5 NDL multilayer sample, no significant differences can be observed.

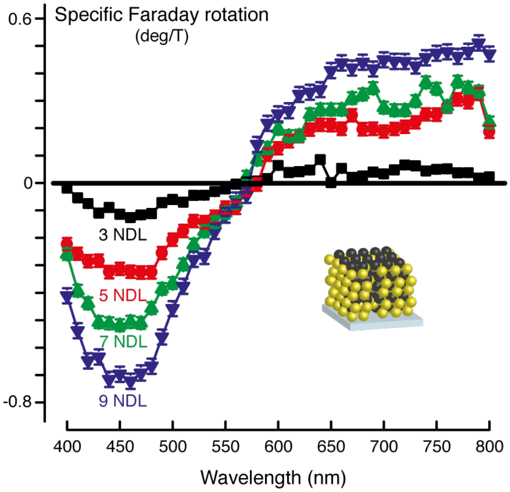

Figure 7.4: Faraday rotation results of the synthesized Au-mag multilayers. Increasing the number of layers in the samples augments the Faraday response at wavelengths of spectral features.

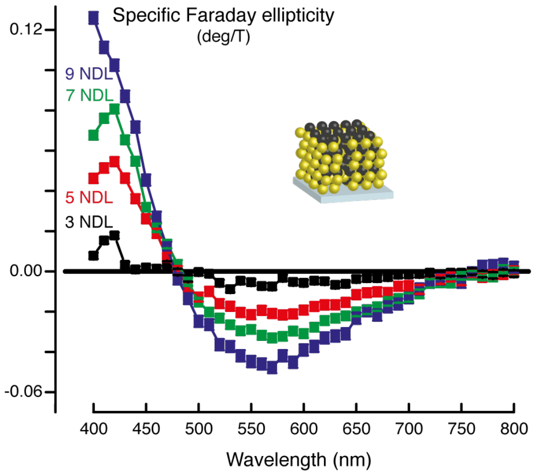

Figure 7.5: Faraday ellipticity results of the synthesized Au-mag multilayers. Increasing the number of layers in the samples augments the Faraday ellipticity responses at wavelengths of spectral features.

response at the positions of the valley and peak features. No wavelength shifts as a function of number of layers for the crossover points are observed.

As for the multilayer thickness and absorbance increase (see Chapter 4 Figure 4.3) the specific Faraday rotation and ellipticity increases linearly as a function of the number of NDLs in the multilayer (see Figure 7.6). This again confirms the Layer-by-Layer nature of the synthesis protocol. Furthermore, as the magneto-optical measurements are dominated by transitions in magnetite, it also confirms the linear relationship between the number of NDLs and the present amount of iron oxide nanoparticles.

Comparison with magnetite ferrofluids

When comparing the Faraday rotation spectra of gold-magnetite multilayers to those of magnetite nanoparticles in a ferrofluid, subtle differences are noticeable (see Chapter 3 and reference[102]). The crossover point is red-shifted, the valley feature is broader and at 550nm wavelength and an extra (small) spectral feature is present due to the LSPR of the gold nanoparticles.

At 400nm and 800nm the Verdet constants of the nanoparticle multilayers

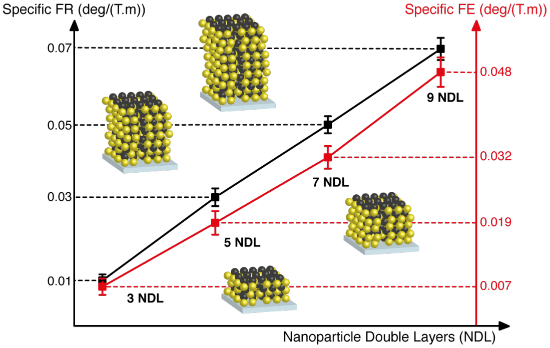

Figure 7.6: Faraday rotation and ellipticity signals increase linearly as a function of the number of NDLs. This confirms the quality of the Layer-by-Layer synthesis method and also proves the linear relationship between the number of NDLs and the amount of iron oxide nanoparticles present.

are 1.6 times larger than for the magnetite ferrofluids, demonstrating the overall enhancement of Faraday rotation by the plasmonic gold component. This enhancement factor agrees with values reported in the literature.[257, 304] While the red-shift of the cross-over point might also be due to the higher local concentration (and thus smaller inter-particle distances) of magnetite nanoparticles in the multilayers,[75] the overall enhancement cannot.

As for the Faraday rotation results, differences are observed when comparing the FE results for gold-magnetite nanoparticle multilayers and magnetite ferrofluids. Both cross-over points are red-shifted from 460nm and 730nm for the ferrofluids to 475nm and 750nm for the nanoparticle multilayers. Also the valley feature becomes much broader. These results again demonstrate the influence of the present gold nanoparticles.

7.4 Conclusions

Faraday rotation and ellipticity responses of gold-magnetite nanoparticle multilayers were measured. No influence of plasmon resonances on the diamagnetic contributions to the magneto-optical response was observed, which was explained by the low volume fraction of gold nanoparticles present as compared to the glass substrate. Both FR and FE increased, just like thickness and absorbance at the plasmon wavelength, linearly with the number of added

NDLs. The FR Verdet constants at 400nm and 800nm were 1.6 times larger for the multilayers as compared to the magnetite ferrofluids, demonstrating plasmonic enhancement effects. For both FR and FE, the cross-over points red-shifted and the main peak feature became broader, pointing to an influence of the presence of metallic gold.

The large magneto-optical responses in such polymer-/polyelectrolyte-free and (partially) transparent Layer-by-Layer deposited thin film sample make them attractive candidates for further research into magnetoplasmonics and for application as e.g. optical isolators.

Chapter 8

General conclusions & perspectives

8.1 General conclusions

Multifunctional magnetic-plasmonic nanoparticle-based materials have many interesting properties that can help to achieve the ambitious goals set for nanotechnology in general. Such materials can be used to address fundamental questions about the interactions between light, matter and magnetism at the nanoscale but also for applications in biomedicine or as optical components.

The aims of the performed work were three-fold. As first, to provide a rational design framework for core-shell magnetic-plasmonic nanoparticles based on their optical properties and focused on biomedical applications. Secondly, to develop a novel synthetic protocol for homogeneous thin film nanoparticle-based magnetic-plasmonic nanoparticles, a variable sample thickness and tuneable optical properties. As last, to characterize the linear, nonlinear and magneto-optical properties of such magnetic-plasmonic nanomaterials.

In Chapter 2 of this dissertation we presented the calculated optical properties of core-shell magnetic-plasmonic nanospheres and nanorods as a function of nanostructure composition, size, and shape with a focus on biomedical applications. Furthermore, the optical characteristics of magnetic-plasmonic nanostructures were quantitatively compared with those of organic dyes applied in biomedical environments. It was calculated that magnetic-plasmonic nanospheres, which can be produced by available chemical synthetic methods, cannot provide efficient tuning of the optical plasmon properties, nor the desired extinction efficiencies, and they are not suited for scattering applications. Core-shell nanorods show much larger extinction cross-section values and the plasmon wavelength shift on a per volume basis than core-shell nanospheres. Furthermore, magnetic-plasmonic nanorods show orders of magnitude larger molar extinction and scattering coefficients than organic materials used in current cancer treatment. With this knowledge it is possible to rationally design and synthesize structures that possess a plasmon band in the advantageous biomedical near-infrared spectral window region and other optical properties as desired for potential application in life sciences.

A novel synthetic protocol for homogeneous thin film nanoparticle-based magnetic-plasmonic nanoparticles without possibly interfering polymers and polyelectrolytes, a variable sample thickness and tuneable optical properties was developed. Furthermore, their linear, nonlinear and magneto-optical properties were measured and analyzed.

The synthesis and functionalization methods together with the results of characterization measurements of magnetite nanoparticles, the magnetic building block of the magnetic-plasmonic assemblies, were described in Chapter 3. Synthesized magnetite nanoparticles showed beneficial saturation magnetization, optical and magneto-optical Faraday rotation and magnetization properties. Straightforward synthesis and functionalization combined with the beneficialproperties showed that these nanoparticles are ideal candidates to be used in magnetic-plasmonic assemblies.

Using short bifunctional molecular linkers, magnetic-plasmonic nanoparticle multilayers based on magnetite and plasmonic nanoparticles were then synthesized on glass substrates. A novel layer-by-layer protocol to obtain homogeneous thin films with a variable sample thickness and tuneable optical properties without the use of polymers or polyelectrolytes was developed for this purpose. Large nanoparticle filling fractions in well-stacked multilayers were obtained. Plasmon resonance wavelengths could be tuned over a very broad spectral range by changing the plasmonic material or the number of added nanoparticle layers. Both thickness and absorbance at the plasmon wavelength increased linearly as a function of added nanoparticle layers. The developed protocol allows to produce large-area high quality magnetic-plasmonic nanocomposites in a straightforward time- and cost-effective way. Synthesis details and characterization results are presented in Chapter 4.

To explain the observed optical properties of the synthesized magnetic-plasmonic nanoparticle multilayers we resorted to theoretical modelling, as detailed in Chapter 5. The optical properties of purely plasmonic and magnetic-plasmonic nanoparticle assemblies were calculated and their dependence on variables such as the medium refractive index, interparticle distance and angle of incidence studied. From the comparison between the calculated and the experimentally obtained spectra we gained more insight in the layer-by-layer synthesis mechanism of these multilayers. The first layer is filled with randomly and spaciously distributed gold nanoparticles. Vacancies left in this layer are converted to attractive pockets by attachment of amino-functionalized iron oxide nanoparticles. These pockets are then filled by newly added Au NPs. As such, with increasing number of NDLs, the multilayer structure becomes not only thicker but also gets a higher filling fraction, increasing the general optical quality of the sample.

Results of both nonlinear optical microscopy and spectroscopy measurements on gold-magnetite nanoparticle multilayers were presented in Chapter 6. Nonlinear optical microscope images confirmed homogeneity of the sample and the generated nonlinear optical signals. Spectroscopic measurements showed large enhancement of the SHG signal but only for wavelengths attributed to near-field coupled plasmon fields. Resonant enhancement for THG was observed at the optical resonance (IVCT) of magnetite. Simultaneous resonance enhancement of both SHG and THG was measured for input wavelengths in the 1100-1300nm range. As such, we synthesized a material that combines and simultaneously enhances second and third order nonlinear optical processes.

Magneto-optical Faraday rotation and ellipticity responses of gold-magnetite nanoparticle multilayers were measured. As a function of the number of layers present in the samples, both FR and FE signals increased linearly. The measured magneto-optical responses were large with Verdet constants up to $9\times \times 10^5$degrees.$T^{-1}.m^{-1}$. Presence of plasmonic gold nanoparticles was manifested as shifts and broadening of spectral features in both FR and FE spectra and an evidenced broadband enhancement of the Faraday rotation response as compared to magnetite ferrofluids.

These results show that the developed Layer-by-Layer synthesis protocol for magnetic-plasmonic nanoparticle multilayers can be used to produce homogeneous thin films of good quality. Advantageous and tuneable optical properties, large magneto-optical responses and the observed resonance enhancements in such polymer-/polyelectrolyte-free and (partially) transparent thin film samples make them attractive candidates for further fundamental research into e.g. magnetoplasmonics and for application in sensors or optical components.

8.2 Perspectives

In this dissertation, first a rational design framework for magnetic-plasmonic core-shell nanoparticles for use in life sciences was presented. Further a novel synthesis protocol for magnetic-plasmonic nanoparticle-based thin films was detailed and the linear, nonlinear and magneto-optical properties measured and analyzed. While the presented results as such are sound and substantial, they also provide a solid foundation for further research. In this section recommendations for future research are described.

For the core-shell magnetic-plasmonic nanoparticles, a first research path would be to experimentally synthesize the core-shell magnetite-gold nanorod structures of which the optical properties were calculated in Chapter 2 and to experimentally characterize their optical properties. If successful, these hybrid nanostructures would be potentially very interesting for biomedical applications such as photothermal therapy. Further, synthesizing and characterizing such particles would also test the validity of the used theoretical calculation (DDA) approach.

For the magnetic-plasmonic nanoparticle multilayers a broad range of possible research activities can be proposed.

As first, to synthesize nanoparticle multilayers based on multiple combinations of plasmonic and magnetite nanoparticle materials. In this dissertation, results were presented for gold-magnetite and silver-magnetite combinations but in principle also any combination of these materials is possible. This would allow to tailor the optical properties of the resulting structure by incorporating definite relative amounts of gold and silver nanoparticles.

Next to gold, silver and magnetite, also nanoparticles of other materials could be incorporated. Magnetite could be replaced by silica to make a non-magnetic analogue while copper or platina nanoparticles could replace silver and gold. By making such combinations, the versatility of the presented synthesis protocol can be exploited to its fullest.

As all these nanoparticle combinations will result in materials with other optical properties in terms of plasmon or other resonances, measuring their optical, nonlinear and magneto-optical is bound to deliver exciting results. As an example, it is expected that when the plasmon resonance spectrally overlaps with the dominant magneto-optical resonance that the magneto-optical response will also be resonantly enhanced. Changing the plasmonic composition of the multilayers from gold to silver or a combination of both would yield detailed insight in this resonance enhancement process.

In addition to measuring ‘static’ linear, nonlinear and magneto-optical properties, concomitantly applying external plasmon-driving optical fields or external magnetic fields in the appropriate techniques could lead to tuneable properties. An example might be to apply a laser beam at the plasmon wavelength of a nanoparticle multilayer while spectrally measuring the magneto-optical properties. It might be possible in this case to modulate the magneto-optical response by modulating the externally applied optical field. Such controllable properties would be a great asset for possible applications.

Another option for introducing additional functionalities in the structure, such as fluorescence or chirality, is through the use of organic molecules. Incorporation of these functionalities is possible in two ways. The first is the use of functional, e.g. chiral, organic linker molecules. Many linker molecules compatible with the presented synthesis protocol are commercially available. The second way is adsorption of functional molecules in the multilayer structure. Because preliminary measurements using dye molecules indicate porosity of the multilayer structures, this method is feasible. Additional functionalities would allow to investigate the relations between the added functionality and the already present properties.

The porosity measured in preliminary experiments, allowing reagents and reaction products to flow through the structures, is also interesting for catalytic processes. Metallic nanoparticles, as also explained in the introductory chapter, show high catalytic activities for a range of reactions. Many reactions, even when supported by a catalyst, require an elevated medium temperature in order to proceed. In magnetic-plasmonic nanoparticle multilayers, this heating can be done locally through plasmonic heating or AC magnetic field loss heating. This would result in a heterogenous catalyst of which the turnover speed can be modulated using external stimuli.

Under influence of femtosecond pulsed laser source plasmonic nanoparticles can be melted together to form conducting wires. In the nanomaterials we synthesize, plasmonic nanoparticle layers are alternated with superparamagnetic iron oxide nanoparticle layers and, possibly, additionally functionalize organic molecules. When melting the plasmonic nanoparticles together, conductors are formed with internally sandwiched magnetically active iron oxide nanoparticles. It would be interesting to investigate whether such laser written wire conductors show magnetorestriction and whether this effect could be modulated by applying external optical or magnetic fields.

A last, a more speculative route for further research might be to investigate whether nanoparticle multilayers that incorporate gold, silver and magnetite nanoparticles exhibit asymmetric transmission. Brown *et al.* showed that plasmonic nanoparticle heterodimers, a combination of e.g. a large and a small gold nanoparticle, show asymmetric scattering properties.[369] In short, this means that forward and backward scattering are not equal in such dimers and that the optical properties for forward and backward directions are thus different. Asymmetric transmission is very useful for the fabrication of e.g. optical isolators.[370–375] Nanoparticle multilayers that incorporate both gold and silver as plasmonic component might be a good candidate for such an effect as gold and silver nanoparticles can form heterodimers.

In conclusion, many interesting routes for future research are available for both the core-shell as the multilayer morphologies.

Appendix A

Supplementary information for Chapter 3

In this appendix we show the supplementary information for Chapter 3 - Synthesis and properties of superparamagnetic iron oxide nanoparticles.

XRD results

In Figure A.1, the diffraction spectrum of dried PEG coated particles is shown together with the diffraction lines as expected for pure magnetite.[333]

VSM results dry functionalized particles

In Figure A.2, the specific magnetization as a function of applied magnetic field at 300K is shown for a sample of dried PEG coated particles as measured by VSM.

FT-IR of n-octylamine and PEG functionalized particles

The FT-IR spectra for newly synthesized and modified nanoparticles are shown in Figures A.3 and A.4. The large peak around 3500cm $^{-1}$ from the n-octylamine coated nanoparticles can be attributed to adsorbed water, the presence of n-octylamine, intermolecular hydrogen bonds between the amine and hydroxyl

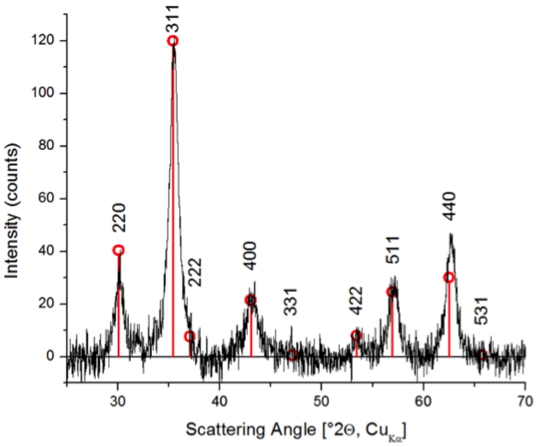

Figure A.1: Background corrected X-ray diffraction pattern of the sample (black curve) together with the diffraction lines (red markers) expected for a powder of pure magnetite.[333] The Miller indices are added to the reflections (space group # 227, Fd-3m)

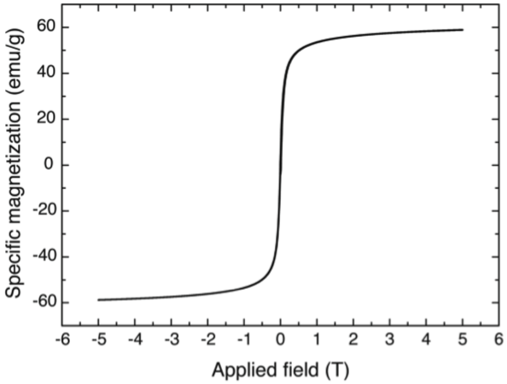

Figure A.2: Specific magnetization as a function of applied magnetic field for a sample of dried PEG coated particles as measured by VSM. As was expected, the sample exhibited superparamagnetic Langevin behavior. Neglible magnetic remanence and coercivity were observed.

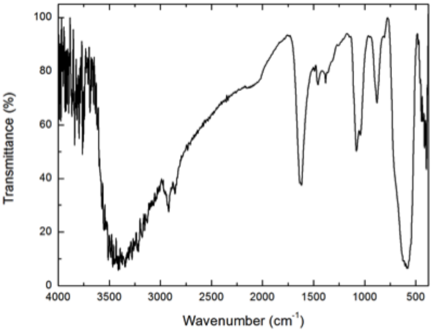

Figure A.3: FTIR spectrum of dried n-octylamine coated nanoparticles diluted in KBr

groups at the surface and possibly free hydroxyl groups at the particle surface. Peaks from n-octylamine are also found at 2931, 2851, 1458, 1080 and 880cm^{-1}, while the absorbance at 2066, 1619 and 1384cm^{-1} is due to small impurities in the KBr used. The peak at 587cm^{-1} arises from Fe-O lattice vibrations in the iron oxide structures and for the modified nanoparticles there is also a possible contribution from Fe-O-Si in this region. In the spectrum of the modified nanoparticles, the noise on the broad peak around 3400cm^{-1} has disappeared; indicating that less amine is present. Peaks for the bonded PEG silane can be found at 1420 and 2920cm^{-1} arising respectively from Si-O-R and CH_2 contributions. Only a very small peak at 1040cm^{-1} can be assigned to Si-O-Si vibrations. Still, some bands also present in the spectrum of n-octylamine, e.g. at 1420 and 2929cm^{-1}, indicate that not all octylamine has been removed. Most peaks due to octylamine overlap with those for PEG silane preventing absolute assignment of peaks to certain substances.

DLS of dispersed PEG functionalized particles

To obtain the hydrodynamic radius, the particle concentration in the DLS experiments must be very low such that they are in a single scattering regime. As very low particle concentrations are difficult to measure, the following procedure was used to make sure the experiments were in the single scattering regime: Step 1, a random low concentration sample was measured. Step 2, the sample in step 1 was diluted by half (by adding equal amount of solvent) and

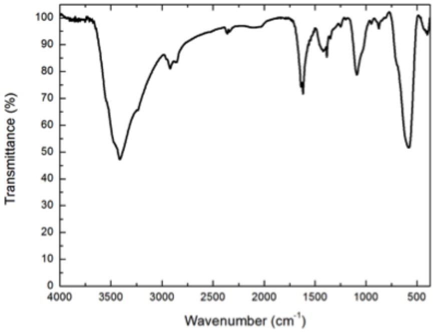

Figure A.4: FTIR spectrum of dried PEG coated nanoparticles diluted in KBr

measured. Step 3, correlations from step 1 and step 2 are compared. The above procedure is repeated until no change in the correlation function is observed between step 1 and 2. Finally, the sample from the last step is diluted by half and the correlation data obtained from this sample is analyzed to obtain the hydrodynamic radius of the particle. Figure A.5 shows the results of the DLS experiments on PEG coated particles dispersed in PEG 400. The time averaged intensity correlation function (g_2(t, q)-1) measured from DLS is fitted with a single exponential function, (g_2(t, q)-1) = $Be^{-\Gamma t}$, where t is the correlation time, B is the value of the auto-correlation function at time t = 0 and Γ=2Dtq^2, where Dt is the translational diffusion, q is the scattering vector. The translational diffusion coefficient is obtained from the slope of Γ versus q^2 plot, as shown in Figure A.5. The effective hydrodynamic radius (R_H) is calculated from Einstein relation $R_H=(k_BT)/(6\pi\eta_0 Dt)$, where k_B is the Boltzmann constant, η_0 is the viscosity of the suspending medium and T the temperature.

VSM results for ferrofluids

The results of hysteresis loop (M vs. H) measurements on ferrofluids with different mass percentages of particles are shown in Figure A.6.

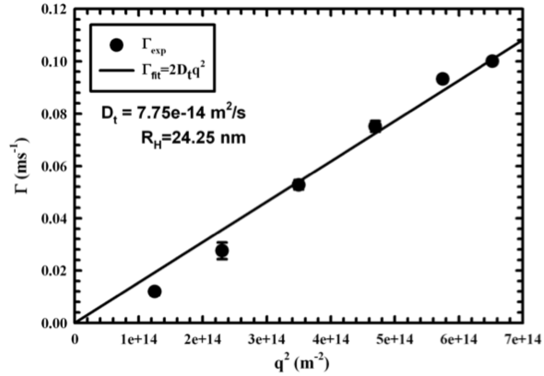

Figure A.5: Inverse relaxation time (Γ) as a function of q^2 obtained from dynamic light scattering

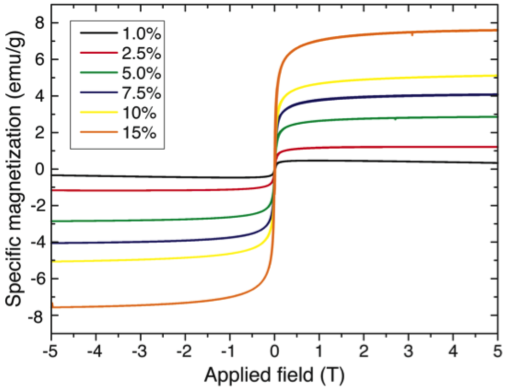

Figure A.6: Hysteresis loop (M vs. H) results on ferrofluids with different mass percentages of particles. As expected for ferrofluids, being an ensemble of non-interacting superparamagnetic nanoparticles, no coercivity or remanent magnetization was observed.

Appendix B

Supplementary information for Chapter 4

In this appendix we show the supplementary information for Chapter 4 - Synthesis of magnetic-plasmonic nanoparticle multilayers.

Gold nanoparticles - UV-visible absorbance spectroscopy

A normalized UV-vis spectrum of a diluted aliquot of the synthesized colloid is shown in Figure B.1. As expected, the localized surface plasmon resonance of the gold nanoparticles was clearly visible with a center location of 530nm. The plasmon resonance band is narrow, indicating that the particles have a narrow size distribution. Furthermore, as no resonance peaks were visible at longer wavelengths, no apparent aggregation of gold nanoparticles had occurred.

Gold nanoparticles - Transmission electron microscopy

A typical image of the gold nanoparticles is shown in Figure B.2. Particles are spherical and particle diameters were estimated using ImageJ and fitted with a lognormal size distribution. Average size was 9.25nm with a standard deviation of 1.31nm.

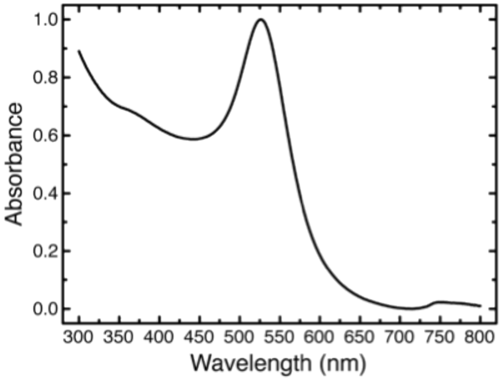

Figure B.1: UV-visible spectrum of the synthesized gold nanoparticles. The localized surface plasmon peak is narrow and located around 530nm.

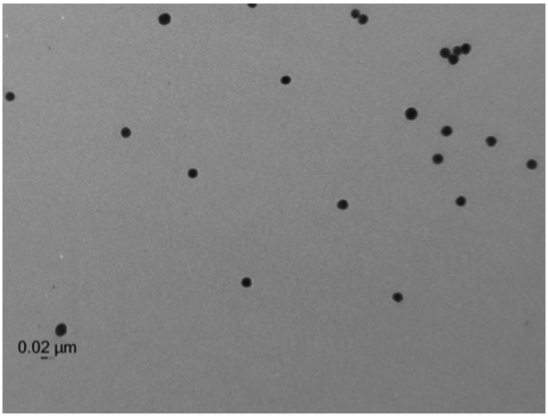

Figure B.2: TEM image of the synthesized gold nanoparticles. Particles are spherical and show a narrow size distribution.

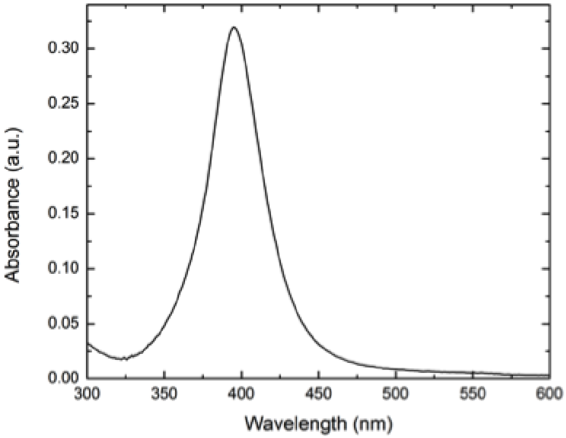

Figure B.3: UV-visible absorbance spectrum of the synthesized Ag colloid. As expected, a surface plasmon resonance can be observed at 400nm wavelength.

Silver nanoparticles - UV-vis-Visible absorbance spectroscopy

A UV-vis spectrum of a diluted aliquot of the synthesized colloid is shown in Figure B.3. The localized surface plasmon resonance of the silver nanoparticles was observed at 400nm. No signs of aggregation or high polydispersity are present.

Silver nanoparticles - Transmission electron microscopy

A TEM image of the synthesized silver nanoparticles in Figure B.4. After measuring the diameters of at least 150 particles and fitting the data with a log-normal distribution, the size of the nanoparticles was determined to be 9.59±0.27nm.

Reproducibility of nanocomposite synthesis

To show the reproducibility of the synthesis procedure, 5 samples with 5 NDLs linked by APTMS molecules were produced. The UV-visible absorbance spectra

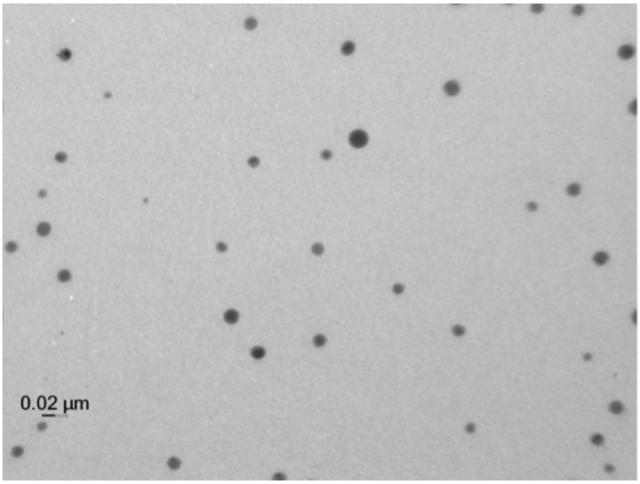

Figure B.4: TEM image of the synthesized Ag nanoparticles. Particles are spherical.

Table B.1: Data on the position (nm) and absorbance value of the coupled gold nanoparticle plasmon as extracted from Figure B.5

Sample nr	Position (nm)	Absorbance
1	634	0.53
2	631	0.51
3	623	0.52
4	622	055
5	621	0.56

of all these samples are shown in Figure B.5. Most important in this analysis is the coupled gold nanoparticle localized surface plasmon (600-700nm). The coupled plasmon is very sensitive to changes in local environment and thus provides an excellent probe for detecting structural differences.

The position (nm) and aborbance values of the 5 samples are shown in Table B.1 below. When taking into account all 5 samples, the position is on average 626±6nm and the absorbance value 0.54±0.02nm. These data prove the reproducibility of the used method.

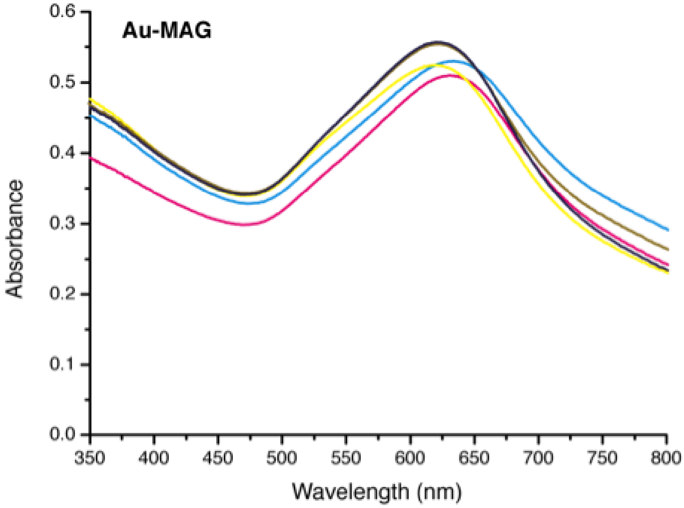

Figure B.5: UV-visible absorbance spectra of 5 samples with 5 NDLs. All samples exhibit very similar spectra.

Optical properties as a function of nanoparticle double layers

A linear relationship can be found for the absorbance at the iron oxide NP IVCT and the AU LSPR and coupled plasmon modes as a function of NDLs. These relationships are shown in Figure B.6.

Angle dependence of optical properties

The optical properties of the composites show, as expected, no strong dependence on the angle of incidence, as shown in Figure B.7. Angle of incidence was varied between 0°(normal incidence) and 45°. Observed variations can be attributed to increased path length in the sample with increasing angle of incidence.

Scanning force microscopy - thickness measurements

The thickness of nanoparticle layers was determined for different samples employing scanning force microscopy (SFM) as a combined manipulation-imaging tool. More specifically, the SFM probe tip was used in a first step to

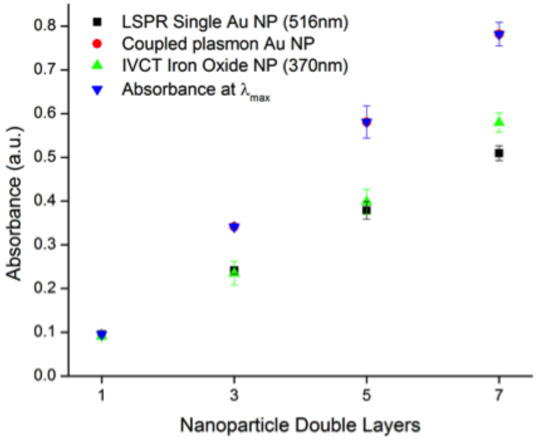

Figure B.6: The absorbance at relevant wavelength increases linearly with the number of NDLs.

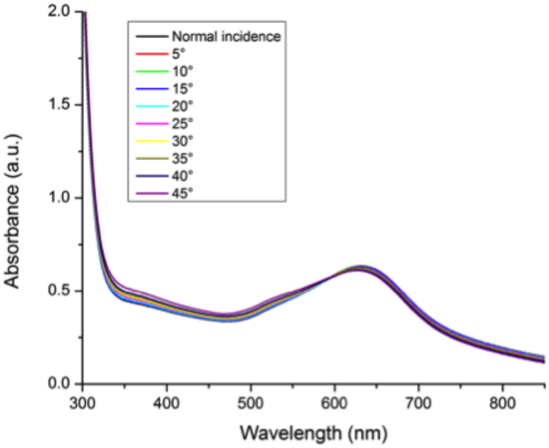

Figure B.7: Angle dependence of the optical properties of the composites. No strong dependence was observed.

Figure B.8: Kymograph representing the topographic changes of a single scan line over time during the tip-induced formation of a scratch in the nanoparticle layer.

remove in a controlled manner the nanoparticle material along a single scan line. To this end, the slow scan axis of the rasterscan is disabled, and the same line is scanned repeatedly in contact mode, with a setpoint deflection value larger as compared to those used for non-destructive imaging. As such, the nanoparticles are mechanically removed by the SFM tip, and this process can be observed in real-time, in the form of a kymograph (Figure B.8). The topographic information of the scan line over time is plotted in 2D, in which one of the spatial axes represents time. The mechanical removal of material was continued up till the point where a flat topography appeared, and no further changes were apparent.

In a second step, the SFM tip was scanned in a raster pattern over the surface area comprising the scratch generated before. Scanning was done in amplitude modulation mode (tapping mode) at a scan angle (angle between the long axis of the cantilever beam and the fast scan axis) of about 45 degrees. As such, the topography of the scratch, as well as the surrounding nanoparticle layer was imaged (Figure B.9).

The entire procedure was repeated three times for every sample; scratches where generated and imaged at different positions on the sample.

For data analysis, the recorded images were corrected for scanner-induced tilt and bow effects of the background. Background correction was performed according to the histogram alignment routine as implemented in SPIP v.6.0.6., and the mean height of the surface was set to zero. For every scratch, the height difference between this sample's mean height (set to zero, see above), and the depth of the scratch was determined at five different positions. According to this procedure, the total thickness of these films was established. The quoted error on the film thickness combines the standard deviation of the measured

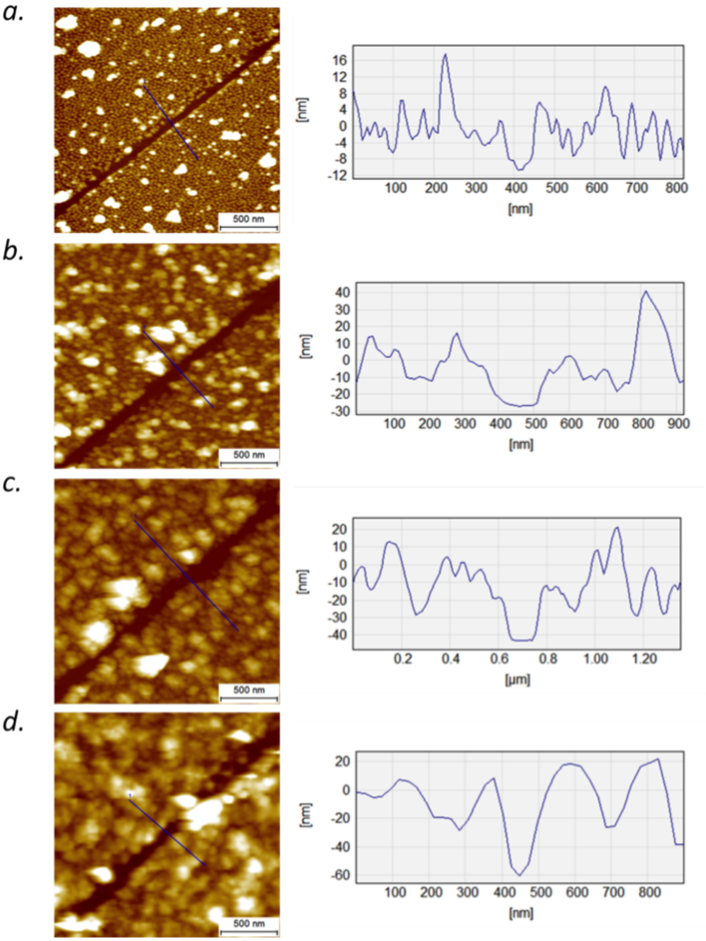

Figure B.9: Imaging and analysis of the scratches for 1 (a), 3 (b), 5 (c) and 7 (d) NDL nanoparticle multilayer.

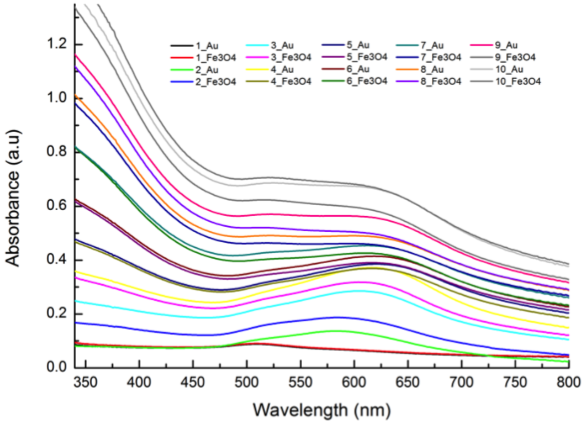

Figure B.10: UV-visible absorbance spectra as a function of added nanoparticle layers show a general gradual increase of absorbance across the recorded spectrum, demonstrating the Layer-by-Layer build-up until 10 NDL.

height of the scratch relative to the mean film height, and the root-mean-square roughness of the intact film.

UV-visible absorbance spectra for Au-magnetite multilayers up to 10 NDL

Measuring the UV-visible absorbance spectra after each addition of a nanoparticle layer shows a gradual general increase of the absorbance for the measured spectra. This demonstrates the Layer-by-Layer build-up of the nanoparticle multilayers.

Silver-magnetite nanocomposites - UV-visible absorbance spectra

The absorbance maximum as a function of added nanoparticle double layers for silver-magnetite nanocomposites is shown below. A linear trend was observed, supporting the reliability of the Layer-by-Layer synthesis method.

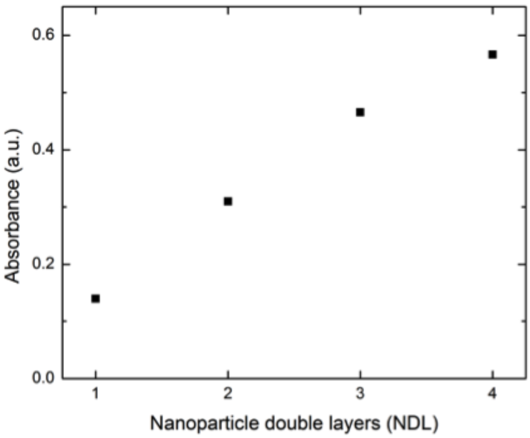

Figure B.11: Absorbance maximum as a function of added nanoparticle double layers for silver-magnetite nanocomposites.

Appendix C

Supplementary information for Chapter 5

In this appendix we show the supplementary information for Chapter 5 - Optical properties of magnetic-plasmonic nanoparticle multilayers.

Supplementary data for the theoretical results

Plasmonic nanoparticle assemblies - Influence of interparticle distance

As stated in the main text, the same trends are observed for the optical properties of a silver nanoparticle dimer as a function of interparticle distance as for a gold dimer. When in close contact, a strongly red-shifted coupled plasmon resonance can be observed. At larger interparticle distances, the plasmon coupling strength reduces and the coupled plasmon resonance diminishes.

Plasmonic nanoparticle assemblies - Influence of the number of coupled plasmonic particles

As for the influence of the interparticle distance on the optical properties, the trends for touching silver nanoparticle chains are the same as for their gold analogues. The dipolar plasmon resonance strongly red-shifts when more

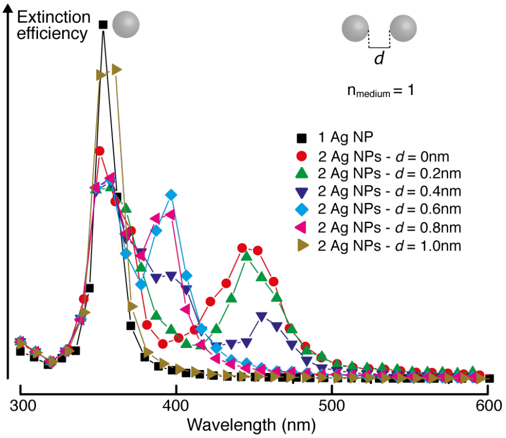

Figure C.1: A red-shifted plasmon resonance band can be observed when 2 Ag NPs are in close contact with each other and plasmonically couple. With increasing interparticle distance, the plasmonic coupling strength decreases, leading to a disappearance of the red-shifted plasmon band.

and more silver nanoparticles are added (see Figure C.2). For the larger silver nanoparticle assemblies also multipolar resonances become visible in the calculated spectrum.

Plasmonic nanoparticle assemblies - Influence of the medium refractive index

The refractive index of the medium in which the assemblies reside has a great influence on the plasmonic coupling strength and thus also on the optical properties of these assemblies.

For 2 contacting gold nanospheres, the dependence of the optical properties on the medium refractive index was shown in Figure 5.5. Here we show that at an interparticle distance of 0.5 in a gold nanoparticle dimer coupling is still possible but only at larger values for the medium refractive index (see Figure C.3). The explanation for this observation can be found in the main text. When the interparticle distance is enlarged to 1nm no near-field coupling occurs, not even at the largest calculated value for the medium refractive index (see Figure C.4).

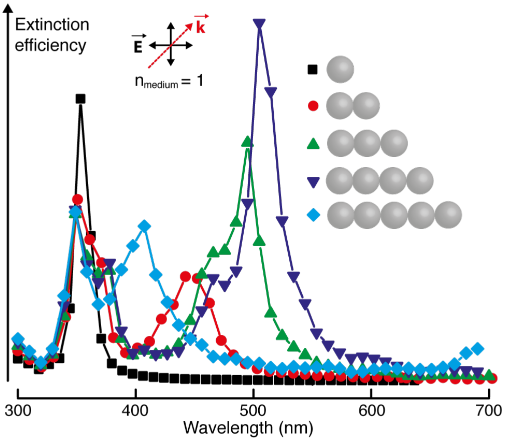

Figure C.2: When Ag NPs are put in a linear chain, the dipolar plasmon resonance strongly red-shifts with increasing numbers of nanoparticles in the chain. Multipolar resonances also become apparent when more than 3 Ag NPs are coupled.

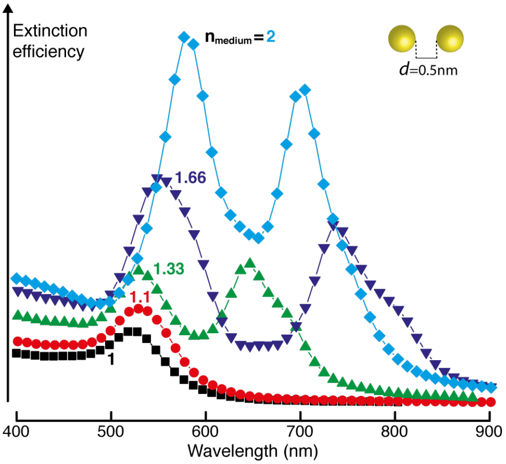

Figure C.3: Two gold nanoparticles at an interparticle distance of 0.5nm show a strong increase of the plasmonic coupling strength with an increasing n_{medium}. While no near-field coupling is present when the medium refractive index is 1, it is very significant at medium refractive index 2.

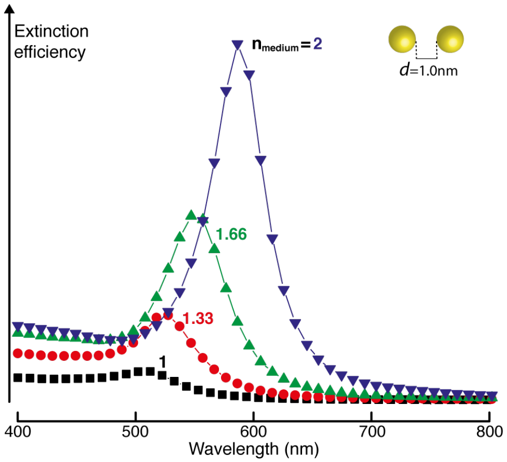

Figure C.4: When the interparticle distance between 2 gold nanospheres is 1nm, no plasmonic coupling is possible even at the largest calculated value for the medium refractive index.

For a Ag nanoparticle dimer, the same statements as for the gold analogue hold true. A dimer of 2 silver nanoparticles in contact shows a great increase of the plasmonic coupling strength with increasing refractive index of the medium (see Figure C.5). When plotting the optical properties as a function of interparticle distance we observe that when this distance is larger than 0.8nm, near-field coupling diminishes (see Figure C.6). This last statement is further demonstrated by calculations that show that at an interparticle distance of 1nm no near-field coupling is possible even at large n_{medium} values (see Figure C.7).

Plasmonic nanoparticle assemblies - Angle dependence of plasmonic near-field coupling

Like for the homodimeric Au-Au nanoparticle dimer, changing the angle of the assembly relative to the incident light beam's propagation direction from perpendicular to parallel reduces the red-shift and the intensity of the red-shifted coupled plasmon resonance (see Figure C.8). This demonstrates a decreased plasmonic coupling strength with increasing deviation from normal incidence. The explanation for this observation using the 'dipole in a constant electric field' model can be found in the main text.

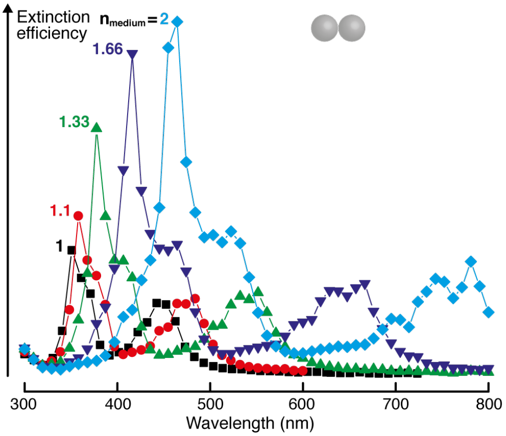

Figure C.5: The plasmonic coupling strength greatly increases with increasing medium refractive index for a pair of touching silver nanospheres in vacuum (medium refractive index = 1). Strongly red-shifted and induced plasmon resonances with increasing n_{medium} prove this statement.

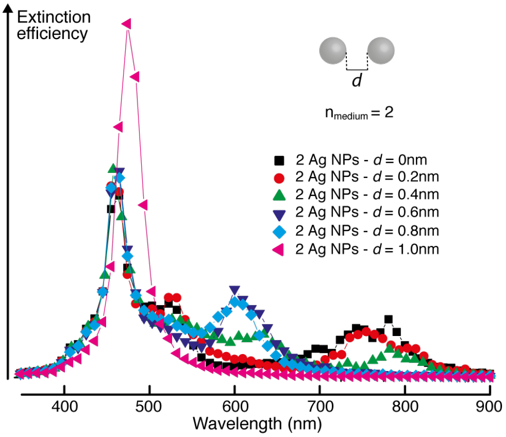

Figure C.6: The increased plasmon coupling strength in a high refractive index medium leads to an extension of the maximal interparticle gap limit for near-field coupling. Near-field coupling between two Ag NPs is possible then up to 0.8nm separation distance.

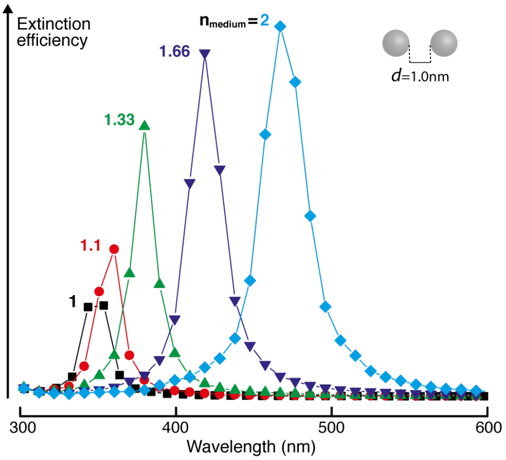

Figure C.7: When the interparticle distance between 2 Ag nanospheres is 1nm, no plasmonic coupling is possible even at the largest calculated value for the medium refractive index.

Plasmonic nanoparticle assemblies - Polarizaton dependence of plasmonic coupling

As stated in the main text, the calculation results for the longitudonal and transversal (along and perpendicular to the assembly's principal axis respectively) polarizations separately for a contacting gold nanoparticle dimer are in agreement with the exciton coupling model. Incident longitudinally polarized light can excite a coupled red-shifted plasmon resonance, while the plasmon resonance for the transversal case is slightly blue-shifted as compared to the LSPR of isolated gold nanoparticles. Although more significant for the longitudinal polarization, the same trends are observed when plotting the results of identical calculations except for using an n_{medium} of 2.

The same statements as made for the gold nanoparticle dimer are also true for the silver analogue. The longitudinally excited plasmon is, as anticipated, responsible for the near-field coupling-induced red-shift of the resonance.

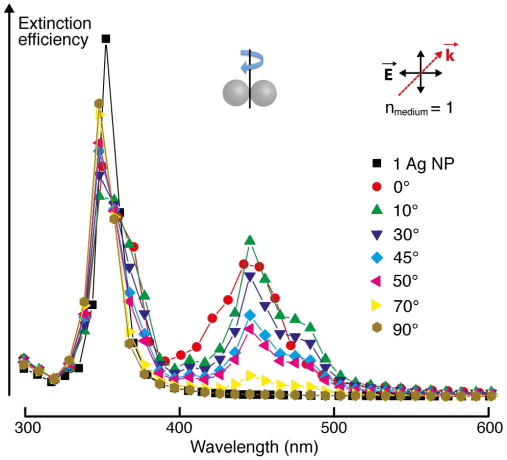

Figure C.8: In agreement with the results for the Au-Au dimer, changing the angle of the Ag-Ag homodimeric assembly's principal axis relative to the propagation direction of the incident light beam from perpendicular to parallel reduces the red-shift and the intensity of the red-shifted coupled plasmon resonance.

Magnetic-plasmonic nanoparticle assemblies - Influence of interparticle distance

The optical properties of Ag-magnetite nanoparticle dimers as a function of distance show that when both nanoparticles are in close contact, the slight increase of the medium refractive index due to the close proximity of the large refractive index material magnetite slightly red-shifts Ag's LSPR (see Figure C.11). Furthermore also a small extinction band at around 380nm is observed due to magnetite's IVCT resonance. When increasing the interparticle distance, no coupling or refractive index effects are observed.

Magnetic-plasmonic nanoparticle multilayers - nanoparticle strings

For magnetite-Ag magnetic-plasmonic nanoparticle strings, the trends for the optical properties as a function of the number of nanoparticles are in general the same as for the magnetite-Au case (see Figures C.12 and C.13). With increasing

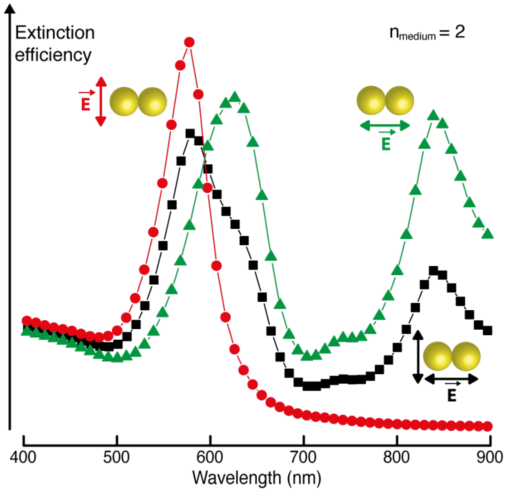

Figure C.9: When calculating the optical properties of a touching gold nanosphere dimer as a function of the polarization of the incident light with n_{medium}=2, we can observe the same trends as for in vacuum (n_{medium}=1) except for a significantly red-shifted longitudinal coupled plasmon resonance.

number of magnetite and silver nanoparticles and thus magnetic-plasmonic nanoparticle string length, the LSPR wavelength of the silver nanoparticles gradually red-shifts with increasing string length and from a certain length on, a second resonance peak is induced. Furthermore, when changing the angle between the incident light and the nanoparticles string from perpendicular to parallel, the calculated extinction spectrum strongly resembles that of a single Ag NP as anticipated.

Model packing structures

As stated in the main text, we consider two types of spherical packing models to simulate the experimental nanoparticle multilayers, the hexagonal close-packing and a more general cubic lattice packing. To use these model structures in calculations and to verify their resemblance with the experimentally measured thicknesses it is important to know how thick these 'virtual' samples are. We calculated the thickness of 1 NDL in both model structures using 10nm spheres and also the increase in thickness for consecutively added NDLs. The used

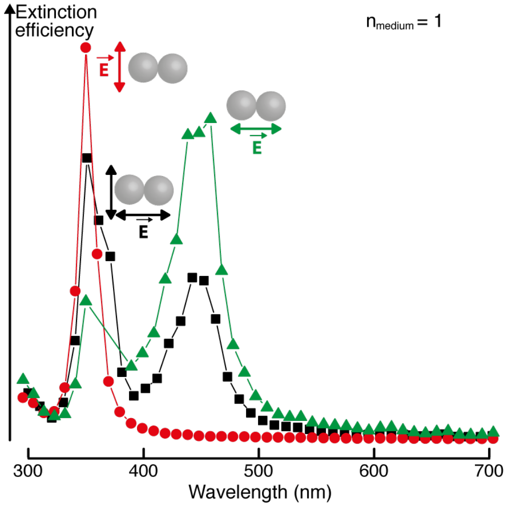

Figure C.10: The red-shifted coupled plasmon resonance is only excited by longitudinally polarized light, while for transversally polarized light a slight blue-shift as compared to the LSPR of single Ag NPs is observed.

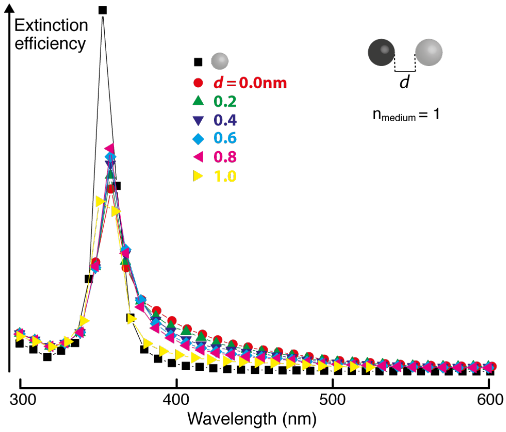

Figure C.11: In the case of a touching Ag-magnetite heterodimer, the LSPR for Ag slightly redshifts due to refractive index effects and a small extinction band at around 380nm arises due to magnetite's IVCT resonance. For larger interparticle distances, no optical coupling or refractive index effects are observed.

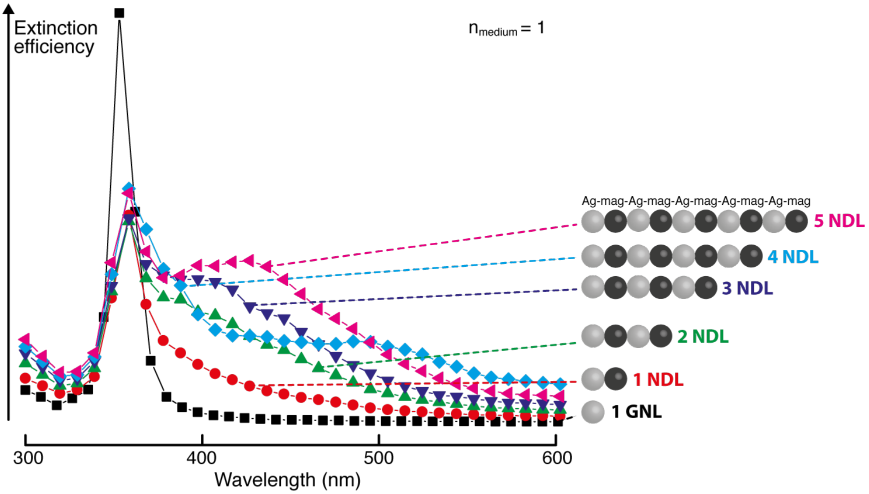

Figure C.12: With increasing number of magnetite and silver nanoparticles and thus magnetic-plasmonic nanoparticle string length, the LSPR wavelength of the silver nanoparticles gradually red-shifts with increasing string length and from a certain length on, a second resonance peak is induced.

geometries are depicted in Figures C.14 and C.15.

Comparing theory and experiment

As for the gold-magnetite 1, 3, 5 and 7 NDL samples, the angle dependence of the experimental UV-visible absorbance spectra for Ag-magnetite and Au-magnetite-Ag-magnetite samples shows that there must be in-plane plasmon coupling present in the sample and this plasmon coupling increases with the number of NDLs.

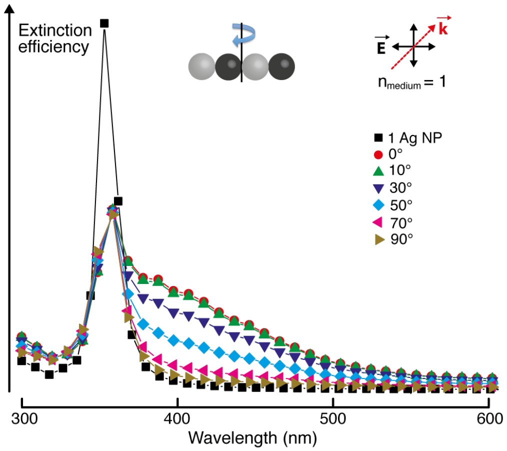

Figure C.13: The newly induced red-shifted resonance for long nanoparticle strings vanishes when the angle between the incident light and the string is changed. This can be explained by a reduced effective length of the string as 'seen' by the incident light. When the light's propagation direction and the interparticle axis are parallel, the plasmon properties resemble those of a single silver nanoparticle. Since the incident light has no electric field component in the propagation directed, this result is anticipated.

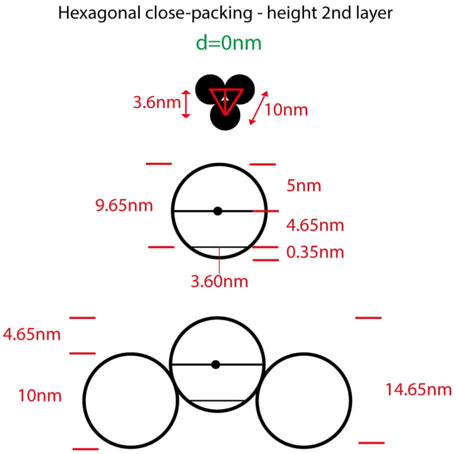

Figure C.14: Based on geometrical considerations, the total thickness of a 1 NDL sample of 10nm particles in a hcp structure is 14.65nm. Adding an extra NDL gives an extra thickness of about 10nm.

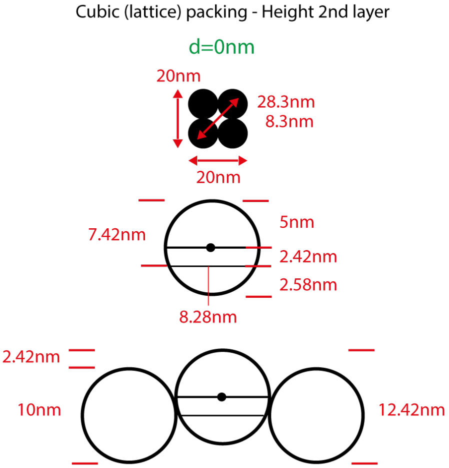

Figure C.15: The total thickness of a 1 NDL sample in a cp structure is 12.41nm, adding an extra NDL results in an increased thickness of 10nm as calculated using geometrical relationships.

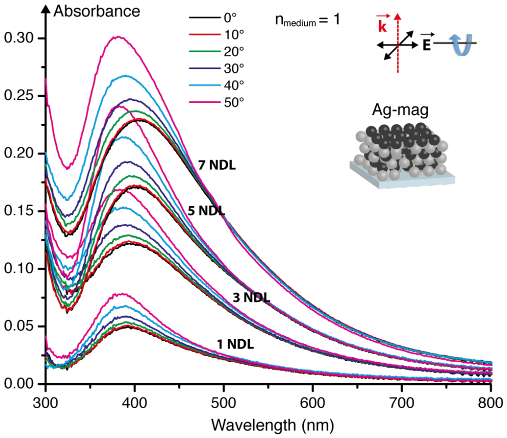

Figure C.16: Experimental optical spectra of 1, 3, 5 and 7 NDL Ag-magnetite samples as a function of angle between the incident light and the sample demonstrate in-plane plasmon coupling and increased structural quality with increasing number of NDLs.

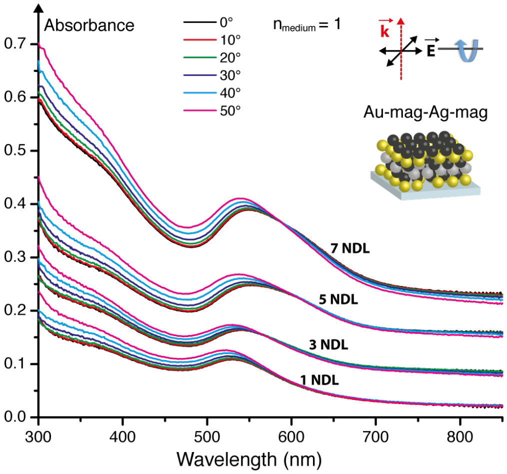

Figure C.17: Experimental optical spectra of 1, 3, 5 and 7 NDL Au-magnetite-Ag-magnetite samples as a function of angle between the incident light and the sample demonstrate in-plane plasmon coupling and increased structural quality with increasing number of NDLs.

Appendix D

Supplementary information for Chapter 6

In this appendix the supplementary information to Chapter 6, which are 4 figures showing the results of third harmonic generation measurements at 1300nm and 1500nm.

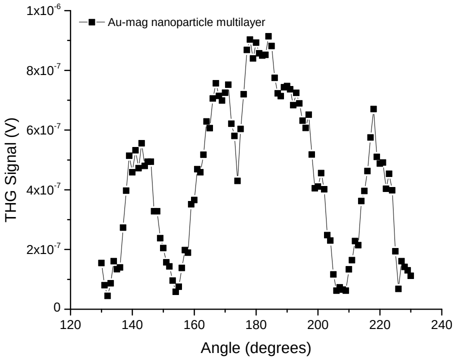

Figure D.1: THG signal as a function of angle for the Au-mag nanoparticle multilayer on a glass substrate for fundamental wavelength 1300nm.

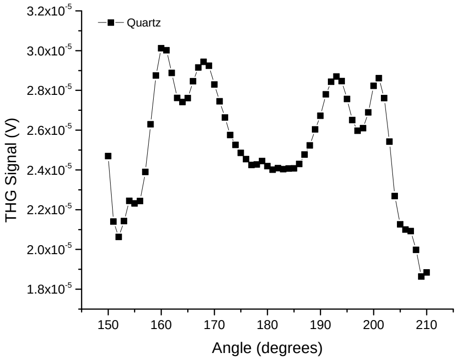

Figure D.2: THG signal as a function of angle for the quartz reference for fundamental wavelength 1300nm.

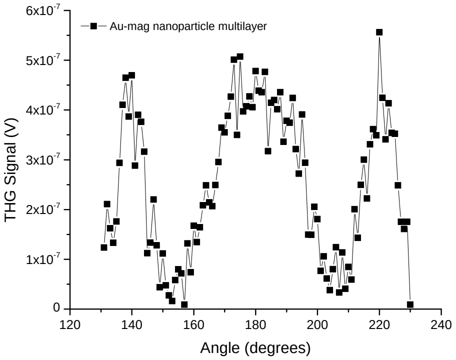

Figure D.3: THG signal as a function of angle for the Au-mag nanoparticle multilayer on a glass substrate for fundamental wavelength 1500nm.

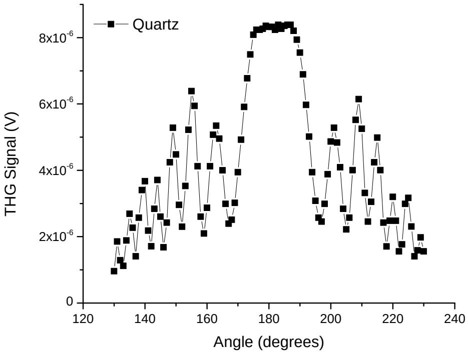

Figure D.4: THG signal as a function of angle for the quartz reference for fundamental wavelength 1500nm.

Bibliography

[1] OECD, NNI, *Symposium on Assessing the Economic Impact of Nanotechnology.* Technical report, OECD, NNI, Washington, USA (2012).

[2] ObservatoryNANO, *European nanotechnology landscape report.* Technical report, European Community (2011).

[3] Y. Dang, Y. Zhang, L. Fan, et al., *Trends in worldwide nanotechnology patent applications: 1991 to 2008.* Journal of Nanoparticle Research **12** (3), 687–706 (2010).

[4] H. Chen, M. C. Roco, X. Li, et al., *Trends in nanotechnology patents.* Nature Nanotechnology **3**, 123–125 (2008).

[5] B. F. Johnson, *Nanoparticles in catalysis.* Topics in Catalysis **24**, 147–159 (2003).

[6] Y. Mikami, A. Dhakshinamoorthy, M. Alvaro, et al., *Catalytic activity of unsupported gold nanoparticles.* Catalysis Science & Technology **3** (1), 58 (2013).

[7] X. Meng, F.-S. Xiao, *Green routes for synthesis of zeolites.* Chemical reviews **114** (2), 1521–1543 (2014).

[8] G. A. Ozin, A. Arsenault, *Nanochemistry: A Chemical Approach to Nanomaterials.* The Royal Society of Chemistry, Cambridge, UK, 2nd edition (2009).

[9] A. A. Popov, S. Yang, L. Dunsch, *Endohedral fullerenes.* Chemical Reviews **113** (8), 5989–6113 (2013).

[10] M. Terrones, *Synthesis, Properties, and Applications of Carbon Nanotubes.* Annual Review of Materials Research **33** (1), 419–501 (2003).

[11] A. K. Geim, *Graphene: status and prospects.* Science **324** (5934), 1530–1534 (2009).

[12] R. P. Goodman, I. A. T. Schaap, C. F. Tardin, et al., *Rapid chiral assembly of rigid DNA building blocks for molecular nanofabrication.* Science **310** (5754), 1661–1665 (2005).

[13] Y. Yamada, M.-a. Okada, K. Tanaka, *Repetitive stepwise rotaxane formation toward programmable molecular arrays.* Chemical Communications **49** (94), 11053–11055 (2013).

[14] P. Zrazhevskiy, M. Sena, X. Gao, *Designing multifunctional quantum dots for bioimaging, detection, and drug delivery.* Chemical Society Reviews **39** (11), 4326–43254 (2010).

[15] A. K. Gupta, M. Gupta, *Synthesis and surface engineering of iron oxide nanoparticles for biomedical applications.* Biomaterials **26** (18), 3995–4021 (2005).

[16] C. N. R. Rao, G. U. Kulkarni, P. J. Thomas, et al., *Metal nanoparticles and their assemblies.* Chemical Society Reviews **29** (1), 27–35 (2000).

[17] P. K. Jain, X. Huang, I. H. El-Sayed, et al., *Review of some interesting surface plasmon resonance-enhanced properties of noble metal nanoparticles and their applications to biosystems.* Plasmonics **2** (3), 107–118 (2007).

[18] M. Altissimo, *E-beam lithography for micro-nanofabrication.* Biomicrofluidics **4** (2), 2–7 (2010).

[19] J. Fischer, M. Wegener, *Three-dimensional optical laser lithography beyond the diffraction limit.* Laser & Photonics Reviews **7** (1), 22–44 (2013).

[20] H. Zeng, D. Martella, P. Wasylczyk, et al., *High-Resolution 3D Direct Laser Writing for Liquid-Crystalline Elastomer Microstructures.* Advanced Materialsaterials (2014).

[21] I. Freestone, N. Meeks, M. Sax, et al., *The Lycurgus Cup - A Roman Nanotechnology.* Gold Bulletin **40** (4), 270–277 (2007).

[22] A. Medalia, *Effect of Carbon Black on Dynamic Properties of Rubber Vulcanizates.* Rubber Chemistry and Technology **51** (3), 437–523 (1978).

[23] R. Merget, T. Bauer, H. Küpper, et al., *Health hazards due to the inhalation of amorphous silica.* Archives of Toxicology **75** (11-12), 625–634 (2002).

[24] A. Cecconello, C.-H. Lu, J. Elbaz, et al., *Au nanoparticle/DNA rotaxane hybrid nanostructures exhibiting switchable fluorescence properties.* Nano Letters **13** (12), 6275–6280 (2013).

[25] R. Schreiber, N. Luong, Z. Fan, et al., *Chiral plasmonic DNA nanostructures with switchable circular dichroism.* Nature Communications **4**, 2948 (2013).

[26] P. T. Yin, T.-H. Kim, J.-W. Choi, et al., *Prospects for graphene-nanoparticle-based hybrid sensors.* Physical Chemistry Chemical Physicss **15** (31), 12785–12799 (2013).

[27] P. B. Santhosh, N. P. Ulrih, *Multifunctional superparamagnetic iron oxide nanoparticles: promising tools in cancer theranostics.* Cancer Letters **336** (1), 8–17 (2013).

[28] S. Y. Chou, P. R. Krauss, P. J. Renstrom, *Imprint lithography with 25-nanometer resolution.* Science **272** (5258), 85–87 (1996).

[29] K. Jain, C. Willson, B. Lin, *Ultrafast deep UV Lithography with excimer lasers.* IEEE Electron Device Letters **3** (3), 53–55 (1982).

[30] Y. Vladimirsky, A. Bourdillon, *Demagnification in proximity x-ray lithography and extensibility to 25 nm by optimizing Fresnel diffraction.* Journal of Physics D: Applied Physics **32**, L114–L118 (1999).

[31] S. Khizroev, D. Litvinov, *Focused-ion-beam-based rapid prototyping of nanoscale magnetic devices.* Nanotechnology **15** (3), R7–R15 (2004).

[32] S. Reyntjens, R. Puers, *A review of focused ion beam applications in microsystem technology.* Journal of Micromechanics and Microengineering **11** (4), 287–300 (2001).

[33] J. A. van Kan, A. A. Bettiol, F. Watt, *Three-dimensional nanolithography using proton beam writing.* Applied Physics Letters **83** (8), 1629–1631 (2003).

[34] R. D. Piner, J. Zhu, F. Xu, et al., *"Dip-pen" nanolithography.* Science **283** (5402), 661–663 (1999).

[35] F.-h. Lin, R.-a. Doong, *Bifunctional Au-Fe3O4 Heterostructures for Magnetically Recyclable Catalysis of Nitrophenol Reduction.* Journal of Physical Chemistry C **115**, 6591–6598 (2011).

[36] R. Ghosh Chaudhuri, S. Paria, *Core/shell nanoparticles: classes, properties, synthesis mechanisms, characterization, and applications.* Chemical Reviews **112** (4), 2373–433 (2012).

[37] D. Siegwart, K. Whitehead, *Combinatorial synthesis of chemically diverse core-shell nanoparticles for intracellular delivery.* Proceedings of the National Academy of Sciences of the United States of America **108** (32), 12996–13001 (2011).

[38] Y. Yang, Y. Wang, *Polymeric core-shell nanoparticles for therapeutics.* Clinical and experimental Pharmacology and Physiology **33**, 557–562 (2006).

[39] J. Wang, X. C. Zeng, *Nanoscale Magnetic Materials and Applications.* Springer US, Boston, MA (2009).

[40] W. Schärtl, *Current directions in core-shell nanoparticle design.* Nanoscale **2** (6), 829–43 (2010).

[41] S. Wei, Q. Wang, J. Zhu, et al., *Multifunctional composite core-shell nanoparticles.* Nanoscale **3** (11), 4474–502 (2011).

[42] M. Bloemen, W. Brullot, T. T. Luong, et al., *Improved functionalization of oleic acid-coated iron oxide nanoparticles for biomedical applications.* Journal of Nanoparticle Research **14** (9), 1100 (2012).

[43] W. Brullot, N. Reddy, J. Wouters, et al., *Versatile ferrofluids based on polyethylene glycol coated iron oxide nanoparticles.* Journal of Magnetism and Magnetic Materials **324** (11), 1919–1925 (2012).

[44] P. Tartaj, M. del Puerto Morales, S. Veintemillas-Verdaguer, et al., *The preparation of magnetic nanoparticles for applications in biomedicine.* Journal of Physics D: Applied Physics **36** (13), 182–197 (2003).

[45] M. Bloemen, D. Debruyne, P.-J. Demeyer, et al., *Catechols as ligands for CdSe-ZnS quantum dots.* RSC Advances **4**, 10208–10211 (2014).

[46] K. S. Kumar, V. B. Kumar, P. Paik, *Recent advancement in functional core-shell nanoparticles of polymers: synthesis, physical properties, and applications in medical biotechnology.* Journal of Nanoparticles **2013**, 1–24 (2013).

[47] D. Bochicchio, R. Ferrando, *Morphological instability of core-shell metallic nanoparticles.* Physical Review B **87** (16), 165435 (2013).

[48] R. K. Iler, *Multilayers of colloidal particles.* Journal of Colloid and Interface Science **594** (21), 569–594 (1966).

[49] G. Decher, *Multilayer thin films - sequential assembly of nanocomposite materials.* Wiley-VCH, Weinheim, Germany, 2nd edition (2012).

[50] Y.-H. Su, Y.-F. Ke, S.-L. Cai, et al., *Surface plasmon resonance of layer-by-layer gold nanoparticles induced photoelectric current in environmentally-friendly plasmon-sensitized solar cell.* Light: Science & Applications **1** (6), e14 (2012).

[51] S. S. Qureshi, Z. Zheng, M. I. Sarwar, et al., *Nanoprotective Layer-by-Layer coatings with epoxy components for enhancing abrasion resistance: toward robust multimaterial nanoscale films.* ACS Nano **7** (10), 9336–9344 (2013).

[52] M. Lefort, G. Popa, E. Seyrek, et al., *Spray-on organic/inorganic films: a general method for the formation of functional nano- to microscale coatings.* Angewandte Chemie (International ed. in English) **122** (52), 10308–10311 (2010).

[53] S. W. Morton, K. P. Herlihy, K. E. Shopsowitz, et al., *Scalable manufacture of built-to-order nanomedicine: spray-assisted layer-by-layer functionalization of PRINT nanoparticles.* Advanced Materials **25** (34), 4707–4713 (2013).

[54] N. C. Vieira, A. Figueiredo, A. D. Faceto, et al., *Dendrimers/TiO2 nanoparticles layer-by-layer films as extended gate FET for pH detection.* Sensors and Actuators B: Chemical **169**, 397–400 (2012).

[55] D. Dontsova, V. Keller, N. Keller, et al., *Photocatalytically active polyelectrolyte/nanoparticle films for the elimination of a model odorous gas.* Macromolecular Rapid Communications **32** (15), 1145–1149 (2011).

[56] K. C. Krogman, N. S. Zacharia, D. M. Grillo, et al., *Photocatalytic Layer-by-Layer Coatings for Degradation of Acutely Toxic Agents.* Chemistry of Materials **20** (5), 1924–1930 (2008).

[57] P. J. Rivero, J. Goicoechea, A. Urrutia, et al., *Multicolor Layer-by-Layer films using weak polyelectrolyte assisted synthesis of silver nanoparticles.* Nanoscale Research Letters **8** (1), 438 (2013).

[58] V. dos Santos, M. dos Santos, C. Guadalupe de Jesus, et al., *The role of a layer-by-layer film containing Pt nanoparticle on the performance of a glucose enzymatic biosensor.* International Journal of Electrochemical Science **8**, 10601–10620 (2013).

[59] K. K. Lee, C. H. Ahn, *Superhydrophilic multilayer silica nanoparticle networks on a polymer microchannel using a spray layer-by-layer nanoassembly method.* ACS Applied Materials & Interfaces **5** (17), 8523–8530 (2013).

[60] F. Aliev, M. Correa-Duarte, A. Mamedov, et al., *Layer-by-Layer assembly of core-shell magnetite nanoparticles : effect of silica coating on interparticle interactions and magnetic properties.* Advanced Materials **11** (12), 1006–1010 (1999).

[61] A. Mamedov, N. Kotov, *Free-standing layer-by-layer assembled films of magnetite nanoparticles.* Langmuir **16**, 5530–5533 (2000).

[62] B. P. Pichon, P. Louet, O. Felix, et al., *Magnetotunable hybrid films of stratified iron oxide nanoparticles assembled by the Layer-by-Layer technique.* Chemistry of Materials **23**, 3668–3675 (2011).

[63] S. W. Morton, N. J. Shah, M. a. Quadir, et al., *Osteotropic therapy via targeted Layer-by-Layer nanoparticles.* Advanced Healthcare Materials (2013).

[64] B. DeLacy, W. Qiu, M. Soljačić, *Layer-by-layer self-assembly of plexcitonic nanoparticles.* Optics Express **21** (16), 4536–4537 (2013).

[65] H. I. Labouta, M. Schneider, *Tailor-made biofunctionalized nanoparticles using layer-by-layer technology.* International Journal of Pharmaceutics **395** (1-2), 236–242 (2010).

[66] G. B. Sukhorukov, E. Donath, H. Lichtenfeld, et al., *Layer-by-layer self assembly of polyelectrolytes on colloidal particles.* Colloids and Surfaces A: Physicochemical and Engineering Aspects **137**, 253–266 (1998).

[67] M. Willard, L. Kurihara, E. Carpenter, et al., *Chemically prepared magnetic nanoparticles.* International Materials Reviews **49** (3-4), 125–170 (2004).

[68] M. Bloemen, S. Vandendriessche, V. Goovaerts, et al., *Synthesis and Characterization of Holmium-Doped Iron Oxide Nanoparticles.* Materials **7** (2), 1155–1164 (2014).

[69] T. Indira, P. Lakshmi, *Magnetic nanoparticles - A review.* International Journal of Pharmaceutical Sciences and Nanotechnology **3** (3), 1035–1042 (2010).

[70] S. P. Gubin, Y. a. Koksharov, G. B. Khomutov, et al., *Magnetic nanoparticles: preparation, structure and properties.* Russian Chemical Reviews **74** (6), 489–520 (2005).

[71] A.-H. Lu, E. L. Salabas, F. Schüth, *Magnetic nanoparticles: synthesis, protection, functionalization, and application.* Angewandte Chemie (International ed. in English) **46** (8), 1222–1244 (2007).

[72] N. A. Frey, S. Peng, K. Cheng, et al., *Magnetic nanoparticles: synthesis, functionalization, and applications in bioimaging and magnetic energy storage.* Chemical Society reviews **38** (9), 2532–42 (2009).

[73] W. F. J. Fontijn, P. J. V. D. Zaag, M. A. C. Devillers, et al., *Optical and magneto-optical polar Kerr spectra of Fe3O4 and Mg2+-orAl3+-substituted Fe3O4.* Physical Review B **56** (9), 5432–5442 (1997).

[74] D. A. Smith, Y. A. Barnakov, B. L. Scott, et al., *Magneto-optical spectra of closely spaced magnetite nanoparticles.* Journal of Applied Physics **97** (10), 10M504 (2005).

[75] Y. Barnakov, B. L. Scott, V. Golub, et al., *Spectral dependence of Faraday rotation in magnetite-polymer nanocomposites.* Journal of Physics and Chemistry of Solids **65** (5), 1005–1010 (2004).

[76] H. a. Garcia, R. P. Melo, A. Azevedo, et al., *Optical and structural characterization of iron oxide and cobalt oxide thin films at 800 nm.* Applied Physics B **111** (2), 313–321 (2013).

[77] T. Hashimoto, T. Yamada, T. Yoko, *Third-order nonlinear optical properties of sol–gel derived alpha-Fe2O3, gamma-Fe2O3, and Fe3O4 thin films.* Journal of Applied Physics **80** (6), 3184–3190 (1996).

[78] Z. Liao, H. Wang, R. Lv, et al., *Polymeric liposomes-coated superparamagnetic iron oxide nanoparticles as contrast agent for targeted magnetic resonance imaging of cancer cells.* Langmuir **27** (6), 3100–3105 (2011).

[79] B. Cullity, C. Graham, *Introduction to magnetic materials.* John Wiley & Sons, Inc., New Jersey, second edition (2009).

[80] M. Andrés Vergés, R. Costo, a. G. Roca, et al., *Uniform and water stable magnetite nanoparticles with diameters around the monodomain–multidomain limit.* Journal of Physics D: Applied Physics **41** (13), 134003 (2008).

[81] A. S. Teja, P.-Y. Koh, *Synthesis, properties, and applications of magnetic iron oxide nanoparticles.* Progress in Crystal Growth and Characterization of Materials **55** (1-2), 22–45 (2009).

[82] P. Ramdohr, *The Ore Minerals and Their Intergrowths.* Pergamon Press, Oxford, third edition (1969).

[83] C. Kittel, *Introduction to Solid State Physics.* John Wiley & Sons, Inc., eight edition (2004).

[84] R. Vandenberghe, C. Barrero, G. da Costa, et al., *Mössbauer characterization of iron oxides and (oxy) hydroxides: the present state of the art.* Hyperfine Interactions **126**, 247–259 (2000).

[85] A. Tavakoli, M. Sohrabi, A. Kargari, *A review of methods for synthesis of nanostructured metals with emphasis on iron compounds.* Chemical Papers **61** (3), 151–170 (2007).

[86] K. Shalini, G. N. Subbanna, S. Chandrasekaran, et al., *Thin films of iron oxide by low pressure MOCVD using a novel precursor : tris (t-butyl-3-oxo-butanoato) iron (III).* Thin Solid Films **424**, 56–60 (2003).

[87] R. Alexandrescu, I. Morjan, I. Voicu, et al., *Combining resonant/non-resonant processes : Nanometer-scale iron-based material preparation via CO2 laser pyrolysis.* Applied Surface Science **248**, 138–146 (2005).

[88] C. Lin, Y. Chu, S. Wang, *Magnetic properties of magnetite nanoparticles prepared by mechanochemical reaction.* Materials Letters **60** (4), 447–450 (2006).

[89] X. Cao, R. Prozorov, Y. Koltypin, et al., *Synthesis of pure amorphous Fe2O3.* Journal of Materials Research **12** (2), 402–406 (1997).

[90] M. Pósfai, B. M. Moskowitz, B. Arató, et al., *Properties of intracellular magnetite crystals produced by Desulfovibrio magneticus strain RS-1.* Earth and Planetary Science Letters **249** (3-4), 444–455 (2006).

[91] Z. Wang, Y. Liu, Z. Zhang (Editors) *Handbook of Nanophase and Nanostructured Materials.* Kluwer Academic Publishers Group, New York, USA (2003).

[92] S. Ammar, A. Helfen, N. Jouini, et al., *Magnetic properties of ultrafine cobalt ferrite particles synthesized by hydrolysis in a polyol medium.* Journal of Materials Chemistry **11** (1), 186–192 (2001).

[93] W. Cai, J. Wan, *Facile synthesis of superparamagnetic magnetite nanoparticles in liquid polyols.* Journal of Colloid and Interface Science **305** (2), 366–370 (2007).

[94] G. F. Goya, T. S. Berquo, F. C. Fonseca, et al., *Static and dynamic magnetic properties of spherical magnetite nanoparticles.* Journal of Applied Physics **94** (5), 3520–3528 (2003).

[95] O. Palchik, J. Zhu, A. Gedanken, *Microwave assisted preparation of binary oxide nanoparticles.* Journal of Materials Chemistry **10** (5), 1251–1254 (2000).

[96] R. Serway, J. J. Jewett, *Physics for Scientists and Engineers with Modern Physics.* Thomson Brooks/Cole, sixt edition (2004).

[97] M. Knobel, W. Nunes, L. Socolovsky, et al., *Superparamagnetism and other magnetic features in granular materials: A review on ideal and real systems.* Journal of Nanoscience and Nanotechnology **8**, 2836–2857 (2008).

[98] C. Kittel, *Theory of the structure of ferromagnetic domains in films and small particles.* Physical Review **70** (11-12), 965–971 (1946).

[99] R. Kodama, A. Berkowitz, *Atomic-scale magnetic modeling of oxide nanoparticles.* Physical Review B **59** (9), 6321–6336 (1999).

[100] C. Scherer, A. Figueiredo Neto, *Ferrofluids: properties and applications.* Brazilian Journal of Physics **35** (3), 718–727 (2005).

[101] D. Kim, W. Voit, W. Zapka, et al., *Biomedical application of ferrofluids containing magnetite nanoparticles. In MRS Proceedings*, Y8.32 (2001).

[102] W. Brullot, N. Reddy, J. Wouters, et al., *Versatile ferrofluids based on polyethylene glycol coated iron oxide nanoparticles.* Journal of Magnetism and Magnetic Materials **324** (11), 1919–1925 (2012).

[103] R. Cannon, *Solvent effects on intervalence charge transfer.* Chemical Physics Letters **49** (2), 299–304 (1977).

[104] D. M. D'Alessandro, F. R. Keene, *Current trends and future challenges in the experimental, theoretical and computational analysis of intervalence charge transfer (IVCT) transitions.* Chemical Society Reviews **35** (5), 424–440 (2006).

[105] D. M. D'Alessandro, F. R. Keene, *Intervalence charge transfer (IVCT) in trinuclear and tetranuclear complexes of iron, ruthenium, and osmium.* Chemical Reviews **106** (6), 2270–2298 (2006).

[106] T. Verbiest, K. Clays, V. Rodriguez, *Second-order Nonlinear Optical Characterization Techniques: An Introduction.* CRC Press, Boca Raton, FL (2009).

[107] Y. Shen, *The Principles of Nonlinear optics.* John Wiley & Sons, Inc., New York, USA (1984).

[108] R. W. Boyd, *Nonlinear Optics.* Academic Press, Inc, San Diego, USA (1992).

[109] M. K. Vanbel, V. K. Valev, B. Vincent, et al., *Second-harmonic generation reveals the oxidation steps in semiconductor processing.* Journal of Applied Physics **111** (6), 064504 (2012).

[110] S. Vandendriessche, V. K. Valev, T. Verbiest, *Characterization of magnetization-induced second harmonic generation in iron oxide polymer nanocomposites.* Applied Optics **51** (2), 209–213 (2012).

[111] V. K. Valev, A. V. Silhanek, W. Gillijns, et al., *Asymmetric second harmonic generation in chiral optical metamaterials.* Proceedings of SPIE **7711**, 77111S1–6 (2010).

[112] V. K. Valev, M. Gruyters, a. Kirilyuk, et al., *Influence of quadratic contributions in magnetization-induced second harmonic generation studies of magnetization reversal.* Physica Status Solidi (B) **242** (15), 3027–3031 (2005).

[113] M. A. van der Veen, V. K. Valev, T. Verbiest, et al., *In situ orientation-sensitive observation of molecular adsorption on a liquid/zeolite interface by second-harmonic generation.* Langmuir **25** (8), 4256–4261 (2009).

[114] V. Valev, A. Kirilyuk, F. Dalla Longa, et al., *Observation of periodic oscillations in magnetization-induced second harmonic generation at the Mn-Co interface.* Physical Review B **75** (1), 3–6 (2007).

[115] H. Zhang, D. Zelmon, L. Deng, *Optical limiting behavior of nanosized polyicosahedral gold-silver clusters based on third-order nonlinear optical effects.* Journal of the American Chemical Society **123**, 11300–11301 (2001).

[116] M. Sheik-Bahae, A. Said, T.-H. Wei, et al., *Sensitive measurement of optical nonlinearities using a single beam.* IEEE Journal of Quantum Electronics **26** (4), 760–769 (1990).

[117] L. Brzozowski, E. Sargent, *Azobenzenes for photonic network applications: Third-order nonlinear optical properties.* Journal of Materials Science: Materials in Electronics **2**, 483–489 (2001).

[118] Y.-C. Chen, N. R. Raravikar, L. S. Schadler, et al., *Ultrafast optical switching properties of single-wall carbon nanotube polymer composites at 1.55 μm.* Applied Physics Letters **81** (6), 975 (2002).

[119] C. P. Singh, K. S. Bindra, G. M. Bhalerao, et al., *Investigation of optical limiting in iron oxide nanoparticles.* Optics Express **16** (12), 8440–8450 (2008).

[120] D. Cotter, *Conversion from 3371 to 1124A by nonresonant optical frequency tripling in compressed krypton gas.* Optics Letters **4** (5), 134–136 (1979).

[121] F. Castet, V. Rodriguez, J.-L. Pozzo, et al., *Design and characterization of molecular nonlinear optical switches.* Accounts of Chemical Research **46** (11), 2656–2565 (2013).

[122] M. Bloemen, W. Brullot, C. Denis, et al., *Core-shell nanoparticles as enhanced probes for imaging applications. In Proceedings of SPIE*, (Edited by J. Popp, W. Drexler, V. V. Tuchin, et al.), volume 8427, 84272Q1–7 (2012).

[123] M. Faraday, *Experimental Researches in Electricity Vol. III.* Bernard Quaritch, London (1855).

[124] A. K. Zvezdin, V. A. Kotov, *Modern Magnetooptics and Magnetooptical Materials.* IOP Publishing, Bristol (1997).

[125] P. Hansen, M. Rosenkranz, K. Witter, *Temperature and wavelength dependence of the Faraday ellipticity of lead-substituted gadolinium iron garnet films.* Physical Review B **25** (7), 4396–4405 (1982).

[126] K. Thamaphat, P. Bharmanee, P. Limsuwan, *Measurement of Verdet constant in diamagnetic glass using Faraday effect.* Kasetsart Journal **40**, 18–23 (2006).

[127] S. Pakdel, M. Miri, *Faraday rotation and circular dichroism spectra of gold and silver nanoparticle aggregates.* Physical Review B **86** (23), 235445 (2012).

[128] G. M. Wysin, V. Chikan, N. Young, et al., *Effects of interband transitions on Faraday rotation in metallic nanoparticles.* Journal of Physics: Condensed Matter **25** (32), 325302 (2013).

[129] J. Furdyna, M. Brodwin, *Dependence of the free-carrier Faraday ellipticity in semiconductors on scattering mechanisms.* Physical Review **124** (3), 740–744 (1961).

[130] S. Vandendriessche, V. K. Valev, T. Verbiest, *Faraday rotation and its dispersion in the visible region for saturated organic liquids.* Physical Chemistry Chemical Physics **14** (6), 1860–1864 (2012).

[131] E. Botek, B. Champagne, T. Verbiest, et al., *A joint theoretical-experimental investigation of the Faraday effect in benzene, toluene, and p-xylene.* ChemPhysChem **7** (8), 1654–1656 (2006).

[132] K. Binnemans, C. Görller-Walrand, *Magnetic circular dichroism and optical absorption spectra of holmium-doped fluorozirconate (ZBLAN) glass: a prospective study.* Journal of Alloys and Compounds **225**, 80–84 (1995).

[133] P. Gangopadhyay, R. Voorakaranam, A. Lopez-Santiago, et al., *Faraday rotation measurements on thin films of regioregular alkyl-substituted polythiophene derivatives.* Journal of Physical Chemistry C **112** (21), 8032–8037 (2008).

[134] F. Araoka, M. Abe, T. Yamamoto, et al., *Large Faraday rotation in a pi-conjugated poly(arylene ethynylene) thin film.* Applied Physics Express **2** (1), 011501 (2009).

[135] G. Koeckelberghs, M. Vangheluwe, K. V. Doorsselaere, et al., *Regioregularity in poly(3-alkoxythiophene)s: effects on the Faraday rotation and polymerization mechanism.* Macromolecular Rapid Communications **27** (22), 1920–1925 (2006).

[136] I. Crassee, J. Levallois, A. L. Walter, et al., *Giant Faraday rotation in single- and multilayer graphene.* Nature Physics **7** (1), 48–51 (2010).

[137] S. Vandendriessche, S. Van Cleuvenbergen, P. Willot, et al., *Giant Faraday Rotation in Mesogenic Organic Molecules.* Chemistry of Materials **25** (7), 1139–1143 (2013).

[138] D. Budker, D. Kimball, S. Rochester, et al., *Sensitive magnetometry based on nonlinear magneto-optical rotation.* Physical Review A **62** (4), 043403 (2000).

[139] S. Zaidi, R. Tatam, *Faraday-effect magnetometry: compensation for the temperature-dependent Verdet constant.* Measurement Science and Technology **1471** (1994).

[140] N. Inoue, K. Yamasawa, *Stabilization of temperature dependence of verdet constant of bi-doped garnet and development of high sensitive optical fiber magnetic field sensor.* Electrical Engineering in Japan **117** (1) (1996).

[141] L. Martinez, F. Cecelja, R. Rakowski, *A novel magneto-optic ferrofluid material for sensor applications.* Sensors and Actuators **124**, 438–443 (2005).

[142] A. Lvovsky, B. Sanders, W. Tittel, *Optical quantum memory.* Nature Photonics **3**, 706–714 (2009).

[143] R. Bahuguna, M. Mina, R. Weber, *Mach–Zehnder interferometric switch utilizing Faraday rotation.* IEEE Transactions on Magnetics **43** (6), 2680–2682 (2007).

[144] H. Dötsch, N. Bahlmann, O. Zhuromskyy, et al., *Applications of magneto-optical waveguides in integrated optics: review.* Journal of the Optical Society of America B **22** (1), 240 (2005).

[145] H. Takeda, S. John, *Compact optical one-way waveguide isolators for photonic-band-gap microchips.* Physical Review A **78** (2), 023804 (2008).

[146] K. Shiraishi, F. Tajima, S. Kawakami, *Compact Faraday rotator for an optical isolator using magnets arranged with alternating polarities.* Optics Letters **11** (2), 82 (1986).

[147] A. Tervonen, A. Khanna, A. Säynätjoki, et al., *Modeling study of nonreciprocal phase shift in magnetooptic asymmetric slot waveguides.* Journal of Lightwave Technology **29** (5), 656–660 (2011).

[148] A. Lopez-Santiago, P. Gangopadhyay, J. Thomas, et al., *Faraday rotation in magnetite-polymethylmethacrylate core-shell nanocomposites with high optical quality.* Applied Physics Letters **95** (14), 143302 (2009).

[149] F. Bentivegna, M. Nyvlt, J. Ferre, et al., *Magnetically textured γ-Fe2O3 nanoparticles in a silica gel matrix: Optical and magneto-optical properties.* Journal of Applied Physics **85** (4), 2270–2278 (1999).

[150] D. Jamon, F. Donatini, a. Siblini, et al., *Experimental investigation on the magneto-optic effects of ferrofluids via dynamic measurements.* Journal of Magnetism and Magnetic Materials **321** (9), 1148–1154 (2009).

[151] P. Drude, *Zur Elektronentheorie der Metalle.* Annalen der Physik **306** (3), 566–613 (1900).

[152] M. Ware, *Photographic Printing in Colloidal Gold.* The Journal of Photographic Science **42** (5), 157–161 (1994).

[153] P. Charlier, J. Poupon, I. Huynh-Charlier, et al., *Fatal alchemy.* BMJ **339**, 1402–1403 (2009).

[154] M. Faraday, *The Bakerian Lecture: Experimental Relations of Gold (and Other Metals) to Light.* Philosophical Transactions of the Royal Society of London **147**, 145–181 (1857).

[155] R. Zsigmondy, *Uber wässrige Lösungen metallischen Goldes.* Justus Liebigs Annalen der Chemie **301** (1), 29–54 (1898).

[156] G. Mie, *Beiträge zur Optik trüber Medien, speziell kolloidaler Metallösungen.* Annalen der Physik **330** (3), 377–445 (1908).

[157] K.-S. Lee, M. a. El-Sayed, *Gold and silver nanoparticles in sensing and imaging: sensitivity of plasmon response to size, shape, and metal composition.* Journal of Physical Chemistry B **110** (39), 19220–19225 (2006).

[158] S. Link, M. A. El-Sayed, *Shape and size dependence of radiative, non-radiative and photothermal properties of gold nanocrystals.* International Reviews in Physical Chemistry **19** (3), 409–453 (2000).

[159] K.-S. Lee, M. a. El-Sayed, *Dependence of the enhanced optical scattering efficiency relative to that of absorption for gold metal nanorods on aspect ratio, size, end-cap shape, and medium refractive index.* Journal of Physical Chemistry B **109** (43), 20331–20338 (2005).

[160] P. K. Jain, K. S. Lee, I. H. El-Sayed, et al., *Calculated absorption and scattering properties of gold nanoparticles of different size, shape, and composition: applications in biological imaging and biomedicine.* Journal of Physical Chemistry B **110** (14), 7238–7248 (2006).

[161] G. Armelles, A. Cebollada, A. García-Martín, et al., *Magnetoplasmonics: Combining Magnetic and Plasmonic Functionalities.* Advanced Optical Materials **1** (1), 10–35 (2013).

[162] U. Kreibig, M. Vollmer, *Optical properties of Metal Clusters.* Springer, Berlin, Germany (1995).

[163] R. Thomas, R. Swathi, *Organization of metal nanoparticles for surface-enhanced spectroscopy: a difference in size matters.* Journal of Physical Chemistry C **116**, 21982–21991 (2012).

[164] R. Naraoka, H. Okawa, K. Hashimoto, et al., *Surface plasmon resonance enhanced second-harmonic generation in Kretschmann configuration.* Optics Communications **248** (1-3), 249–256 (2005).

[165] P. Jais, C. V. Bilderling, A. Bragas, *Plasmon-enhanced second harmonic generation in semiconductor quantum dots close to metal nanoparticles.* Papers in Physics **3**, 1–5 (2011).

[166] K. Chen, C. Durak, J. Heflin, et al., *Plasmon-enhanced second-harmonic generation from ionic self-assembled multilayer films.* Nano Letters **7** (2), 254–258 (2007).

[167] C. Hubert, L. Billot, P.-M. Adam, et al., *Role of surface plasmon in second harmonic generation from gold nanorods.* Applied Physics Letters **90** (18), 181105 (2007).

[168] P. K. Jain, Y. Xiao, R. Walsworth, et al., *Surface plasmon resonance enhanced magneto-optics (SuPREMO): Faraday rotation enhancement in gold-coated iron oxide nanocrystals.* Nano Letters **9** (4), 1644–1650 (2009).

[169] R. K. Dani, H. Wang, S. H. Bossmann, et al., *Faraday rotation enhancement of gold coated Fe2O3 nanoparticles: comparison of experiment and theory.* Journal of Chemical Physics **135** (22), 224502 (2011).

[170] P. K. Jain, M. A. El-Sayed, *Plasmonic coupling in noble metal nanostructures.* Chemical Physics Letters **487** (4-6), 153–164 (2010).

[171] L. Gunnarsson, T. Rindzevicius, J. Prikulis, et al., *Confined plasmons in nanofabricated single silver particle pairs: experimental observations of strong interparticle interactions.* Journal of Physical Chemistry B **109** (3), 1079–1087 (2005).

[172] M. Kasha, H. Rawls, M. El-Bayoumi, *The exciton model in molecular spectroscopy.* Pure and Applied Chemistry **11** (3-4), 371–392 (1965).

[173] B. Niesen, B. P. Rand, P. Van Dorpe, et al., *Near-field interactions between metal nanoparticle surface plasmons and molecular excitons in thin-films. Part II: emission.* Journal of Physical Chemistry C **116** (45), 24215–24223 (2012).

[174] M. Van der Auweraer, I. Scheblykin, *One-dimensional J-aggregates : Dependence of the properties of the exciton band on the model of the intermolecular coupling.* Chemical Physics **275**, 285–306 (2002).

[175] E. K. Payne, K. L. Shuford, S. Park, et al., *Multipole plasmon resonances in gold nanorods.* Journal of Physical Chemistry B **110** (5), 2150–2154 (2006).

[176] N. J. Halas, S. Lal, W.-S. Chang, et al., *Plasmons in strongly coupled metallic nanostructures.* Chemical Reviews **111** (6), 3913–3961 (2011).

[177] J. R. Krenn, G. Schider, W. Rechberger, et al., *Design of multipolar plasmon excitations in silver nanoparticles.* Applied Physics Letters **77** (21), 3379 (2000).

[178] K.-H. Su, Q.-H. Wei, X. Zhang, et al., *Interparticle coupling effects on plasmon resonances of nanogold particles.* Nano Letters **3** (8), 1087–1090 (2003).

[179] M. Benkovičová, K. Végsö, P. Šiffalovič, et al., *Preparation of sterically stabilized gold nanoparticles for plasmonic applications.* Chemical Papers **67** (9), 1225–1230 (2013).

[180] P. Alexandridis, *Gold nanoparticle synthesis, morphology control, and stabilization facilitated by functional polymers.* Chemical Engineering & Technology **34** (1), 15–28 (2011).

[181] Q. H. Tran, V. Q. Nguyen, A.-T. Le, *Silver nanoparticles: synthesis, properties, toxicology, applications and perspectives.* Advances in Natural Sciences: Nanoscience and Nanotechnology **4** (3), 033001 (2013).

[182] S. Prabhu, E. K. Poulose, *Silver nanoparticles: mechanism of antimicrobial action, synthesis, medical applications, and toxicity effects.* International Nano Letters **2** (1), 32 (2012).

[183] P. Nalawade, T. Mukherjee, S. Kapoor, *Green synthesis of gold nanoparticles using glycerol as a reducing agent.* Advances in Nanoparticles **2**, 78–86 (2013).

[184] X. Lu, M. Rycenga, S. E. Skrabalak, et al., *Chemical synthesis of novel plasmonic nanoparticles.* Annual Review of Physical Chemistry **60**, 167–192 (2009).

[185] M. Brust, M. Walker, D. Bethell, et al., *Synthesis of thiol-derivatised gold nanoparticles in a two-phase liquid–liquid system.* Chemical Communications (7), 801–802 (1994).

[186] B. Mondal, N. Kamatham, S. R. Samanta, et al., *Synthesis, characterization, guest inclusion, and photophysical studies of gold nanoparticles stabilized with carboxylic acid groups of organic cavitands.* Langmuir **29** (41), 12703–12709 (2013).

[187] N. Li, P. Zhao, D. Astruc, *Anisotropic gold nanoparticles: synthesis, properties, applications, and toxicity.* Angewandte Chemie (International ed. in English) **53**, 1756–1789 (2014).

[188] J. Kimling, M. Maier, B. Okenve, et al., *Turkevich method for gold nanoparticle synthesis revisited.* Journal of Physical Chemistry B **110** (32), 15700–15707 (2006).

[189] M. Grzelczak, J. Pérez-Juste, P. Mulvaney, et al., *Shape control in gold nanoparticle synthesis.* Chemical Society Reviews **37** (9), 1783–1791 (2008).

[190] C. Keating, M. Musick, M. Keefe, et al., *Kinetics and thermodynamics of Au colloid monolayer self-assembly: undergraduate experiments in surface and nanomaterials chemistry.* Journal of chemical education **76** (7), 949 (1999).

[191] K. M. Abou El-Nour, A. Eftaiha, A. Al-Warthan, et al., *Synthesis and applications of silver nanoparticles.* Arabian Journal of Chemistry **3** (3), 135–140 (2010).

[192] M. Moritz, M. Geszke-Moritz, *The newest achievements in synthesis, immobilization and practical applications of antibacterial nanoparticles.* Chemical Engineering Journal **228**, 596–613 (2013).

[193] X. Z. Huang, X. X. Zhong, Y. Lu, et al., *Plasmonic Ag nanoparticles via environment-benign atmospheric microplasma electrochemistry.* Nanotechnology **24** (9), 095604 (2013).

[194] A. Chauhan, S. Zubair, S. Tufail, et al., *Fungus-mediated biological synthesis of gold nanoparticles: potential in detection of liver cancer.* International Journal of Nanomedicine **6**, 2305–2319 (2011).

[195] A. Govorov, H. Richardson, *Generating heat with metal nanoparticles.* Nano Today **2** (1), 30–38 (2007).

[196] S. Bhattacharyya, R. A. Kudgus, R. Bhattacharya, et al., *Inorganic nanoparticles in cancer therapy.* Pharmaceutical Research **28** (2), 237–259 (2011).

[197] R. R. Letfullin, C. B. Iversen, T. F. George, *Modeling nanophotothermal therapy: kinetics of thermal ablation of healthy and cancerous cell organelles and gold nanoparticles.* Nanomedicine : Nanotechnology, Biology, and Medicine **7** (2), 137–145 (2011).

[198] M. Y. Spivak, R. V. Bubnov, I. M. Yemets, et al., *Gold nanoparticles - the theranostic challenge for PPPM: nanocardiology application.* The EPMA Journal **4** (1), 18 (2013).

[199] S. Sershen, S. Westcott, N. Halas, et al., *Temperature-sensitive polymer–nanoshell composites for photothermally modulated drug delivery.* Journal of Biomedical Materials Research **51** (3), 293–298 (2000).

[200] E. C. Dreaden, M. a. Mackey, X. Huang, et al., *Beating cancer in multiple ways using nanogold.* Chemical Society Reviews **40** (7), 3391–404 (2011).

[201] A. Agarwal, S. W. Huang, M. O'Donnell, et al., *Targeted gold nanorod contrast agent for prostate cancer detection by photoacoustic imaging.* Journal of Applied Physics **102** (6), 064701 (2007).

[202] L. Tong, Q. Wei, A. Wei, et al., *Gold nanorods as contrast agents for biological Imaging: optical properties, surface conjugation and photothermal effects.* Photochemistry and Photobiology **85** (1), 21–32 (2009).

[203] A. Taglietti, Y. a. Diaz Fernandez, E. Amato, et al., *Antibacterial activity of glutathione-coated silver nanoparticles against Gram positive and Gram negative bacteria.* Langmuir **28** (21), 8140–8148 (2012).

[204] Z.-J. Jiang, C.-Y. Liu, L.-W. Sun, *Catalytic properties of silver nanoparticles supported on silica spheres.* Journal of Physical Chemistry B **109** (5), 1730–1735 (2005).

[205] N. Pradhan, A. Pal, T. Pal, *Silver nanoparticle catalyzed reduction of aromatic nitro compounds.* Colloids and Surfaces A: Physicochemical and Engineering Aspects **196** (2-3), 247–257 (2002).

[206] M. Stratakis, H. Garcia, *Catalysis by supported gold nanoparticles: beyond aerobic oxidative processes.* Chemical Reviews **112** (8), 4469–506 (2012).

[207] T. Mitsudome, K. Kaneda, *Gold nanoparticle catalysts for selective hydrogenations.* Green Chemistry **15** (10), 2636 (2013).

[208] M. Haruta, *When gold is not noble: catalysis by nanoparticles.* Chemical Record **3** (2), 75–87 (2003).

[209] D. Thompson, *Using gold nanoparticles for catalysis.* Nano Today **2** (4), 40–43 (2007).

[210] J. Xuan, X.-d. Jia, L.-P. Jiang, et al., *Gold nanoparticle-assembled capsules and their application as hydrogen peroxide biosensor based on hemoglobin.* Bioelectrochemistry **84**, 32–7 (2012).

[211] Y. Li, H. J. Schluesener, S. Xu, *Gold nanoparticle-based biosensors.* Gold Bulletin **43** (1), 29–41 (2010).

[212] J. Homola, *Surface plasmon resonance sensors for detection of chemical and biological species.* Chemical Reviews **108** (2), 462–493 (2008).

[213] W. Cui, W. Lu, Y. Zhang, et al., *Gold nanoparticle ink suitable for electric-conductive pattern fabrication using in ink-jet printing technology.* Colloids and Surfaces A: Physicochemical and Engineering Aspects **358** (1-3), 35–41 (2010).

[214] O. Neumann, C. Feronti, A. D. Neumann, et al., *Compact solar autoclave based on steam generation using broadband light-harvesting nanoparticles.* Proceedings of the National Academy of Sciences of the United States of America **110** (29), 11677–11681 (2013).

[215] B. Kenens, M. Rybachuk, J. Hofkens, et al., *Silver Nanowires Terminated by Metallic Nanoparticles as Effective Plasmonic Antennas.* Journal of Physical Chemistry C **117**, 2547–2553 (2013).

[216] M.-C. Chen, Y.-L. Yang, S.-W. Chen, et al., *Self-assembled monolayer immobilized gold nanoparticles for plasmonic effects in small molecule organic photovoltaic.* Applied Materials & Interfaces **5**, 511–517 (2013).

[217] M. Giangregorio, M. Losurdo, G. Bianco, et al., *Synthesis and characterization of plasmon resonant gold nanoparticles and graphene for photovoltaics.* Materials Science and Engineering: B **178** (9), 559–567 (2013).

[218] M.-K. Chuang, S.-W. Lin, F.-C. Chen, et al., *Gold nanoparticle-decorated graphene oxides for plasmonic-enhanced polymer photovoltaic devices.* Nanoscale **6** (3), 1573–1579 (2014).

[219] F. Monnaie, W. Brullot, T. Verbiest, et al., *Synthesis of end-group functionalized P3HT: general protocol for P3HT/nanoparticle hybrids.* Macromolecules **46** (21), 8500–8508 (2013).

[220] K. L. Kelly, E. Coronado, L. L. Zhao, et al., *The optical properties of metal nanoparticles: the influence of size, shape, and dielectric environment.* Journal of Physical Chemistry B **107**, 668–677 (2003).

[221] O. Peña Rodríguez, P. P. González Pérez, U. Pal, *MieLab: a software tool to perform calculations on the scattering of electromagnetic waves by multilayered spheres.* International Journal of Spectroscopy **2011**, 583743 (2011).

[222] E. Moreno, D. Erni, C. Hafner, et al., *Multiple multipole method with automatic multipole setting applied to the simulation of surface plasmons in metallic nanostructures.* Journal of the Optical Society of America A **19** (1), 101–111 (2002).

[223] J.-Y. Lu, K.-P. Chiu, H.-Y. Chao, et al., *Multiple metallic-shell nanocylinders for surface-enhanced spectroscopes.* Nanoscale Research Letters **6** (1), 173 (2011).

[224] N. K. Balla, P. T. C. So, C. J. R. Sheppard, *Second harmonic scattering from small particles using Discrete Dipole Approximation.* Optics Express **18** (21), 21603–21611 (2010).

[225] P. J. Flatau, B. T. Draine, *Fast near field calculations in the discrete dipole approximation for regular rectilinear grids.* Optics Express **20** (2), 1247 (2012).

[226] B. T. Draine, P. J. Flatau, *Discrete-dipole approximation for scattering calculations.* Journal of the Optical Society of America A **11** (4), 1491 (1994).

[227] B. T. Draine, P. J. Flatau, *Discrete-dipole approximation for periodic targets: theory and tests.* Journal of the Optical Society of America. A **25** (11), 2693–2703 (2008).

[228] H. DeVoe, *Optical properties of molecular aggregates. II. classical theory of the refraction, absorption, and optical activity of solutions and crystals.* Journal of Chemical Physics **43**, 3199 (1965).

[229] E. Purcell, C. Pennypacker, *Scattering and absorption of light by nonspherical dielectric grains.* The Astrophysical Journal **186**, 705–714 (1973).

[230] J. R. Lakowicz, *Principles of fluorescence spectroscopy.* Springer, third edition (2006).

[231] V. K. Valev, J. J. Baumberg, C. Sibilia, et al., *Chirality and chiroptical effects in plasmonic nanostructures: fundamentals, recent progress, and outlook.* Advanced Materials **25** (18), 2517–2534 (2013).

[232] Y. El Harfouch, E. Benichou, F. Bertorelle, et al., *Hyper Rayleigh scattering from gold nanorods.* Journal of Physical Chemistry C **118**, 609–616 (2013).

[233] M. Lippitz, M. a. van Dijk, M. Orrit, *Third-harmonic generation from single gold nanoparticles.* Nano Letters **5** (4), 799–802 (2005).

[234] G. X. Li, T. Li, H. Liu, et al., *Spectral analysis of enhanced third harmonic generation from plasmonic excitations.* Applied Physics Letters **98** (26), 261909 (2011).

[235] B. Metzger, M. Hentschel, M. Lippitz, et al., *Third-harmonic spectroscopy and modeling of the nonlinear response of plasmonic nanoantennas.* Optics Letters **37** (22), 4741–4743 (2012).

[236] T. Utikal, T. Zentgraf, T. Paul, et al., *Towards the origin of the nonlinear response in hybrid plasmonic systems.* Physical Review Letters **106** (13), 133901 (2011).

[237] S. Xiao, H. Gong, X. Su, et al., *Two- and three-photon luminescence of Au nanoparticles and resonant energy transfer from CdSe quantum dots.* Journal of Physical Chemistry C **111** (28), 10185–10189 (2007).

[238] R. Farrer, F. Butterfield, V. Chen, et al., *Highly efficient multiphoton-absorption-induced luminescence from gold nanoparticles.* Nano Letters **5** (6), 1139–1142 (2005).

[239] S. Viarbitskaya, L. Ryderfors, T. Mikaelsson, et al., *Luminescence enhancement from silica-coated gold nanoparticle agglomerates following multi-photon excitation.* Journal of Fluorescence **21**, 257–264 (2011).

[240] B. Sepúlveda, J. B. González-Díaz, A. García-Martín, et al., *Plasmon-induced magneto-optical activity in nanosized gold disks.* Physical Review Letters **104** (14), 1–4 (2010).

[241] G. X. Du, T. Mori, M. Suzuki, et al., *Magneto-optical effects in nanosandwich array with plasmonic structure of Au/[Co/Pt]n/Au.* Journal of Applied Physics **107** (9), 09A928 (2010).

[242] G. X. Du, T. Mori, M. Suzuki, et al., *Evidence of localized surface plasmon enhanced magneto-optical effect in nanodisk array.* Applied Physics Letters **96** (8), 081915 (2010).

[243] M. Osada, N. Hajduková-Šmídová, K. Akatsuka, et al., *Gigantic plasmon resonance effects on magneto-optical activity of molecularly thin ferromagnets near gold surfaces.* Journal of Materials Chemistry C **1** (14), 2520 (2013).

[244] J. Y. Chin, T. Steinle, T. Wehlus, et al., *Nonreciprocal plasmonics enables giant enhancement of thin-film Faraday rotation.* Nature Communications **4**, 1599 (2013).

[245] V. I. Belotelov, I. a. Akimov, M. Pohl, et al., *Enhanced magneto-optical effects in magnetoplasmonic crystals.* Nature Nanotechnology **6** (6), 370–376 (2011).

[246] V. Valev, A. Silhanek, W. Gillijns, et al., *Plasmons reveal the direction of magnetization in nickel nanostructures.* ACS Nano **5** (1), 91–96 (2011).

[247] J. F. Torrado, J. B. González-Díaz, M. U. González, et al., *Magneto-optical effects in interacting localized and propagating surface plasmon modes.* Optics Express **18** (15), 15635–15642 (2010).

[248] G. Armelles, A. Cebollada, A. García-Martín, et al., *Magnetoplasmonic nanostructures: systems supporting both plasmonic and magnetic properties.* Journal of Optics A **11** (11), 114023 (2009).

[249] C. S. Levin, C. Hofmann, T. a. Ali, et al., *Magnetic-plasmonic core-shell nanoparticles.* ACS Nano **3** (6), 1379–1388 (2009).

[250] B. E. Brinson, J. B. Lassiter, C. S. Levin, et al., *Nanoshells made easy: improving Au layer growth on nanoparticle surfaces.* Langmuir **24** (24), 14166–14171 (2008).

[251] I. Robinson, L. D. Tung, S. Maenosono, et al., *Synthesis of core-shell gold coated magnetic nanoparticles and their interaction with thiolated DNA.* Nanoscale **2** (12), 2624–30 (2010).

[252] T. Hienpham, C. Cao, S. Sim, *Application of citrate-stabilized gold-coated ferric oxide composite nanoparticles for biological separations.* Journal of Magnetism and Magnetic Materials **320** (15), 2049–2055 (2008).

[253] J. L. Lyon, D. A. Fleming, M. B. Stone, et al., *Synthesis of Fe oxide core/Au shell nanoparticles by iterative hydroxylamine seeding.* Nano Letters **4** (4), 719–723 (2004).

[254] J. Lim, A. Eggeman, F. Lanni, et al., *Synthesis and single-particle optical detection of low-polydispersity plasmonic-duperparamagnetic nanoparticles.* Advanced Materials **20** (9), 1721–1726 (2008).

[255] G. Sharma, P. Jeevanandam, *A facile synthesis of multifunctional iron oxide@Ag core-shell Nanoparticles and their catalytic applications.* European Journal of Inorganic Chemistry **36**, 6126–6136 (2013).

[256] Y. Wang, S. Ravindranath, *Separation and detection of multiple pathogens in a food matrix by magnetic SERS nanoprobes.* Analytical and Bioanalytical Chemistry **399** (3), 1271–1278 (2011).

[257] M. Caminale, L. Anghinolfi, E. Magnano, et al., *Tuning the magneto-optical response of iron oxide nanocrystals in Au- and Ag-based plasmonic media.* ACS Applied Materials & Interfaces **5** (6), 1955–1960 (2013).

[258] N. Hassan, V. Cabuil, A. Abou-Hassan, *Assembling magneto-plasmonic microcapsules using a microfluidic device.* Chemical Communications **49** (4), 412–414 (2013).

[259] L. Wang, J. Luo, M. M. Maye, et al., *Iron oxide–gold core–shell nanoparticles and thin film assembly.* Journal of Materials Chemistry **15** (18), 1821 (2005).

[260] J. Xie, S. Lee, X. Chen, *Nanoparticle-based theranostic agents.* Advanced Drug Delivery Reviews **62** (11), 1064–1079 (2010).

[261] P. Rai, S. Mallidi, X. Zheng, et al., *Development and applications of photo-triggered theranostic agents.* Advanced Drug Delivery Reviews **62** (11), 1094–1124 (2010).

[262] W. Chen, N. Xu, L. Xu, et al., *Multifunctional magnetoplasmonic nanoparticle assemblies for cancer therapy and diagnostics (theranostics).* Macromolecular Rapid Communications **31**, 228–236 (2010).

[263] J. Lim, S. A. Majetich, *Composite magnetic–plasmonic nanoparticles for biomedicine: Manipulation and imaging.* Nano Today **8** (1), 98–113 (2013).

[264] C. Hoskins, Y. Min, M. Gueorguieva, et al., *Hybrid gold-iron oxide nanoparticles as a multifunctional platform for biomedical application.* Journal of Nanobiotechnology **10**, 27 (2012).

[265] H. W. Chen, A. Murugadoss, T. S. A. Hor, et al., *Magnetically recoverable magnetite/gold catalyst stabilized by poly(N-vinyl-2-pyrrolidone) for aerobic oxidation of alcohols.* Molecules **16** (1), 149–161 (2011).

[266] P. Li, L. Wang, L. Zhang, et al., *Magnetic nanoparticles-supported palladium: a highly efficient and reusable catalyst for the Suzuki, Sonogashira, and Heck reactions.* Advanced Synthesis & Catalysis **354** (7), 1307–1318 (2012).

[267] Y. Deng, Y. Cai, Z. Sun, et al., *Multifunctional mesoporous composite microspheres with well-designed nanostructure: a highly integrated catalyst system.* Journal of the American Chemical Society **132** (24), 8466–8473 (2010).

[268] P. Quaresma, I. Osório, G. Dória, et al., *Star-shaped magnetite@gold nanoparticles for protein magnetic separation and SERS detection.* RSC Advances **4** (8), 3659 (2014).

[269] H. Salehizadeh, E. Hekmatian, M. Sadeghi, et al., *Synthesis and characterization of core-shell FeO-gold-chitosan nanostructure.* Journal of Nanobiotechnology **10**, 3 (2012).

[270] Y. Li, T. Verbiest, R. Strobbe, et al., *Silver nanoparticles as localized "nano-heaters" under LED light irradiation to improve membrane performance.* Journal of Materials Chemistry A **2** (9), 3182 (2014).

[271] Y. Li, T. Verbiest, I. Vankelecom, *Improving the flux of PDMS membranes via localized heating through incorporation of gold nanoparticles.* Journal of Membrane Science **428**, 63–69 (2013).

[272] A. M. Gajda, M. Ulbricht, *Magnetic Fe3O4 nanoparticle heaters in smart porous membrane valves.* Journal of Materials Chemistry B **2** (10), 1317 (2014).

[273] K. Chiu, J. Quinn, *Magnetoplasma surface waves in metals.* Physical Review B **5** (12), 4707–4709 (1972).

[274] K. Chiu, J. Quinn, *Magnetoplasma surface waves in polar semiconductors: retardation effects.* Physical Review Letters **29** (9), 600–603 (1972).

[275] J. Brion, R. Wallis, A. Hartstein, et al., *Theory of surface magnetoplasmons in semiconductors.* Physical Review Letters **28** (22), 1455–1458 (1972).

[276] W. Zheng, S. Wang, D. Qian, *The magneto-optical properties of Co-Ag granular films.* Journal of Magnetism and Magnetic Materials **198-199**, 210–212 (1999).

[277] W. Zheng, L. Chen, J. Chu, *The magneto-optical Kerr effect enhancement in Co_x Ag_{1-x} granular films.* Physica Status Solidi (B) **214**, 463–470 (1999).

[278] S.-Y. Wang, W.-M. Zheng, D.-L. Qian, et al., *Study of the Kerr effect of Co x Ag 100x granular films Study of the Kerr effect of Co x Ag 100x granular films.* Journal of Applied Physics **85** (8), 5121 (1999).

[279] C. Hermann, V. Kosobukin, G. Lampel, et al., *Surface-enhanced magneto-optics in metallic multilayer films.* Physical Review B **64** (23), 235422 (2001).

[280] W. Reim, D. Weller, *Magneto-optical properties of metallic bilayer thin films.* IEEE Transactions on Magnetics **25** (5), 3752–3754 (1989).

[281] V. Safarov, V. Kosobukin, C. Hermann, et al., *Magneto-optical effects enhanced by surface plasmons in metallic multilayer films.* Physical Review Letters **73** (26), 3584–3587 (1994).

[282] H. Feil, C. Haas, *Magneto-optical Kerr effect, enhanced by the plasma resonance of charge carriers.* Physical Review Letters **58** (1), 65–68 (1987).

[283] T. Katayama, Y. Suzuki, H. Awano, et al., *Enhancement of the magneto-optical Kerr rotation in Fe/Cu bilayered films.* Physical Review Letters **60** (14), 1426–1429 (1988).

[284] V. I. Belotelov, L. E. Kreilkamp, I. a. Akimov, et al., *Plasmon-mediated magneto-optical transparency.* Nature Communications **4**, 2128 (2013).

[285] W. Barnes, A. Dereux, T. Ebbesen, *Surface plasmon subwavelength optics.* Nature **424**, 824–830 (2003).

[286] V. V. Temnov, G. Armelles, U. Woggon, et al., *Active magneto-plasmonics in hybrid metal–ferromagnet structures.* Nature Photonics **4**, 107–111 (2010).

[287] J. Gosciniak, S. I. Bozhevolnyi, T. B. Andersen, et al., *Thermo-optic control of dielectric-loaded plasmonic waveguide components.* Optics Express **18** (2), 1207–1216 (2010).

[288] A. V. Krasavin, N. I. Zheludev, *Active plasmonics: Controlling signals in Au/Ga waveguide using nanoscale structural transformations.* Applied Physics Letters **84** (8), 1416 (2004).

[289] R. A. Pala, K. T. Shimizu, N. A. Melosh, et al., *A nonvolatile plasmonic switch employing photochromic molecules.* Nano Letters **8** (5), 1506–1510 (2008).

[290] K. F. Macdonald, Z. L. Samson, M. I. Stockman, et al., *Ultrafast active plasmonics.* Nature Photonics **3**, 55–58 (2009).

[291] A. V. Kimel, A. Kirilyuk, P. A. Usachev, et al., *Ultrafast non-thermal control of magnetization by instantaneous photomagnetic pulses.* Nature **435** (7042), 655–7 (2005).

[292] B. Sepúlveda, A. Calle, L. Lechuga, et al., *Highly sensitive detection of biomolecules with the magneto-optic surface-plasmon-resonance sensor.* Optics Letters **31** (8), 1085–1087 (2006).

[293] B. Sepúlveda, L. M. Lechuga, G. Armelles, *Magnetooptic effects in surface-plasmon-polaritons slab waveguides.* Journal of Lightwave Technology **24** (2), 945–955 (2006).

[294] P. Hui, D. Stroud, *Theory of Faraday rotation by dilute suspensions of small particles.* Applied Physics Letters **50**, 950–952 (1987).

[295] T. Xia, P. Hui, D. Stroud, *Theory of Faraday rotation in granular magnetic materials.* Journal of Applied Physics **67** (6), 2736 (1990).

[296] G. Shemer, G. Markovich, *Enhancement of magneto-optical effects in magnetite nanocrystals near gold surfaces.* Journal of Physical Chemistry B **106** (36), 9195–9197 (2002).

[297] Y. Li, Q. Zhang, A. V. Nurmikko, et al., *Enhanced magnetooptical response in dumbbell-like Ag-CoFe2O4 nanoparticle pairs.* Nano Letters **5** (9), 1689–1692 (2005).

[298] A. V. Baryshev, H. Uchida, M. Inoue, *Peculiarities of plasmon-modified magneto-optical response of gold–garnet structures.* Journal of the Optical Society of America B **30** (9), 2371 (2013).

[299] H. Uchida, Y. Masuda, R. Fujikawa, et al., *Large enhancement of Faraday rotation by localized surface plasmon resonance in Au nanoparticles embedded in Bi:YIG film.* Journal of Magnetism and Magnetic Materials **321** (7), 843–845 (2009).

[300] S. Tomita, T. Kato, S. Tsunashima, et al., *Magneto-optical Kerr effects of yttrium-iron garnet thin films incorporating gold nanoparticles.* Physical Review Letters **96** (16), 167402 (2006).

[301] A. Kawashima, T. Nakanishi, T. Shibayama, et al., *Enhanced magneto-optical properties of semiconductor EuS nanocrystals assisted by surface plasmon resonance of gold nanoparticles.* Chemistry - A European Journal **19** (43), 14438–45 (2013).

[302] N. Maccaferri, A. Berger, S. Bonetti, et al., *Tuning the magneto-optical response of nanosize ferromagnetic Ni disks using the phase of localized plasmons.* Physical Review Letters **111** (16), 167401 (2013).

[303] E. Prodan, C. Radloff, N. J. Halas, et al., *A hybridization model for the plasmon response of complex nanostructures.* Science **302** (5644), 419–422 (2003).

[304] F. Moolekamp, K. Stokes, *Magnetooptical response of gold-magnetite nanocomposite films.* IEEE Transactions on Magnetics **45** (10), 4888–4891 (2009).

[305] J. Wouters, O. I. Lebedev, G. Van Tendeloo, et al., *Preparing polymer films doped with magnetic nanoparticles by spin-coating and melt-processing can induce an in-plane magnetic anisotropy.* Journal of Applied Physics **109** (7), 076105 (2011).

[306] R. Kappiyoor, M. Liangruksa, R. Ganguly, et al., *The effects of magnetic nanoparticle properties on magnetic fluid hyperthermia.* Journal of Applied Physics **108** (9), 094702 (2010).

[307] C. M. Cobley, J. Chen, E. C. Cho, et al., *Gold nanostructures: a class of multifunctional materials for biomedical applications.* Chemical Society Reviews **40** (1), 44–56 (2011).

[308] S. Chen, J. Feng, X. Guo, et al., *One-step wet chemistry for preparation of magnetite nanorods.* Materials Letters **59** (8-9), 985–988 (2005).

[309] R. V. Kumar, Y. Koltypin, X. N. Xu, et al., *Fabrication of magnetite nanorods by ultrasound irradiation.* Journal of Applied Physics **89** (11), 6324 (2001).

[310] C. Bergemann, D. Mueller-Schulte, J. Oster, et al., *Magnetic ion-exchange nano- and microparticles for medical, biochemical and molecular biological applications.* Journal of Magnetism and Magnetic Materials **194**, 45–52 (1999).

[311] C. Alexiou, R. Tietze, E. Schreiber, et al., *Cancer therapy with drug loaded magnetic nanoparticles — magnetic drug targeting.* Journal of Magnetism and Magnetic Materials **323** (10), 1404–1407 (2010).

[312] R. Weissleder, *A clearer vision for in vivo imaging.* Nature Biotechnology **19** (4), 316–317 (2001).

[313] J. Frangioni, *In vivo near-infrared fluorescence imaging.* Current Opinion in Chemical Biology **7** (5), 626–634 (2003).

[314] J. B. González-Díaz, A. García-Martín, J. M. García-Martín, et al., *Plasmonic Au/Co/Au nanosandwiches with enhanced magneto-optical activity.* Small **4** (2), 202–205 (2008).

[315] L. Wang, C. Clavero, Z. Huba, et al., *Plasmonics and enhanced magneto-optics in core-shell Co-Ag nanoparticles.* Nano Letters **11** (3), 1237–1240 (2011).

[316] S. Albaladejo, R. Gómez-Medina, L. S. Froufe-Pérez, et al., *Radiative corrections to the polarizability tensor of an electrically small anisotropic dielectric particle.* Optics Express **18** (4), 3556–3567 (2010).

[317] P. Johnson, R. Christy, *Optical constants of the noble metals.* Physical Review B **6** (12), 4370–4379 (1972).

[318] V. Goossens, J. Wielant, S. Van Gils, et al., *Optical properties of thin iron oxide films on steel.* Surface and Interface Analysis **38**, 489–493 (2006).

[319] S. Link, M. a. El-Sayed, *Size and temperature dependence of the plasmon absorption of colloidal gold nanoparticles.* Journal of Physical Chemistry B **103** (21), 4212–4217 (1999).

[320] B. T. Draine, P. J. Flatau, *User guide to the discrete dipole approximation code DDSCAT 7.1.* Technical report (2010).

[321] N. Hooshmand, P. Jain, *Plasmonic spheroidal metal nanoshells showing larger tunability and stronger near fields than their spherical counterparts: an effect of enhanced plasmon coupling.* Journal of Physical Chemistry Letters **2**, 374–378 (2011).

[322] P. N. Prasad, *Introduction to biophotonics.* John Wiley & Sons, Inc., Hoboken, NJ, USA (2003).

[323] H. Du, R.-c. A. Fuh, J. Li, et al., *Technical and Software Note PhotochemCAD: A Computer-Aided Design and Research Tool in Photochemistry.* Photochemistry and Photobiology **68** (2), 141–142 (1998).

[324] A. Schmitt, B. Hinkeldey, M. Wild, et al., *Synthesis of the core compound of the BODIPY dye class: 4,4'-difluoro-4-bora-(3a,4a)-diaza-s-indacene.* Journal of Fluorescence **19** (4), 755–758 (2009).

[325] V. S. Abraham, S. S. Nair, S. Rajesh, et al., *Magnetic field induced assembling of nanoparticles in ferrofluidic liquid thin films based on Ni_x Fe1_-x Fe2O4.* Bulletin of Materials Science **27** (2), 155–161 (2004).

[326] R. Massart, *Preparation of aqueous magnetic liquids in alkaline and acidic media.* IEEE Transactions on Magnetics **17** (2), 1247–1248 (1981).

[327] C. Barrera, A. P. Herrera, C. Rinaldi, *Colloidal dispersions of monodisperse magnetite nanoparticles modified with poly(ethylene glycol).* Journal of Colloid and Interface Science **329** (1), 107–113 (2009).

[328] R. Rosensweig, *Ferrohydrodynamics.* Courier Dover Publications, New York, USA (1997).

[329] A. S. Karakoti, S. Das, S. Thevuthasan, et al., *PEGylated inorganic nanoparticles.* Angewandte Chemie (International ed. in English) **50** (9), 1980 – 1994 (2011).

[330] P. Gangopadhyay, S. Gallet, E. Franz, et al., *Novel superparamagnetic Core(Shell) nanoparticles for magnetic targeted drug delivery and hyperthermia treatment.* IEEE Transactions on Magnetics **41** (10), 4194–4196 (2005).

[331] V. K. Valev, J. Wouters, T. Verbiest, *Precise measurements of Faraday rotation using ac magnetic fields.* American Journal of Physics **76** (7), 626 (2008).

[332] V. K. Valev, J. Wouters, T. Verbiest, *Differential detection for measurements of Faraday rotation by means of ac magnetic fields.* European Journal of Physics **29** (5), 1099–1104 (2008).

[333] M. E. Fleet, *The structure of magnetite: Symmetry of cubic spinels.* Journal of Solid State Chemistry **62** (1), 75–82 (1986).

[334] S. P. Gubin, *Magnetic Nanoparticles.* Wiley, Hoboken, NJ, USA (2009).

[335] J. Tang, M. Myers, K. a. Bosnick, et al., *Magnetite Fe3O4 nanocrystals: spectroscopic observation of aqueous oxidation kinetics.* Journal of Physical Chemistry B **107** (30), 7501–7506 (2003).

[336] J. Li, X. Liu, Y. Lin, et al., *Field modulation of light transmission through ferrofluid film.* Applied Physics Letters **91** (25), 253108 (2007).

[337] S. Wittekoek, T. Popma, J. Robertson, et al., *Magneto-optic spectra and the dielectric tensor elements of bismuth-substitued iron garnets at photon energies between 2.2-5.2 eV.* Physical Review B **12** (7), 2777–2788 (1975).

[338] M. Bass, G. Li, E. Van Stryland, *Handbook of Optics.* McGraw-Hill, third edition (2010).

[339] G. Armelles, A. Cebollada, *Magneto-optical Properties of Core-Shell Magneto-plasmonic Au-CoxFe3-xO4 Nanowires.* Langmuir **28** (24), 9127–9130 (2012).

[340] M. Tejamaya, I. Römer, R. C. Merrifield, et al., *Stability of citrate, PVP, and PEG coated silver nanoparticles in ecotoxicology media.* Environmental Science & Technology **46** (13), 7011–7017 (2012).

[341] H. R. Gwon, S. H. Lee, *Spectral and angular responses of surface plasmon resonance based on the Kretschmann prism configuration.* Materials Transactions **51** (6), 1150–1155 (2010).

[342] L. A. Lyon, D. J. Pen, M. J. Natan, *Surface plasmon resonance of Au colloid-modified Au films: particle size dependence.* Journal of Physical Chemistry B **103**, 5826–5831 (1999).

[343] T. C. Hales, S. P. Ferguson, *The Hales-Ferguson Proof. In The Kepler Conjecture*, (Edited by J. C. Lagarias), Spinger (2011).

[344] P. K. Jain, M. a. El-Sayed, *Noble metal nanoparticle pairs: effect of medium for enhanced nanosensing.* Nano Letters **8** (12), 4347–4352 (2008).

[345] S. K. Ghosh, T. Pal, *Interparticle coupling effect on the surface plasmon resonance of gold nanoparticles: from theory to applications.* Chemical Reviews **107** (11), 4797–4862 (2007).

[346] E. Ringe, M. Langille, K. Sohn, et al., *Plasmon length: a universal parameter to describe size effects in gold nanoparticles.* Journal of Physical Chemistry Letters **3**, 1479–1483 (2012).

[347] W. Brullot, R. Strobbe, M. Bynens, et al., *Layer-by-Layer synthesis and tunable optical properties of hybrid magnetic-plasmonic nanocomposites using short bifunctional molecular linkers.* Materials Letters **118**, 99–102 (2014).

[348] P. K. Jain, X. Huang, I. H. El-Sayed, et al., *Noble metals on the nanoscale: optical and photothermal properties and some applications in imaging, sensing, biology, and medicine.* Accounts of Chemical Research **41** (12), 1578–1586 (2008).

[349] P. K. Jain, W. Huang, M. a. El-Sayed, *On the universal scaling behavior of the distance decay of plasmon coupling in metal nanoparticle pairs: a plasmon ruler equation.* Nano Letters **7** (7), 2080–2088 (2007).

[350] B. Yan, S. Boriskina, B. Reinhard, *Optimizing gold nanoparticle cluster configurations (n 7) for array applications.* Journal of Physical Chemistry C **115** (11), 1–13 (2011).

[351] W. Brullot, V. K. Valev, T. Verbiest, *Magnetic-plasmonic nanoparticles for the life sciences: calculated optical properties of hybrid structures.* Nanomedicine : Nanotechnology, Biology, and Medicine **8** (5), 559–568 (2012).

[352] P. Ginzburg, A. Krasavin, Y. Sonnefraud, et al., *Nonlinearly coupled localized plasmon resonances: Resonant second-harmonic generation.* Physical Review B **86** (8), 085422 (2012).

[353] A. Slablab, L. Le Xuan, M. Zielinski, et al., *Second-harmonic generation from coupled plasmon modes in a single dimer of gold nanospheres.* Optics Express **20** (1), 220 (2011).

[354] G. F. Walsh, L. Dal Negro, *Enhanced second harmonic generation by photonic-plasmonic Fano-type coupling in nanoplasmonic arrays.* Nano Letters **13**, 3111–3117 (2013).

[355] M. Shopa, K. Kolwas, *Dipole and quadrupole surface plasmon resonance contributions in formation of near-field images of a gold nanosphere.* Opto-Electronics Review **18** (4), 421–428 (2010).

[356] J. Berthelot, G. Bachelier, M. Song, et al., *Silencing and enhancement of second-harmonic generation in optical gap antennas.* Optics Express **20** (10), 10498 (2012).

[357] J. Butet, I. Russier-Antoine, C. Jonin, *Nonlinear Mie theory for the second harmonic generation in metallic nanoshells.* JOSA B **29** (8), 2213 (2012).

[358] L. Wang, D. Dehe, T. Philippi, et al., *Electrostatic grafting of a triphenylphosphine sulfonate on SBA-15: application in palladium catalyzed hydrogenation.* Catalysis Science & Technology **2** (6), 1188 (2012).

[359] D. Espinosa, L. B. Carlsson, a. M. F. Neto, et al., *Influence of nanoparticle size on the nonlinear optical properties of magnetite ferrofluids.* Physical Review E **88** (3), 032302 (2013).

[360] Y. Sahoo, A. Goodarzi, M. T. Swihart, et al., *Aqueous ferrofluid of magnetite nanoparticles: Fluorescence labeling and magnetophoretic control.* Journal of Physical Chemistry B **109** (9), 3879–3885 (2005).

[361] N. Chekina, D. Horák, P. Jendelová, et al., *Fluorescent magnetic nanoparticles for biomedical applications.* Journal of Materials Chemistry **21** (21), 7630 (2011).

[362] A. S. Al-Kady, M. Gaber, M. M. Hussein, et al., *Structural and fluorescence quenching characterization of hematite nanoparticles.* Spectrochimica Acta. Part A, Molecular and Biomolecular Spectroscopy **83** (1), 398–405 (2011).

[363] N. Turro, P. Lakshminarasimhan, *Spectroscopic probe of the surface of Iron oxide nanocrystals.* Nano Letters **1** (4), 325–328 (2002).

[364] L. Zhang, B. Liu, S. Dong, *Bifunctional nanostructure of magnetic core luminescent shell and its application as solid-state electrochemiluminescence sensor material.* Journal of Physical Chemistry B **111** (35), 10448–10452 (2007).

[365] A. Mooradian, *Photoluminescence of Metals.* Physical Review Letters **22** (5), 185–187 (1969).

[366] J. A. Dionne, *Plasmons rock in metal bands.* Nature Materials **12**, 380–381 (2013).

[367] S. Viarbitskaya, A. Teulle, R. Marty, et al., *Tailoring and imaging the plasmonic local density of states in crystalline nanoprisms.* Nature Materials **12** (5), 426–32 (2013).

[368] M. Eichelbaum, B. E. Schmidt, H. Ibrahim, et al., *Three-photon-induced luminescence of gold nanoparticles embedded in and located on the surface of glassy nanolayers.* Nanotechnology **18** (35), 355702 (2007).

[369] L. V. Brown, H. Sobhani, J. B. Lassiter, et al., *Heterodimers: plasmonic properties of mismatched nanoparticle pairs.* ACS Nano **4** (2), 819–832 (2010).

[370] T. Pakizeh, M. Kall, *Unidirectional ultracompact optical nanoantennas.* Nano Letters **9** (6), 2343–2349 (2009).

[371] S. Sheikholeslami, Y.-w. Jun, P. K. Jain, et al., *Coupling of optical resonances in a compositionally asymmetric plasmonic nanoparticle dimer.* Nano Letters **10** (7), 2655–2560 (2010).

[372] M. Kang, J. Chen, H. Cui, et al., *Asymmetric transmission for linearly polarized electromagnetic radiation.* Optics Express **19** (9), 8347–8356 (2011).

[373] A. S. Schwanecke, V. A. Fedotov, V. V. Khardikov, et al., *Nanostructured metal film with asymmetric optical transmission.* Nano Letters **8** (9), 2940–2943 (2008).

[374] V. Fedotov, P. Mladyonov, S. Prosvirnin, et al., *Asymmetric propagation of electromagnetic waves through a planar chiral structure*. Physical Review Letters **97** (16), 167401 (2006).

[375] Z. Li, M. Mutlu, E. Ozbay, *Highly asymmetric transmission of linearly polarized waves realized with a multilayered structure including chiral metamaterials*. Journal of Physics D: Applied Physics **47** (7), 075107 (2014).

Health, safety and environment

In recent years the awareness on health, safety and environment issues in physico-chemical research contexts has drastically increased in general and certainly more specifically at the Department of Chemistry of the KU Leuven.

During the research conducted for the work presented in this dissertation all regulations and guidelines as imposed by the HSE department of the KU Leuven were followed and implemented.

Risk analysis, including chemical risks, waste treatment and others, were submitted for all chemical proceedings and processes and appropriate personal protection measures taken.

Specific to the conducted research is the use of nanoparticles. Although gold, silver and magnetite nanoparticles are used in biomedical context and have been proven to be safe in small quantities, general concerns about nanotoxicity remain. Therefore, nanoparticles were kept as much as possible as dispersions (wet) as their spreading into the environment and connected health and safety hazards are then strongly reduced. Further, nanoparticles or their dispersions were kept as much as possible under the fume hood and gloves were always worn.

When using high power lasers, all appropriate protective measures were applied as thought in laser safety courses followed in Belgium (Spectra-Physics) and in the USA (University of Arizona).

With the applied appropriate protective measures and by executing experiments with caution, risks and potential hazards were mitigated and health, safety and environmental concerns were taken into account as required.

List of publications

Articles in international peer-reviewed academic journals

10. **W. Brullot**, S. Van Cleuvenbergen, M. K. Vanbel, M. A. van der Veen, R. Paesen, M. Ameloot, T. Verbiest.
    Nonlinear optical processes in gold-magnetite nanoparticle multilayers.
    Submitted to The Journal of Physical Chemistry C (2014).
9. D. Dupont, **W. Brullot**, M. Bloemen, T. Verbiest, K. Binnemans.
    Selective uptake of rare earths from aqueous solutions by EDTA-functionalized magnetic and non-magnetic nanoparticles.
    ACS Applied Materials & Interfaces (2014). *Accepted.*
8. M. Bloemen, S. Vandendriessche, V. Goovaerts, **W. Brullot**, M. Vanbel, S. Carron, N. Geukens, T. Parac-Vogt, T. Verbiest.
    Synthesis and characterization of holmium-doped iron oxide nanoparticles.
    Materials **7**, 1155-1164 (2014).
7. **W. Brullot**, R. Strobbe, M. Bynens, M. Bloemen, PJ. Demeyer, W. Vanderlinden, S. De Feyter, V. K. Valev, T. Verbiest.
    Layer-by-Layer synthesis and tunable optical properties of hybrid magnetic-plasmonic nanocomposites using short bifunctional molecular linkers.
    Materials Letters **118**, 99-102 (2014).
6. F. Monnaie, **W. Brullot**, T. Verbiest, J. De Winter, P. Gerbeaux, A. Smeets, G. Koeckelberghs.
    Synthesis of end-group functionalized P3HT: general protocol for P3HT/nanoparticle hybrids.
    Macromolecules **46** (21), 8500-8508 (2013).
5. E. K. M. Lebbe, S. Peigneur, **W. Brullot**, T. Verbiest, J. Tytgat.
    Ala-7, His-10 and Arg-12 are crucial amino acids for activity of a

synthetically engineered μ-conotoxin.
Peptides (2013). *In Press.*

4. S. Vandendriessche, **W. Brullot**, D. Slavov, V. K. Valev, T. Verbiest.
Magneto-optical harmonic susceptometry of superparamagnetic materials.
Applied Physics Letters **102**, 161903 (2013).

3. **W. Brullot**, N. K. Reddy, J. Wouters, V. K. Valev, B. Goderis, J. Vermant, T. Verbiest.
Versatile ferrofluids based on polyethylene glycol coated iron oxide nanoparticles.
Journal of Magnetism and Magnetic Materials **324**, 1919-1925 (2012).

2. M. Bloemen, **W. Brullot**, T. T. Luong, N. Geukens, A. Gils, T. Verbiest.
Improved functionalization of oleic acid-coated iron oxide nanoparticles for biomedical applications.
Journal of Nanoparticle Research **14**, 1100 (2012).

1. **W. Brullot**, V.K. Valev, T. Verbiest.
Magnetic-plasmonic nanoparticles for the life sciences: Calculated optical properties of hybrid structures.
Nanomedicine: NBM **8** (5), 559-568 (2012).

Papers presented at international scientific conferences and symposia, published in full proceedings

3. **W. Brullot**, S. Vandendriessche, V. K. Valev, T. Verbiest.
Spectral measurements to probe the magneto-optical properties of commonly used organic dyes.
SPIE Photonics Europe, Brussels (Belgium), 16-19 April 2012
Proceedings of SPIE **8434**, 84341-G-1 (2012)

2. S. Vandendriessche, **W. Brullot**, V. K. Valev, T. Verbiest.
Switching Faraday rotation on a molecular level.
SPIE Photonics Europe, Brussels (Belgium), 16-19 April 2012
Proceedings of SPIE **8434**, 84341-E-1 (2012)

1. M. Bloemen, **W. Brullot**, C. Denis, L. Vanysacker, T. Verbiest.
Core-shell nanoparticles as enhanced probes for imaging applications.
SPIE Photonics Europe, Brussels (Belgium), 16-19 April 2012
Proceedings of SPIE **8427**, 8427-Q-1 (2012)

Meeting abstracts, presented at international scientific conferences and symposia, published or not published in proceedings or journals

8. **W. Brullot**, Stefaan Vandendriessche, Thierry Verbiest.
   Magneto-optical characterization of magnetic-plasmonic gold-magnetite hybrid nanoparticle networks (AuMag-HyNANs).
   Frontiers in Optics 2013, Orlando (U.S.A.), 6-10 October 2013
   Abstract FTh4C.1.
   Laureate OSA Emil Wolf Prize 2013 - Outstanding graduate student paper and presentation competition

7. M. K. Vanbel, R. Paesen, **W. Brullot**, S. Vandendriessche, I. Asselberghs, K. Markey, P. Valvekens, M. A. van der Veen, D. De Vos, M. Ameloot, V. K. Valev; J.-P. Locquet, T. Verbiest.
   Fast Fourier-transform second-harmonic generation (FFT-SHG) provides a solution for measuring nonlinear effects on fragile structures.
   Frontiers in Optics 2013, Orlando (U.S.A.), 6-10 October 2013
   Abstract FTu2F.5

6. **W. Brullot**, R. Strobbe, M. Bynens, M. Bloemen, PJ. Demeyer, W. Vanderlinden, S. De Feyter, V. K. Valev, T. Verbiest.
   Hybrid nanoparticle networks (HyNANs): a modular Layer-by-Layer approach to nanomaterials.
   CC3DMR 2013, Jeju Island (South Korea), 24-28 June 2013

5. G. Depotter, **W. Brullot**, T. Verbiest, K. Clays.
   In situ study of directional silver and magnetite nanoparticle coupling using second-harmonic scattering.
   CC3DMR 2013, Jeju Island (South Korea), 24-28 June 2013

4. **W. Brullot**, S. Vandendriessche, T. Verbiest.
   Magneto-optical effects in clusters of superparamagnetic iron oxide and plasmonic gold nanoparticles.
   CLEO:2013, San Jose (U.S.A.), 9-14 June 2013
   Abstract JTu4A.77

3. **W. Brullot**, T. Verbiest.
   Study of plasmonic effects on the magneto-optical response in clusters of magnetic and plasmonic nanoparticles.
   NLO50 International symposium, Barcelona (Spain), 8-10 October 2012

2. T. Verbiest, **W. Brullot**, V. K. Valev.
   Chiral and multifunctional meta-materials.

SPIE Photonics Europe, Brussels (Belgium), 16-19 April 2012
Abstract 8423-6

1. A. R. D. Voet, **W. Brullot**, M. de Maeyer.
   Analysis of protein-protein interaction based pharmacophores as a screening tool for small molecule protein-protein interaction inhibitiors.
   XXth International Symposium on Medecinal Chemistry, Vienna (Austria), 31 August - 4 September 2008
   Drugs of the Future **33** suppl. A, (2008).

Patent applications

1. Title of application: *Ferrofluid compositions*
   Inventors: **W. Brullot**, J. Wouters, T. Verbiest
   Country of filing: GB
   Date: 8 December 2010 (Journal 6342)
   Application number: GB1017975.2

FACULTY OF SCIENCE
DEPARTMENT OF CHEMISTRY
MOLECULAR IMAGING AND PHOTONICS
Celestijnenlaan 200D box 2425
B-3001 Heverlee
ward.brullot@fys.kuleuven.be